

# **An Experimental Study on Volatiles and Metals in Fluids of Magma Chambers and Porphyry Ore Deposits**

## **Dissertation**

zur Erlangung der Würde eines  
Doktors der Naturwissenschaften

- Dr. rer. nat. -

der Bayreuther Graduiertenschule für Mathematik und Naturwissenschaften

vorgelegt von

**Haihao Guo**

aus Liaoning (China)

Bayreuth, 2017

Die vorliegende Arbeit wurde in der Zeit von September 2014 bis November 2017 in Bayreuth am Bayerischen Geoinstitut unter Betreuung von Herrn Professor Dr. Hans Keppler and Dr. Andreas Audétat angefertigt.

Vollständiger Abdruck der von der Bayreuther Graduiertenschule für Mathematik und Naturwissenschaften (BayNAT) der Universität Bayreuth genehmigten Dissertation zur Erlangung des akademischen Grades eines Doktors der Naturwissenschaften (Dr. rer. nat.).

Dissertation eingereicht am: 25.07.2017

Zulassung durch das Leitungsgremium: 27.07.2017

Wissenschaftliches Kolloquium: 22.11.2017

Amtierender Direktor: Prof. Dr. Dick Schüler

Prüfungsausschuss:

Prof. Dr. Hans Keppler (Erstgutachter)

Prof. Dr. Reiner Klemd (Zweitgutachterin)

PD. Dr. Catherine McCammon (Vorsitz)

Prof. Dr. Daniel Frost

# Table of contents

Summary.....	1
Zusammenfassung.....	4
1. Introduction.....	8
1.1. Generation of arc magmas.....	8
1.2. Volatiles in arc magmas .....	10
1.3. Fluids in magma chambers.....	13
1.4. Overview of previous experimental studies on gold solubility.....	15
1.5. Postentrapmental modification of fluid inclusions.....	17
1.6. Research objective of this thesis .....	19
2. Experimental and analytical methods .....	21
2.1. High-temperature and high-pressure experiments .....	21
2.1.1. Starting materials .....	21
2.1.2. Piston cylinder experiments.....	22
2.1.3. Cold-seal pressure vessel experiments.....	23
2.2. Analytical Methods .....	27
2.2.1. Scanning electron microscopy and electron microprobe .....	27
2.2.2. Microthermometry .....	28
2.2.3. Raman spectroscopy .....	30
2.2.4. LA-ICP-MS.....	31
3. Results and discussions.....	34
3.1. Transfer of volatiles and metals from mafic to felsic magmas in composite magma chambers .....	34
3.2. Solubility of gold in oxidized, sulfur-bearing fluids at 500-850 °C and 200-230 MPa: a synthetic fluid inclusion study .....	35
3.3. Gold diffusion into and out of quartz-hosted fluid inclusions during re-equilibration experiments at 600-800 °C and 2 kbar.....	38
4. References.....	41
5. List of manuscripts and statements of author's contribution .....	53
6. Transfer of volatiles and metals from mafic to felsic magmas in composite magma chambers: an experimental study.....	54
6.1. Abstract .....	54

6.2.	Introduction .....	55
6.3.	Experimental methods.....	56
6.3.1.	Experimental strategy .....	56
6.3.2.	Starting materials .....	57
6.3.3.	High temperature and pressure experiments.....	59
6.3.4.	Analytical Methods.....	63
6.4.	Results .....	64
6.4.1.	Run products .....	64
6.4.2.	Composition of glasses and mafic run products .....	67
6.4.3.	Composition of synthetic fluid inclusions .....	69
6.4.4.	Fluid-rock partition coefficients and relative element mobilities.....	71
6.5.	Discussion .....	75
6.5.1.	Attainment of equilibrium.....	75
6.5.2.	Comparison with data from natural samples .....	76
6.5.3.	Effect of magmatic sulfides .....	79
6.5.4.	Monitors of volatile fluxing.....	80
6.6.	Conclusions .....	82
6.7.	Acknowledgments.....	83
6.8.	References .....	83
6.9.	Supplementary material.....	90
6.9.1.	Potential other reasons for the discrepancies between our experimental data and enrichment factors determined on natural fumarole condensates.....	91
6.9.2.	Determination of MSS/SM partition coefficients in natural rhyolite samples .....	94
6.9.3.	References.....	94
7.	Solubility of gold in oxidized, sulfur-bearing fluids at 500-850 °C and 200-230 MPa: a synthetic fluid inclusion study .....	100
7.1.	Abstract .....	100
7.2.	Introduction .....	100
7.3.	Methods.....	102
7.3.1.	Experimental methods .....	102
7.3.2.	Analytical methods .....	104
7.4.	Results .....	107
7.4.1.	Appearance of fluid inclusions .....	107
7.4.2.	Factors affecting Au solubility.....	109

7.4.3.	Raman spectra.....	114
7.5.	Discussion .....	116
7.5.1.	Au speciation .....	116
7.5.2.	Comparison with Au solubility data of previous studies .....	119
7.5.3.	Implications for porphyry Cu-Au ore formation .....	120
7.6.	Conclusions .....	121
7.7.	Acknowledgments .....	122
7.8.	References .....	122
7.9.	Supplementary material.....	128
7.9.1.	References.....	132
8.	Gold diffusion into and out of quartz-hosted fluid inclusions during re-equilibration experiments at 600-800 °C and 2 kbar.....	133
8.1.	Abstract .....	133
8.2.	Introduction .....	134
8.3.	Methods.....	135
8.3.1.	Experimental procedure .....	135
8.3.2.	Analytical methods .....	136
8.4.	Results .....	140
8.4.1.	Appearance of fluid inclusions .....	140
8.4.2.	Compositional modification of fluid inclusions during re-equilibration .....	140
8.5.	Discussion .....	150
8.5.1.	Interpretation of observed gains and losses .....	150
8.5.2.	Geological implications .....	151
8.6.	Conclusions .....	152
8.7.	Acknowledgements .....	153
8.8.	References .....	153
8.9.	Supplementary material.....	157
9.	In-situ infrared spectra of OH in rutile up to 1000 °C .....	163
9.1.	Abstract .....	163
9.2.	Introduction .....	163
9.3.	Methods.....	164
9.3.1.	Synthesis of hydrous rutile.....	164
9.3.2.	In situ infrared spectroscopy .....	165
9.4.	Results and discussions .....	166

9.5. Conclusion.....	171
9.6. Acknowledgments .....	172
9.7. References .....	172
Acknowledgments.....	176
Erklärung.....	177

## Summary

This thesis is a comprehensive experimental study of three topics related to the formation of magmatic-hydrothermal ore deposits: (i) the geochemical behavior of elements in fluids exsolved from mafic alkaline magmas, (ii) Au solubility in oxidized sulfur-bearing aqueous fluids that are similar to those responsible for porphyry Cu-Au ( $\pm$ Mo) deposit formation, and (iii) Au diffusion into and out of quartz-host fluid inclusions at magmatic-hydrothermal conditions.

### *Transfer of volatiles and metals from mafic to felsic magmas in composite magma chambers*

Fluid-rock partition coefficients ( $D_{\text{fluid/rock}}$ ) of Li, B, Na, S, Cl, K, Mn, Fe, Rb, Sr, Ba, Ce, Cu, Zn, Ag, Cd, Mo, As, Se, Sb, Te, W, Tl, Pb and Bi were determined experimentally at 2 kbar and 850 °C close to the solidus of mafic magmas in upper crustal magma chambers. In a first step, volatile-bearing mafic glasses were prepared by melting a natural basaltic trachyandesite in the presence of volatile-bearing fluids at 1200 °C / 10 kbar in piston cylinder presses. The hydrous glasses were then equilibrated in a second experiment at 850 °C / 2 kbar in cold-seal pressure vessels, which caused 80-90% of the melt to crystallize. After 0.5-2.0 days of equilibration, the exsolved fluids were trapped via in-situ fracturing as synthetic fluid inclusions in quartz. Both the mafic rock residue and the fluid inclusions were subsequently analyzed by laser-ablation ICP-MS for major and trace elements. Reversed experiments were conducted by equilibrating metal-bearing aqueous solutions with rock powders and then initiating the formation of fluid inclusions. The comparison of element concentrations in fluid inclusions between forward and reverse runs demonstrates that equilibrium was attained by in-situ cracking after 2 days.

In two additional runs information on relative element mobilities were obtained by reacting fluids that exsolved from crystallizing mafic magma with juxtaposed silicic melts (haplogranite and rhyolite). This method has the advantage that it is more sensitive and thus allows very fluid-immobile elements such as Ti and Zr to be studied. The combined results suggest that under the studied conditions S, Cl, Cu, Se, Br, Cd and Te are most volatile ( $D_{\text{fluid/rock}} > 10$ ), followed by Li, B, Zn, As, Ag, Sb, Cs, W, Tl, Pb and Bi ( $D_{\text{fluid/rock}} = 1-10$ ). Less volatile are Na, Mg, K, Ca, Mn, Fe, Rb, Sr, Mo and Rb ( $D_{\text{fluid/rock}} = 0.1-1$ ), and the least fluid-mobile elements are Al, Si, Ti, Zr, Ba and Ce ( $D_{\text{fluid/rock}} < 0.1$ ). This trend is broadly consistent with relative element volatilities

determined on natural high-temperature fumarole gases, although some differences exist. Based on the volatility data and measured mineral–melt and sulfide–melt partition coefficients, volatile fluxing in felsic natural samples may be identified by Cu, Se, Te and Cd-enrichment in magmatic sulfides, and by As, Se, Cd and Bi-enrichment in magmatic apatite.

### ***Solubility of gold in oxidized, sulfur-bearing fluids at 500-850 °C and 200-230 MPa: a synthetic fluid inclusion study***

Gold solubility was studied in fluids containing variable amounts of sulfate, chlorine and alkalis, at 500-850 °C and 200-230 MPa, with oxygen fugacity ranging from FMQ+1 to ~FMQ+6 (FMQ: fayalite-magnetite-quartz buffer). These experiments aimed at investigating gold solubility in oxidized, sulfur-bearing aqueous fluids similar to those responsible for porphyry Cu-Au ( $\pm$ Mo)-formation. Fluids were trapped as synthetic fluid inclusions in quartz during high P-T experiments performed in cold-seal pressure vessels and subsequently analyzed by LA-ICP-MS. Aqueous solutions containing various amounts of HCl, H<sub>2</sub>SO<sub>4</sub>, Na<sub>2</sub>SO<sub>4</sub>, LiCl, KCl, CsCl and MnCl<sub>2</sub> were prepared from analytical-grade chemicals and deionized water. Sodium chloride and elemental sulfur were added as solids. Fluid inclusions were synthesized by either growing new quartz on etched quartz in single Au capsules without oxygen buffers, or by in-situ cracking of quartz pieces in double capsules (AuPd/Au-Au) or open Au capsules with external oxygen buffers. Additionally, Raman spectra were collected in a modified hydrothermal diamond-anvil cell from quartz-hosted fluid inclusions at temperatures up to 600 °C to help identifying the nature of dissolved gold- and sulfur species.

Gold solubility was found to be affected most strongly by the HCl content of the fluid, followed by  $fO_2$ , fluid salinity and temperature. Compared to these factors, the sulfur content of the fluid has relatively little influence. At 600 °C and 230 MPa, fluids with geologically realistic HCl contents (~1.1 wt%) and salinities (7-50 wt% NaCl<sub>equiv</sub>) dissolve ~1000-3000 ppm Au at oxygen fugacities buffered by the magnetite-hematite buffer. At even more oxidized conditions (three log units above the hematite-magnetite  $fO_2$  buffer), HCl-, NaCl- and H<sub>2</sub>SO<sub>4</sub>-rich fluids can dissolve up to 5 wt% Au at 800 °C. The observed Au solubility trends suggest that most of the Au dissolved in the form of NaAuCl<sub>2</sub> in our experiments.

Natural, high-temperature fluid inclusions from porphyry Cu-Au (-Mo) deposits contain at least 100 times less Au than the solubilities predicted based on our experimental data, implying that at temperatures  $>500$  °C the natural fluids were strongly Au-undersaturated. Consequently, gold grades in Au-rich porphyries were not controlled by the precipitation of native Au, but rather by those factors that caused the precipitation of Au-bearing hydrothermal sulfides such as bornite.

### *Gold diffusion into and out of quartz-hosted fluid inclusions during re-equilibration experiments at 600-800 °C and 2 kbar*

Fluid inclusions were synthesized in quartz and re-equilibrated in cold-seal pressure vessel experiments to investigate the modification of Au concentrations in quartz-hosted fluid inclusions after entrapment. In a first step, fluid inclusions containing ~5 wt% KCl were synthesized in platinum capsules at 800 °C and 600 °C, 2 kbar. The recovered samples were then loaded into new gold capsules together with Cs-spiked, HCl- and NaCl-bearing solutions, and re-equilibrated at the same P-T conditions for 4-14 days. LA-ICP-MS analysis of 5-18 fluid inclusions before and after the re-equilibration experiments demonstrate that significant amounts of Na (up to 0.23 wt%) and Au (up to 570 ppm) were gained during the re-equilibration process. The high K-content and absence of Cs in re-equilibrated fluid inclusions proves that they did not crack open during the re-equilibration, implying that Na and Au were gained by diffusion through the quartz lattice. Reverse experiments were conducted by synthesizing Au-bearing fluid inclusions in gold capsules and then re-equilibrating them in platinum capsules, which resulted in significant Au depletion. In both type of experiments Au diffusion appears to have been driven solely by concentration gradients. We did not find any evidence for diffusional exchange with  $H^+$ , nor for Au uptake by Cu-bearing sulfide daughter crystals in  $H_2S$ -bearing experiments in which weight-percent levels of Cu diffused into the fluid inclusions due to a pH change in the external fluid.

If Au concentrations in natural, quartz-hosted fluid inclusions from magmatic-hydrothermal ore deposits are affected by re-equilibration, they most likely lost Au rather than gained it. At temperatures below 400 °C, diffusional loss or gain of Au is considered unlikely in magmatic-hydrothermal systems, but potentially was significant in samples from mesothermal Au gold deposits.

## **Zusammenfassung**

Diese Dissertation beschreibt die umfassende experimentelle Studie dreier Themen, die sich auf die Bildung von magmatisch-hydrothermalen Erzvorkommen beziehen: (i) das geochemische Verhalten von Elementen in Fluiden, die sich aus mafischen, alkalischen Magmen entmischen, (ii) Goldlöslichkeit in oxidierten, schwefelhaltigen wässrigen Fluiden, ähnlich jenen, die für die Entstehung von porphyrischen Cu-Au(-Mo)-Lagerstätten verantwortlich sind, und (iii) Golddiffusion in und aus Fluideinschlüssen in Quarz unter magmatisch-hydrothermalen Bedingungen.

### ***Transfer von volatilen Elementen und Metallen von mafischen zu felsischen Magmen in gemischten Magmakammern***

Die Fluid-Gestein-Verteilungskoeffizienten ( $D_{\text{Fluid} / \text{Gestein}}$ ) von Li, B, Na, S, Cl, K, Mn, Fe, Rb, Sr, Ba, Ce, Cu, Zn, Ag, Cd, Mo, As, Se, Sb, Te, W, Tl, Pb und Bi wurden experimentell bei 2 kbar und 850 °C nahe dem Solidus eines mafischen Magmas in einer Magmakammer der oberen Erdkruste bestimmt. Im ersten Schritt wurden Gläser durch Schmelzen eines natürlichen basaltischen Trachyandesits in Anwesenheit von Fluiden bei 1200 °C / 10 kbar in Kolbenzylinderpressen mit volatilen Elementen angereichert. In einem zweiten Experiment wurden die wasserhaltigen Gläser bei 850 °C / 2 kbar in kalt versiegelten Druckbehältern ins Gleichgewicht gebracht, was zu einer Kristallisierung von 80-90% der Schmelze führte. Nach 0,5-2,0 Tagen wurden die entmischten Fluide durch induzierte Rissbildung in Quarz in situ als synthetische Fluideinschlüsse eingefangen. Sowohl das Residuum der mafischen Schmelze als auch die Fluideinschlüsse wurden anschließend durch Laser-Ablation ICP-MS auf Haupt- und Spurenelemente analysiert. Als Gegenprobe wurden metallhaltige wässrige Lösungen mit Gesteinspulver ins Gleichgewicht gebracht und dann die Bildung von Fluideinschlüssen initiiert. Der Vergleich der Elementkonzentrationen in Fluideinschlüssen zwischen den direkten Experimenten und den Gegenproben zeigt, dass sich nach 2 Tagen ein Gleichgewicht eingestellt hat.

Durch die Reaktion von Fluiden, die sich aus einem kristallisierenden mafischen Magma entmischten, mit gleichzeitig anwesenden silikatischen Schmelzen (Haplogranit und Rhyolith)

wurden in zwei weiteren Experimenten Informationen über die relativen Elementmobilitäten gewonnen. Diese Methode hat den Vorteil, dass sie empfindlicher ist und somit die Untersuchung relativ fluid-immobiler Elemente wie Ti und Zr ermöglicht. Die kombinierten Ergebnisse deuten darauf hin, dass sich unter den untersuchten Bedingungen S, Cl, Cu, Se, Br, Cd und Te am flüchtigsten verhalten ( $D_{\text{Fluid}/\text{Gestein}} > 10$ ), gefolgt von Li, B, Zn, As, Ag, Sb, Cs, W, Tl, Pb und Bi ( $D_{\text{Fluid}/\text{Gestein}} = 1-10$ ). Weniger flüchtig verhalten sich Na, Mg, K, Ca, Mn, Fe, Rb, Sr, Mo und Rb ( $D_{\text{Fluid}/\text{Gestein}} = 0,1-1$ ) sowie Al, Si, Ti, Zr, Ba und Ce als die am wenigsten fluidmobilen Elemente ( $D_{\text{Fluid}/\text{Gestein}} < 0,1$ ). Dieser Trend stimmt weitgehend mit den relativen Elementvolatilitäten überein, die an natürlichen Hochtemperatur-Fumarol-Gasen bestimmt wurden, obwohl einige Unterschiede auffallen. Basierend auf den Volatilitätsdaten und den gemessenen Mineral-Schmelz- und Sulfid-Schmelz-verteilungskoeffizienten kann fluidbasierter Transport von volatilen Elementen in natürlichen felsischen Proben durch Cu-, Se-, Te- und Cd-Anreicherung in magmatischen Sulfiden sowie durch As-, Se-, Cd- und Bi-Anreicherung in magmatischem Apatit identifiziert werden.

### ***Löslichkeit von Gold in oxidierten, schwefelhaltigen Fluiden bei 500-850 °C und 200-230 MPa: eine Studie an synthetischen Fluideinschlüssen***

Die Goldlöslichkeit wurde in Fluiden mit variablen Gehalten an Sulfat, Chlor und Alkalien zwischen 500-850 °C und 200-230 MPa bei Sauerstoff fugazitäten zwischen FMQ + 1 bis ~ FMQ + 6 (FMQ: Fayalit-Magnetit-Quarz-Puffer) untersucht. Die Experimente zielten darauf ab, die Goldlöslichkeit in oxidierten, schwefelhaltigen wässrigen Fluiden zu untersuchen, ähnlich jenen, die für die Entstehung porphyrischer Cu-Au(-Mo)-Lagerstätten verantwortlich sind.

Fluide wurden in kalt versiegelten Druckbehältern bei hoher Temperatur und unter hohem Druck als synthetische Fluideinschlüsse eingefangen und anschließend mittels LA-ICP-MS analysiert. Wässrige Lösungen mit unterschiedlichen Gehalten an HCl, H<sub>2</sub>SO<sub>4</sub>, Na<sub>2</sub>SO<sub>4</sub>, LiCl, KCl, CsCl und MnCl<sub>2</sub> wurden aus analysenreinen Chemikalien und entionisiertem Wasser hergestellt. Natriumchlorid und elementarer Schwefel wurden als Feststoffe zugegeben. Fluideinschlüsse wurden entweder durch Aufwachsen von neuem Quarz auf geätzten Quarz in Goldkapseln ohne Sauerstoffpuffer, oder durch in situ induzierte Rissbildung in Quarzstücken in Doppelkapseln (AuPd / Au-Au) bzw. offenen Goldkapseln mit Sauerstoffpuffern synthetisiert. Zusätzlich wurden Raman-Spektren von Fluideinschlüssen in Quarz in einer modifizierten Hydrothermal-

Diamantstempelzelle bei Temperaturen von bis zu 600 °C aufgenommen, um die gelösten Gold- und Schwefelspezies zu identifizieren.

Es wurde festgestellt, dass die Goldlöslichkeit am stärksten vom HCl-Gehalt der Flüssigkeit abhängt, gefolgt von  $fO_2$ , Salinität und Temperatur. Im Vergleich zu diesen Faktoren hat der Schwefelgehalt der Flüssigkeit einen vergleichsweise geringen Einfluss. Bei 600 °C, 230 MPa und dem Magnetit-Hämatit-Puffer entsprechenden Sauerstoffugazitäten lösen Fluide mit geologisch realistischen HCl-Gehalten (~ 1,1 Gew.-%) und Salinitäten (7-50 Gew.-% NaCl<sub>equiv</sub>) etwa 1000-3000 ppm Gold. Bei noch oxidierteren Bedingungen (drei logarithmische Einheiten oberhalb des Hämatit-Magnetit-Puffers) können HCl-, NaCl- und H<sub>2</sub>SO<sub>4</sub>-reiche Fluide bis zu 5 Gew.-% Gold bei 800 °C lösen. Die beobachteten Goldlöslichkeitstrends deuten darauf hin, dass in unseren Experimenten der Großteil des Goldes in Form von NaAuCl<sub>2</sub> gelöst wurde.

Natürliche Hochtemperatur-Fluideinschlüsse aus porphyrischen Cu-Au(-Mo)-Lagerstätten enthalten mindestens 100 mal weniger Gold als die von unserer experimentellen Daten vorhergesagten Löslichkeiten, was darauf hindeutet, dass bei Temperaturen von über 500 °C die natürlichen Fluide stark Gold-untersättigt waren. Demnach wurden die Goldgehalte in Goldreichen porphyrischen Lagerstätten nicht durch Ausfällung von nativem Gold kontrolliert sondern eher durch Ausfällung von Gold-reichen hydrothermalen Sulfiden wie Bornit.

### ***Golddiffusion in und aus Fluideinschlüssen in Quarz während Experimenten zur erneuten Gleichgewichtseinstellung bei 600-800 °C und 2 kbar***

Es wurden Fluideinschlüsse in Quarz synthetisiert und in kalt versiegelten Druckbehältern mit anderen Fluiden ins Gleichgewicht gebracht, um die Änderung von Goldkonzentrationen in Fluideinschlüssen in Quarz nach ihrer Bildung zu untersuchen. Im ersten Schritt wurden Fluideinschlüsse, die ca. 5 Gew.-% KCl enthielten, in Platinkapseln bei 800 °C bzw. 600 °C und 2 kbar synthetisiert. Die so erhaltenen Proben wurden dann zusammen mit Cs-versetzten HCl-NaCl-Lösungen in neue Goldkapseln geladen und bei den gleichen P-T-Bedingungen für 4-14 Tage erneut ins Gleichgewicht gebracht. Die LA-ICP-MS-Analyse von 5-10 Fluideinschlüssen vor und nach den Experimenten zeigt, dass signifikante Mengen von Natrium (bis zu 0,23 Gew.-%) und Gold (bis zu 570 ppm) während der erneuten Einstellung des Gleichgewichts aufgenommen wurden. Der hohe Kaliumgehalt und die Abwesenheit von Cäsium beweisen, dass

es nicht zur Rissbildung kam und damit, dass Natrium und Gold durch das Quarzgitter hindurch diffundierten. Als Gegenprobe wurden goldhaltige Fluideinschlüsse in Goldkapseln synthetisiert und dann in Platinkapseln erneut ins Gleichgewicht gebracht, was in einem deutlichen Goldverlust resultierte. Bei beiden Arten von Experimenten scheint die Golddiffusion nur durch Konzentrationsgradienten angetrieben worden zu sein. Wir fanden keine Beweise weder für den diffusiven Austausch mit  $H^+$  noch für die Goldaufnahme durch kupferhaltige Sulfid-Tochterkristalle in  $H_2S$ -haltigen Experimenten, bei denen aufgrund einer pH-Änderung im externen Fluid mehrere Gewichtsprozent Kupfer in die Fluideinschlüsse diffundierten.

Wenn Goldkonzentrationen in natürlichen Fluideinschlüssen in Quarz aus magmatisch-hydrothermalen Erzlagerstätten durch eine erneute Einstellung des Gleichgewichts beeinflusst wurden, kam es höchstwahrscheinlich zu einem Goldverlust anstatt zu einer Goldaufnahme. Bei Temperaturen unterhalb von 400 °C gelten diffusiver Verlust oder Aufnahme von Gold in magmatisch-hydrothermalen Systemen als unwahrscheinlich, könnten aber in mesothermalen Goldlagerstätten möglicherweise signifikant gewesen sein.

## 1. Introduction

### 1.1. Generation of arc magmas

Since arc magmatism is an essential process for the formation of continents and porphyry deposits, the generation of arc magmas has to be understood. Types of arc magmas include basalt, andesite, as well as potassium rich-magmas, which are difficult to trace in terms of their sources, because erupted magmas may experience wall rock interaction, assimilation and fractional crystallization (DePaolo, 1981) and/or magma mixing. These processes may significantly modify the geochemical composition of the erupted rocks. Possible sources of arc magmas will be reviewed below.

Generally, basaltic oceanic crust together with the overlying sediments undergo low-temperature and high-pressure metamorphism (e.g., 700-800 °C; ~3 GPa), releasing fluids by prograde dehydration reactions to form metamorphic mafic rock, i.e., eclogite (Fig. 1.1). At a depth of ca. 100 km, hydrous minerals such as serpentine, talc, amphibole, zoisite, micas and lawsonite break down (e.g., Schmidt and Poli, 1998; Forneris and Holloway, 2003) and release fluids. The slab-derived fluids are thought to be enriched in volatiles (H<sub>2</sub>O, S and halogens), fluid-mobile large ion lithophile elements (LILE; such as K, Rb, Cs, Ca, Ba and Sr), and Li, B, Pb, As, and Sb (e.g., Tatsumi et al., 1986; Keppler, 1996; Kogiso et al., 1997; Hattori and Guillot, 2003; Manning, 2004). These slab fluids may directly percolate into the mantle wedge to metasomatize the hot zone (e.g., Peacock, 1993; Kelley et al., 2010) and the metasomatized peridotite may be transferred into the hot zone by corner-flow (Fig. 1.1) (Tatsumi, 1986; Schmidt and Poli, 1998). Partial melting of hydrated peridotite caused by the fluid-fluxing leads to the formation of arc basalt magmas that are rich in water, halogens, sulfur and incompatible elements. Arc basalt magmas are also relatively oxidized, with the oxygen fugacity ranging from 1 to 3 log units above the fayalite-magnetite-quartz buffer, i.e.,  $\Delta \text{FMQ} + 1 \sim \Delta \text{FMQ} + 3$  (Brandon and Draper, 1996; Jugo et al., 2010).

The hydrous basaltic magmas generated from the mantle wedge have high temperatures ranging from 1000 °C to 1400 °C (Schmidt and Poli, 1998; Ulmer, 2001; Wallace, 2005), which make their densities lower than the surrounding mantle (Herzberg et al., 1983; Hildreth and Moorbath,

1988). For this reason, the arc magmas tend to rise and accumulate at the crust/mantle boundary. The arc magmas start to crystallize and transfer heat to the lower crust rock, leading to partial melting and extensive magmas mixing (Annen et al., 2006; Rushmer, 1993). The melting-assimilation-storage-homogenization (MASH) model (Hildreth and Moorbath, 1988) described above is a widely accepted mechanism for the origin of andesite, even though many details are still being debated.

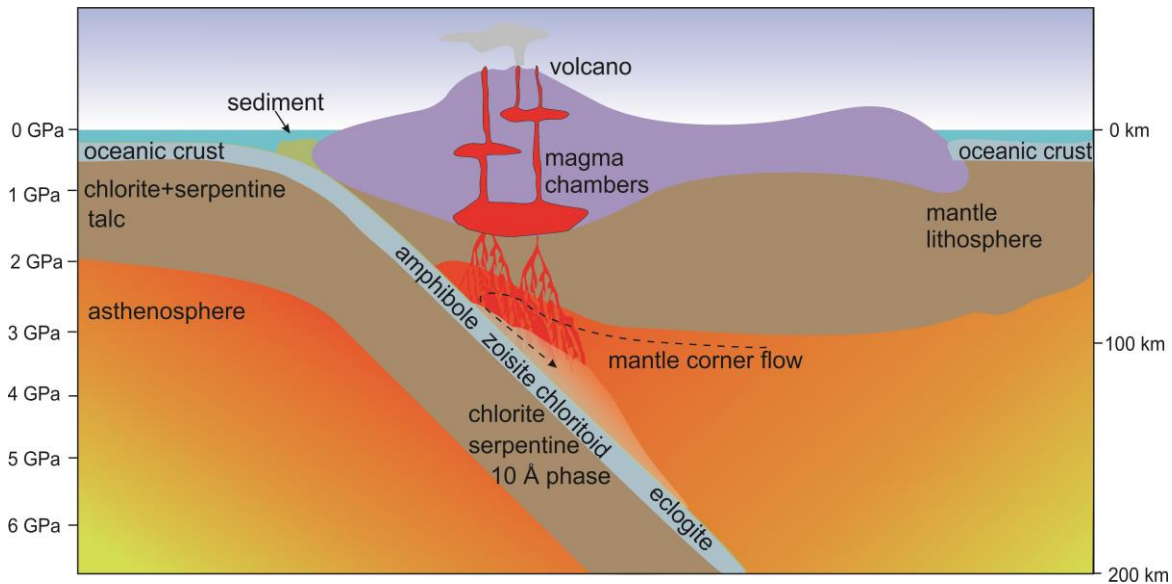


**Fig. 1.1.** Schematic diagram illustrating the structure of subduction zone beneath an oceanic island arc. Primary, hydrous arc magmas within the oceanic island arc form by partial melting of the metasomatized asthenospheric ( $\pm$ lithospheric) mantle (modified from Schmidt and Poli, 1998; Richards, 2011).

Only under special circumstances the basaltic oceanic crust within the subducted slab may melt itself during the subduction processes, generating an intermediate ‘fertile’ melt. Such products were termed as ‘adakite’ (Drummond and Defant, 1990), after the Adak Island in the Aleutians, where an anomalous lava was discovered (Kay, 1978). The ‘slab melts’ should be characterized by anomalously low heavy earth elements and Y (compatible in garnet) as compared to the light earth elements, and by high concentration of Sr (absence of plagioclase at that pressure), as garnet is a residual phase in the eclogitic source of the magmas (Drummond and Defant, 1990). Because the thermal state of the subducting slab limits the possibility of slab melting, this process may occur only during subduction of young, hot oceanic crust (e.g., Drummond and Defant, 1990; Peacock et al., 1994). Slab melts are proposed to be volatile-rich and oxidized, and thus, they would be expected to be effective in transport its metals and may act as ore-forming agents

(Oyarzun et al., 2001; Mungall, 2002). However, there is a lack of direct constraint from melt inclusions studies on the capacity of such melts to transfer metals. Furthermore, it has been shown that melts with high Sr/Y ratios can form as a result of fractional crystallization of hydrous magmas at high pressure (e.g., Richards et al., 2011; Loucks, 2014). Potassic magmas such as shoshonites, lamprophyres, absarokites are more K-rich than typical subduction zone magmas (i.e.  $K > Na$ ), (Peccerillo, 1992). These magmas are characterized by high LILE and LREE abundances, negative anomalies of niobium and tantalum, and positive lead anomalies. Potassic magmas may form by low-degree partial melting of metasomatized mantle soon after the cessation of subduction, i.e., in the regime of extensional tectonics (e.g., Foley, 1992; Farmer, 2014). Additionally, these magmas are highly oxidizing ( $\sim 3-7 \log fO_2$  units higher than FMQ buffer) and rich in volatiles ( $H_2O$  and F greater than 2 wt%; Feldstein and Lange, 1999).

### 1.2. Volatiles in arc magmas

The subducting slab has been proposed to transfer oxidizing volatiles such as  $H_2O$ ,  $CO_2$ , sulfur and possibly halogens (Alt et al., 1993; Mungall, 2002) into the mantle wedge, leading to the oxidized character of arc magmas. Melt inclusions from natural samples provide constraints on the volatile content of these magmas prior to degassing (e.g., Wallace, 2005; Métrich and Wallace, 2008). Table 1.1 summarizes the volatile contents in some mafic magmas, showing that arc magmas generated by partial melting of the mantle wedge mostly contain  $\leq 6$  wt% water,  $\leq 4000$  ppm sulfur,  $\leq 3000$  ppm chlorine,  $\leq 4000$  ppm fluorine, and variable concentrations of  $CO_2$  (normally  $\leq 3000$  ppm) (e.g., Wallace, 2005; Johnson et al., 2010).

Water is the most abundance volatile component and plays a major role on the properties of magmas. Water solubility ( $X_{H_2O}$ ) in silicate melt is approximately proportional to the square root of water fugacity (Burnham, 1979a). Water dissolves in the melt in the form of  $OH^-$  groups that are structurally bound to the aluminosilicate network of the melt, or as molecule water ( $H_2O$ ) (e.g., Stolper, 1982a; McMillan, 1994). Water is suggested to be firstly incorporated as  $OH^-$  groups in the melt structure at low concentration, while molecular water becomes the dominant species at high concentration (Stolper, 1982a, b). Infrared spectroscopic studies of quenched silicate glasses have shown that  $CO_2$  dissolve in the melt as molecular  $CO_2$  (in rhyolite) and  $CO_3^{2-}$  (in basalt) or as both species (in andesite and dacite) (Fine and Stolper, 1985; Blank and Brooker, 1994; Behrens

et al., 2004; Ni and Keppler, 2013). Korschak and Keppler (2014) found molecular CO<sub>2</sub> in basaltic andesite melt at high temperature by in-situ synchrotron infrared spectroscopy in diamond anvil cell. A model on CO<sub>2</sub>-H<sub>2</sub>O-melt equilibrium for rhyolite and basalt (Fig. 1.2) has been developed to compute H<sub>2</sub>O-CO<sub>2</sub> degassing paths (Newman and Lowenstern, 2002; Papale et al., 2006).

**Table 1.1**

A summary of volatile contents in natural some mafic arc magmas, all components are in wt%.

Reference	Locality	P (kbar) <sup>a</sup>	SiO <sub>2</sub>	K <sub>2</sub> O	Na <sub>2</sub> O	H <sub>2</sub> O	S	Cl	F	CO <sub>2</sub>
<u>Vigouroux et al. (2008)</u>	Colima	0.1-7	48-55	1.5-3.5	1.7-3.8	4~5	0.2-0.5	0.2	0.4	0.3-0.4
<u>Rowe et al. (2009)</u>	Cascades		~50	2	3	little	0.2-0.4	0.1-0.2		
<u>Spilliaert et al. (2006)</u>	Etna	>=3	44-49	1.7-3.5	3.0-4.8	0.4-3.6	0.09-0.35	0.13-0.24		0.2-2.3
<u>Esposito et al. (2011)</u>	Phlegrean	>2.4	47-51	0.5-4.2	2.2-3.2	1.1-1.5	0.003-0.17	0.01-0.31	0.1-0.19	0.01-0.12
<u>Fourmentraux et al. (2012)</u>	Averno	~1.5	58-62	6.4-8.2	4.7-5.8	0.4-5	0.01-0.06	0.75-1	0.2-0.5	
<u>Sadofsky et al. (2008)</u>	GNC <sup>b</sup>		47-60	0.1-4.2	1.8-3.5	1.0-5.2	0.12-0.36	0.04-0.12	0.01-0.06	
<u>Johnson et al. (2009)</u>	MGVF <sup>c</sup>		50-57	0.50-1.52	1.6-4.2	0.4-4.2	<0.21	<0.13		<0.63
<u>Benjamin et al. (2007)</u>	Costa Rica		47-63	1.5-4.4	2.9-4.5	0.2-3.3	<0.40	<0.27	<0.24	<0.02
<u>Harris and Anderson (1984)</u>	Fuego	0.3-0.85	50.7-53.8	0.67-0.95	2.2-4.2	1.3-3.4		0.08-0.1		<0.41
<u>Roggensack (2001)</u>	Cerro Negro		48-53	1.4-3.2	1.8-3.0	<4.2	<0.15	0.02-0.13		<0.11

<sup>a</sup>Entrapment pressure;

<sup>b</sup>Guatemala, Nicaragua and Cost Rica;

<sup>c</sup>Michoaca-Guanajuato Volcanic Field (MGVF) in central Mexico.

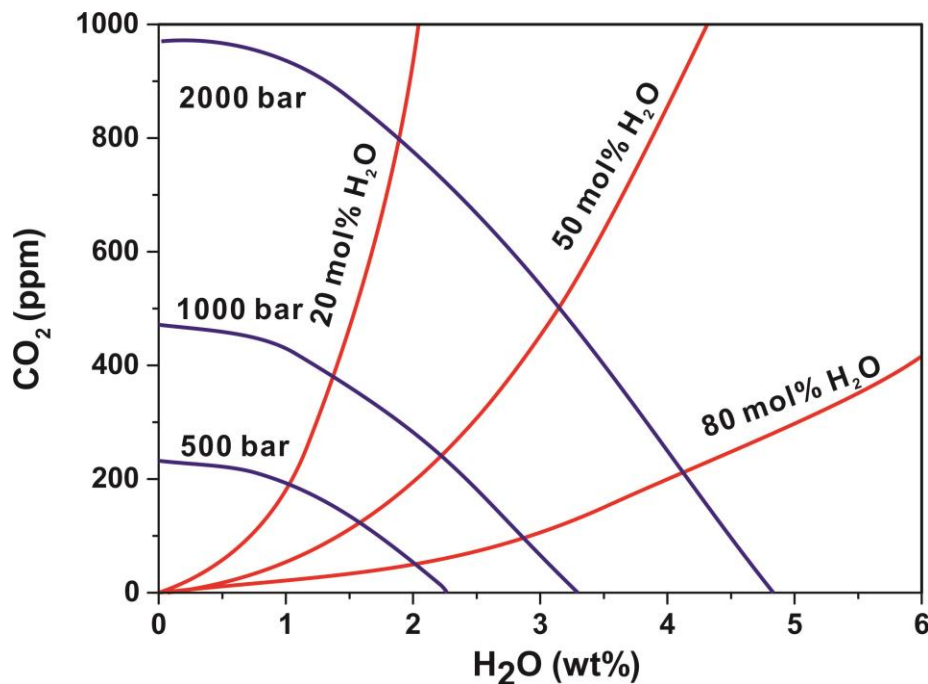


**Fig. 1.2.** Vapor saturation curves for H<sub>2</sub>O and CO<sub>2</sub> (ppm) in basaltic melt (at 1200 °C) (modified from Oppenheimer et al., 2014). Red curves denote H<sub>2</sub>O concentrations in the coexisting fluid phase, with the rest being CO<sub>2</sub>.

Sulfur solubility and speciation in magmas are complicated due to multiple valencies, and strongly depend on the oxygen fugacity (e.g., Carroll and Rutherford, 1987; Simon and Ripley, 2011).  $S^{2-}$  and  $SO_4^{2-}$  are the main species thought to be present in silicate melts of petrological significance (Carroll and Webster, 1994; Jugo et al., 2010). Sulfur solubility in silicate melts increases dramatically as the S species in the melt changes from dominantly  $S^{2-}$  to  $S^{6+}$  (Fig. 1.3, Carroll and Rutherford, 1987; Luhr, 1990; Jugo et al., 2010).

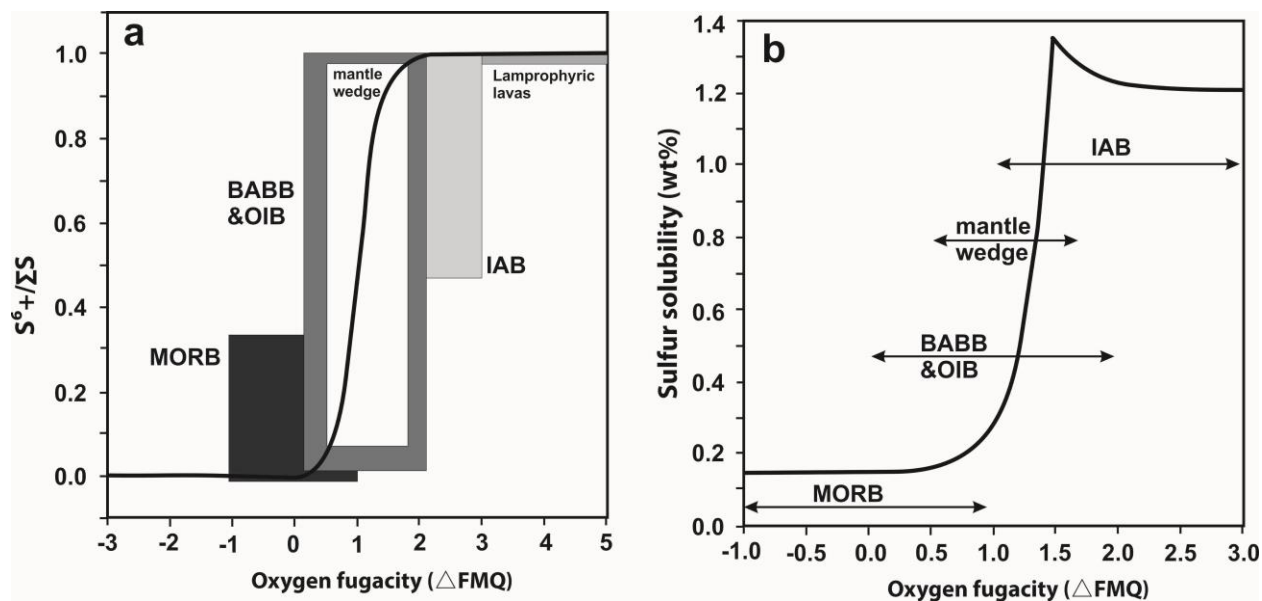


**Fig. 1.3.** (a) Sulfur speciation curve vs.  $fO_2$  in mafic silicate melt (black line), and typical  $fO_2$  ranges of magmas from different tectonic settings. (b) Sulfur content at sulfide saturation (SCSS) and at “anhydrite” (sulfate) saturation (SCAS) of mafic melts, with  $fO_2$  ranges shown for various tectonic environments. MORB=mid-ocean ridge basalts; BABB=back-arc basin basalts; OIB=ocean island basalts; IAB=island-arc basalts. (modified from Jugo et al., 2010)

Chlorine solubility in silicate melts decreases with pressure in water-bearing, brine-saturated systems, and strongly depends on melt structure and composition (e.g., Carroll and Webster, 1994; Webster et al., 1999; Signorelli and Carroll, 2000, 2001; Webster et al., 2001). The absence of a systematic relation of Cl with  $H_2O$  for arc basaltic melt inclusions may be related to a limited range in Cl/ $H_2O$  (2-50% NaCl brine) of slab fluids (Kent et al., 2002). However, some Cl- $H_2O$  fractionation should occur during fluid expulsion from the slab or during migration through the mantle prior to melting (Kent et al., 2002).

### 1.3. Fluids in magma chambers

Magmas may ascend from the mantle to the crust along faults or fractures, or as diapirs (Hawkesworth et al., 2000; Condomines et al., 2003; Reid, 2014). When a magma cannot find a path upwards or encounters low-density crust, it may accumulate into a magma chamber. Magma chambers in arc settings are structurally and chemically complex, commonly being either compositionally stratified or showing evidence for repeated mingling/mixing between mafic and intermediate to felsic magmas. Detailed studies on volcanic systems have shown that most magma chambers contain partly solidified magmas or crystal mushes that are periodically re-activated and partially re-melted by mafic magmas ascending from depth (Bachmann and Bergantz, 2008). Pressure exerts a first-order control on the solubility of volatiles, as volatile solubilities generally decrease with pressure. Therefore, decompression caused by magma ascent, or failure of the confining rock, often leads to fluids saturation and exsolution. Magma ascent also promotes undercooling, resulting in crystallization of anhydrous or water-poor phases, which increases the fraction of volatiles dissolved in melts. These two factors favor fluid oversaturation and exsolution from the magma chamber, enhancing fluid flux into the Earth's crust or the atmosphere.

Fluids play an important role in upper crustal magma chambers for several reasons: (1) their exsolution from magmas commonly triggers volcanic eruptions (Tait et al., 1989); (2) they extract sulfur and metals from the magma and concentrate them in the form of ore deposits (e.g., Audétat and Simon, 2013; Wilkinson, 2013); (3) they govern critical rheological properties of magmas (e.g., Sparks, 2003), and (4) if erupted in large quantities they affect the Earth's climate (e.g., McCormick et al., 1995; Briffa et al., 1998; Robock, 2002). Understanding the formation, distribution and composition of fluids in upper crustal magma chambers is therefore of broad interest in Earth sciences.

Fluids are present at various depth levels and at different evolutionary stages of magma chambers (Burnham, 1979b; Métrich and Wallace, 2008; Wallace and Edmonds, 2011): (1) relatively H<sub>2</sub>O-poor but CO<sub>2</sub> and/or SO<sub>2</sub>-rich fluids exsolve from mafic magmas as they quench against more evolved, stagnant magma (2) these fluids rise and interact with overlying, more felsic magmas (i.e., "volatile fluxing"; Fig. 1.4) and may be stored in larger quantities at the top of the magma chamber, (3) progressively H<sub>2</sub>O (±Cl)-rich fluids exsolve from intermediate to felsic magmas as cooling and

crystallization proceeds, and (4) dominantly meteoric fluids circulate through fully solidified magma at subsolidus conditions.

Accumulation of sulfur-rich fluids in the upper parts of magma chambers and their preferential release during volcanic eruptions is responsible for the "excess sulfur problem" (i.e., the eruption of more sulfur than could have been stored in the erupted magma volume) and the presence of magmatic anhydrite in intermediate and felsic magmas (Parat et al., 2011). The same fluids also contain significant amounts of metals (e.g., Hattori, 1993), as demonstrated by high metal concentrations measured in volcanic gases (Williams-Jones and Heinrich, 2005; Nadeau et al., 2010; Zelenski et al., 2013; Menard et al., 2014; Zelenski et al., 2014), evidence for Cu-enrichment in magmas stored magma at Mt. Etna (Collins et al., 2009), and the presence of Cu-, Zn-, Se-, Cd-, Ag- and As-rich sulfides in the dacitic to rhyodacitic magmas of Mt. Pinatubo (Hattori, 1993, 1996). The concentration of chalcophile elements in magmatic fluids depends strongly on the presence or absence of sulfides in the magma and the preservation/destruction of these sulfides at late-magmatic to subsolidus stages (e.g., Keith et al., 1997; Halter et al., 2005; Aud  tat and Pettke, 2006; Simon and Ripley, 2011).

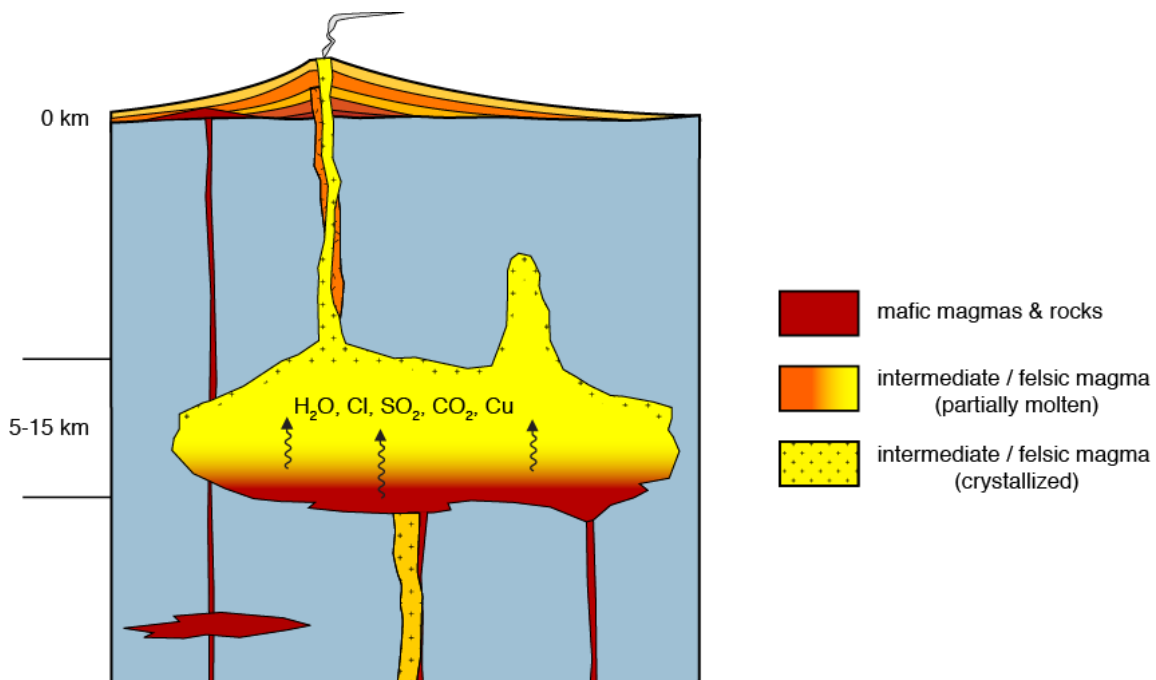


**Fig. 1.4.** Schematic view of a compositionally stratified magma chamber underneath a stratovolcano in an arc setting. Volatiles and metals such as Cu are transported by a fluid phase from mafic magmas to overlying intermediate and felsic magmas (modified from Aud  tat and Simon, 2013).

The exsolved fluid phase is dominated by water, and contains lesser amount of  $\text{CO}_2$ , S (speciation dependent on oxygen fugacity), HCl, NaCl, KCl, etc. (e.g., Kouzmanov and Pokrovski, 2012). The formation and properties of these fluids strongly depend on the PVTX properties of aqueous solution, which may be approximated by the well-known simple  $\text{H}_2\text{O}$ -NaCl system. At high pressures, a single-phase magmatic fluid may exsolve from the magma (Burnham, 1979b) above the two phases curves of the  $\text{H}_2\text{O}$ -NaCl system (Fig. 1.5) with a typical salinity in the range of 2-13 wt%  $\text{NaCl}_{\text{equiv}}$  (e.g., Hedenquist and Richards, 1998; Redmond et al., 2004; Rusk et al., 2004; Audéat et al., 2008; Rusk et al., 2008). During decompression, the ascending magmatic fluid will intersect the two-phase liquid+vapor surface (V-L solvus), leading to two phases, a liquid and vapor, with distinct density, salinity, and concentrations of volatiles and metals (e.g., Heinrich et al., 1999; Ulrich et al., 1999; Audéat and Pettke, 2003; Williams-Jones and Heinrich, 2005).

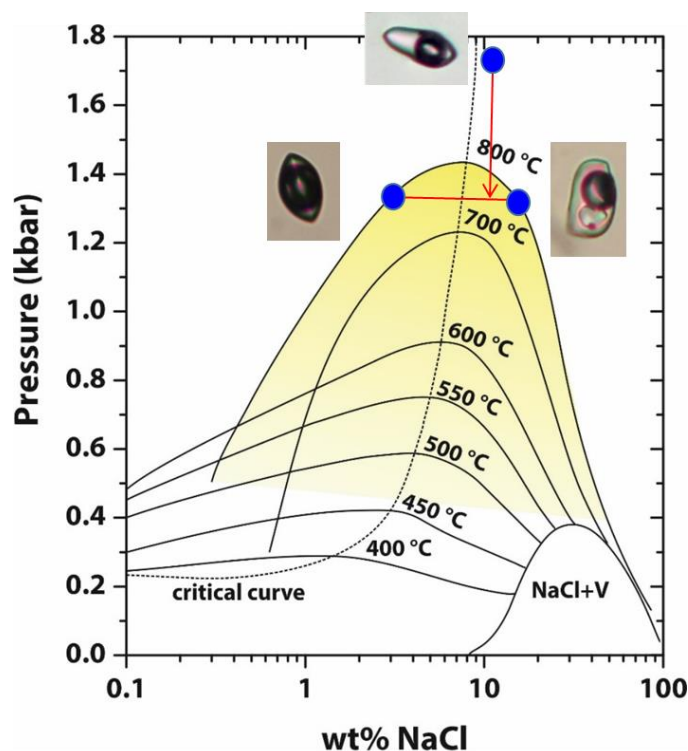


**Fig. 1.5.** Pressure vs. composition (NaCl)-temperature phase diagram of the  $\text{H}_2\text{O}$ -NaCl system. A single fluid phase (e.g., at 800 °C) composed of 10 wt% NaCl aqueous evolves from 2.3 kbar (out of the diagram) to 1.3 kbar. The fluid phase intersects the solvus and separates into a small amount of hypersaline liquid and a large volume of low-density aqueous vapor ('fluid boiling'). The former phase will form a halite daughter crystal upon cooling (modified from Bodnar et al., 1985).

#### 1.4. Overview of previous experimental studies on gold solubility

Gold is a strongly siderophile and moderately chalcophile element, occurring mostly in native form or as an alloy, but also as a variety of telluride minerals. It belongs to Group IB of periodic table, with atomic number 79 and atomic weight 196.9665. The average abundance of gold in iron meteorites is about 1.15 ppm. Chondritic meteorites typically contain much higher gold

concentrations as compared to terrestrial rocks, in the range of 100–200 ppb Au. The Earth's crust contains with an average abundance of ca. 1.5 ppb Au 2–3 orders of magnitude less Au than iron meteorites of chondrites, (Rudnick and Gao, 2014). However, in some special parts of the Earth's crust, gold can be concentrated during ore deposits formation (Kesler, 1994; Robb, 2005), leading to average Au abundances in excess of 1–10 ppm, which are the minimum grades required for economic exploitation. Most primary gold deposits formed via hydrothermal fluids, hence knowledge of the factors that influence gold solubility in hydrothermal fluids is essential for understanding the formation of ore deposits.

The solubility of gold in fluids has attracted the attention of geologists since early on (see reviews by e.g., Williams-Jones et al., 2009; Pokrovski et al., 2014). Most previous experimental studies (Table 1.2) on gold solubility focused on the lower temperature hydrothermal conditions representative of epithermal environments (e.g., Gibert et al., 1998; Pokrovski et al., 2009), sulfur-free fluid systems (e.g., Frank et al., 2002; Hanley et al., 2005; Simon et al., 2005) or fluids in which reduced sulfur is the dominant fluid species (e.g., Loucks and Mavrogenes, 1999; Simon et al., 2007; Tagirov et al., 2005). Loucks and Mavrogenes (1999) used synthetic fluid inclusions to study Au solubility in aqueous fluid at 550–700 °C and 1.1–4.0 kbar. They observed up to 1000 ppm gold in the fluid and suggested that  $\text{AuHS}(\text{H}_2\text{S})_3$  is the dominant Au species at this condition. Subsequent studies on compositionally similar fluids identified  $\text{Au}(\text{HS})_2^-$ ,  $\text{Au}(\text{HS})$ ,  $\text{Au}(\text{OH})$  as major Au species (Tagirov et al., 2005; Pokrovski et al., 2009; Liu et al., 2011). Frank et al. (2002) found gold solubilities of 40–840 ppm in a brine, increasing with HCl content at 800 °C and 1.0 kbar. They suggested  $\text{HAuCl}_2$  as gold species. However, Hanley et al. (2005) found that Au solubility decreases with the fluid salinity, consistent with  $\text{AuOH}$  in the fluid. Simon et al. (2005; 2007) conducted experiments with NaCl–KCl–HCl–Fe–As–S fluids and suggested that gold chlorine complexes dominate both in the brine and in the  $\text{H}_2\text{S}$ -bearing vapor phase. Most recently, Pokrovski et al. (2014, 2015) suggested an important role of the trisulfur ion ( $\text{S}_3^-$ ) in complexing gold, leading to Au solubilities up to ~640 ppm in  $\text{K}_2\text{S}_2\text{O}_3$ –HCl-bearing fluids at 350 °C, 35 MPa. It needs to be noticed that all these studies were carried out at relatively reduced conditions, in which sulfur occurs either in reduced state ( $\text{S}^{2-}$ ) or had a near-neutral valence ( $\text{S}_3^-$ ).

**Table 1.2**

Representative published Au solubility data and proposed Au species in aqueous fluid.

Reference	starting system composition	P (kbar)	T (°C)	pH	fO <sub>2</sub>	Au solubility (ppm)	proposed species
<u>Loucksand&amp;Mavrogenes, 1999</u>	H <sub>2</sub> O+KCl+HCl+PPM <sup>a</sup>	1-4	550-725	4.3-6.7	QFM <sup>b</sup> +PPM	up to 1000	AuHS(H <sub>2</sub> S) <sub>3</sub>
<u>Frank et al., 2002</u>	H <sub>2</sub> O+NaCl+HCl	1	800	-	NNO	40-840	AuOH, HAuCl <sub>2</sub>
<u>Hanley et al., 2005</u>	H <sub>2</sub> O+NaCl+HCl	1.5	600-800	4.5-6.1	NNO	900-6000	AuCl, HAuCl <sub>2</sub>
<u>Simon et al., 2005</u>	H <sub>2</sub> O+NaCl	1.1-1.45	800	1.5-1.7	NNO	28-50	HAuCl <sub>2</sub>
<u>Simon et al., 2007</u>	H <sub>2</sub> O+NaCl+KCl+HCl+FeAsS	1.2	800	-	NNO	12-30	-
<u>Zajacz et al., 2010</u>	H <sub>2</sub> O+NaCl/KCl/LiCl/CaCl <sub>2</sub> +HCl+S	1.5	1000	-	NNO-0.5- NNO+1.9	up to 1500	AuCl, Na/KAuCl <sub>2</sub> , Na/KAu(HS) <sub>2</sub>
<u>Frank et al., 2011</u>	H <sub>2</sub> O+HCl+sulphides	1	800	-	NNO	up to 240	-

<sup>a</sup> pyrrhotite+pyrite+magnetite<sup>b</sup> quartz+fayalite+magnetite

### 1.5. Postentrapmental modification of fluid inclusions

Fluid inclusions (FI) are micro-scale fluid samples trapped within minerals. They thus represent direct samples of ancient geological fluids. Fluid inclusions form mainly in two manners, either during initial growth (primary inclusions) or during healing of fractures that developed in the host mineral (secondary or pseudosecondary inclusion). Provided that time relationships can be established, fluid inclusions can provide the most direct information on the physical and chemical properties of fluids in the geological processes related to the mineral formation. The size of fluid inclusions can range from the nanometer scale to a few hundreds of micrometers, and rarely up to millimeters. Most studied fluid inclusions range from ~5 to ~ 50 μm in size.

Quartz is the most frequent host mineral of fluid inclusions studied from magmatic and hydrothermal ore deposits, because quartz commonly precipitated during the ore-forming process, and because of its transparency, hardness and simple chemical composition. Quartz veins, euhedral quartz phenocrystals within relatively high temperature magmatic ore deposits, and miarolitic cavities in granite contain numerous large fluid inclusions in various assemblages, providing abundant information on temperature-pressure evolution, phases of fluids, and element concentrations (e.g., Roedder, 1984; Bodnar and Vityk, 1994; Audétat et al., 1998; Audétat et al., 2008). However, most conclusions drawn from fluid inclusions studies are based on the assumptions that both the bulk volume and the chemical composition of the fluid inclusions remained constant since fluid entrapment.

Quartz is composed of  $[\text{SiO}_4]^{4-}$  tetrahedra forming channel-like structures along the *c*-axis (Weil, 1984). The  $\text{Si}^{4+}$  is usually substituted by a trivalent cation, commonly with  $\text{Al}^{3+}$ ,  $\text{Ga}^{3+}$ ,  $\text{Fe}^{3+}$ ,  $\text{B}^{3+}$  or  $\text{As}^{3+}$  (Götze, 2009; Weil, 1984). The charge balance is created either by the incorporation of a monovalent cation (e.g.,  $\text{Na}^+$ ,  $\text{Li}^+$ ,  $\text{Cu}^+$ ,  $\text{H}^+$ ) in the interstitial space or by the substitution of one  $\text{Si}^{4+}$  by a pentavalent cation (e.g.,  $\text{P}^{5+}$ ). The channels parallel to the *c*-axis with a diameter of  $\sim 1.0$  Å (Verhoogen, 1952; White, 1970), allow small cations (such as  $\text{H}^+$ ,  $\text{Li}^+$ ,  $\text{Na}^+$ ,  $\text{Cu}^+$ , and  $\text{Ag}^+$ ) to diffuse in this direction.

Numerous studies on synthetic and/or natural fluid inclusions have challenged the common view that fluid inclusions in quartz preserve the chemical composition of the fluid at the time of entrapment (Audétat and Günther, 1999; Doppler et al., 2013; Lerchbaumer and Audétat, 2012a; Li et al., 2009; Zajacz et al., 2009). Several studies found that molecular  $\text{H}_2\text{O}$  and  $\text{H}_2$  could be gained or lost in fluid inclusions of quartz (Hall and Bodnar, 1990; Qin et al., 1992; Mavrogenes and Bodnar, 1994; Audétat and Günther, 1999; Ridley and Hagemann, 1999). Doppler et al. (2013) experimentally demonstrated that the hydrogen isotope compositions of fluid inclusions in quartz may be easily modified by  $\text{H}_2\text{O}$  and  $\text{D}_2\text{O}$  diffusion in re-equilibration processes at evaluated P-T conditions. Modifications of Cu, Ag, Li and concentrations in fluid inclusions in quartz via cation exchange have been shown in Zajacz et al. (2009), Li et al. (2009) and Lerchbaumer and Audétat (2012a). The same phenomenon was also found in melt inclusions in quartz (Kamenetsky and Danyushevsky, 2005; Zajacz et al., 2009). Lerchbaumer and Audétat (2012a) performed re-equilibration experiments on coexisting brine and vapor inclusions and were able to demonstrate that high Cu concentrations in natural vapor inclusions are an artifact and formed via diffusional uptake of Cu due to a change in the pH of the surrounding fluid from acid to more neutral and due to a higher abundance of S in the vapor phase (Fig. 1.6).

Gold is situated in the same group (IB) of the periodic table as copper and silver, thus it has similar chemical properties. Several studies have reported Au concentrations in natural fluid inclusions (e.g., Ulrich et al., 1999; Seo et al., 2009). Gold has been considered to be immobile in quartz (Pokrovski et al., 2014) because the  $\text{Au}^+$  ion ( $1.37$  Å; Shannon, 1976) has a similar size as  $\text{K}^+$ , which is larger than the diameter of the channels in quartz ( $\sim 1.0$  Å). Seo and Heinrich (2013) modeled the evolution of Au solubility in fluid inclusions vs. external fluid during cooling in porphyry environment and concluded that if any diffusional change occurred, then Au rather was

lost than gained by the fluid inclusions. However, no experiments were ever carried out to see whether gold concentrations in quartz-hosted fluid inclusions can be modified after fluid entrapment.

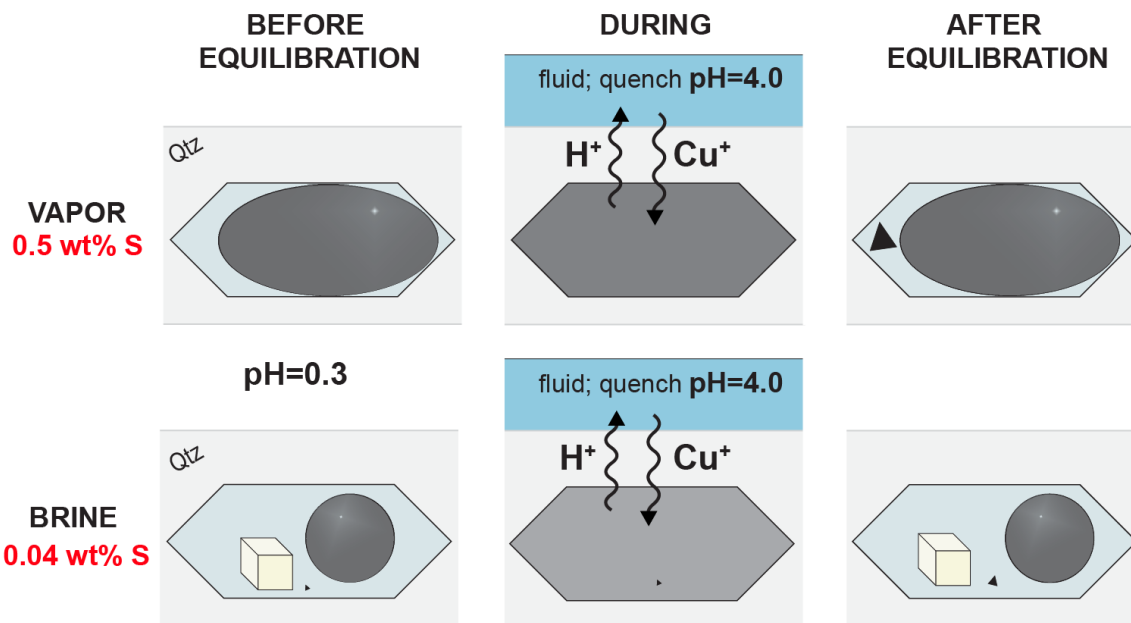


**Fig. 1.6.** Schematic diagram illustrating the mechanism of preferential Cu diffusion into vapor-type fluid inclusions. A gradient in fluid acidity causes protons to diffuse out of the fluid inclusions, which in turn causes Cu (+Na, Ag) to diffuse inward to maintain charge balance. The incoming Cu combines with S to precipitate as sulfides (black triangles). Because the amount of Cu that can be gained by this process is limited by the amount of sulfur present in the fluid inclusion, sulfur-rich vapor inclusions can take up more Cu than sulfur-poor brine inclusions. (Lerchbaumer and Audétat, 2012a)

## 1.6. Research objective of this thesis

The aim of this thesis is to study the behavior of trace and major elements in fluids present in magma chambers and porphyry Cu-Au ( $\pm$ Mo) systems in Earth's upper crust. More than 100 successful hydrothermal experiments have been done to evaluate: (1) the major and trace element composition (including Na, K, Fe, Ca, S, Cl, Li, B, Cu, Zn, Ag, Cd, Mo, As, Se, Sb, Te, Ce, Tl, Pb, and Bi) of fluids that exsolve from mafic alkaline magmas intruding into the base of compositionally stratified magma chambers and the geochemical signature imparted by these fluids on the overlying, more evolved magmas; and (2) gold solubility in oxidized ( $\log fO_2 > FMQ+2.5$ ), sulfur-bearing aqueous fluids similar to those responsible for the formation of

porphyry Cu-Au ( $\pm$ Mo) deposits. During the experiments, we found that Au diffuses into and out of quartz-hosted fluid inclusions, thus we systemically studied post-entrapmental modifications of Au contents in quartz-hosted fluid inclusions at typical magmatic-hydrothermal conditions. The experimental results are fundamental for understanding the volatility of elements during the intrusion of mafic alkaline magmas into felsic magma chambers, and for Au solubility in fluids responsible for porphyry-type ore deposits. The data also has important implications for interpreting Au abundancen measured in natural, quartz-hosted fluid inclusions. The thesis consists of three manuscripts, which are either already published in, or have been submitted to, international scientific journals.

## 2. Experimental and analytical methods

### 2.1. High-temperature and high-pressure experiments

#### 2.1.1. Starting materials

The mafic starting material used for synthesis of mafic hydrous glasses was a natural basaltic trachyandesite from Two Buttes, southeastern Colorado (David and Smith, 1993; David et al., 1996). This rock consists of phenocrysts of clinopyroxene (~40 vol%), phlogopite (~10 vol%), olivine (~2 vol%) and magnetite (~1 vol%) set in a finely crystalline groundmass consisting of ~30 vol% glass, ~25 vol% plagioclase, ~20 vol% phlogopite, ~15 vol% magnetite and ~10% pyroxene. The rock was finely crushed into powder ( $\leq 10 \mu\text{m}$  grain size) to facilitate equilibration during the experiments. The hydrous mafic glass was prepared such that it ultimately contained 0.3 wt% S, 0.2 wt% Cl and 5 wt% H<sub>2</sub>O.

Two different felsic starting materials were used to study fluid transport from mafic to felsic melts: one is a haplogranite of the 1 kbar eutectic melt composition (79.47wt% SiO<sub>2</sub>; 11.73wt% Al<sub>2</sub>O<sub>3</sub>; 3.90 wt% Na<sub>2</sub>O; 4.91wt% K<sub>2</sub>O), and the other one is a natural obsidian from China (76.3wt% SiO<sub>2</sub>; 11.3wt% Al<sub>2</sub>O<sub>3</sub>; 3.6 wt% Na<sub>2</sub>O; 4.5wt% K<sub>2</sub>O; 2.5wt% FeO<sub>tot</sub>; 0.20 wt% CaO).

To increase the chance of being able to analyze all trace elements of interest within the synthetic fluid inclusions, the hydrous starting glass was doped with trace elements such that their concentration was about 50 ppm each. At a melt water content of 5 wt%, this required the trace elements to be added at a concentration of ~1000 ppm each in the aqueous solution. However, because it was not possible to dissolve all trace elements in a single aqueous solution, we used three different solutions containing ~3000 ppm trace elements each (Table 2.1) and then added the three solutions in equal quantities to the solid starting material. Sulfur, Cl, Li, B, Cu, Zn, Cd, As, Se, Sb and Tl were added to the aqueous solution in the form of H<sub>2</sub>SO<sub>4</sub>, HCl, LiCl, H<sub>3</sub>BO<sub>3</sub>, CuCl<sub>2</sub>, ZnCl<sub>2</sub>, CdCl<sub>2</sub>, As<sub>3</sub>O<sub>5</sub>, Na<sub>2</sub>SeO<sub>3</sub>·5H<sub>2</sub>O, SbCl<sub>3</sub>, Na<sub>2</sub>TeO<sub>4</sub> and TiCl, respectively. Silver, Mo, Pb and Bi were not soluble enough in any of these solutions, for which reason we added these four elements in the form of diluted standard solutions for ICP-MS (Plasma CAL) to the rock powder and subsequently allowed the slurry to dry to remove H<sub>2</sub>O and HNO<sub>3</sub>.

**Table 2.1**

Compositions of the three aqueous solutions that were used in the experiments

Solution No.	Components	Concentrations
A	H <sub>2</sub> SO <sub>4</sub> , HCl, LiCl, CuCl <sub>2</sub> , ZnCl <sub>2</sub> , CdCl <sub>2</sub> , SbCl <sub>3</sub>	S~10wt%, Cl~6.6wt%, Li, Cu, Zn, Cd, Sb~3000ppm each
B	H <sub>2</sub> SO <sub>4</sub> , HCl, Na <sub>2</sub> SeO <sub>3</sub> ·5H <sub>2</sub> O, Na <sub>2</sub> TeO <sub>4</sub> , NaBr	S~10wt%, Cl~6.6wt%, Br~0.5wt%, Se, Te ~3000ppm
C	H <sub>3</sub> BO <sub>3</sub> , As <sub>3</sub> O <sub>5</sub> , TlCl	B, As, Tl ~3000ppm each

For the Au-related experiments, aqueous solutions containing various amounts of HCl, H<sub>2</sub>SO<sub>4</sub>, Na<sub>2</sub>SO<sub>4</sub>, LiCl, KCl, CsCl and MnCl<sub>2</sub> were prepared from analytical-grade chemicals and deionized water. Sodium chloride, and in some cases, elemental sulfur were added as solids.

Fluid inclusions were trapped in quartz pieces of 3×3×6 mm or 1.0×1.8×10 mm size that were cut from inclusion-free synthetic quartz in such a way that the longest dimension was parallel to the c-axis of quartz crystal. The quartz pieces were then etched in concentrated hydrofluoric acid for about 1 hour to form numerous etched channels, which favor the formation of large fluid inclusions during overgrowth of new quartz (Li and Audéat, 2009). For some in-situ cracking experiments, large fluid inclusions are first synthesized in a fluid of different composition at favorable P-T conditions, and then re-opened during the main experiment via in-situ cracking. In the present study we conducted these pre-runs at 800 °C and 2 kbar using aqueous solutions containing either 5 wt% KCl and 5000 ppm Cs or 5 wt% KCl.

### 2.1.2. Piston cylinder experiments

Piston cylinder experiments were performed to synthesize volatile- and trace element-rich mafic glasses at 10 kbar and 1200 °C. Approximately 0.009 g solution and 0.2 g mafic rock powder were welded into Pt capsules of 5.0 mm O.D. (outer diameter), 4.6 mm I.D. (inner diameter) and 10 mm length. The capsules were then inserted into a hot-piston-in end-loaded, solid-media piston cylinder apparatus using 1/2-inch diameter MgO-NaCl assemblies with stepped graphite heaters. A friction correction of 5% was applied to the nominal pressure based on calibration using the quartz-coesite phase transition at 790 °C (Bose and Ganguly, 1995). The temperature was monitored by Pt-Pt<sub>90</sub>Rh<sub>10</sub> (S-type) thermocouples with an estimated uncertainty of ±10 °C. The

duration of the experiments was only three hours to minimize loss of iron and other elements to the platinum capsule. The experiments were terminated by switching off the electrical power, resulting in cooling below the glass transition temperature in less than 10 seconds. <sup>2</sup>The recovered platinum capsules were immersed in dilute sulfuric acid (~10 wt% H<sub>2</sub>SO<sub>4</sub>) at ~50 °C for a few hours to dissolve any attached MgO and were then weighted to check for potential leaks during the experiments. Only runs that showed no significant weight change were used for subsequent experiments.

### **2.1.3. Cold-seal pressure vessel experiments**

Hydrothermal experiments were conducted at 500-850 °C and 1.3-2.3 kbar in cold-seal pressure vessels. The instruments used in this study were rapid-quench cold-seal pressure vessels (conventional autoclaves made of Inconel 713LC super alloy) and TZM alloy (Ti- and Zr-reinforced molybdenum) pressure vessels. The conventional autoclaves used water as pressure medium, which was supplied via capillary tubing through the cone seal at the cold end of the bomb (Fig. 2.1). Temperature was measured by means of NiCr-Ni (type K) thermocouples placed in an external borehole of the vessels, which introduces an uncertainty of ca. +5 °C for the sample temperature (Boettcher and Kerrick, 1971). Cooling water circles through the double cone of the autoclave, and rapid quench can be obtained by dragging the capsule with the help of an external magnet within a few seconds from the hot end of the vessel to its cold end. Since water was used as pressure medium, the intrinsic oxygen fugacity of the autoclaves was ~0.5-1 log units above the Ni-NiO buffer due to the reaction of water and the Ni-alloy (Keppler, 2010).

For the TZM pressure vessels, the temperature on the samples (at the top inside the vessels) was calibrated by an internal thermocouple against the temperature of the furnace, with an uncertainty of ca. ±20 °C. Pressure was measured by a pressure gauge with an accuracy to ±50 bar. Since Ar was used as pressure medium, the intrinsic oxygen fugacity imposed on the sample was controlled by Ar, about 2-3 log units above the Ni-NiO buffer for water-rich samples (Bell et al., 2011).

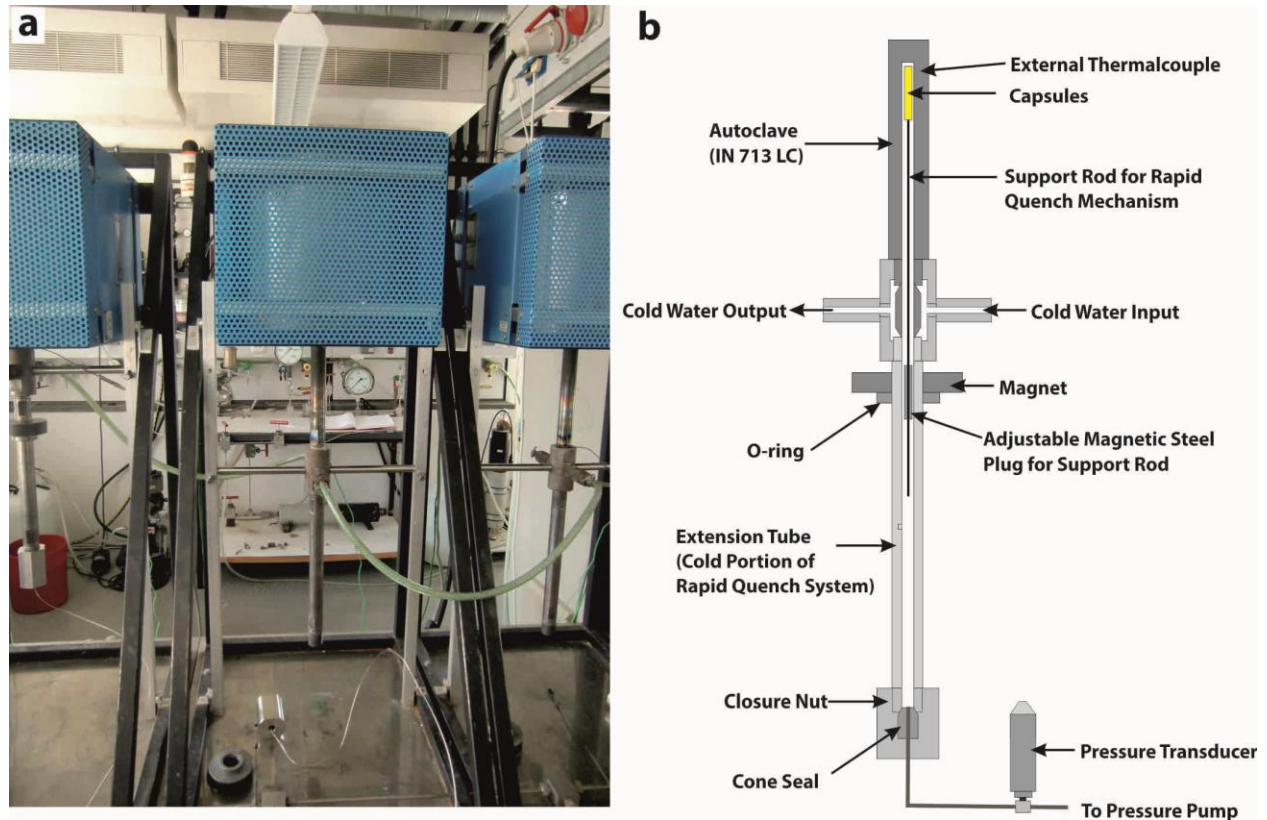


**Fig. 2.1.** (a) the vertical rapid quench autoclaves with a furnace at the top in the hydrothermal lab of Bayerisches Geoinstitut. (b) Schematic diagram of the rapid-quench cold-seal pressure vessel (modified from Matthews et al., 2003).

### 2.1.3.1. Volatile fluxing experiments

The oxygen fugacity in these experiments was not specifically controlled but must have been rather high because sulfur was added in the form of  $\text{H}_2\text{SO}_4$ , and because most experiments appear to have been saturated in anhydrite rather than sulfide, which constrains  $\log f\text{O}_2$  to  $\geq \text{QFM}+2.5$  (Parat et al., 2011). The cold-seal pressure experiments were conducted with three different capsule setups. In the first setup, a piece of inclusion-free quartz and a slightly smaller piece of quartz with pre-synthesized, large fluid inclusions were loaded together with mafic starting material (either finely crushed rock powder or crushed hydrous glass)  $\pm$  aqueous solution into a gold capsule of 4.3 mm O.D., 4.0 mm I.D. and 30 mm length, which was then welded shut. After 0.5-2.0 days of equilibration, the quartz cores were fractured in situ to initiate the re-opening of pre-synthesized fluid inclusions and allow the formation of new fluid inclusions. The second setup with the quartz beaker, which was used only in a single experiment, is based on the design described in

Lerchbaumer and Audétat (2012b) and effectively minimizes loss of metals to the gold capsule, but has the disadvantage that the formation of fluid inclusions cannot be initiated after a specific time of equilibration by in-situ cracking, because that would fracture also the quartz beaker. The quartz beaker was manufactured out of a single quartz crystal and had the following dimensions: 4.4 mm O.D., 2.0 mm I.D. and 16 mm length. For this setup, the quartz beaker was filled with fine-grained mafic rock powder, aqueous solution, and a small (1.0×1.8×10 mm) piece of quartz containing large, pre-synthesized fluid inclusions that were already re-opened by heating the quartz piece in a 1 atm furnace to 700 °C and then quenching it in distilled water. The quartz beaker was then closed with a neatly-fitting SiO<sub>2</sub> glass plug and loaded together with fine quartz powder into a gold capsule of 5.0 mm O.D., 4.6 mm I.D. and 30 mm length. The third capsule setup was designed to simulate the interaction of fluids exsolving from a crystallizing mafic magma with overlying felsic magma. No fluid was trapped in the form of fluid inclusions in this setup. To minimize loss of Cu, Ag, Se, Cd, Te and Bi to the gold capsule, also this setup features a quartz beaker. A neatly fitting plug of SiO<sub>2</sub> glass was placed between the mafic starting material (crushed volatile-bearing glass) and the overlying, crushed, hydrated felsic glass (haplogranite or natural obsidian from China) to avoid direct contact between the two reservoirs. The SiO<sub>2</sub> plug was necessary to be able to assign compositional changes in the felsic melt to volatile fluxing, otherwise it would not have been clear whether they arised due to simple chemical equilibration of the two reservoirs or due to volatile fluxing. During the experiments, the SiO<sub>2</sub> glass plug crystallized to a polycrystalline aggregate of quartz that was permeable to fluid but not to silicate melt. In all cases, the prepared gold capsules were welded using a pulsed arc welder, then subjected to ~1 kbar H<sub>2</sub>O pressure, and finally weighed to check for the presence of leaks. In-situ cracking of the quartz pieces was performed after 0.5~2 days by dragging the sample with the help of an external magnet from the hot end of the vessel to its cold end and then back up to the hot end within seconds. The experiments were terminated by dragging the sample slowly (within 30-60 seconds; to prevent re-opening of the fluid inclusions) to the cold end of the pressure vessel.

### *2.1.3.2. Au solubility experiments*

Three capsule setups were used to study gold solubility at 500-850 °C and 2-2.3 kbar. In the first setup, gold capsules of 3.5 mm O.D. (outer diameter), 3.1 mm I.D. (inner diameter) and 20 mm length were loaded with a piece of etched quartz, ~40 mg solution, 0-16 mg of NaCl, 0-1 mg S,

and a small SiO<sub>2</sub> glass rod (~4 mg). Run durations using this setup were kept short (10 hrs at 800 °C, 20 hrs at 700 °C; 40 hrs at 600 °C; 80 hrs at 500 °C), such that  $fO_2$  was controlled by the starting materials rather than by the intrinsic  $fO_2$  of the pressure vessel. In the second setup, the starting materials were contained in an inner Au or Au<sub>80</sub>Pd<sub>20</sub> capsule of 3.0 mm O.D., 2.7 mm I.D. and 20 mm length, which was then loaded with ~40 mg H<sub>2</sub>O and solid oxygen buffers (Re-ReO<sub>2</sub> (RRO), MnO-Mn<sub>3</sub>O<sub>4</sub> (MMO) or hematite-magnetite (HM)) into an outer Au capsule (O.D. 4.6 mm; I.D. 4.3 mm; 35 mm length). Gold rather than Au<sub>80</sub>Pd<sub>20</sub> had to be used as inner capsules in the sulfur-bearing experiments because Au<sub>80</sub>Pd<sub>20</sub> was found to react with sulfur and to become very brittle during this process. In this setup, entrapment of fluid was initiated after 24-192 hours by in-situ cracking, after which the runs were continued for another 24-120 hours to allow for crack healing. However, in order to obtain larger fluid inclusions, the runs were started either with an etched quartz piece and a SiO<sub>2</sub> glass rod as in the previous capsule setup, or with a quartz piece that already contained large fluid inclusions that were pre-synthesized from H<sub>2</sub>O-KCl fluid. In both cases, already existing fluid inclusions were re-opened during the in-situ cracking, leading to distinctly larger fluid inclusions than if fluid inclusion-free quartz pieces were used (Li and Audétat, 2009). Fluid inclusions that were re-opened during in-situ cracking could be recognized by small fluid inclusion trails leading to them, and by the absence of K-signals during LA-ICP-MS analysis. It is those re-opened inclusions that were preferentially chosen for LA-ICP-MS analysis (Li and Audétat, 2009). The third setup is similar to the second setup, except that an unetched quartz piece was used (to avoid fluid entrapment before Au solubility in the fluid reached a low, stable value) and that the external nickel-nickel oxide (NNO) buffer was placed in an open Au capsule below the sample capsule instead of within a sealed outer capsule. The latter is possible because the material of the pressure vessel is very Ni-rich (~76 wt% Ni) and thus imposes a  $fO_2$  that is already close to the NNO-buffer. The pH of the quench solution was measured with pH-indicator papers. The quartz pieces were gently polished on Al<sub>2</sub>O<sub>3</sub> and SiC grit papers and subsequently using diamond spray on paper to remove excess quartz on the sample surface and render fluid inclusions ready for observation and analysis.

### 2.1.3.3. *Au diffusion experiments*

Each experiment consisted of two steps: a pre-run and a re-equilibration run. In the pre-runs, fluid inclusions were first synthesized using the methods described above. In the re-equilibration

experiments, the quartz pieces recovered from pre-runs were loaded together with a new piece of etched quartz and fluid into new gold, or platinum capsules, or into Au<sub>95</sub>Cu<sub>05</sub> alloy capsules of 5.0 mm O.D., 4.6 mm I.D. and 20 mm length. The new piece of etched quartz served to trap the new external fluid, whereas the fluid inclusions occurring in the pieces recovered from pre-runs started to diffusively re-equilibrate with the external fluid. All re-equilibration runs were performed in the same manner and at the same P-T conditions as the corresponding pre-runs to avoid pressure gradients between the re-equilibrating fluid inclusions and the external fluid. After the experiments, the capsules were opened by a razor blade and the pH of the solution was checked by pH-indicator paper. The recovered quartz pieces were gently polished to remove excess quartz on the sample surface for optical observation and analysis.

## **2.2. Analytical Methods**

### **2.2.1. Scanning electron microscopy and electron microprobe**

The mafic run products were first analyzed by scanning electron microscopy (SEM), which is suitable for imaging and identifying mineral phases. The electron gun of the SEM generates a beam of electrons that focuses and scans across the surface of polished samples. The highly energetic electron beam interacts with the atoms in the sample, resulting in generation of different emissions. The secondary electrons (SE) emitted from the surface of specimen have relatively low energy, providing very high-resolution three-dimensional (3-D) morphology information. Back-scattered electrons (BSE) are beam electrons that are scattered from deeper locations within the specimen with much higher energy than the secondary electrons. The intensity of BSE is proportional to the average atom mass ( $Z$ ), and thus provides the image with a brightness that is a function of the chemistry composition of the sample. In addition, the collision of the electron beam with the sample kicks out electrons from atomic shells and causes electrons from more distal (=higher-energy) shells to drop to more proximal shells, thereby releasing energy in the form of element-specific X-rays. These characteristic X-rays are detected by energy-dispersive spectrometer (EDS) and used to measure the abundance of elements in the sample.

Backscattered electron (BSE) images were taken on a Zeiss Gemini 1530 field emission scanning electron microscope (FE-SEM) using an accelerating voltage of 20 kV, a working distance of 14

mm and an aperture of 60  $\mu\text{m}$ . An energy-dispersive spectrometer (EDS) was used to qualitatively identify mineral phases in the mafic run products.

Electron microprobe analysis were conducted in order to obtain accurate quantification of the chemical composition of various mineral phases in the fine-grained mafic run products. Similar to SEM, characteristic X-rays are emitted once the electron beam hits a mineral phase. The characteristic X-rays can be analyzed either by an energy-dispersive spectrometer (EDS) or by a wavelength-dispersive spectrometer (WDS). In the WDS mode, the characteristic X-rays are selected based on different crystal spectrometers each with a known  $d$  spacing. The intensity and position of spectral line are then compared with the characteristic X-rays emitted by the standard samples, allowing to quantify the unknown sample compositions.

Major element compositions were measured with a JEOL JXA 8200 microprobe that was operated with 15 kV acceleration voltage, 10 nA beam current, and a beam defocused to 1-2  $\mu\text{m}$  diameter. The following standards were used to calibrate the instrument: albite for Na and Si, wollastonite for Ca, orthoclase for K, ilmenite for Ti, forsterite for Mg, spinel for Al, metallic iron for Fe, vanadinite for Cl, and barite for S.

### **2.2.2. Microthermometry**

After observation and selection of fluid inclusions, microthermometric measurements were performed with a Linkam THMSG-600 heating-cooling stage attached to a Zeiss microscope. The heating-cooling stage was calibrated using standard fluid inclusions to an uncertainty of  $\pm 0.1^\circ\text{C}$  in the range of  $-56.6$  (melting of  $\text{CO}_2$ ), to  $0.0^\circ\text{C}$  (melting of  $\text{H}_2\text{O}$ ). For simplification, the PVTX state of the fluids was always reported with regard to the NaCl- $\text{H}_2\text{O}$  model system.

For measuring the salinity of fluid inclusions that were trapped in the single-phase field, they were first cooled to  $-50^\circ\text{C}$  to  $-100^\circ\text{C}$  with the help of liquid  $\text{N}_2$ , and phase changes within the fluid inclusions were then monitored during slow heating back to room temperature. In most cases the liquid part of the inclusions crystallized to ice, which then melted again during heating (Fig. 2.2a). The temperature at which the last piece of ice melted was recorded, which corresponds to the ice melting temperature,  $T_{\text{m, ice}}$  of the fluid inclusion. No evidence for the presence of clathrates or

other solid phases at the time of last ice melting (such as double freezing, or melting of phases at temperatures above 0 °C) were observed.

The ice melting point of the fluid inclusions is a function of the total solute concentration (mainly NaCl, and expressed as  $\text{NaCl}_{\text{equiv}}$  wt %; shown in Fig. 2.2a). The salinity of the fluid was calculated based on the melting temperature of ice using the equation given in Bodnar and Vityk (1994):

$$\text{Salinity (wt\%)} = 0.00 + 1.78\theta - 0.0442\theta^2 + 0.000557\theta^3$$

where  $\theta$  is the melting point in Celsius.

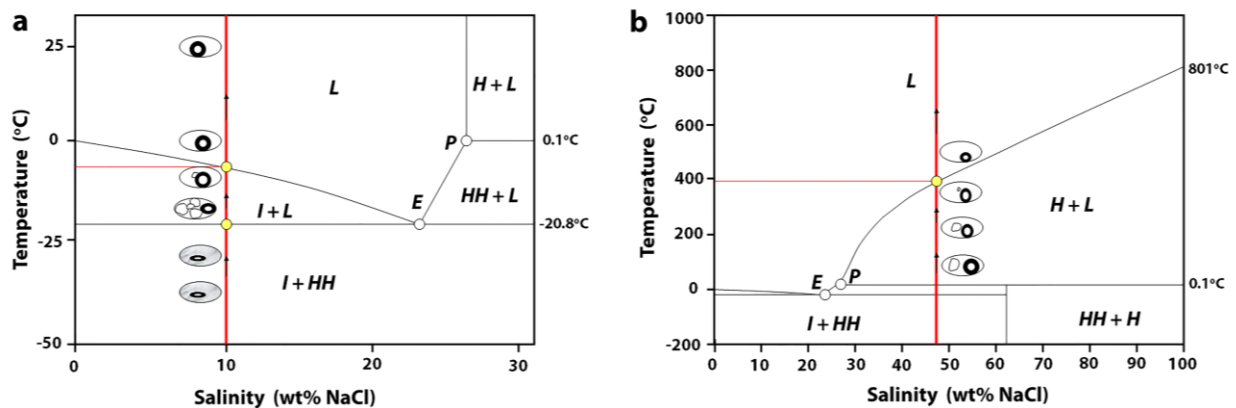


**Fig. 2.2.** Vapor-saturated phase diagrams of the NaCl-H<sub>2</sub>O system at (a) low temperature; (b) high temperature. I-ice; L-liquid; HH-hydrohalite (NaCl·2H<sub>2</sub>O); H-halite (NaCl); P-peritectic (0.1 °C, 26.3 wt% NaCl); E-eutectic (-1.2 °C, 23.2 wt% NaCl). The halite solubility curve extends from the peritectic to the NaCl triple point of 801 °C (modified from Bodnar and Vityk, 1994).

For measuring the salinity of brine inclusions (containing halite daughter crystals), fluid inclusions were heated to determine the halite dissolution temperatures. The final melting temperature of halite is related to the NaCl solubility in the fluid phase, i.e., corresponding to the salinity (wt% NaCl) of the solution (Fig. 2.2b). The salinity of the brine fluid inclusions was calculated based on the melting temperature of halite using the equation from Bodnar and Vityk (1994):

$$\text{Salinity (wt\%)} = 26.242 + 0.4928 \psi + 1.42 \psi^2 - 0.223 \psi^3 + 0.04129 \psi^4 +$$

$$6.292 \times 10^{-3} \psi^5 - 1.967 \times 10^{-3} \psi^6 + 1.1112 \times 10^{-4} \psi^7$$

where  $\psi=T(^{\circ}\text{C})/100$ . This equation allows to calculate NaCl solubility in water from the peritectic temperature (0.1  $^{\circ}\text{C}$ , 26.3 wt% NaCl) up to the NaCl triple point of 801  $^{\circ}\text{C}$ .

The NaCl concentration of vapor fluid inclusions was estimated from the phase relations in the  $\text{H}_2\text{O}$ -NaCl model system.

### 2.2.3. Raman spectroscopy

Various sulfur species ( $\text{H}_2\text{S}$ ,  $\text{SO}_2$ ,  $\text{SO}_4^{2-}$  and  $\text{HSO}_4^-$ ) in synthetic fluid inclusions were identified and quantified by Raman spectroscopic measurements. Raman spectroscopy is a very efficient and non-destructive technique for the investigation of fluid phases and solids. The vibrational information is specific to the chemical bonds and the symmetry of molecules, resulting in characteristic Raman shifts. In this study, Raman spectra of fluid inclusions were taken in confocal mode using a Horiba LabRAM HR UV spectrometer equipped with a CCD detector, 1800  $\text{mm}^{-1}$  grating, and a 50 $\times$  magnification objective. The spectral resolution of this instrument setup is 3.5  $\text{cm}^{-1}$ , and a confocal pinhole of 30-60  $\mu\text{m}$  was used for the measurements. Excitation was promoted using the 514.5 nm line of an  $\text{Ar}^+$  ion laser with an output laser power of 0.2 W. Most spectra were taken at room temperature, using six overlapping windows with acquisition times of 2 $\times$ 30 s each to cover the entire range of 100 to 4500  $\text{cm}^{-1}$  (Fig. 2.3).

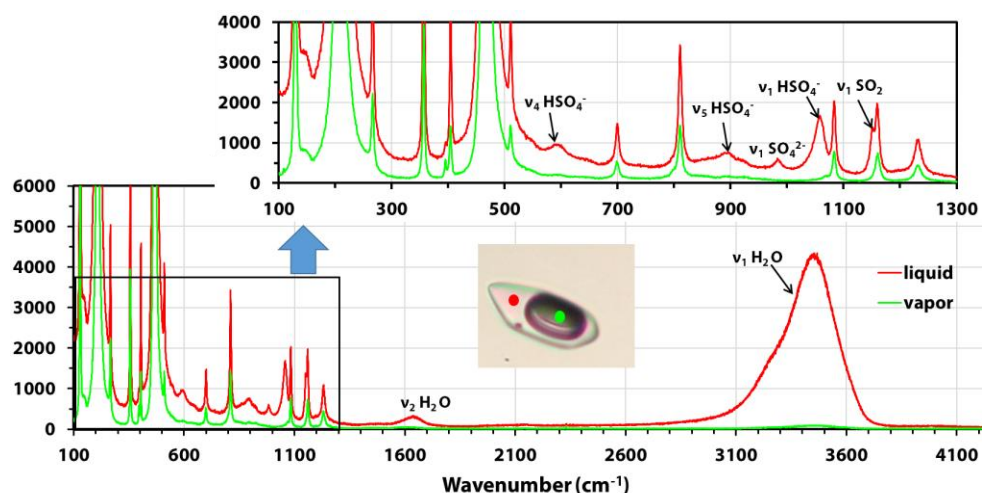


**Fig. 2.3.** Representative Raman spectra taken at room temperature from the liquid and vapor phase of quartz-hosted fluid inclusions synthesized at 800  $^{\circ}\text{C}$ , 2 kbar from a starting fluid containing 3.5 wt% HCl, 16.4 wt%  $\text{H}_2\text{SO}_4$  and 20 wt% NaCl (HG-AU-14).

Spectra covering a more restricted spectral range of 350-1250  $\text{cm}^{-1}$  were collected at temperatures up to 600 °C with an output laser power of 0.2 W in order to investigate potential changes in the speciation of sulfur and/or gold during heating. For the latter purpose, fluid inclusion-bearing quartz chips ( $\sim 2 \times 1.6 \times 0.5$  mm) were heated at 100 °C intervals in a modified hydrothermal diamond anvil cell of the Bassett type (Bassett et al., 1993) in which the diamond anvils were replaced with cylinders made of  $\text{SiO}_2$  glass. The upper cylinder contained a central borehole, such that no solid parts occurred between the sample and the microscope lens. Temperature was calibrated to an accuracy of  $\pm 5$  °C using the melting points of  $\text{NaNO}_3$  (308 °C),  $\text{CsCl}$  (645 °C) and  $\text{NaCl}$  (801 °C), but due to manual heating the overall accuracy during the collection of the Raman spectra was  $\pm 20$  °C. No force was applied to the quartz chip, but the pressure inside the fluid inclusions increased continuously during heating due to their isochoric behavior, reaching ca. 100 MPa at 600 °C.

To be able to quantitatively interpret the Raman Spectra, standard solutions of  $\text{H}_2\text{SO}_4$  and  $\text{SO}_2$  (the latter in the form of  $\text{H}_2\text{SO}_3$  dissolved in water) were prepared as described in Binder and Keppler (2011), and ratios of the intensity integral areas of sulfur species over the intensity integral area of the  $\sim 1640$   $\text{cm}^{-1}$   $\text{H}_2\text{O}$  absorption band were determined. The resulting conversion factors for  $\text{HSO}_4^-$  ( $I_{\text{HSO}_4^-}/I_{\text{H}_2\text{O}} = 1.5799$  molal  $\text{HSO}_4^-$ ),  $\text{SO}_4^{2-}$  ( $I_{\text{SO}_4^{2-}}/I_{\text{H}_2\text{O}} = 31.0286$  molal  $\text{SO}_4^{2-}$ ) and  $\text{SO}_2$  ( $I_{\text{SO}_2}/I_{\text{H}_2\text{O}} = 1.9880$  molal  $\text{SO}_2$ ) differ by up to a factor of 4 from those determined by Binder and Keppler ( $I_{\text{HSO}_4^-}/I_{\text{H}_2\text{O}} = 1.0453$  molal  $\text{HSO}_4^-$ ),  $\text{SO}_4^{2-}$  ( $I_{\text{HSO}_4^{2-}}/I_{\text{H}_2\text{O}} = 11.324$  molal  $\text{SO}_4^{2-}$ ) and  $\text{SO}_2$  ( $I_{\text{SO}_2}/I_{\text{H}_2\text{O}} = 0.5411$  molal  $\text{SO}_2$ ), which probably is due to the use of a different Raman spectrometer setup.

### 2.2.4. LA-ICP-MS

Major and trace element concentrations in hydrous glasses, fine-grained mafic run products, and synthetic fluid inclusions were measured by Laser Ablation (LA)- Inductively Coupled Plasma (ICP)- Mass Spectrometry (MS). The LA-ICP-MS setup at Bayerisches Geoinstitut features a 193 nm ArF Excimer laser (GeolasPro, Coherent, USA) attached to an Elan DRC-e (Perkin Elmer, Canada) quadrupole mass spectrometer, similar to the equipment described in Günther et al. (1998). The laser was operated at a frequency of 10 Hz with an energy density of  $\sim 10$   $\text{J}\cdot\text{cm}^{-2}$  on

the sample surface. The sample chamber ( $\sim 8 \text{ cm}^3$ ) was flushed by 0.4 L/min He gas to which 5 mL/min  $\text{H}_2$  gas was added on the way to the ICP-MS (Guillong and Heinrich, 2007). The ICP-MS system was tuned to a thorium oxide rate of  $\sim 0.05\%$  and a rate of doubly-charged calcium ions of  $\sim 0.1\%$  based on measurements on the NIST-610 standard.

The laser pit size was 70  $\mu\text{m}$  diameter for bulk analyses of the solid rocks samples, 50-70  $\mu\text{m}$  for hydrous glasses, and 30-50  $\mu\text{m}$  for fluid inclusions. Mafic rocks and hydrous glasses were analyzed at 7-10 points along profiles parallel to the long axis of the capsule, and averages plus standard deviations were calculated. Due to the fine-grained nature of the mafic run product ( $\leq 10 \mu\text{m}$  grain size) a laser pit size of 70  $\mu\text{m}$  diameter was sufficient to produce stable signals. Measured isotopes include  $^7\text{Li}$ ,  $^{11}\text{B}$ ,  $^{23}\text{Na}$ ,  $^{25}\text{Mg}$ ,  $^{27}\text{Al}$ ,  $^{30}\text{Si}$ ,  $^{32}\text{S}$ ,  $^{35}\text{Cl}$ ,  $^{39}\text{K}$ ,  $^{43}\text{Ca}$ ,  $^{49}\text{Ti}$ ,  $^{55}\text{Mn}$ ,  $^{57}\text{Fe}$ ,  $^{60}\text{Ni}$ ,  $^{65}\text{Cu}$ ,  $^{66}\text{Zn}$ ,  $^{75}\text{As}$ ,  $^{79}\text{Br}$ ,  $^{82}\text{Se}$ ,  $^{85}\text{Rb}$ ,  $^{88}\text{Sr}$ ,  $^{90}\text{Zr}$ ,  $^{98}\text{Mo}$ ,  $^{107}\text{Ag}$ ,  $^{114}\text{Cd}$ ,  $^{121}\text{Sb}$ ,  $^{125}\text{Te}$ ,  $^{133}\text{Cs}$ ,  $^{137}\text{Ba}$ ,  $^{140}\text{Ce}$ ,  $^{184}\text{W}$ ,  $^{185}\text{Re}$ ,  $^{195}\text{Pt}$ ,  $^{197}\text{Au}$ ,  $^{205}\text{Tl}$ ,  $^{208}\text{Pb}$  and  $^{209}\text{Bi}$ , measured using dwell times of 10-50 ms per isotope. Due to the large number of elements two separate element menus were used for the analysis of fluid inclusions, each containing Na, Al, Si, S, Cl, K, Ca, Fe, Br and Cs plus 11-13 of the remaining elements. With each element menu 4-10 fluid inclusions were measured, and the results were then combined to a single data set. Corrections for contributions of ablated host quartz were made for Li, Na, S, Cl, As, Sb and Br, assuming that the fluid inclusions themselves do not contain any  $\text{SiO}_2$ . External standardization was based mostly on NIST-610 (Jochum et al., 2011), except for S, Cl and Br, which were quantified based on afghanite (S, Cl; Seo et al., 2011) and an in-house scapolite standard that was calibrated against the standards BB1 and BB2 of Kendrick (2012) using the revised Br concentrations listed in Table S4 of Kendrick et al. (2013). Analyses of up to 14 unknowns were bracketed by 2 analyses of NIST-610 plus 1 analysis of either afghanite or scapolite at the beginning and the end of each analysis block. Internal standardization for the glasses and mafic run products was done by normalizing the sum of all major element oxides to 100 wt%, whereas microthermometrically determined Na concentrations (corrected for the presence of other major cations; Heinrich et al., 2003) or loaded Na, K, Rb or Cs concentrations were used in the case of fluid inclusions. In the re-equilibration experiments, K or average Rb concentrations determined in the fluid inclusions prior to the re-equilibration experiments were used as the internal standard, because Na concentrations proved to become modified during re-equilibration and thus are not reliable. The overall uncertainty associated with LA-ICP-MS

analyses of synthetic fluid inclusions with known internal standard element concentration is about 10% (Heinrich et al., 2003); for S, Cl and Br it is about 20% (Seo et al., 2011).

### 3. Results and discussions

#### 3.1. Transfer of volatiles and metals from mafic to felsic magmas in composite magma chambers

Partition coefficients ( $D_{\text{fluid/rock}} = C_{\text{fluid}}/C_{\text{rock}}$ ) of elements between fluid and mafic rock residue at 850 °C and 2 kbar were calculated from their concentrations in the fluid inclusions and the mafic residue (Fig. 3.1). In two additional runs, information on relative element mobilities were obtained by reacting fluids that exsolved from crystallizing mafic magma with juxtaposed silicic melts (haplogranite and rhyolite), which has the advantage that it is more sensitive and thus allows very fluid-immobile elements such as Ti and Zr to be studied. Loss factors in the mafic part of the two runs (Fig. 3.1) were calculated as follows:

$$\text{loss factor} = \frac{|C_0 - C_T|}{C_T} \quad (3-1)$$

where  $C_0$  is the element concentration in mafic starting glass and  $C_T$  is the element concentration in mafic end product.

The combined results suggest that at the studied P-T conditions, S, Cl, Cu, Se, Br, Cd and Te are most volatile ( $D_{\text{fluid/rock}} > 10$ ), followed by Li, B, Zn, As, Ag, Sb, Cs, W, Tl, Pb and Bi ( $D_{\text{fluid/rock}} = 1-10$ ). Less volatile are Na, Mg, K, Ca, Mn, Fe, Rb, Sr and Mo ( $D_{\text{fluid/rock}} = 0.1-1$ ), and the least fluid-mobile elements are Al, Si, Ti, Zr, Ba and Ce ( $D_{\text{fluid/rock}} < 0.1$ ).

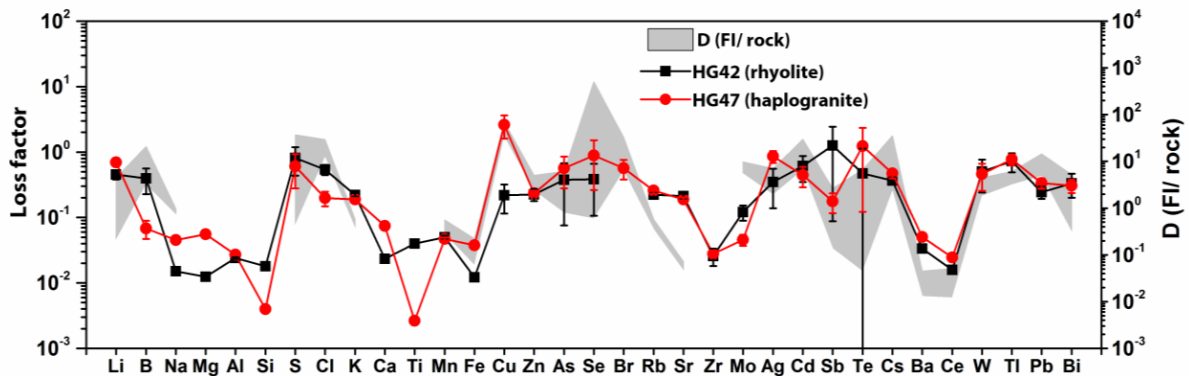


**Fig. 3.1.** Comparison of loss factors calculated from experiments involving a felsic melt reservoir (HG42 and HG47) with fluid-rock partition coefficients calculated from experiments involving synthetic fluid inclusions (grey area).

The volatile elements identified in this study are consistent with observations in nature: magmatic sulfides in the rhyodacite of Mount Pinatubo are enriched in Cu, Zn, Se and probably also Ag, Cd and Te (Hattori, 1993; 1996); melt inclusions and silicate minerals studied by Berlo et al. (2004), Kent et al. (2007), Rowe et al. (2008) and Collins et al. (2009) show anomalously high concentrations of Li and/or Cu, reflecting addition of Cu- and Li-rich fluids to magmas; and similar metal abundances are found in natural fluid inclusions (e.g., Williams-Jones and Heinrich, 2005), volcanic plume particles (e.g., Moune et al., 2010), and fumarolic condensates (e.g., Zelenski et al., 2014). Our experimental data trend is broadly consistent with relative element volatilities determined from natural high-temperature fumarole gases (Fig. 3.2). The differences are probably due to the lower density of fumarolic gases or other factors (see manuscript for details).

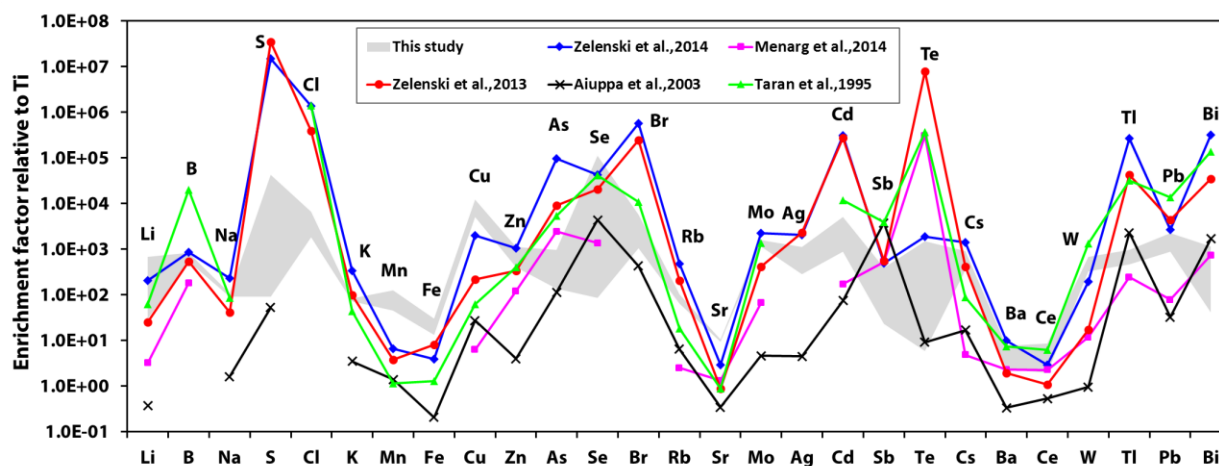


**Fig. 3.2.** Enrichment factors (EF) of elements in the fluid phase relative to the mafic source, normalized to corresponding Ti contents. Data obtained from our experiments involving synthetic fluid inclusions (gray array) are compared with data obtained from the analysis of fumarolic gases/aerosols and whole-rocks from five arc volcanoes worldwide: Tolbachik (Zelenski et al., 2014), Erta Ale (Zelenski et al., 2013), Kudryavy (Taran et al., 1995), Lascar (Menard et al., 2014) and Etna (Aiuppa et al., 2003).

Based on the volatility data and measured mineral–melt and sulfide–melt partition coefficients, volatile fluxing in felsic natural samples may be monitored by Cu, Se, Te and Cd-enrichment in magmatic sulfides, and by As, Se, Cd and Bi-enrichment in magmatic apatite.

### 3.2. Solubility of gold in oxidized, sulfur-bearing fluids at 500-850 °C and 200-230 MPa: a synthetic fluid inclusion study

Gold solubility in sulfur-free fluids increases with a slope of  $\sim 0.25$  in  $\log [\text{Au}]$  vs.  $\log f\text{O}_2$  diagrams (Fig. 3.3), and with a slope of  $\sim 1$  in the  $\log [\text{Au}]$  vs.  $\log [\text{NaCl}]$  diagram, suggesting that Au had a valence state of +1 in the Au-bearing complex(es). Therefore, gold likely dissolved mainly in the form of  $\text{NaAuCl}_2$  in sulfur-free fluids as the followed dissolution reaction:

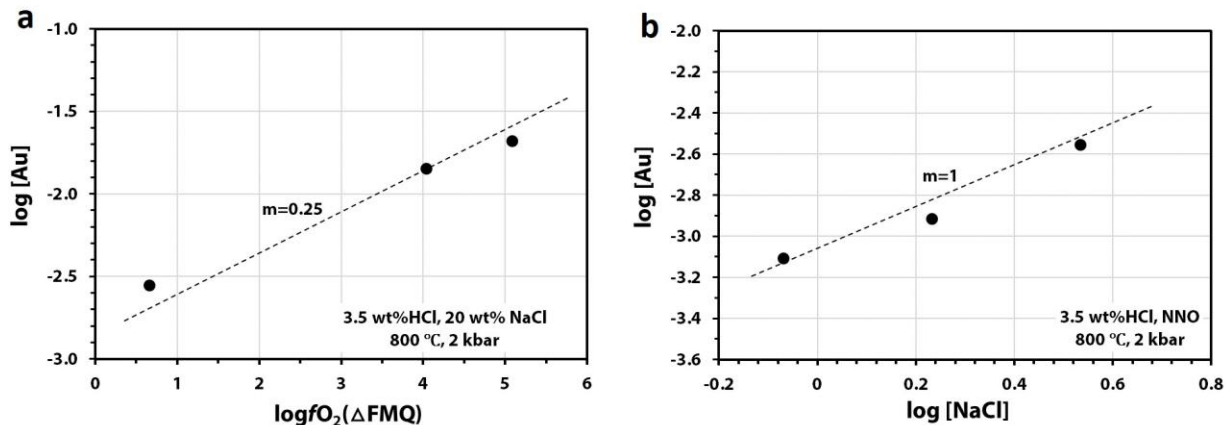
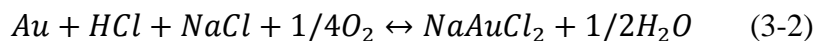


**Fig. 3.3.** Logarithmic plots showing the Au solubility in sulfur-free fluids at 800 °C, 2 kbar as a function of: (a)  $f\text{O}_2$  relative to the fayalite-magnetite-quartz (FMQ) buffer, and (b) starting NaCl concentration. All concentrations are given in moles per 1000 g water.

Gold solubility in fluids was also found to depend positively on temperature, starting sulfate concentration, HCl-content, fluid salinity and oxygen fugacity (Fig. 3.4). The in-situ Raman spectra of such fluid inclusions to 600 °C demonstrated that the sulfur species at high temperature and pressure were dominantly  $\text{HSO}_4^-$  and  $\text{SO}_2$ , and that the  $\text{S}^{6+}/\text{S}^{4+}$  ratio in the bulk fluid probably remained constant. Weight-percent level Au solubilities were observed in  $f\text{O}_2$ -unbuffered fluids containing sulfate and chlorine, which appears to be due to the formation of  $\text{NaAuCl}_2$  complexes via the reactions:



Fluids in porphyry Cu-Au ( $\pm\text{Mo}$ ) ore forming environments (containing 7 wt% NaCl, 1.0 wt% S and 1.1 wt% HCl;  $f\text{O}_2$  buffered by hematite-magnetite at 600 °C, 2 kbar) can dissolve  $\sim 600$  ppm Au, which is about two orders of magnitude higher than actual Au contents in natural magmatic-

hydrothermal brines in porphyry Cu-Au ( $\pm$ Mo) deposits. Therefore, Au precipitation in porphyry Cu-Au ( $\pm$ Mo) deposits is unlikely to be controlled via Au solubility in the fluid, but rather via the precipitation of Cu-Fe sulfides that incorporate Au as a minor or trace constituent and then exsolve native Au during cooling.

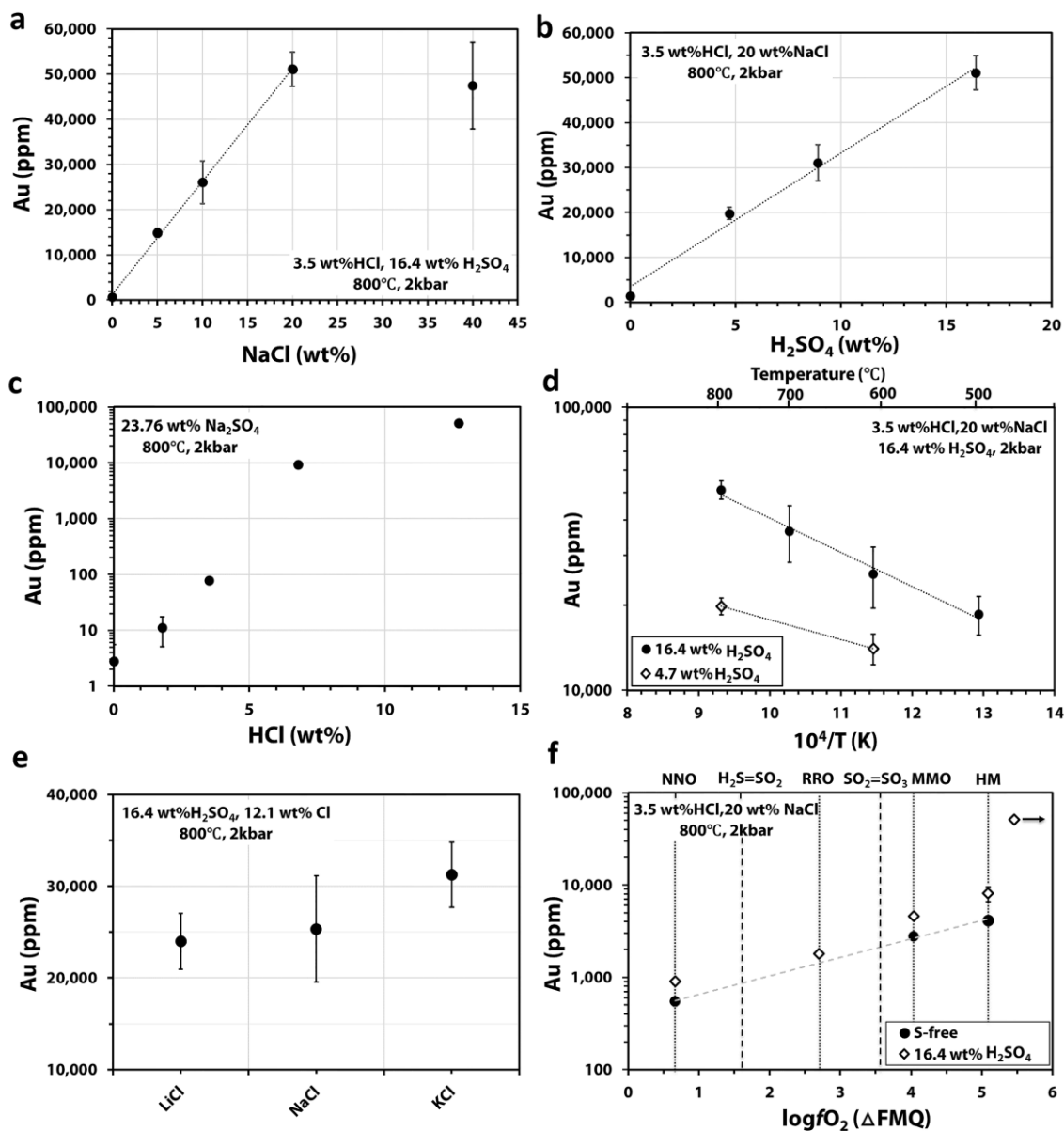


**Fig. 3.4.** Gold solubility as a function of: (a) NaCl concentration in the starting fluid, (b) H<sub>2</sub>SO<sub>4</sub> concentration in the starting fluid, (c) HCl concentration in the starting fluid, (d) temperature, (e) type of alkali ion and (f) oxygen fugacity. Sulfur speciation boundaries in (f) are from Binder and Keppler (2011). FMQ: fayalite-magnetite-quartz buffer.

### 3.3. Gold diffusion into and out of quartz-hosted fluid inclusions during re-equilibration experiments at 600-800 °C and 2 kbar

Fluid inclusions synthesized in pre-runs display a large variety in shapes and measure up to ~50  $\mu\text{m}$  in length (Figs. 3.5a, c). After re-equilibration, some fluid inclusions show notable changes in morphology, i.e., originally irregular and elongated fluid inclusions attained more isometric and regular shapes (Figs. 3.5b, d). In the sulfur-bearing re-equilibration experiment conducted in a  $\text{Au}_{95}\text{Cu}_5$  alloy capsule, the fluid inclusions contained large Cu sulfide daughter crystals after re-equilibration (Fig. 3.5d).

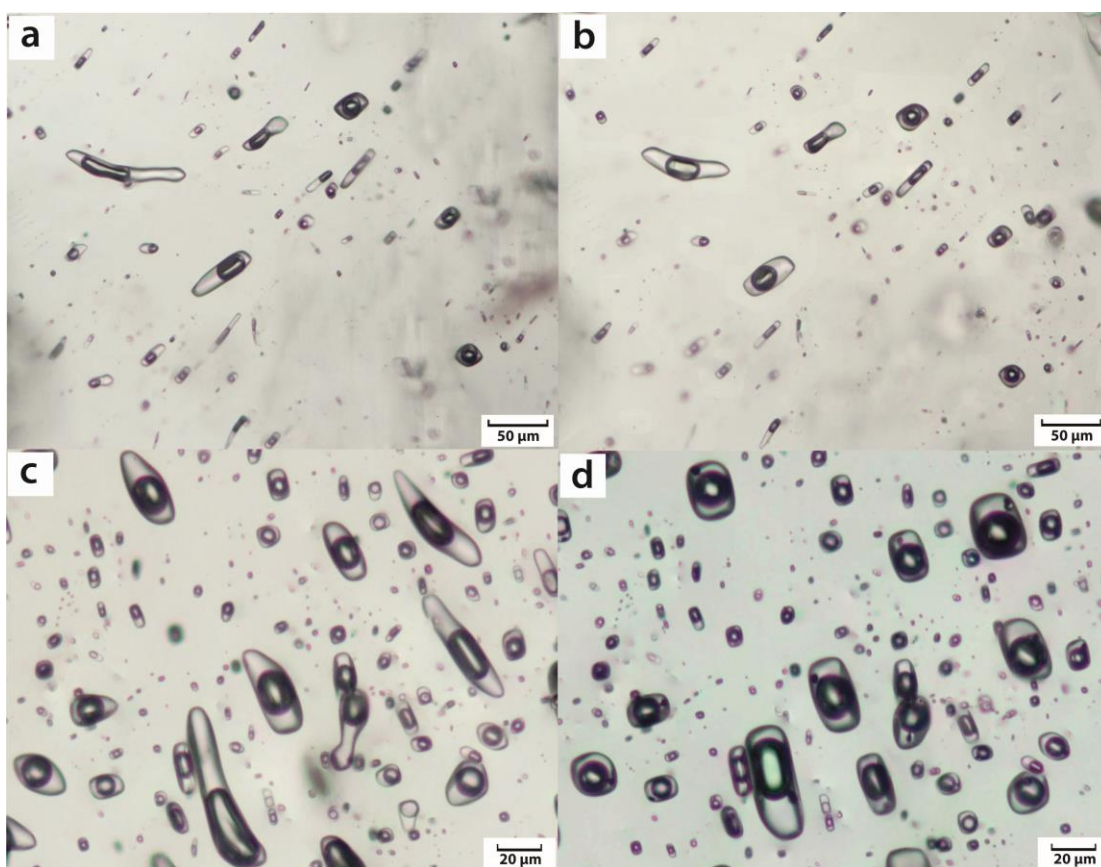


**Fig. 3.5.** Transmitted-light photomicrographs of fluid inclusions synthesized in the study: (a) fluid inclusions synthesized at 800 °C and 2 kbar (run #10; 4 days), photographed before re-equilibration, (b) the same fluid inclusions after re-equilibration at 800 °C and 2 kbar (run #11; 4 days), (c) sulfur-bearing fluid inclusions synthesized at 800 °C and 2 kbar (run #22; 4 days), photographed before re-equilibration, (d) the same fluid inclusions after re-equilibration in a  $\text{Au}_{95}\text{Cu}_5$  capsule at 800 °C and 2 kbar (run #23; 7 days). Notice the presence of sulfide daughter crystals in the fluid inclusions in (d).

Fluid inclusions containing ~5 wt% KCl synthesized in platinum capsules at 800 °C and 600 °C, 2 kbar were re-equilibrated in Cs-spiked, HCl- and NaCl-bearing solutions in new gold capsules at the same P-T conditions for 4-14 days. Both Na and Au concentrations significantly increased during the re-equilibration process, with Na increasing up to 0.23 wt% and Au increasing up to 570 ppm at 800 °C (Fig. 3.6a). Similar observations were made in an experiment conducted at 600 °C, 2 kbar (Fig. 3.6b). The high K-content and absence of Cs in the fluid inclusions proves that they did not crack open during the re-equilibration, implying that Na and Au were gained by diffusion through the quartz lattice. Reversed experiments were conducted by synthesizing Au-bearing fluid inclusions in gold capsules and then re-equilibrating them in a platinum capsule, which resulted in up to ~900 ppm Au depletion (Fig. 3.6c). Two experiments were performed to test whether Au could be gained by fluid inclusions as a result of decreasing acidity in the external fluid. However, no evidence for diffusional exchange of Au with H<sup>+</sup> was found. To test whether the formation of Cu-rich sulfide phases within fluid inclusions has any influence on Au uptake, fluid inclusions of a pre-run containing 9.8 wt% NaCl, 2.3 wt% S, ~400 ppm Rb, and 370±70 ppm Au with a pH of <1, were re-equilibrated in an aqueous fluid containing 9.9 wt% NaCl, 1.5 wt% KOH, 1.5 wt% sulfur, ~70 ppm Cs, 48±13 ppm Au with a pH of 2 in a Au<sub>95</sub>Cu<sub>05</sub> alloy capsule. This re-equilibration caused the fluid inclusions to gain 6.8± 2.1 wt% Cu and ~0.7 wt% Na, but no gain of Au was detected (Fig. 3.6d).

In summary, Au diffusion appears to be driven solely by Au concentration gradients. In contrast to the behavior of Na<sup>+</sup> and Cu<sup>+</sup>, no evidence was found that Au<sup>+</sup> diffusively exchanges with H<sup>+</sup> or gets incorporated into Cu-bearing sulfide daughter crystals in H<sub>2</sub>S-bearing experiments. Since Au solubilities in cooling magmatic-hydrothermal fluids tend to decrease, natural fluid inclusions are more likely to have lost Au rather than to have gained some.

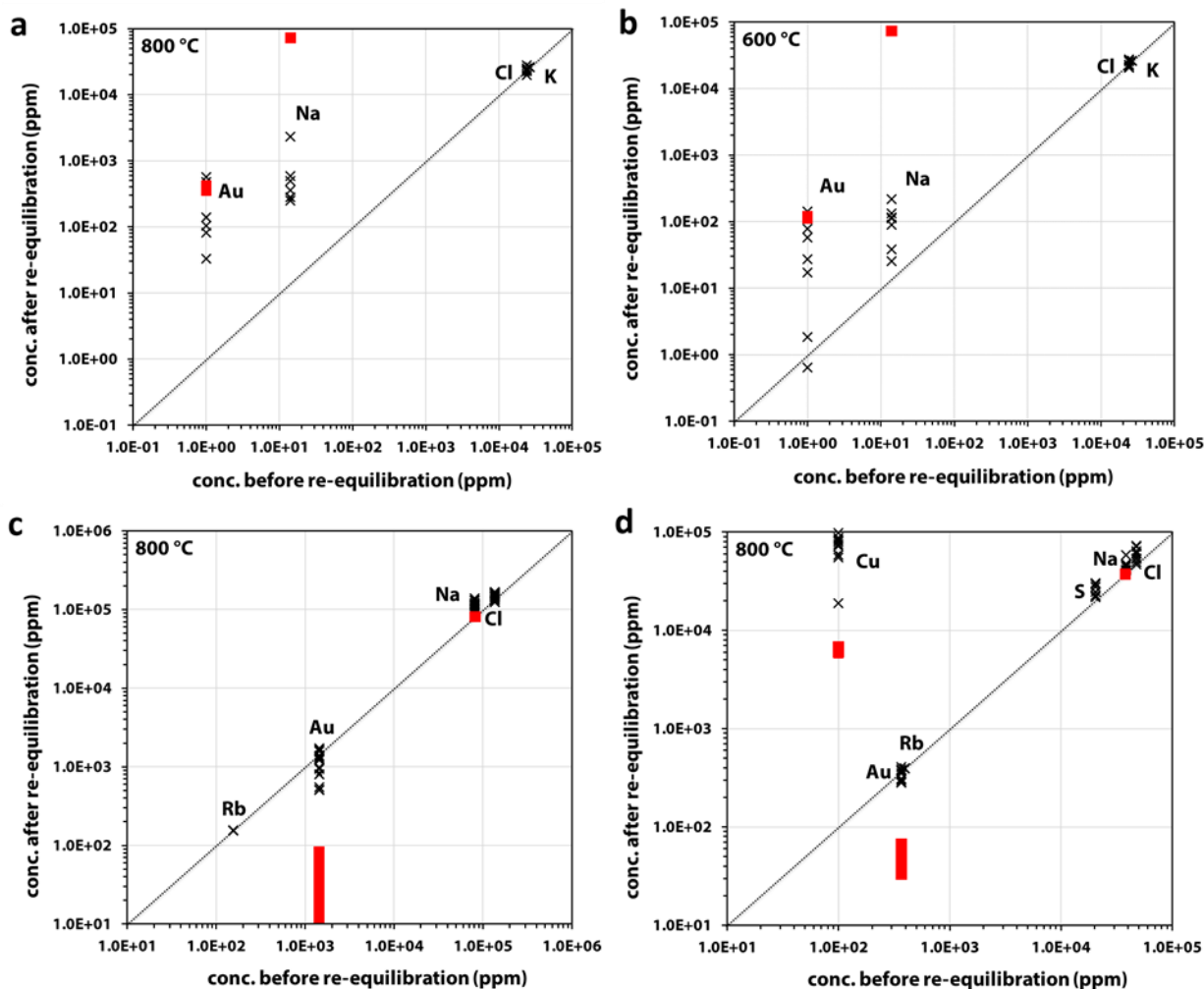


**Fig. 3.6.** Composition of fluid inclusions before vs. after re-equilibration (crosses), plus composition of the external fluid present during the re-equilibration experiment (red bars): (a) fluid inclusions containing 5.0 wt% KCl, re-equilibrated in an external fluid containing 3.5 wt% HCl + 20.1 wt% NaCl + 115±9 ppm Cs at 800 °C, 2 kbar for 4 days (runs #1+2). (b) similar fluid inclusions re-equilibrated at 600 °C, 2 kbar for 14 days (runs #3+4). (c) fluid inclusions which originally contained 20.6 wt% NaCl, 1440±250 ppm Au, and 156±11 ppm Rb, re-equilibrated in an external fluid containing 20.3 wt% NaCl + 14.9 wt% KCl + 0.2 wt% KOH within a Pt capsule at 800 °C, 2 kbar for 4 days (runs #8+10). (d) fluid inclusions which originally contained 9.8 wt% NaCl + 2.3 wt% elemental S + 393±22 ppm Rb + 370±70 ppm Au, re-equilibrated in an external fluid containing 9.9 wt% NaCl + 72±7 ppm Cs + 1.5 wt% KOH within a Au<sub>95</sub>Cu<sub>05</sub> capsule at 800 °C, 2 kbar for 7 days (runs #22+23). The Cu content of the fluid inclusions after the pre-run (run #22) was below the detection limit of 30-100 ppm.

---

## 4. References

- Aiuppa A., Dongarrà G., Valenza M., Federico C. and Pecoraino G. (2003) Degassing of trace volatile metals during the 2001 eruption of Etna. In *Volcanism and the Earth's Atmosphere* (eds. A. Robock and C. Oppenheimer). Geophysical Monograph **139**, American Geophysical Union Washington, DC, pp. 41–54.
- Alt J.C., Shanks W.C. and Jackson M.C. (1993) Cycling of sulfur in subduction zones: The geochemistry of sulfur in the Mariana Island Arc and back-arc trough. *Earth Planet. Sci. Lett.* **119**, 477-494.
- Annen C., Blundy J. and Sparks R. (2006) The genesis of intermediate and silicic magmas in deep crustal hot zones. *J. Petrol.* **47**, 505-539.
- Audétat A. and Günther D. (1999) Mobility and H<sub>2</sub>O loss from fluid inclusions in natural quartz crystals. *Contrib. Mineral. Petrol.* **137**, 1-14.
- Audétat A., Gunther D. and Heinrich C.A. (1998) Formation of a magmatic-hydrothermal ore deposit: Insights with LA-ICP-MS analysis of fluid inclusions. *Science* **279**, 2091-2094.
- Audétat A. and Pettke T. (2003) The magmatic-hydrothermal evolution of two barren granites: A melt and fluid inclusion study of the Rito del Medio and Canada Pinabete plutons in northern New Mexico (USA). *Geochim. Cosmochim. Acta* **67**, 97-121.
- Audétat A. and Pettke T. (2006) Evolution of a porphyry-Cu mineralized magma system at Santa Rita, New Mexico (USA). *J. Petrol.* **47**, 2021-2046.
- Audétat A., Pettke T., Heinrich C.A. and Bodnar R.J. (2008) The Composition of Magmatic-Hydrothermal Fluids in Barren and Mineralized Intrusions. *Econ. Geol.* **103**, 877-908.
- Audétat A. and Simon A.C. (2013) Magmatic controls on porphyry Cu genesis, In *Geology and genesis of major copper deposits and districts of the world: a tribute to Richard Sillitoe* (eds. J.W. Hedenquist, M. Harris and F. Camus). Society of Economic Geologists Special Publication 16, pp. 553-572.
- Bachmann O. and Bergantz G.W. (2008) Deciphering magma chamber dynamics from styles of compositional zoning in large silicic ash flow sheets. *Rev. Mineral. Geochem.* **69**, 651-674.
- Bassett W.A., Shen A., Bucknum M. and Chou I.M. (1993) A new diamond anvil cell for hydrothermal studies to 2.5 GPa and from -190 to 1200 °C. *Rev. Sci. Instrum.* **64**, 2340-2345.
- Behrens H., Ohlhorst S., Holtz F. and Champenois M. (2004) CO<sub>2</sub> solubility in dacitic melts equilibrated with H<sub>2</sub>O-CO<sub>2</sub> fluids: Implications for modeling the solubility of CO<sub>2</sub> in silicic melts. *Geochim. Cosmochim. Acta* **68**, 4687-4703.

- Bell A.S., Simon A. and Guillong M. (2011) Gold solubility in oxidized and reduced, water-saturated mafic melt. *Geochim. Cosmochim. Acta* **75**, 1718-1732.
- Benjamin E.R., Plank T., Wade J.A., Kelley K.A., Hauri E.H. and Alvarado G.E. (2007) High water contents in basaltic magmas from Irazú Volcano, Costa Rica. *J. Volcanol. Geotherm. Res.* **168**, 68-92.
- Berlo K., Blundy J., Turner S., Cashman K., Hawkesworth C. and Black S. (2004) Geochemical precursors to volcanic activity at Mount St. Helens, USA. *Science* **306**, 1167-1169.
- Binder B. and Keppler H. (2011) The oxidation state of sulfur in magmatic fluids. *Earth Planet. Sci. Lett.* **301**, 190-198.
- Blank J.G. and Brooker R.A. (1994) Experimental studies of carbon dioxide in silicate melts; solubility, speciation, and stable carbon isotope behavior. *Rev. Mineral. Geochem.* **30**, 157-186.
- Bodnar R., Burnham C. and Sterner S. (1985) Synthetic fluid inclusions in natural quartz. III. Determination of phase equilibrium properties in the system H<sub>2</sub>O-NaCl to 1000 °C and 1500 bars. *Geochim. Cosmochim. Acta* **49**, 1861-1873.
- Bodnar R. and Vityk M.O. (1994) Interpretation of microthermometric data for H<sub>2</sub>O-NaCl fluid inclusions. *Fluid inclusions in minerals: methods and applications*, 117-130.
- Boettcher A. and Kerrick D. (1971) Temperature calibration in cold-seal pressure vessels, In *Research Techniques for High Pressure and High Temperature* (ed. G.C.Ulmer). Springer, pp. 179-193.
- Bose K. and Ganguly J. (1995) Quartz-coesite transition revisited; reversed experimental determination at 500-1200 °C and retrieved thermochemical properties. *Am. Mineral.* **80**, 231-238.
- Brandon A.D. and Draper D.S. (1996) Constraints on the origin of the oxidation state of mantle overlying subduction zones: an example from Simcoe, Washington, USA. *Geochim. Cosmochim. Acta* **60**, 1739-1749.
- Briffa K.R., Jones P.D., Schweingruber F.H. and Osborn T.J. (1998) Influence of volcanic eruptions on Northern Hemisphere summer temperature over the past 600 years. *Nature* **393**, 450-455.
- Burnham C.W. (1979a) The importance of volatile constituents, In *The evolution of the igneous rocks: Fiftieth Anniversary Perspectives* (ed. H.J. Yoder), Princeton, NJ: Princeton University Press 16, pp. 439-482.
- Burnham C.W. (1979b) Magmas and hydrothermal fluids, In *Geochemistry of Hydrothermal Ore Deposits* (ed. H.L. Barnes), John Wiley, New York, pp. 71-136.

- Carroll M.R. and Rutherford M.J. (1987) The stability of igneous anhydrite: experimental results and implications for sulfur behavior in the 1982 El Chichon trachyandesite and other evolved magmas. *J. Petrol.* **28**, 781-801.
- Carroll M.R. and Webster J.D. (1994) Solubilities of sulfur, noble gases, nitrogen, chlorine, and fluorine in magmas. *Rev. Mineral. Geochem.* **30**, 231-279.
- Collins S.J., Pyle D.M. and Maclennan J. (2009) Melt inclusions track pre-eruption storage and dehydration of magmas at Etna. *Geology* **37**, 571-574.
- Condomines M., Gauthier P.-J. and Sigmarsson O. (2003) Timescales of magma chamber processes and dating of young volcanic rocks. *Rev. Mineral. Geochem.* **52**, 125-174.
- Davis L.L. and Smith D. (1993) Ni-rich olivine in minettes from Two Buttes, Colorado: A connection between potassic melts from the mantle and low Ni partition coefficients. *Geochim. Cosmochim. Acta* **57**, 123-129.
- Davis L.L., Smith D., McDowell F.W., Walker N.W. and Borg L.E. (1996) Eocene potassic magmatism at Two Buttes, Colorado, with implications for Cenozoic tectonics and magma generation in the western United States. *Geol. Soc. Am. Bull.* **108**, 1567-1579.
- DePaolo D.J. (1981) Trace element and isotopic effects of combined wallrock assimilation and fractional crystallization. *Earth Planet. Sci. Lett.* **53**, 189-202.
- Doppler G., Bakker R.J. and Baumgartner M. (2013) Fluid inclusion modification by H<sub>2</sub>O and D<sub>2</sub>O diffusion: the influence of inclusion depth, size, and shape in re-equilibration experiments. *Contrib. Mineral. Petrol.* **165**, 1259-1274.
- Drummond M.S. and Defant M.J. (1990) A Model for Trondhjemite-Tonalite-Dacite Genesis and Crustal Growth Via Slab Melting - Archean to Modern Comparisons. *J Geophys Res-Solid* **95**, 21503-21521.
- Esposito R., Bodnar R.J., Danyushevsky L.V., De Vivo B., Fedele L., Hunter J., Lima A. and Shimizu N. (2011) Volatile Evolution of Magma Associated with the Solchiaro Eruption in the Phlegrean Volcanic District (Italy). *J. Petrol.* **52**, 2431-2460.
- Farmer G.L. (2014) 4.3 - Continental Basaltic Rocks, In *Treatise on Geochemistry (Second Edition)* (ed. K.K. Turekian). Elsevier, Oxford, pp. 75-110.
- Feldstein S.N. and Lange R.A. (1999) Pliocene potassic magmas from the Kings River region, Sierra Nevada, California: Evidence for melting of a subduction-modified mantle. *J. Petrol.* **40**, 1301-1320.
- Fine G. and Stolper E. (1985) The speciation of carbon dioxide in sodium aluminosilicate glasses. *Contrib. Mineral. Petrol.* **91**, 105-121.
- Foley S. (1992) Vein-plus-wall-rock melting mechanisms in the lithosphere and the origin of potassic alkaline magmas. *Lithos* **28**, 435-453.

- Forneris J.F. and Holloway J.R. (2003) Phase equilibria in subducting basaltic crust: implications for H<sub>2</sub>O release from the slab. *Earth Planet. Sci. Lett.* **214**, 187-201.
- Fourmentraux C., Métrich N., Bertagnini A. and Rosi M. (2012) Crystal fractionation, magma step ascent, and syn-eruptive mingling: the Averno 2 eruption (Phlegraean Fields, Italy). *Contrib. Mineral. Petrol.* **163**, 1121-1137.
- Frank M.R., Candela P.A., Piccoli P.M. and Glascock M.D. (2002) Gold solubility, speciation, and partitioning as a function of HCl in the brine-silicate melt-metallic gold system at 800 °C and 100 MPa. *Geochim. Cosmochim. Acta* **66**, 3719-3732.
- Gibert F., Pascal M.L. and Pichavant M. (1998) Gold solubility and speciation in hydrothermal solutions: Experimental study of the stability of hydrosulphide complex of gold (AuHS °) at 350 to 450 °C and 500 bars. *Geochim. Cosmochim. Acta* **62**, 2931-2947.
- Götze J. (2009) Chemistry, textures and physical properties of quartz – geological interpretation and technical application. *Mineral. Mag.* **73**, 645-671.
- Günther D., Audétat A., Frischknecht R. and Heinrich C.A. (1998) Quantitative analysis of major, minor and trace elements in fluid inclusions using laser ablation inductively coupled plasma mass spectrometry. *J. Anal. At. Spectrom.* **13**, 263-270.
- Guillong M. and Heinrich C.A. (2007) Sensitivity enhancement in laser ablation ICP-MS using small amounts of hydrogen in the carrier gas. *J. Anal. At. Spectrom.* **22**, 1488-1494.
- Hall D.L. and Bodnar R.J. (1990) Methane in fluid inclusions from granulites: A product of hydrogen diffusion? *Geochim. Cosmochim. Acta* **54**, 641-651.
- Halter W.E., Heinrich C.A. and Pettke T. (2005) Magma evolution and the formation of porphyry Cu–Au ore fluids: evidence from silicate and sulfide melt inclusions. *Mineral. Deposita* **39**, 845-863.
- Hanley J.J., Pettke T., Mungall J.E. and Spooner E.T.C. (2005) The solubility of platinum and gold in NaCl brines at 1.5 kbar, 600 to 800°C: A laser ablation ICP-MS pilot study of synthetic fluid inclusions. *Geochim. Cosmochim. Acta* **69**, 2593-2611.
- Harris D.M. and Anderson A.T. (1984) Volatiles H<sub>2</sub>O, CO<sub>2</sub>, and Cl in a subduction related basalt. *Contrib. Mineral. Petrol.* **87**, 120-128.
- Hattori K. (1993) High-sulfur magma, a product of fluid discharge from underlying mafic magma: evidence from Mount Pinatubo, Philippines. *Geology* **21**, 1083-1086.
- Hattori K. (1996) Occurrence and origin of sulfide and sulfate in the 1991 Mount Pinatubo eruption products, In *Fire and mud: Eruptions and lahars of Mount Pinatubo, Philippines* (eds. C.G. Newhall and R.S. Punongbayan). University of Washington Press, pp. 807-824.
- Hattori K.H. and Guillot S. (2003) Volcanic fronts form as a consequence of serpentinite dehydration in the forearc mantle wedge. *Geology* **31**, 525-528.

- Hawkesworth C.J., Blake S., Evans P., Hughes R., Macdonald R., Thomas L.E., Turner S.P. and Zellmer G. (2000) Time Scales of Crystal Fractionation in Magma Chambers—Integrating Physical, Isotopic and Geochemical Perspectives. *J. Petrol.* **41**, 991-1006.
- Hedenquist J. and Richards J. (1998) The influence of geochemical techniques on the development of genetic models for porphyry copper deposits, In *Techniques in hydrothermal ore deposits geology* (eds. J.P. Richards and P.B. Larson). Reviews in Economic Geology 10, pp. 235-256.
- Heinrich C.A., Günther D., Audétat A., Ulrich T. and Frischknecht R. (1999) Metal fractionation between magmatic brine and vapor, determined by microanalysis of fluid inclusions. *Geology* **27**, 755.
- Heinrich C.A., Pettke T., Halter W.E., Aigner-Torres M., Audétat A., Günther D., Hattendorf B., Bleiner D., Guillong M. and Horn I. (2003) Quantitative multi-element analysis of minerals, fluid and melt inclusions by laser-ablation inductively-coupled-plasma mass-spectrometry. *Geochim. Cosmochim. Acta* **67**, 3473-3497.
- Herzberg C., Fyfe W. and Carr M. (1983) Density constraints on the formation of the continental Moho and crust. *Contrib. Mineral. Petrol.* **84**, 1-5.
- Hildreth W. and Moorbath S. (1988) Crustal contributions to arc magmatism in the Andes of central Chile. *Contrib. Mineral. Petrol.* **98**, 455-489.
- Jochum K.P., Weis U., Stoll B., Kuzmin D., Yang Q., Raczek I., Jacob D.E., Stracke A., Birbaum K., Frick D.A., Günther D. and Enzweiler J. (2011) Determination of Reference Values for NIST SRM 610-617 Glasses Following ISO Guidelines. *Geostand. Geoanal. Res.* **35**, 397-429.
- Johnson E.R., Wallace P.J., Cashman K.V. and Delgado Granados H. (2010) Degassing of volatiles (H<sub>2</sub>O, CO<sub>2</sub>, S, Cl) during ascent, crystallization, and eruption at mafic monogenetic volcanoes in central Mexico. *J. Volcanol. Geotherm. Res.* **197**, 225-238.
- Johnson E.R., Wallace P.J., Delgado Granados H., Manea V.C., Kent A.J.R., Bindeman I.N. and Donegan C.S. (2009) Subduction-related Volatile Recycling and Magma Generation beneath Central Mexico: Insights from Melt Inclusions, Oxygen Isotopes and Geodynamic Models. *J. Petrol.* **50**, 1729-1764.
- Jugo P.J., Wilke M. and Botcharnikov R.E. (2010) Sulfur K-edge XANES analysis of natural and synthetic basaltic glasses: Implications for S speciation and S content as function of oxygen fugacity. *Geochim. Cosmochim. Acta* **74**, 5926-5938.
- Kamenetsky V.S. and Danyushevsky L.V. (2005) Metals in quartz-hosted melt inclusions: Natural facts and experimental artifacts. *Am. Mineral.* **90**, 1674-1678.
- Kay R. (1978) Aleutian magnesian andesites: melts from subducted Pacific Ocean crust. *J. Volcanol. Geotherm. Res.* **4**, 117-132.

- Keith J., Whitney J., Hattori K., Ballantyne G., Christiansen E., Barr D., Cannan T. and Hook C. (1997) The role of magmatic sulfides and mafic alkaline magmas in the Bingham and Tintic mining districts, Utah. *J. Petrol.* **38**, 1679-1690.
- Kelley K.A., Plank T., Newman S., Stolper E.M., Grove T.L., Parman S. and Hauri E.H. (2010) Mantle melting as a function of water content beneath the Mariana Arc. *J. Petrol.* **51**, 1711-1738.
- Kendrick M.A. (2012) High precision Cl, Br and I determinations in mineral standards using the noble gas method. *Chem. Geol.* **292-293**, 116-126.
- Kendrick M.A., Arculus R., Burnard P. and Honda M. (2013) Quantifying brine assimilation by submarine magmas: Examples from the Galápagos Spreading Centre and Lau Basin. *Geochim. Cosmochim. Acta* **123**, 150-165.
- Kent A.J., Peate D.W., Newman S., Stolper E.M. and Pearce J.A. (2002) Chlorine in submarine glasses from the Lau Basin: seawater contamination and constraints on the composition of slab-derived fluids. *Earth Planet. Sci. Lett.* **202**, 361-377.
- Kent A.J.R., Blundy J., Cashman K.V., Cooper K.M., Donnelly C., Pallister J.S., Reagan M., Rowe M.C. and Thornber C.R. (2007) Vapor transfer prior to the October 2004 eruption of Mount St. Helens, Washington. *Geology* **35**, 231.
- Keppler H. (1996) Constraints from partitioning experiments on the composition of subduction-zone fluids. *Nature* **380**, 237-240.
- Keppler H. (2010) The distribution of sulfur between haplogranitic melts and aqueous fluids. *Geochim. Cosmochim. Acta* **74**, 645-660.
- Kesler S.E. (1994) Mineral resources, economics, and the environment. *McMillan*.
- Kogiso T., Tatsumi Y. and Nakano S. (1997) Trace element transport during dehydration processes in the subducted oceanic crust: 1. Experiments and implications for the origin of ocean island basalts. *Earth Planet. Sci. Lett.* **148**, 193-205.
- Konschak A. and Keppler H. (2014) The speciation of carbon dioxide in silicate melts. *Contrib. Mineral. Petrol.* **167**.
- Kouzmanov K. and Pokrovski G.S. (2012) Hydrothermal controls on metal distribution in porphyry Cu (-Mo-Au) systems, In *Geology and Genesis of Major Copper Deposits and Districts of the World: A Tribute to Richard Sillitoe* (eds. J.W. Hedenquist, M. Harris and F. Camus). Geological Society, London, Special Publications 16, pp. 573–618.
- Lerchbaumer L. and Audétat A. (2012a) High Cu concentrations in vapor-type fluid inclusions: An artifact? *Geochim. Cosmochim. Acta* **88**, 255-274.

- Lerchbaumer L. and Audétat A. (2012b) The quartz capsule - a new method to avoid alloying problems with noble-metal capsules in hydrothermal experiments. *Eur. J. Mineral.* **24**, 683-693.
- Li Y. and Audétat A. (2009) A method to synthesize large fluid inclusions in quartz at controlled times and under unfavorable growth conditions. *Am. Mineral.* **94**, 367-371.
- Li Y., Audétat A., Lerchbaumer L. and Xiong X.L. (2009) Rapid Na, Cu exchange between synthetic fluid inclusions and external aqueous solutions: evidence from LA-ICP-MS analysis. *Geofluids* **9**, 321-329.
- Liu X., Lu X., Wang R., Zhou H. and Xu S. (2011) Speciation of gold in hydrosulphide-rich ore-forming fluids: Insights from first-principles molecular dynamics simulations. *Geochim. Cosmochim. Acta* **75**, 185-194.
- Loucks R.R. and Mavrogenes J.A. (1999) Gold solubility in supercritical hydrothermal brines measured in synthetic fluid inclusions. *Science* **284**, 2159-2163.
- Loucks R.R. (2014) Distinctive composition of copper-ore-forming arc magmas. *Aust. J. Earth Sci.* **61**, 5-16.
- Luhr J.F. (1990) Experimental phase relations of water-and sulfur-saturated arc magmas and the 1982 eruptions of El Chichón volcano. *J. Petrol.* **31**, 1071-1114.
- Manning C.E. (2004) The chemistry of subduction-zone fluids. *Earth Planet. Sci. Lett.* **223**, 1-16.
- Matthews W., Linnen R.L. and Guo Q. (2003) A filler-rod technique for controlling redox conditions in cold-seal pressure vessels. *Am. Mineral.* **88**, 701-707.
- Mavrogenes J. and Bodnar R. (1994) Hydrogen movement into and out of fluid inclusions in quartz: experimental evidence and geologic implications. *Geochim. Cosmochim. Acta* **58**, 141-148.
- McCormick M.P., Thomason L.W. and Trepte C.R. (1995) Atmospheric effects of the Mt Pinatubo eruption. *Nature* **373**, 399.
- McMillan P.F. (1994) Water solubility and speciation models, In *Rev. Mineral. Geochem.* 30, pp. 132-156.
- Menard G., Moune S., Vlastelic I., Aguilera F., Valade S., Bontemps M. and Gonzalez R. (2014) Gas and aerosol emissions from Lascar volcano (Northern Chile): Insights into the origin of gases and their links with the volcanic activity. *J. Volcanol. Geotherm. Res.* **287**, 51-67.
- Metrich N. and Clocchiatti R. (1996) Sulfur abundance and its speciation in oxidized alkaline melts. *Geochim. Cosmochim. Acta* **60**, 4151-4160.
- Métrich N. and Wallace P.J. (2008) Volatile abundances in basaltic magmas and their degassing paths tracked by melt inclusions. *Rev. Mineral. Geochem.* **69**, 363-402.

- Moune S., Gauthier P.-J. and Delmelle P. (2010) Trace elements in the particulate phase of the plume of Masaya Volcano, Nicaragua. *J. Volcanol. Geotherm. Res.* **193**, 232-244.
- Mungall J.E. (2002) Roasting the mantle: Slab melting and the genesis of major Au and Au-rich Cu deposits. *Geology* **30**, 915-918.
- Nadeau O., Williams-Jones A.E. and Stix J. (2010) Sulphide magma as a source of metals in arc-related magmatic hydrothermal ore fluids. *Nat. Geosci.* **3**, 501-505.
- Newman S. and Lowenstern J.B. (2002) VolatileCalc: a silicate melt–H<sub>2</sub>O–CO<sub>2</sub> solution model written in Visual Basic for excel. *Comput. Geosci.* **28**, 597-604.
- Ni H.W. and Keppler H. (2013) Carbon in Silicate Melts. *Rev. Mineral. Geochem.* **75**, 251-287.
- Oppenheimer C., Fischer T.P. and Scaillet B. (2014) 4.4 - Volcanic Degassing: Process and Impact In *Treatise on Geochemistry (Second Edition)* (ed. K.K. Turekian). Elsevier, Oxford, pp. 111-179.
- Oyarzun R., Márquez A., Lillo J., López I. and Rivera S. (2001) Giant versus small porphyry copper deposits of Cenozoic age in northern Chile: adakitic versus normal calc-alkaline magmatism. *Mineral. Deposita* **36**, 794-798.
- Papale P., Moretti R. and Barbato D. (2006) The compositional dependence of the saturation surface of H<sub>2</sub>O+CO<sub>2</sub> fluids in silicate melts. *Chem. Geol.* **229**, 78-95.
- Parat F., Holtz F. and Streck M.J. (2011) Sulfur-bearing Magmatic Accessory Minerals. *Rev. Mineral. Geochem.* **73**, 285-314.
- Peacock S.M. (1993) Large-scale hydration of the lithosphere above subducting slabs. *Chem. Geol.* **108**, 49-59.
- Peacock S.M., Rushmer T. and Thompson A.B. (1994) Partial melting of subducting oceanic crust. *Earth Planet. Sci. Lett.* **121**, 227-244.
- Peccerillo A. (1992) Potassic and ultrapotassic rocks: compositional characteristics, petrogenesis, and geologic significance *Episodes* **15**, 243-251.
- Pokrovski G.S., Tagirov B.R., Schott J., Hazemann J.-L. and Proux O. (2009) A new view on gold speciation in sulfur-bearing hydrothermal fluids from in situ X-ray absorption spectroscopy and quantum-chemical modeling. *Geochim. Cosmochim. Acta* **73**, 5406-5427.
- Pokrovski G.S., Akinfiyev N.N., Borisova A.Y., Zotov A.V. and Kouzmanov K. (2014) Gold speciation and transport in geological fluids: insights from experiments and physical-chemical modelling, In *Gold-Transporting Fluids in the Earth's Crust* (eds. P. Garofalo and E. Ripley), Geological Society, London, Special Publications 402, pp. 9-70.

- Pokrovski G.S., Kokh M.A., Guillaume D., Borisova A.Y., Gisquet P., Hazemann J.-L., Lahera E., Del Net W., Proux O. and Testemale D. (2015) Sulfur radical species form gold deposits on Earth. *Proceedings of the National Academy of Sciences* **112**, 13484-13489.
- Qin Z., Lu F. and Anderson A.T. (1992) Diffuse reequilibration of melt and fluid inclusions. *Am. Mineral.* **77**, 565-576.
- Redmond P., Einaudi M., Inan E., Landtwing M. and Heinrich C. (2004) Copper deposition by fluid cooling in intrusion-centered systems: New insights from the Bingham porphyry ore deposit, Utah. *Geology* **32**, 217-220.
- Reid M.R. (2014) 4.5 - Timescales of Magma Transfer and Storage in the Crust, In *Treatise on Geochemistry (Second Edition)* (ed. K.K. Turekian). Elsevier, Oxford, pp. 181-201.
- Richards J.P. (2011) Magmatic to hydrothermal metal fluxes in convergent and collided margins. *Ore Geol. Rev.* **40**, 1-26.
- Richards J.P. (2011) High Sr/Y arc magmas and porphyry Cu±Mo±Au deposits: just add water. *Econ. Geol.* **106**, 1075-1081.
- Ridley J. and Hagemann S.G. (1999) Interpretation of post-entrapment fluid-inclusion re-equilibration at the Three Mile Hill, Marvel Loch and Griffins Find high-temperature lode-gold deposits, Yilgarn Craton, Western Australia. *Chem. Geol.* **154**, 257-278.
- Robb L.J. (2005) Introduction to ore-forming processes. Oxford, Blackwell, p. 373.
- Robock A. (2002) The climatic aftermath.(Perspectives: Pinatubo eruption). *Science* **295**, 1242-1245.
- Roedder E. (1984) Fluid inclusions. *Rev. Mineral.* **12**, 1-644.
- Roggensack K. (2001) Sizing up crystals and their melt inclusions: a new approach to crystallization studies. *Earth Planet. Sci. Lett.* **187**, 221-237.
- Rowe M.C., Kent A.J.R. and Thornber C.R. (2008) Using amphibole phenocrysts to track vapor transfer during magma crystallization and transport: An example from Mount St. Helens, Washington. *J. Volcanol. Geotherm. Res.* **178**, 593-607.
- Rowe M.C., Kent A.J. and Nielsen R.L. (2009) Subduction influence on oxygen fugacity and trace and volatile elements in basalts across the Cascade Volcanic Arc. *J. Petrol.* **50**, 61-91.
- Rudnick R.L. and Gao S. (2014) 4.1 - Composition of the Continental Crust In *Treatise on Geochemistry (Second Edition)* (ed. K.K. Turekian). Elsevier, Oxford, pp. 1-51.
- Rushmer T. (1993) Experimental high-pressure granulites: Some applications to natural mafic xenolith suites and Archean granulite terranes. *Geology* **21**, 411-414.

- Rusk B., Hofstra A., Emsbo P., Hunt A., Landis G. and Rye R. (2008) Fluid inclusion insights into the origins of fluids and metals in porphyry copper deposits.
- Rusk B.G., Reed M.H., Dilles J.H., Klemm L.M. and Heinrich C.A. (2004) Compositions of magmatic hydrothermal fluids determined by LA-ICP-MS of fluid inclusions from the porphyry copper–molybdenum deposit at Butte, MT. *Chem. Geol.* **210**, 173-199.
- Sadofsky S.J., Portnyagin M., Hoernle K. and van den Bogaard P. (2007) Subduction cycling of volatiles and trace elements through the Central American volcanic arc: evidence from melt inclusions. *Contrib. Mineral. Petrol.* **155**, 433-456.
- Schmidt M.W. and Poli S. (1998) Experimentally based water budgets for dehydrating slabs and consequences for arc magma generation. *Earth Planet. Sci. Lett.* **163**, 361-379.
- Seo J.H., Guillong M. and Heinrich C.A. (2009) The role of sulfur in the formation of magmatic–hydrothermal copper–gold deposits. *Earth Planet. Sci. Lett.* **282**, 323-328.
- Seo J.H., Guillong M., Aerts M., Zajacz Z. and Heinrich C.A. (2011) Microanalysis of S, Cl, and Br in fluid inclusions by LA-ICP-MS. *Chem. Geol.* **284**, 35-44.
- Seo J.H. and Heinrich C.A. (2013) Selective copper diffusion into quartz-hosted vapor inclusions: Evidence from other host minerals, driving forces, and consequences for Cu–Au ore formation. *Geochim. Cosmochim. Acta* **113**, 60-69.
- Shannon R.D. (1976) Revised Effective Ionic-Radii and Systematic Studies of Interatomic Distances in Halides and Chalcogenides. *Acta Crystallogr A* **32**, 751-767.
- Signorelli S. and Carroll M. (2000) Solubility and fluid-melt partitioning of Cl in hydrous phonolitic melts. *Geochim. Cosmochim. Acta* **64**, 2851-2862.
- Signorelli S. and Carroll M. (2001) Experimental constraints on the origin of chlorine emissions at the Soufrière Hills volcano, Montserrat. *Bull. Volcanol.* **62**, 431-440.
- Simon A.C., Frank M.R., Pettke T., Candela P.A., Piccoli P.M. and Heinrich C.A. (2005) Gold partitioning in melt-vapor-brine systems. *Geochim. Cosmochim. Acta* **69**, 3321-3335.
- Simon A.C., Pettke T., Candela P.A., Piccoli P.M. and Heinrich C.A. (2007) The partitioning behavior of As and Au in S-free and S-bearing magmatic assemblages. *Geochim. Cosmochim. Acta* **71**, 1764-1782.
- Simon A.C. and Ripley E.M. (2011) The role of magmatic sulfur in the formation of ore deposits. *Rev. Mineral. Geochem.* **73**, 513-578.
- Sparks R.S.J. (2003) Dynamics of magma degassing. *Geological Society, London, Special Publications* **213**, 5-22.

- Spilliaert N., Allard P., Métrich N. and Sobolev A.V. (2006) Melt inclusion record of the conditions of ascent, degassing, and extrusion of volatile-rich alkali basalt during the powerful 2002 flank eruption of Mount Etna (Italy). *J. Geophys. Res.* **111**.
- Stolper E. (1982a) The speciation of water in silicate melts. *Geochim. Cosmochim. Acta* **46**, 2609-2620.
- Stolper E. (1982b) Water in silicate glasses: an infrared spectroscopic study. *Contrib. Mineral. Petrol.* **81**, 1-17.
- Tagirov B.R., Salvi S., Schott J. and Baranova N.N. (2005) Experimental study of gold-hydrosulphide complexing in aqueous solutions at 350–500°C, 500 and 1000 bars using mineral buffers. *Geochim. Cosmochim. Acta* **69**, 2119-2132.
- Tait S., Jaupart C. and Vergnolle S. (1989) Pressure, gas content and eruption periodicity of a shallow, crystallising magma chamber. *Earth Planet. Sci. Lett.* **92**, 107-123.
- Taran Y.A., Hedenquist J., Korzhinsky M., Tkachenko S. and Shmulovich K. (1995) Geochemistry of magmatic gases from Kudryavy volcano, Iturup, Kuril Islands. *Geochim. Cosmochim. Acta* **59**, 1749-1761.
- Tatsumi Y. (1986) Formation of the volcanic front in subduction zones. *Geophys. Res. Lett.* **13**, 717-720.
- Tatsumi Y., Hamilton D. and Nesbitt R. (1986) Chemical characteristics of fluid phase released from a subducted lithosphere and origin of arc magmas: evidence from high-pressure experiments and natural rocks. *J. Volcanol. Geotherm. Res.* **29**, 293-309.
- Ulmer P. (2001) Partial melting in the mantle wedge—the role of H<sub>2</sub>O in the genesis of mantle-derived ‘arc-related’ magmas. *Phys. Earth Planet. Inter.* **127**, 215-232.
- Ulrich T., Günther D. and Heinrich C. (1999) Gold concentrations of magmatic brines and the metal budget of porphyry copper deposits. *Nature* **399**, 676-679.
- Verhoogen J. (1952) Ionic diffusion and electrical conductivity in quartz. *Am. Mineral.* **37**, 637-655.
- Vigouroux N., Wallace P.J. and Kent A.J. (2008) Volatiles in high-K magmas from the western Trans-Mexican Volcanic Belt: evidence for fluid fluxing and extreme enrichment of the mantle wedge by subduction processes. *J. Petrol.* **49**, 1589-1618.
- Wallace P.J. (2005) Volatiles in subduction zone magmas: concentrations and fluxes based on melt inclusion and volcanic gas data. *J. Volcanol. Geotherm. Res.* **140**, 217-240.
- Wallace P.J. and Edmonds M. (2011) The Sulfur Budget in Magmas: Evidence from Melt Inclusions, Submarine Glasses, and Volcanic Gas Emissions. *Rev. Mineral. Geochem.* **73**, 215-246.

- Webster J., Kinzler R. and Mathez E. (1999) Chloride and water solubility in basalt and andesite melts and implications for magmatic degassing. *Geochim. Cosmochim. Acta* **63**, 729-738.
- Webster J., Raia F., De Vivo B. and Rolandi G. (2001) The behavior of chlorine and sulfur during differentiation of the Mt. Somma-Vesuvius magmatic system. *Mineral. Petrol.* **73**, 177-200.
- Weil J.A. (1984) A review of electron spin spectroscopy and its application to the study of paramagnetic defects in crystalline quartz. *Phys. Chem. Minerals* **10**, 149-165.
- White S. (1970) Ionic diffusion in quartz. *Nature* **225**, 375-376.
- Wilkinson J.J. (2013) Triggers for the formation of porphyry ore deposits in magmatic arcs. *Nat. Geosci.* **6**, 917-925.
- Williams-Jones A.E., Bowell R.J. and Migdisov A.A. (2009) Gold in Solution. *Elements* **5**, 281-287.
- Williams-Jones A.E. and Heinrich C.A. (2005) 100th Anniversary special paper: vapor transport of metals and the formation of magmatic-hydrothermal ore deposits. *Econ. Geol.* **100**, 1287-1312.
- Zajacz Z., Hanley J.J., Heinrich C.A., Halter W.E. and Guillong M. (2009) Diffusive reequilibration of quartz-hosted silicate melt and fluid inclusions: Are all metal concentrations unmodified? *Geochim. Cosmochim. Acta* **73**, 3013-3027.
- Zelenski M., Malik N. and Taran Y. (2014) Emissions of trace elements during the 2012–2013 effusive eruption of Tolbachik volcano, Kamchatka: enrichment factors, partition coefficients and aerosol contribution. *J. Volcanol. Geotherm. Res.* **285**, 136-149.
- Zelenski M.E., Fischer T.P., de Moor J.M., Marty B., Zimmermann L., Ayalew D., Nekrasov A.N. and Karandashev V.K. (2013) Trace elements in the gas emissions from the Erta Ale volcano, Afar, Ethiopia. *Chem. Geol.* **357**, 95-116.

## 5. List of manuscripts and statements of author's contribution

1. Guo H. and Audétat A. (2017) Transfer of volatiles and metals from mafic to felsic magmas in composite magma chambers: An experimental study. *Geochim. Cosmochim. Acta* **198**, 360-378.

In this study, Haihao Guo performed all the experiments, SEM, EMPA and microthermometry analyses. Andreas Audétat conducted the LA-ICP-MS measurements of samples. Haihao Guo wrote the manuscript with great help from Andreas Audétat. Andreas Audétat supervised the whole project.

2. Guo H. and Audétat A. (2017) Solubility of gold in oxidized, sulfur-bearing fluids at 500-850 °C and 200-230 MPa: a synthetic fluid inclusion study. *Geochim. Cosmochim. Acta*, (submitted).

In this study, Haihao Guo performed all the experiments and Raman spectroscopy analyses. Andreas Audétat conducted the LA-ICP-MS measurements of fluid inclusions. Haihao Guo wrote the manuscript with further improvements of Andreas Audétat. Andreas Audétat supervised the whole project.

3. Guo H. and Audétat A. (2017) Gold diffusion into and out of quartz-hosted fluid inclusions during re-equilibration experiments at 600-800 °C and 2 kbar. *Chem. Geol.*, (submitted).

In this study, Haihao Guo performed all the experiments and sample preparation. Andreas Audétat conducted the LA-ICP-MS measurements of fluid inclusions. Haihao Guo wrote the manuscript with further improvements of Andreas Audétat. Andreas Audétat supervised the whole project.

## 6. Transfer of volatiles and metals from mafic to felsic magmas in composite magma chambers: an experimental study

Haihao Guo, Andreas Audétat

*Bayerisches Geoinstitut, Universität Bayreuth, D-95440 Bayreuth, Germany*

### 6.1. Abstract

In order to determine the behavior of metals and volatiles during intrusion of mafic magma into the base of silicic, upper crustal magma chambers, fluid–rock partition coefficients ( $D_{\text{fluid/rock}}$ ) of Li, B, Na, S, Cl, K, Mn, Fe, Rb, Sr, Ba, Ce, Cu, Zn, Ag, Cd, Mo, As, Se, Sb, Te, W, Tl, Pb and Bi were determined experimentally at 2 kbar and 850 °C close to the solidus of mafic magma. In a first step, volatile-bearing mafic glasses were prepared by melting a natural basaltic trachyandesite in the presence of volatile-bearing fluids at 1200 °C / 10 kbar in piston cylinder presses. The hydrous glasses were then equilibrated in subsequent experiments at 850 °C / 2 kbar in cold-seal pressure vessels, which caused 80-90% of the melt to crystallize. After 0.5-2.0 days of equilibration, the exsolved fluid was trapped by means of in-situ fracturing in the form of synthetic fluid inclusions in quartz. Both the mafic rock residue and the fluid inclusions were subsequently analyzed by laser-ablation ICP-MS for major and trace elements. Reverse experiments were conducted by equilibrating metal-bearing aqueous solutions with rock powder and then trapping the fluid. In two additional experiments, information on relative element mobilities were obtained by reacting fluids that exsolved from crystallizing mafic magma with overlying silicic melts. The combined results suggest that under the studied conditions S, Cl, Cu, Se, Br, Cd and Te are most volatile ( $D_{\text{fluid/rock}} > 10$ ), followed by Li, B, Zn, As, Ag, Sb, Cs, W, Tl, Pb and Bi ( $D_{\text{fluid/rock}} = 1-10$ ). Less volatile are Na, Mg, K, Ca, Mn, Fe, Rb, Sr, Mo and Rb ( $D_{\text{fluid/rock}} = 0.1-1$ ), and the least fluid-mobile elements are Al, Si, Ti, Zr, Ba and Ce ( $D_{\text{fluid/rock}} < 0.1$ ). This trend is broadly consistent with relative element volatilities determined on natural high-temperature fumarole gases, although some differences exist. Based on the volatility data and measured mineral–melt and sulfide–melt partition coefficients, volatile fluxing in felsic natural samples may be identified by Cu, Se, Te and Cd-enrichment in magmatic sulfides, and by As, Se, Cd and Bi-enrichment in magmatic apatite.

## 6.2. Introduction

Upper crustal magma chambers commonly show evidence for compositional stratification, with intermediate to felsic magma being present in the upper parts of the magma chamber, and mafic magmas intruding into its base (Fig. 6.1; e.g., Koyaguchi et al., 1986; Riehle, 1992; Matthews et al., 1999; Saito et al., 2002; Halama et al., 2006; Wiebe, 2016). Upon decompression and crystallization the mafic magmas release  $\text{CO}_2$ ,  $\text{SO}_2$  and other volatiles to the overlying intermediate to felsic magmas, which process is thought to be responsible for high fluxes of  $\text{CO}_2$  and  $\text{SO}_2$  from modern volcanoes (e.g., Andres et al., 1991; de Hoog et al., 2004; Roberge et al., 2009; Christopher et al., 2010; Wallace and Edmonds, 2011), the formation of magmatic anhydrite (e.g., Hattori, 1993; Luhr, 2008, Parat et al., 2011), and the triggering of volcanic eruptions (e.g., Pallister et al., 1992, 1996; Richer et al., 2004; Kaneko et al., 2007). Mafic magmas are also thought deliver most of the sulfur and metals present in giant porphyry Cu ( $\pm\text{Mo}$ , Au) deposits associated with dominantly intermediate to felsic magmas (Keith et al., 1997; Hattori and Keith, 2001; Halter et al., 2005; Aud  tat and Pettke, 2006; Stern et al., 2007).

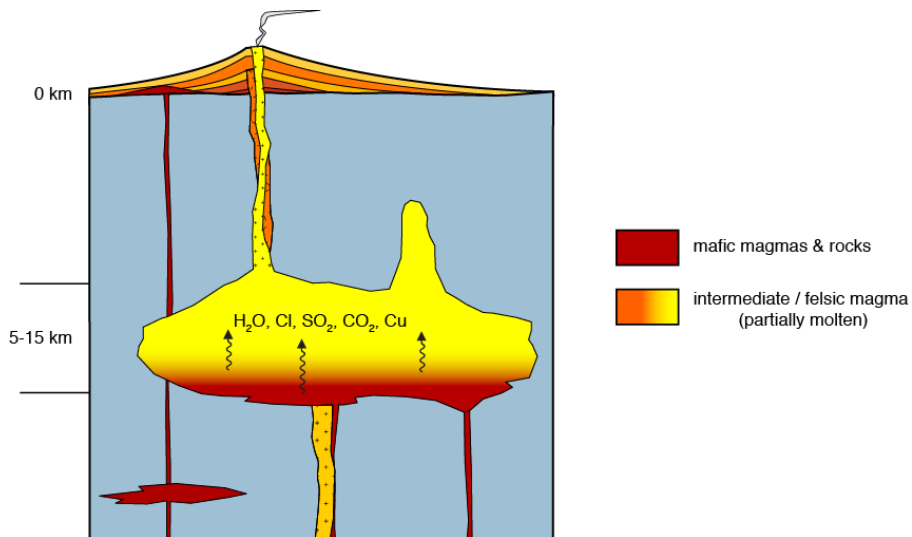


**Fig. 6.1.** Schematic view of a compositionally stratified magma chamber underneath a stratovolcano. Volatiles and metals such as Cu are transported by a fluid phase from mafic magmas to overlying intermediate and felsic magmas (modified from Aud  tat and Simon, 2013).

The aim of this project is to evaluate the major and trace element composition of the fluids that exsolve from mafic alkaline magmas as they quench against – but do not extensively mix with – a larger body of felsic magma. A typical scenario would be the intrusion of  $0.2 \text{ km}^3$  mafic magma

with a temperature of 1000-1100 °C into the base of a 1.0 km<sup>3</sup> crystal-rich dacite magma with a temperature of 750-800 °C. After thermal equilibration the temperature of both magmas is around 850 °C, which means that the mafic magma becomes almost fully crystallized, whereas the dacitic magma mush is partially remelted. Most of the volatiles that are originally dissolved in the mafic magma thus exsolve into a free fluid phase that tends to rise and interact with overlying, more felsic magmas. A perfect analogue of this situation has been documented by Eichelberger (1980) for a mafic enclave within a rhyodacitic lava flow of the Medicine Lake Highland Volcano, California: whereas the mafic enclave is highly crystalline and full of vesicles, the surrounding rhyodacitic lava is entirely glassy and bubble-free, suggesting a snapshot at around 850 °C.

### **6.3. Experimental methods**

#### **6.3.1. Experimental strategy**

Two different kinds of experiments were conducted in this study (Table 6.1): (1) runs in which fluids in equilibrium with an almost fully crystallized mafic magma were trapped as synthetic fluid inclusions in quartz and subsequently analyzed by LA-ICP-MS, and (2) runs in which the same fluids were allowed to react with an overlying reservoir of hydrous felsic melt, resulting in enrichment of trace elements in the felsic melt. The first approach has the advantage that the fluid can be trapped and its composition be directly quantified, whereas the second approach has the advantage that it provides higher sensitivity and thus allows data also for relatively fluid-immobile elements such as Al, Ti and Zr to be collected (see below). An important requirement for both types of experiments is that equilibrium is reached between fluid and mafic residue before the fluid is trapped in the form of synthetic fluid inclusions or reacts with felsic melt. To test whether this requirement was met we performed the first type of experiments in both forward or reverse manner (Fig. 6.2): In the forward experiments volatile-bearing mafic glasses were synthesized at high pressure and temperature in piston cylinder presses, and subsequently crystallized in a separate experiment at lower pressure and temperature in cold-seal pressure vessels. In the reverse experiments aqueous fluid was equilibrated directly with the crystalline starting material at lower pressure and temperature without an intermittent step of melting. In both cases the formation of fluid inclusions was initiated after 0.5-2.0 days run time by in-situ fracturing of the quartz piece.

Experiments in which fluids were allowed to react with an overlying reservoir of felsic melt were performed in forward manner, i.e., using hydrous mafic glass as starting material.

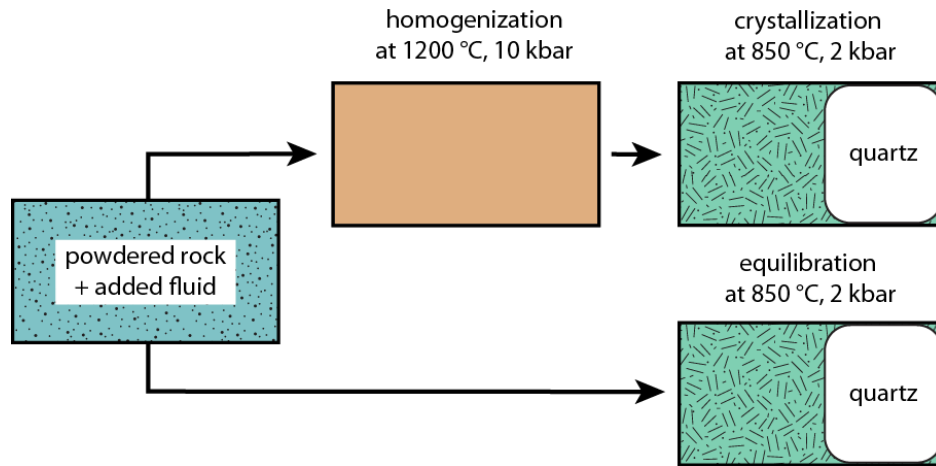


**Fig. 6.2.** Schematic view of forward vs. reverse experiments in which part of the fluid was trapped as synthetic fluid inclusions in quartz. The upper path illustrates a forward experiment that involves a first step of homogenization and hydration at high temperature and pressure, followed by crystallization and fluid exsolution at lower temperature and pressure; the lower path illustrates a reverse experiment in which fluid was directly equilibrated with rock powder at the lower P-T conditions without an intermittent step of homogenization.

### 6.3.2. Starting materials

A natural basaltic trachyandesite from Two Buttes, southeastern Colorado (David and Smith, 1993; David et al., 1996) was used as mafic starting material in all experiments. This rock consists of phenocrysts of clinopyroxene (~40 vol%), phlogopite (~10 vol%), olivine (~2 vol%) and magnetite (~1 vol%) set in a finely crystalline groundmass consisting of ~30 vol% glass, ~25 vol% plagioclase, ~20 vol% phlogopite, ~15 vol% magnetite and ~10% pyroxene. For reverse runs we directly used finely crushed powder of this rock ( $\leq 10 \mu\text{m}$  grain size), whereas for forward runs we prepared volatile-bearing mafic glasses by melting the rock powder in the presence of S-Cl-bearing aqueous fluid spiked with various trace elements (see below) at 1200 °C / 10 kbar in piston cylinder experiments. Melt inclusions in mafic alkaline arc magmas typically contain on the order of 0.3-0.4 wt % S, 0.2-0.3 wt % Cl and 4-5 wt % H<sub>2</sub>O (e.g., Vigouroux et al., 2008; Métrich and

Clocchiatti, 1996; Spilliaert et al., 2006). Therefore, the hydrous mafic glass was prepared such that it ultimately contained 0.3 wt % S, 0.2 wt % Cl and 5 wt % H<sub>2</sub>O.

To increase the chance of being able to analyze all trace elements of interest within the synthetic fluid inclusions we added trace elements in such amounts that their concentration in the hydrous starting glass was about 50 ppm each. At a melt water content of 5 wt%, this requires the trace elements to be added at a concentration of ~1000 ppm each in the aqueous solution. However, because it was not possible to dissolve all trace elements in a single aqueous solution we ultimately used three different solutions containing ~3000 ppm trace elements each (supplementary Table 6-S1) and then added the three solutions in equal quantities to the solid starting material. Sulfur, Cl, Li, B, Cu, Zn, Cd, As, Se, Sb and Tl were added to the aqueous solution in the form of H<sub>2</sub>SO<sub>4</sub>, HCl, LiCl, H<sub>3</sub>BO<sub>3</sub>, CuCl<sub>2</sub>, ZnCl<sub>2</sub>, CdCl<sub>2</sub>, As<sub>3</sub>O<sub>5</sub>, Na<sub>2</sub>SeO<sub>3</sub>·5H<sub>2</sub>O, SbCl<sub>3</sub>, Na<sub>2</sub>TeO<sub>4</sub> and TiCl<sub>4</sub>, respectively. Silver, Mo, Pb and Bi were not soluble enough in any of these solutions, for which reason we added these four elements in the form of diluted standard solutions for ICP-MS (Plasma CAL) to the rock powder and subsequently allowed the slurry to dry to remove H<sub>2</sub>O and HNO<sub>3</sub>.

Fluid inclusions were trapped in quartz pieces of 3×3×6 mm or 1.0×1.8×10 mm size that were cut from inclusion-free synthetic quartz in such a way that the longest dimension was parallel to the c-axis of quartz crystal. In a first series of experiments (not discussed here) the fluid inclusions were formed by fracturing the quartz piece in-situ and then allowing the cracks to heal. However, with this method the fluid inclusions usually turned out too small for all trace elements of interest to be measurable by LA-ICP-MS. For this reason we switched to a technique described by Li and Audéat (2009) to produce larger fluid inclusions. In this technique, large fluid inclusions are first synthesized in a fluid of different composition at favorable P-T conditions, and then re-opened in the "real" experiment by in-situ cracking. In the present study we conducted these pre-runs at 800 °C and 2 kbar using aqueous solutions containing 5 wt% KCl and 5000 ppm Cs.

The two experiments in which the fluids reacted with an overlying reservoir of felsic melt were performed with two different types of felsic melt: one run was performed with a haplogranite of the 1 kbar eutectic melt composition (79.47wt% SiO<sub>2</sub>; 11.73wt% Al<sub>2</sub>O<sub>3</sub>; 3.90 wt% Na<sub>2</sub>O; 4.91wt% K<sub>2</sub>O), and the other one with a natural obsidian from China (76.3wt% SiO<sub>2</sub>; 11.3wt% Al<sub>2</sub>O<sub>3</sub>; 3.6 wt% Na<sub>2</sub>O; 4.5wt% K<sub>2</sub>O; 2.5wt% FeO<sub>tot</sub>; 0.20 wt% CaO). Both felsic melts were saturated with

water (ca. 6 wt% H<sub>2</sub>O) in a pre-run conducted at 850 °C / 2 kbar in cold-seal pressure vessels. This approach provides a higher sensitivity than the one via synthetic fluid inclusions because the felsic glass has a higher density and can be ablated using large pit sizes, hence significantly more material enters the ICP-MS than during the analysis of fluid inclusions. As a consequence, relative volatilities of six more elements (Mg, Al, Si, Ca, Ti and Zr) could be determined using this approach.

### **6.3.3. High temperature and pressure experiments**

For the preparation of volatile- and trace element-rich mafic glasses in piston cylinder experiments approximately 0.09 g solution and 0.2 g rock powder were welded into Pt capsules of 5.0 mm O.D. (outer diameter), 4.6 mm I.D. (inner diameter) and 10 mm length. The capsules were then subjected to 10 kbar and 1200 °C in end-loaded, solid-media piston cylinder apparatus using 0.5-inch diameter MgO-NaCl assemblies with stepped graphite heaters. A friction correction of 5% was applied to the nominal pressure based on the quartz-coesite phase transition at 790 °C (Bose and Ganguly, 1995). Temperature was monitored by Pt-Pt<sub>90</sub>Rh<sub>10</sub> (S-type) thermocouples and is associated with an estimated uncertainty of ±10 °C. The duration of the experiments was only three hours to minimize loss of iron and certain trace elements to the platinum capsule. The experiments were terminated by switching off the electrical power, resulting in cooling below the glass transition temperature in less than 10 seconds. The recovered platinum capsules were immersed in dilute sulfuric acid (~10 wt% H<sub>2</sub>SO<sub>4</sub>) at ~50 °C for a few hours to dissolve any attached MgO and were then weighted to check for potential leaks during the experiments. Only runs that showed no significant weight change were used for subsequent experiments in cold-seal pressure vessels.

The cold-seal pressure experiments were conducted with three different capsule setups (Fig. 6.3; Table 6.1). In the first setup, a piece of inclusion-free quartz and a slightly smaller piece of quartz with pre-synthesized, large fluid inclusions were loaded with mafic starting material (either finely crushed rock powder or crushed hydrous glass) ±aqueous solution into a gold capsule of 4.3 mm O.D., 4.0 mm I.D. and 30 mm length (Fig. 6.3a) and then welded shut. After 0.5-2.0 days of equilibration, the quartz cores were fractured in situ to initiate the re-opening of pre-synthesized fluid inclusions and formation of small, new fluid inclusions. The second setup (Fig. 6.3b), which was used only in a single experiment (HG38), is based on the design described in Lerchbaumer

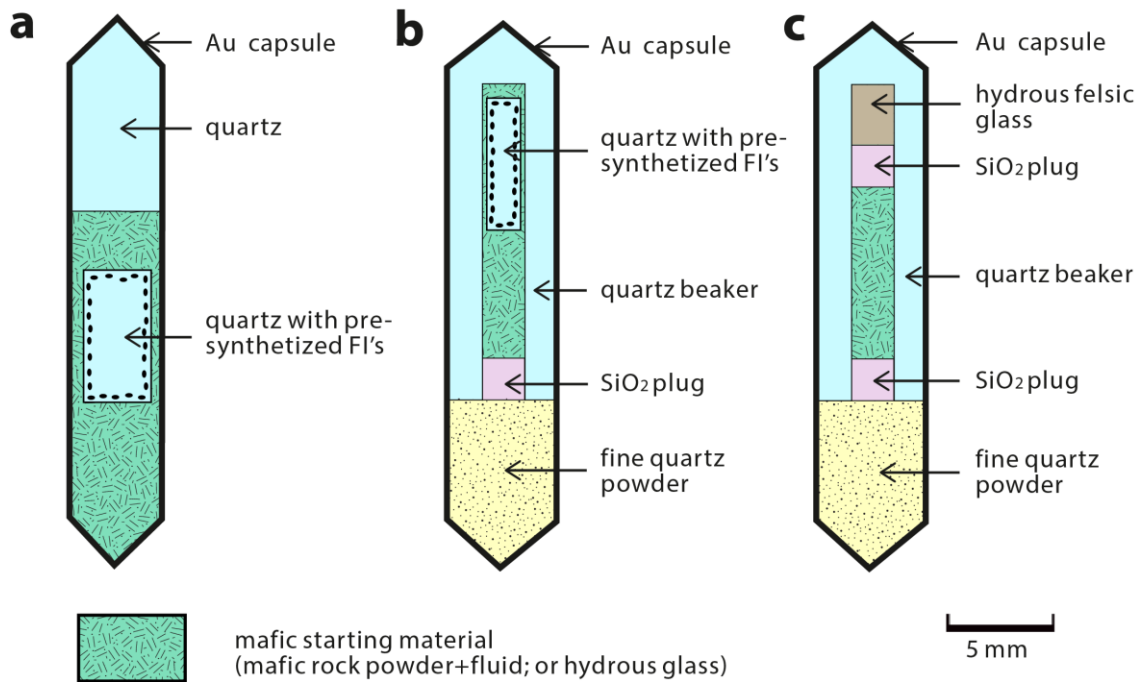


**Fig. 6.3.** Illustration of the three different capsule setups used for the cold-seal pressure vessel experiments: (a) capsule setup for crystallizing / equilibrating mafic starting material at 850 °C / 2 kbar and trapping fluid after a specific amount of time in the form of synthetic fluid inclusions in quartz. (b) capsule setup with a rigid quartz beaker to reduce loss of certain elements to the gold capsule. The pressure is transmitted into the quartz beaker via the movable SiO<sub>2</sub> glass plug and the fine quartz powder in the bottom of the capsule. (c) capsule setup for simulating the interaction of volatiles exsolved from crystallizing mafic magma with overlying felsic magma. The SiO<sub>2</sub> glass plugs crystallize during the experiments and thereby are permeable to aqueous fluids. FI = fluid inclusion.

and Audétat (2012) and effectively minimizes loss of metals to the gold capsule, but has the disadvantage that the formation of fluid inclusions cannot be initiated after a specific amount of equilibration by in-situ cracking because that would fracture also the quartz beaker. The quartz beaker was manufactured out of a single quartz crystal and had the following dimensions: 4.4 mm O.D., 2.0 mm I.D. and 16 mm length. For this setup, the quartz beaker was filled with fine-grained mafic rock powder, aqueous solution, and a small (1.0×1.8×10 mm) piece of quartz containing large, pre-synthesized fluid inclusions that were already re-opened by heating the quartz piece in a 1 atm furnace to 700 °C and then quenching it in distilled water. The quartz beaker was then closed with a neatly fitting SiO<sub>2</sub> glass plug and loaded with fine quartz powder into a gold capsule of 5.0 mm O.D., 4.6 mm I.D. and 30 mm length. The third capsule setup (Fig. 6.3c) was designed

to simulate the interaction of fluids exsolving from a crystallizing mafic magma with overlying felsic magma. No fluid is trapped in the form of fluid inclusions in this setup. To minimize loss of Cu, Ag, Se, Cd, Te and Bi to the gold capsule, also this setup features a quartz beaker. A neatly fitting plug of SiO<sub>2</sub> glass was placed between the mafic starting material (crushed volatile-bearing glass) and the overlying, crushed, hydrated felsic glass (haplogranite or natural obsidian from China) to avoid direct contact between the two reservoirs. The SiO<sub>2</sub> plug was necessary to be able to assign compositional changes in the felsic melt to volatile fluxing, otherwise it would not be clear whether they are due to chemical equilibration of the two reservoirs or due to volatile fluxing. During the experiments the SiO<sub>2</sub> glass plug crystallized to a polycrystalline aggregate of quartz that was permeable to fluid but not to silicate melt.

In all cases the prepared gold capsules were welded with a pulsed arc welder, then subjected to ~1 kbar H<sub>2</sub>O pressure, and finally weighed to check for the presence of leaks. The finished capsules were then loaded into rapid-quench cold-seal pressure vessels made of Inconel 713LC super alloy in a setup similar to that described in Matthews et al. (2003), using water as the pressure medium. Temperatures were measured with NiCr-Ni (K-type) thermocouples in external boreholes of the vessels. Uncertainties in the temperature and pressure readings are considered  $\pm 5^{\circ}\text{C}$  and  $\pm 30$  bar, respectively. Oxygen fugacity was not specifically controlled in our experiments but must have been rather high because sulfur was added in the form of H<sub>2</sub>SO<sub>4</sub>, and because most experiments appear to have been saturated in anhydrite but not in sulfide, which constrains  $\log f\text{O}_2$  to  $\geq \text{QFM}+2.5$  (Parat et al., 2011). As mentioned in the introduction, anhydrite is a relatively common mineral phase in arc magmas (e.g., Luhr et al., 2008; Parat et al., 2011), hence conducting the experiments at oxidized, anhydrite-saturated conditions is geologically reasonable. All experiments were run at 2 kbar and 850 °C for 7 to 9 days. In the runs with capsule setup (a), in-situ cracking of the quartz pieces was performed after 0.5~2 days by dragging the sample with the help of an external magnet within seconds from the hot end of the vessel to its cold end and then back up to the hot end. The experiments were terminated by dragging the sample slowly (within 30-60 seconds; to prevent re-opening of the fluid inclusions) to the cold end of the pressure vessel.

**Table 6.1**

Overview of performed experiments and obtained run products.

Sample No.	T (°C)	P (kbar)	Duration (days)	In-situ cracking after (days)	Capsule setup <sup>a</sup>	Starting materials	Run type	Phases in mafic run product
HG30	850	2	8.5	1	a	mafic rock powder + fluid	reverse	cpx, plg, phl, amp, mag, ~15 vol% melt
HG32	850	2	9	2	a	volatile-bearing mafic glass	forward	cpx, plg, phl, amp, mag, ~15 vol% melt
HG33	850	2	9	2	a	mafic rock powder + fluid	reverse	cpx, plg, phl, amp, mag, anh, ~ 15 vol% melt
HG34	850	2	8	0.5	a	volatile-bearing mafic glass	forward	cpx, plg, phl, amp, mag, ~10 vol% melt
HG35	850	2	8	0.5	a	mafic rock powder + fluid	reverse	cpx, plg, phl, amp, mag, ~20 vol% melt
HG36	850	2	8	1	a	mafic rock powder + fluid	reverse	cpx, plg, phl, amp, mag, ~10 vol% melt
HG38	850	2	7	none	b	mafic rock powder + fluid	reverse	cpx, plg, phl, amp, mag, ~15 vol% melt
HG42	850	2	7	none	c	volatile-bearing mafic glass + obsidian	forward	cpx, plg, phl, amp, po, ~15 vol% melt
HG47	850	2	7	none	c	volatile-bearing mafic glass + haplogranite	forward	cpx, plg, phl, amp, mag, ~15 vol% melt

Abbreviations: cpx – clinopyroxene; plg – plagioclase; phl – phlogopite; amp – amphibole; qtz – quartz; mag – magnetite; po – pyrrhotite; anh – anhydrite.

<sup>a</sup> as shown in Fig. 6.3.

#### 6.3.4. Analytical Methods

Major and trace element concentrations in hydrous glasses, fine-grained mafic run products, and synthetic fluid inclusions were measured by LA-ICP-MS using a 193 nm ArF Excimer laser (GeolasPro, Coherent, USA) attached to an Elan DRC-e (Perkin Elmer, Canada) quadrupole mass spectrometer (Günther et al., 1998). The laser was operated at a frequency of 10 Hz with an energy density of  $\sim 10 \text{ J}\cdot\text{cm}^{-2}$  on the sample surface. The laser pit size was 70  $\mu\text{m}$  diameter for bulk analyses of the mafic run product, 50-70  $\mu\text{m}$  for hydrous glasses, and 30-50  $\mu\text{m}$  for fluid inclusions. Mafic run products and hydrous glasses were analyzed at 7-10 points along profiles parallel to the long axis of the capsule, and averages plus standard deviations were calculated. Due to the fine-grained nature of the mafic run product ( $\leq 10 \mu\text{m}$ , see below) a laser pit size of 70  $\mu\text{m}$  diameter was sufficient to produce fairly stable signals. Measured isotopes include  $^7\text{Li}$ ,  $^{11}\text{B}$ ,  $^{23}\text{Na}$ ,  $^{25}\text{Mg}$ ,  $^{27}\text{Al}$ ,  $^{30}\text{Si}$ ,  $^{32}\text{S}$ ,  $^{35}\text{Cl}$ ,  $^{39}\text{K}$ ,  $^{43}\text{Ca}$ ,  $^{49}\text{Ti}$ ,  $^{55}\text{Mn}$ ,  $^{57}\text{Fe}$ ,  $^{65}\text{Cu}$ ,  $^{66}\text{Zn}$ ,  $^{75}\text{As}$ ,  $^{79}\text{Br}$ ,  $^{82}\text{Se}$ ,  $^{85}\text{Rb}$ ,  $^{88}\text{Sr}$ ,  $^{90}\text{Zr}$ ,  $^{98}\text{Mo}$ ,  $^{107}\text{Ag}$ ,  $^{114}\text{Cd}$ ,  $^{121}\text{Sb}$ ,  $^{125}\text{Te}$ ,  $^{133}\text{Cs}$ ,  $^{137}\text{Ba}$ ,  $^{140}\text{Ce}$ ,  $^{184}\text{W}$ ,  $^{195}\text{Pt}$ ,  $^{197}\text{Au}$ ,  $^{205}\text{Tl}$ ,  $^{208}\text{Pb}$  and  $^{209}\text{Bi}$ , measured using dwell times of 10-50 ms per isotope. Due to the large number of elements two separate element menus were used, each containing Na, Al, Si, S, Cl, K, Ca, Fe, Br and Cs plus 11-13 other elements. With each element menu 4-10 fluid inclusions were measured and the results then combined to a single data set. Corrections for contributions of ablated host quartz were made for Li, Na, S, Cl, As, Sb and Br, assuming that the fluid inclusions themselves do not contain any  $\text{SiO}_2$ . External standardization was based mostly on NIST-610 (Jochum et al., 2011), except for S, Cl and Br, which were quantified based on afghanite (S, Cl; Seo et al., 2011) and a scapolite that was calibrated against the standards BB1 and BB2 of Kendrick (2012) using the revised Br concentrations listed in Table S4 of Kendrick et al. (2013). Internal standardization for the glasses and mafic run products was done by normalizing the sum of all major element oxides to 100 wt%, whereas microthermometrically determined Na concentrations (corrected for the presence of other major cations; Heinrich et al., 2003) were used in the case of fluid inclusions.

Major element compositions of various mineral phases in the fine-grained mafic run products were measured with a JEOL JXA 8200 microprobe. The minerals were analyzed with 15 kV acceleration voltage, 10 nA beam current, and a beam size defocused to 1-2  $\mu\text{m}$ . The following standards were used to calibrate the instrument: albite for Na and Si, wollastonite for Ca, orthoclase

for K, ilmenite for Ti, forsterite for Mg, spinel for Al, metallic Fe for Fe, vanadinite for Cl, and barite for S.

Backscattered electron (BSE) images of polished sections through the recovered samples were taken on a Zeiss Gemini 1530 field emission scanning electron microscope (FE-SEM) using an accelerating voltage of 20 kV, a working distance of 14 mm and an aperture of 60  $\mu\text{m}$ . An energy-dispersive spectrometer (EDS) was used to qualitatively identify mineral phases in the mafic run products.

Microthermometry was performed with a Linkam THMSG-600 heating-cooling stage that was calibrated to an uncertainty of  $\pm 0.1^\circ\text{C}$  in the range of  $-56.6$  to  $0.0^\circ\text{C}$ . The salinity of the fluid (expressed as  $\text{NaCl}_{\text{equiv}}$  wt %) was calculated based on the melting temperature of ice using the equations given in Bodnar and Vityk (1994). No evidence for the presence of clathrates or other solid phases at the time of last ice melting (such as double freezing, or melting of phases at temperatures above  $0^\circ\text{C}$ ) were observed.

## **6.4. Results**

### **6.4.1. Run products**

Experimental conditions and obtained run products are summarized in Table 6.1. Photographs of run products from an experiment involving synthetic fluid inclusions and one involving an overlying felsic magma are shown in Figs. 6.4 and 6.5, respectively. In runs conducted with capsule designs (a) and (b) the recovered quartz pieces are strongly fractured and contain numerous fluid inclusions (Figs. 6.4a, b). Three types of fluid inclusions can be distinguished based on their size, spatial distribution, and composition: (1) abundant, small (typically  $<20\text{-}30\ \mu\text{m}$  mean diameter) inclusions arranged on healed fracture planes, (2) fewer, large inclusions (commonly  $>40\ \mu\text{m}$  mean diameter) located near the edges of the quartz piece, representing fluid inclusions that were present in the quartz already before the start of the experiment and then were opened and filled with new fluid at the time of in-situ fracturing, and (3) rare inclusions of the latter type that were not re-opened during the in-situ cracking. The last type of fluid inclusions can be easily distinguished from the former two types by their high K and Cs content, and since they did not trap any new fluid they will not be discussed any further. The former two types of inclusions are

compositionally identical, showing microthermometrically determined salinities of 2.8-4.7 wt%  $\text{NaCl}_{\text{equiv}}$  and the following average major element composition based on LA-ICP-MS analyses: 1.9-2.8 wt% K, 3.6-7.6 wt% Cl, 0.11-4.3 wt% S, and 0.40-1.4 wt% Fe.

The mafic starting material (either powdered rock + fluid; or hydrous mafic glass) always transformed to a highly crystallized aggregate consisting of various mineral phases (occupying a

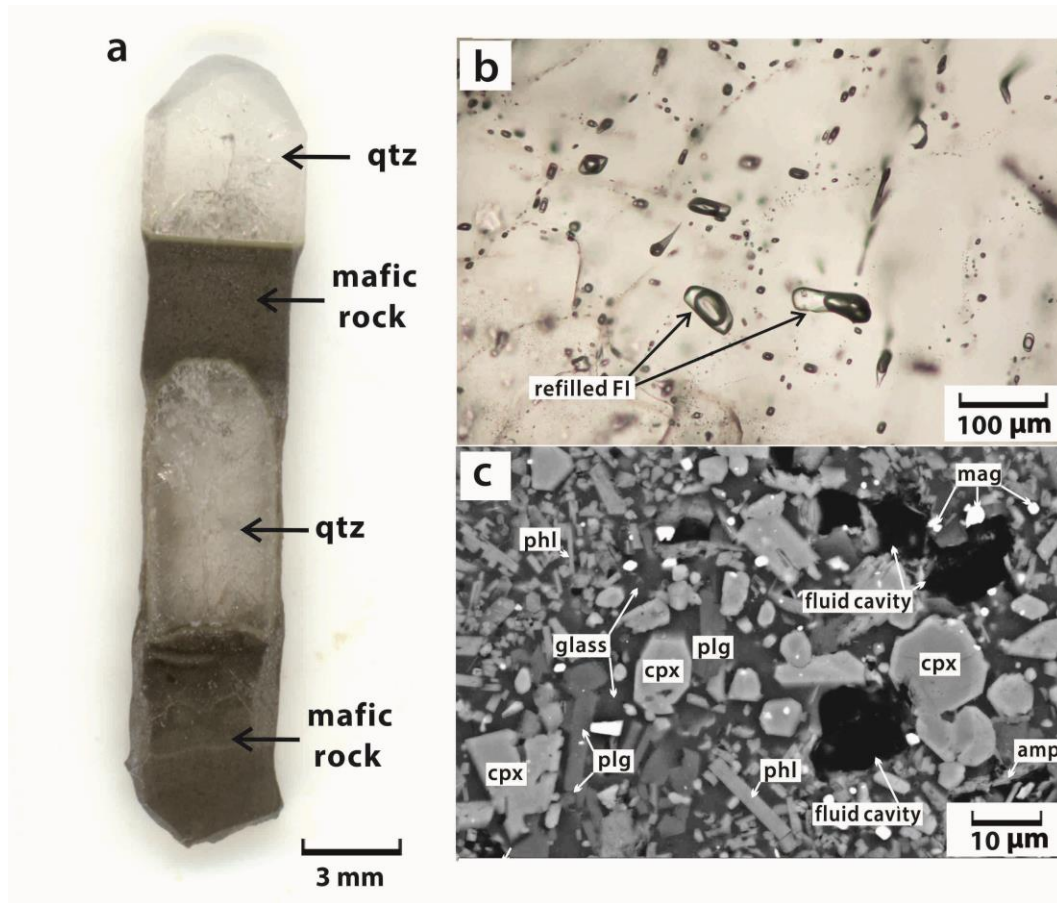


**Fig. 6.4.** Photographs of samples recovered from experiments involving synthetic fluid inclusions. (a) Polished section through sample HG33 (incident light). (b) Transmitted-light photomicrograph of the quartz piece recovered from run HG32, showing numerous healed cracks decorated with small fluid inclusions and some larger inclusions that were present already before the experiment but were re-opened and filled with new fluid at the time of in-situ cracking. (c) Back-scattered electron (BSE) image of the mafic run product of sample HG32 after a run time of 9 days at 850 °C and 2 kbar. Notice the euhedral shape of all minerals.

total volume of 80-90 %) plus smaller amounts of silicate melt (10-20 vol%) and cavities that were filled with fluid (0.5-3 vol%) (Figs. 6.4c, 6.5b), independent of whether the run was performed in forward or reverse manner. The hydrous nature of the mineral assemblage (which differs significantly from that in the starting rock) and the euhedral shape of the minerals suggest that major re-crystallization and formation of new minerals occurred during the runs. In the two experiments conducted with capsule design (c), a large fluid bubble developed in the overlying pool of felsic melt (Fig. 6.5c), suggesting that significant amounts of volatiles moved from the underlying mafic magma into the felsic melt reservoir.

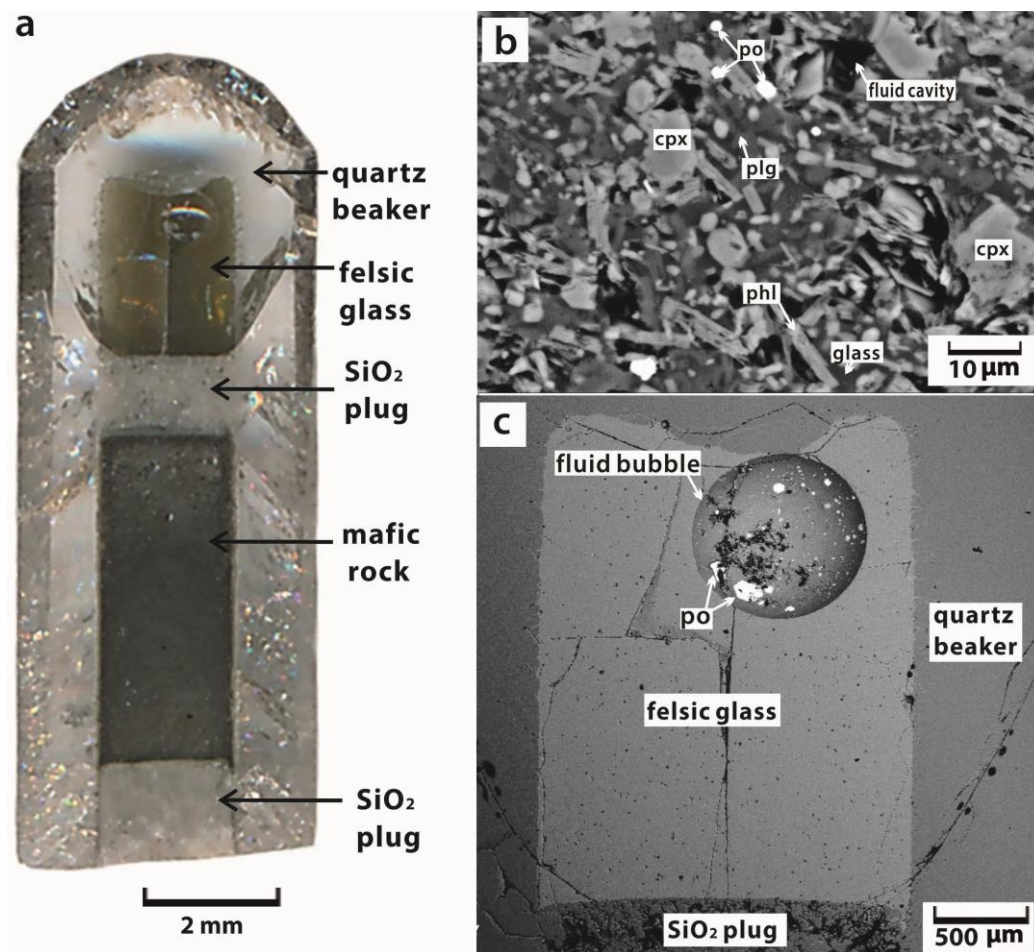


**Fig. 6.5.** Photographs of the run products of experiment HG42, which was designed to explore the flux of volatiles from a crystallizing mafic magma into an overlying pool of felsic melt. (a) Polished longitudinal section. (b) BSE image of the mafic run product. (c) BSE image of the quenched pool of felsic melt in the top of the assembly. Notice the presence of a large bubble containing precipitates of pyrrhotite.

### 6.4.2. Composition of glasses and mafic run products

Average compositions of hydrous starting glasses, mafic run products, and overlying felsic melts are reported in Table 6.2, whereas representative analyses of individual mineral phases are listed in Table 6.3 and plotted in supplementary Fig. 6-S1. A representative LA-ICP-MS signal of a bulk analysis of a mafic run product is shown in Fig. 6.6a. The most abundant mineral phases in the mafic run product are diopside, Mg-hornblende, phlogopite, andesine ( $Ab_{30-50}$ ) and magnetite (the latter being too small to be measured quantitatively). One run additionally contained small amounts of pyrrhotite, whereas anhydrite was observed in another run (Table 6.1). However, based on leaching tests (see below) anhydrite was probably present in all experiments but usually was dissolved away during sample preparation. The hydrous starting glasses were quite homogeneous with respect to the added elements (S, Cl, Li, B, Cu, Zn, Ag, Cd, Mo, As, Se, Sb, Te, Tl, Pb and Bi) and retained a trachybasaltic bulk composition similar to the whole-rock analyses published by David and Smith (1993) and David et al. (1996). After crystallization of these glasses in forward experiments the mafic run products were still fairly homogeneous with respect to both major and trace elements, although the absolute concentrations of many trace elements scattered considerably and were now significantly lower due to partitioning into the fluid phase. The concentrations of Cu, Ag, Se, Te were extremely low both in the mafic run products and in the fluid inclusions analyzed from runs performed with capsule design (a) (e.g., HG30, HG32, HG33), suggesting that these elements were lost to the gold capsule. Indeed, a run performed with capsule design (b) that involves a quartz beaker (HG38) shows no significant loss of these elements (see below). The felsic melt reservoirs in two experiments performed with capsule design (c) were homogeneous with respect to both major and minor elements.

**Table 6.2**

Composition of mafic and felsic starting glasses and corresponding end products after the experiments.

Element	Mafic glass		Haplogranite		Rhyolite glass		Haplogranite		Rhyolite		Mafic rock		Mafic rock		Mafic rock		Mafic rock		Mafic rock		Mafic rock		Mafic rock		Mafic rock			
wt %	orig	δ	orig	δ	orig	δ	HG	δ	HG	δ	HG	δ	HG	δ	HG	δ	HG 34	δ	HG 35	δ	HG 36	δ	HG 38	δ	HG 42	δ	HG 47	δ
Na <sub>2</sub> O	2.8	0.04	4	0.1	4.9	0.1	3.6	0.1	4.3	0.2	2.7	0.2	2.4	0.1	2.4	0.2	2.5	0.2	2.5	0.1	2.5	0.1	2.6	0.1	2.7	0.05	2.7	0.1
MgO	7.8	0.1	0.015	0.001	0.005	0.001	0.019	0.001	0.018	0.003	7.6	0.7	8	0.3	8	0.2	7.6	0.7	8.2	0.3	8	0.4	8.5	0.3	8	0.2	8.2	0.3
Al <sub>2</sub> O <sub>3</sub>	12.7	0.1	12.3	0.1	11.3	0.05	12.1	0.2	10.5	0.4	13	1	12.9	0.4	13.5	0.5	12.8	0.4	13.2	0.5	12.8	0.2	13.2	0.4	13	0.2	13.1	0.1
SiO <sub>2</sub>	55.2	0.5	78.8	0.1	76.3	0.2	78.5	0.3	77.5	0.7	55.9	1.3	55	0.8	55.6	0.5	56.4	1.7	55.6	1.4	55.4	0.6	54.4	0.9	55.5	0.4	55	0.5
K <sub>2</sub> O	5.5	0.03	4.9	0.04	4.7	0.1	5.5	0.1	5.1	0.1	4.9	0.7	4.9	0.4	5.5	0.6	5.4	0.5	5.3	0.9	5.1	0.6	5	0.5	4.7	0.1	4.6	0.2
CaO	8.1	0.1	0.06	0.01	0.2	0.01	0.09	0.02	0.2	0.01	8.7	1.5	8.8	0.8	7.4	1.4	7.4	1.3	7.7	2.1	8.2	0.9	8.5	0.8	8.4	0.5	8.8	0.3
FeO <sub>T</sub>	6.7	0.1	0.05	0.002	2.5	0.03	0.06	0.01	2.3	0.1	6.2	0.3	6.4	0.3	6.5	0.3	6.9	1	6.5	0.4	6.9	0.5	6.7	0.2	6.6	0.1	6.5	0.2
TiO <sub>2</sub>	1.1	0.01	0.02	0.001	0.14	0.001	0.02	0.001	0.13	0.01	1.1	0.2	1.1	0.1	1.2	0.2	1.1	0.1	1.1	0.1	1.1	0.1	1.1	0.02	1.1	0.03	1.1	0.04
S	0.37	0.05	0.07	0.001	0.04	2E-04	0.06	0.01	0.04	0.003	0.24	0.28	0.26	0.04	0.12	0.03	0.25	0.06	0.16	0.14	0.22	0.16	0.25	0.37	0.2	0.02	0.23	0.06
Cl	0.33	0.02	0.1	0.002	0.15	0.003	0.11	0.01	0.18	0.02	0.29	0.14	0.21	0.03	0.21	0.03	0.22	0.04	0.25	0.06	0.2	0.03	0.26	0.06	0.18	0.02	0.28	0.04
ppm																												
Li	61	2	1.5	0.3	37	1	52	2	78	3	54	5	51	3	50	6	54	4	57	3	56	6	49	4	38	3	36	2
B	54	4	23	2	35	0.5	29	2	34	1	41	20	34	3	33	7	32	3	36	12	36	14	29	8	31	5	50	8
Mn	980	11	3.1	0.3	590	7	7.7	1.4	550	19	900	82	990	75	810	43	860	120	850	120	910	54	940	54	920	35	930	28
Cu	360	14	<0.25		0.09	0.07	7.1	0.8	8.2	0.7	0.9	0.4	1.8	0.6	1.6	1	1.2	0.8	1	0.2	1.1	0.2	300	135	230	72	100	19
Zn	170	5	2.3	0.9	130	3	14	0.5	140	6	124	28	140	7	160	35	140	14	133	28	132	22	135	41	128	10	139	7
As	69	16	0.7	0.1	4.7	0.11	2.1	1.1	6	0.6	49	44	41	2	33	19	39	4	27	25	65	86	38	18	37	7	44	6
Se	75	22	1.2	0.6	<1.1		2.9	1.6	1.3	0.2	5	7	46	12	29	19	26	11	19	18	27	13	18	8	42	4	40	6
Br	380	16	29	3.1	27	1.2	41	16	35	5	n.a.	n.a.	n.a.	n.a.	n.a.	n.a.	n.a.	n.a.	n.a.	180	7	n.a.	n.a.	20	3	240	47	
Rb	170	1	2.3	0.1	170	1	36	3	170	2	160	24	150	12	170	22	170	16	160	26	160	21	150	18	150	5	140	11
Sr	990	16	119	2	0.8	0.1	130	4	6.4	2.7	1100	260	1100	29	970	220	980	150	1000	230	1000	170	1100	110	1300	64	1200	53
Zr	580	13	9	1.3	770	0.1	10	2	660	32	540	100	520	200	620	240	520	53	540	180	820	390	500	45	570	120	600	48
Mo	41	1	0.13	0.01	9	0.2	0.93	0.28	11	1	36	3	51	4	36	6	49	3	40	10	33	3	39	3	50	8	39	5
Ag	48	1	<0.04		0.1	0.004	2.5	0.2	3.7	0.3	0.18	0.09	0.79	0.2	0.34	0.18	0.17	0.04	0.15	0.08	0.22	0.07	46	18	40	16	26	3
Cd	66	3	0.1	0.03	0.5	0.002	1.8	0.5	2.9	0.6	9	6	18	4	7.2	3.1	9	4	7.5	4	11	3	46	27	36	6	46	10
Sb	33	6	<0.08		0.8	0.1	0.6	0.66	1.1	0.2	27	30	34	3	18	14	25	5	18	22	110	200	29	19	38	8	40	6
Te	82	24	0.15	0.02	<0.14		0.38	0.08	0.12	0.06	6.5	8.7	32	11	35	30	42	23	35	38	25	32	48	55	43	26	37	8
Cs	4	0.1	0.1	0.01	3.9	0.1	0.4	0.1	3.9	0.2	15	4	21	10	10	1	19	3	11	2	16	2	2.7	0.4	2.8	0.2	2.7	0.2
Ba	1300	27	19	1	2.7	0.3	28	3	7	2	1200	250	1300	150	1400	170	1300	77	1300	135	1300	43	1400	89	1300	47	1300	55
Ce	110	2	8.7	0.3	140	3	8.5	0.3	140	10	110	5	110	5	100	4	110	5	100	9	110	2	110	5	110	3	110	3
W	1.7	0.7	11.2	1.2	2.6	0.05	15	2	4	1	1.3	0.3	1.9	0.3	1.1	0.1	3.7	0.4	2.2	0.6	1	0.1	2.7	1.2	4.1	1.3	3.2	0.6
Tl	67	3	0.11	0.03	0.7	0.05	19	0.6	9.2	0.4	44	9.4	39	3	48	10	42	4	52	11	46	8	59	6	33	2	38	3
Pb	69	2	3	0.4	24	0.36	10	1.8	28	3	52	11	58	4	52	8	55	5	54	2	51	3	61	11	58	8	52	6
Bi	35	1	0.014	0.007	0.2	0.02	1.0	0.6	1.5	0.3	13	10	20	8	6.2	1.9	11	3	13	6	14	3	21	4	42	11	27	4

Abbreviations: orig – starting material composition; δ – 1 sigma standard deviation of the measurements; n.a. – not analyzed

**Table 6.3**

Representative electron microprobe analyses of mineral phases in the mafic run product.

No.	Mineral	SiO <sub>2</sub>	Na <sub>2</sub> O	FeO	Al <sub>2</sub> O <sub>3</sub>	MgO	K <sub>2</sub> O	CaO	TiO <sub>2</sub>	Cl	SO <sub>3</sub>	Total
HG32	cpx	49.4	0.74	6.3	4.1	15.6	0.11	21.1	0.68	0.013	0.063	98.2
	amp	49.7	0.85	6.4	4.39	16.1	0.17	20.5	0.49	0.008	0.008	98.7
	phl	39.6	0.53	9.2	14.25	19.6	6.22	0.6	2.27	0.073	0.045	92.4
	plg	55.9	5.56	1.6	25.2	0.11	0.93	8.6	0.17	0.018	0.011	98.1
HG33	cpx	50.5	0.49	6.4	3.67	14.75	0.19	22.6	0.62	0.011	0.029	99.2
	amp	49.9	0.61	6.8	4.8	13.38	0.48	20.9	0.74	0.014	0.019	97.8
	phl	39.6	0.67	12.8	14.4	15.24	6.59	0.8	2.87	0.107	0.035	93
	anh	0.6	0	0.3	0.3	0.3	0.4	43.4	0.1	0.005	49.8	95.2
HG36	cpx	50.9	0.41	5.9	2.07	16.3	0.12	22	0.59	0.004	0.007	98.3
	amp	49.2	0.7	7.3	5.04	13.8	0.3	21.4	1	0.011	0.012	98.8
	phl	41.2	0.65	8.8	14.69	16.34	7.45	1.1	1.92	0.097	0.034	92.2
	plg	55.9	5.45	0.9	25.85	0.37	0.85	8.6	0.12	0.014	0.011	98.1
HG38	cpx	52	0.45	5.7	3.7	15.4	0.45	21.3	0.7	0.032	0.032	99.7
	amp	52.4	1.1	5.2	6.9	13.2	1.3	16.7	0.7	0.174	0.071	97.7
	phl	46.8	1.08	7.1	12.3	15	6.14	5.2	1.78	0.169	0.053	95.6
	plg	57	5.45	1.1	22.8	1.1	1.68	7.6	0.16	0.049	0.012	97
HG42	cpx	50.8	0.74	6.2	3.85	15.9	0.13	21.2	0.5	0.009	0.006	99.3
	amp	49.8	1.32	8.4	7.04	11.5	0.22	20.6	0.8	0.016	0.029	99.7
	phl	39.9	0.65	12	13.18	16.1	6.4	1.4	2.85	0.128	0.037	92.7
	plg	59.5	5.41	0.9	21.92	0.8	1	6.7	0.11	0.075	0.01	96.5

### 6.4.3. Composition of synthetic fluid inclusions

Average compositions of synthetic fluid inclusions are listed in Table 6.4, and a representative LA-ICP-MS signal obtained from a fluid inclusion is shown in Fig. 6.6b. For a given sample the fluid inclusion compositions turned out fairly reproducible ( $\pm 10\text{-}30\%$  relative standard deviation), except for elements that require major host corrections (S, Cl, Br, Li, As, Sb), and elements that easily alloy with gold (Cu, Ag, Se, Te, Cd, Sb and Bi). Importantly, fluid inclusion compositions measured in forward experiments are within uncertainty the same as those measured in reverse runs, suggesting that equilibrium between fluid and mafic residue was reached (Fig. 6.7).

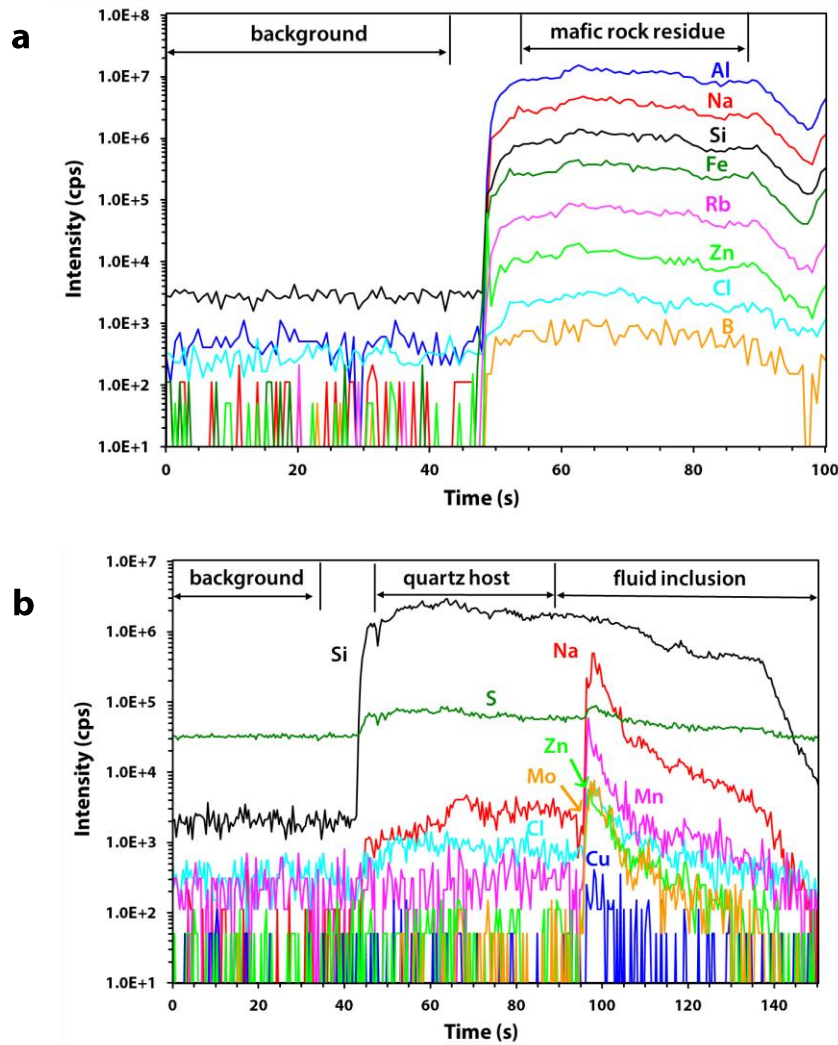


**Fig. 6.6.** (a) LA-ICP-MS signal (15Ap21d04) of the mafic rock residue of experiment HG34, analyzed with a laser pit size of 70  $\mu\text{m}$  diameter. (b) LA-ICP-MS signal of a 60  $\mu\text{m}$ -sized fluid inclusion (15Ma03h06) analyzed from experiment HG30. Notice that in the case of S, Na and Cl significant signals are obtained when ablating pure quartz, meaning that corrections had to be made to accurately quantify the concentrations of these elements in the fluid inclusion.

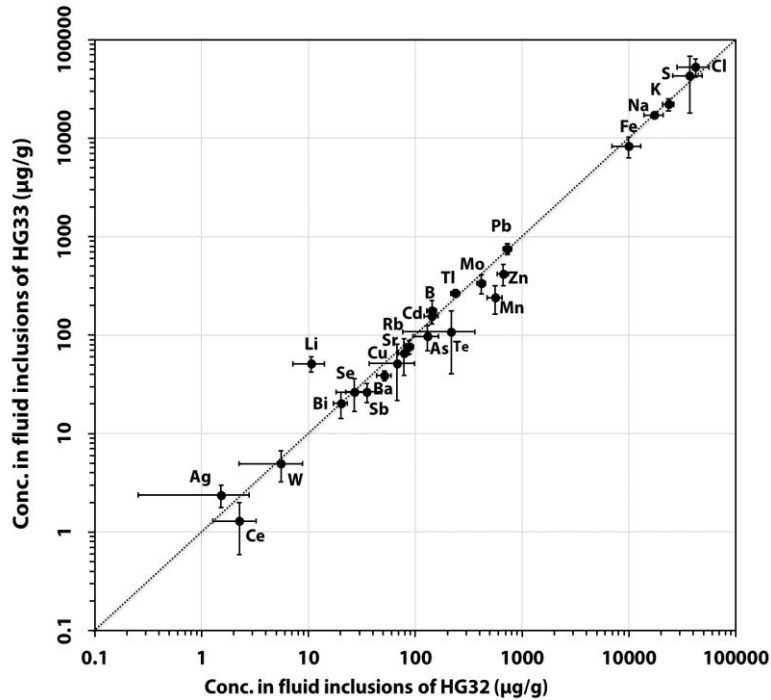


**Fig. 6.7.** Element concentrations in fluid inclusions from run HG32 (forward experiment) vs. run HG33 (reverse experiment) at 850 °C and 2 kbar, both cracked in situ after 2 days. The relatively good match suggests that equilibrium between the fluid and rock was attained in both experiments. Uncertainties for Ag, Ce and W are high because these elements were close to the detection limit. The cause for the discrepancy of Li is not clear.

#### 6.4.4. Fluid-rock partition coefficients and relative element mobilities

For experiments in which aliquots of fluid were trapped in the form of synthetic fluid inclusions, partition coefficients ( $D_{\text{fluid/rock}} = C_{\text{fluid}}/C_{\text{rock}}$ ) of elements between fluid and mafic rock residue were calculated from their concentrations in the fluid inclusions and mafic residue, respectively. The data are listed in Table 6.4 and are summarized in Fig. 6.8a. Mass balance calculations based on an estimated fluid abundance of 2.3 wt% (the remaining 2.7 wt% H<sub>2</sub>O residing in phlogopite, amphibole and residual melt in the mafic residue) demonstrate that the experiments behaved as  $\pm$ closed systems with respect to of Li, B, Na, S, Cl, K, Mn, Fe, Rb, Sr, Ba, Ce, Zn, Mo, As, Sb, W, Tl, and Pb, whereas significant amounts of Cu, Ag, Se, Te, Cd, Sb and Bi were lost to the gold

**Table 6.4**

Element concentrations in fluid inclusions and calculated partition coefficients (D) between fluid and mafic residue.

	HG 30		HG30		HG 32		HG32		HG 33		HG33		HG 34		HG34		HG 35		HG 35		HG 36		HG 36		HG 38		HG 38		
	FI	$\delta$	D	$\delta$	FI	$\delta$	D	$\delta$	FI	$\delta$	D	$\delta$	FI	$\delta$	D	$\delta$													
Li	240	160	4.5	2.9	11	3.5	0.21	0.07	51	9	1	0.22	120	100	2.3	1.9	65	8	1.1	0.2	32	14	0.57	0.25	28		0.56	0.05	
B	220	51	5.3	2.9	140	15	4.3	0.5	180	47	5.4	1.8	140	34	4.3	1.1	190	47	5.3	2.2	120	13	3.2	1.2	620	170	21	8	
Na <sup>a</sup>	1.6	0.11	0.83	0.07	1.7	0.4	1	0.2	1.7	0.1	0.9	0.1	1.3	0.02	0.72	0.06	1.9	0.1	1	0.05	1.5	0.4	0.79	0.24	1.1	0.19	0.57	0.1	
S <sup>a</sup>	0.87	0.34	3.6	4.4	3.7	1.1	14	4.8	4.3	2.5	37	24	0.86	0.59	3.4	2.5	1.4	0.3	8.4	7.5	0.25	0.12	1.1	1	0.1	0.9	0.4	3.4	
Cl <sup>a</sup>	3.6	1.4	12	7.7	4.2	1.4	20	7.4	5.3	1.1	25	6.3	3.7	0.9	17	5.2	5.2	1.1	21	7.1	5.4	1.7	27	9.1	7.6	3.4	30	15	
K <sup>a</sup>	2.3	0.3	0.48	0.09	2.8	0.3	0.58	0.08	2.7	0.4	0.48	0.09	2.2	0.4	0.4	0.08	2.8	0.3	0.54	0.1	2.3	0.3	0.44	0.08	1.9	0.6	0.37	0.1	
Mn	510	150	0.56	0.17	560	90	0.56	0.1	240	78	0.3	0.1	240	41	0.28	0.06	440	110	0.52	0.15	500	70	0.55	0.08	530	140	0.56	0.15	
Fe <sup>a</sup>	0.97	0.28	0.16	0.05	1.3	0.4	0.2	0.06	1.1	0.2	0.16	0.04	0.69	0.1	0.1	0.02	1.4	0.3	0.22	0.05	0.65	0.2	0.1	0.03	0.4	0.21	0.06	0.03	
Cu	39	17	43	26	68	31	37	20	52	30	33	29	62	35	50	41	51	27	50	28	79	17	70	18	16000	1700	54	26	
Zn	410	130	3.3	1.3	670	78	4.8	0.6	420	100	2.6	0.9	320	110	2.3	0.8	510	120	3.8	1.2	534	201	4	1.7	680	91	5	1.6	
As	172	129	3.6	4.2	130	35	3.2	0.9	97	28	3	1.9	180	79	4.8	2.1	170	49	6.2	5.9	52	35	0.8	1.2	170	51	4.3	2.5	
Se	66	42	12	17	27	8.9	0.59	0.25	26	10	0.91	0.67	160	40	6.1	3	19	8.1	1	1	29	19	1.1	0.9	9000	2100	510	260	
Br	n.a.	n.a.	n.a.	n.a.	n.a.	n.a.	n.a.	n.a.	n.a.	3400	2400	20	13	n.a.	n.a.	n.a.	n.a.												
Rb	82	12	0.53	0.11	88	7.8	0.58	0.07	76	12	0.45	0.09	59	16	0.35	0.1	83	23	0.51	0.16	77	14	0.49	0.11	66	19	0.46	0.14	
Sr	72	16	0.06	0.02	79	9.2	0.07	0.01	65	26	0.07	0.03	51	15	0.05	0.02	73	23	0.07	0.03	64	10	0.06	0.01	52	26	0.05	0.02	
Mo	350	59	9.8	1.9	420	39	8.1	1	340	74	9.3	2.6	360	110	7.4	2.2	340	90	8.6	3.1	300	110	9.2	3.4	210	130	5.5	3.5	
Ag	1.2	0.6	6.6	4.4	1.5	1.3	1.9	1.7	2.4	0.6	7	4.1	1.1	0.9	6.1	5.2	0.9	0.4	5.9	4.2	1.3	0.9	5.9	4.8	170	140	3.8	3.3	
Cd	99	45	10.6	8.3	140	21	7.9	2.2	160	26	22	10	150	27	17	7.5	49	10	6.5	3.8	340	160	30	15	780	120	17	10	
Sb	71	47	2.6	3.5	35	13	1	0.39	27	6	1.5	1.2	37	8.5	1.5	0.5	18	7.8	1	1.3	15	3.5	0.14	0.25	32	11	1.1	0.8	
Te	1.4	0.3	0.22	0.3	220	140	6.7	4.9	110	68	3.1	3.2	110	45	2.6	1.8	1.5	0.6	0.04	0.05	22	20	0.86	1.4	320	67	6.6	8	
Cs	35	12	2.32	1.02	84	24	4	2	57	45	5.9	5	45	24	2.4	1.4	48	31	4.2	2.8	40	24	2.6	1.6	96	61	36	23	
Ba	47	14	0.04	0.01	51	8	0.04	0.01	39	4.6	0.03	0.01	17	6	0.01	0.01	35	15	0.03	0.01	58	8	0.05	0.01	40	8	0.03	0.01	
Ce	1.7	0.03	0.02	0	2.3	1	0.02	0.01	1.3	0.7	0.01	0.01	1.8	1.4	0.02	0.01	2.8	1.1	0.03	0.01	5.5	3	0.05	0.03	1.3	0.8	0.01	0.01	
W	4	1.8	3.1	1.6	5.5	3.3	2.9	1.8	4.9	1.7	4.5	1.6	6.7	1.3	1.8	0.4	8.2	0.9	3.7	1.2	2.3	1.3	2.2	1.3	4.9	0.6	1.8	0.8	
Tl	140	26	3.1	0.9	240	21	6	0.7	270	24	5.5	1.3	130	30	3.2	0.8	190	30	3.7	1	150	77	3.2	1.7	260	17	4.4	0.5	
Pb	440	36	8.4	1.9	730	66	13	1.5	750	99	15	3	270	58	4.8	1.1	510	83	9.4	1.6	470	160	9.1	3.2	600	120	9.7	2.6	
Bi	17	8	1.3	1.1	20	3	1	0.5	20	6	3.3	1.4	34	14	3.1	1.6	4.1	1.1	0.3	0.2	17	9.1	1.3	0.7	110	58	5.3	3	

<sup>a</sup> Na, S, Cl, K, Fe are reported in wt%, all other elements in ppm by weight.Abbreviations:  $\delta$  – 1 sigma standard deviation of the measurements; n.a. – not analyzed.

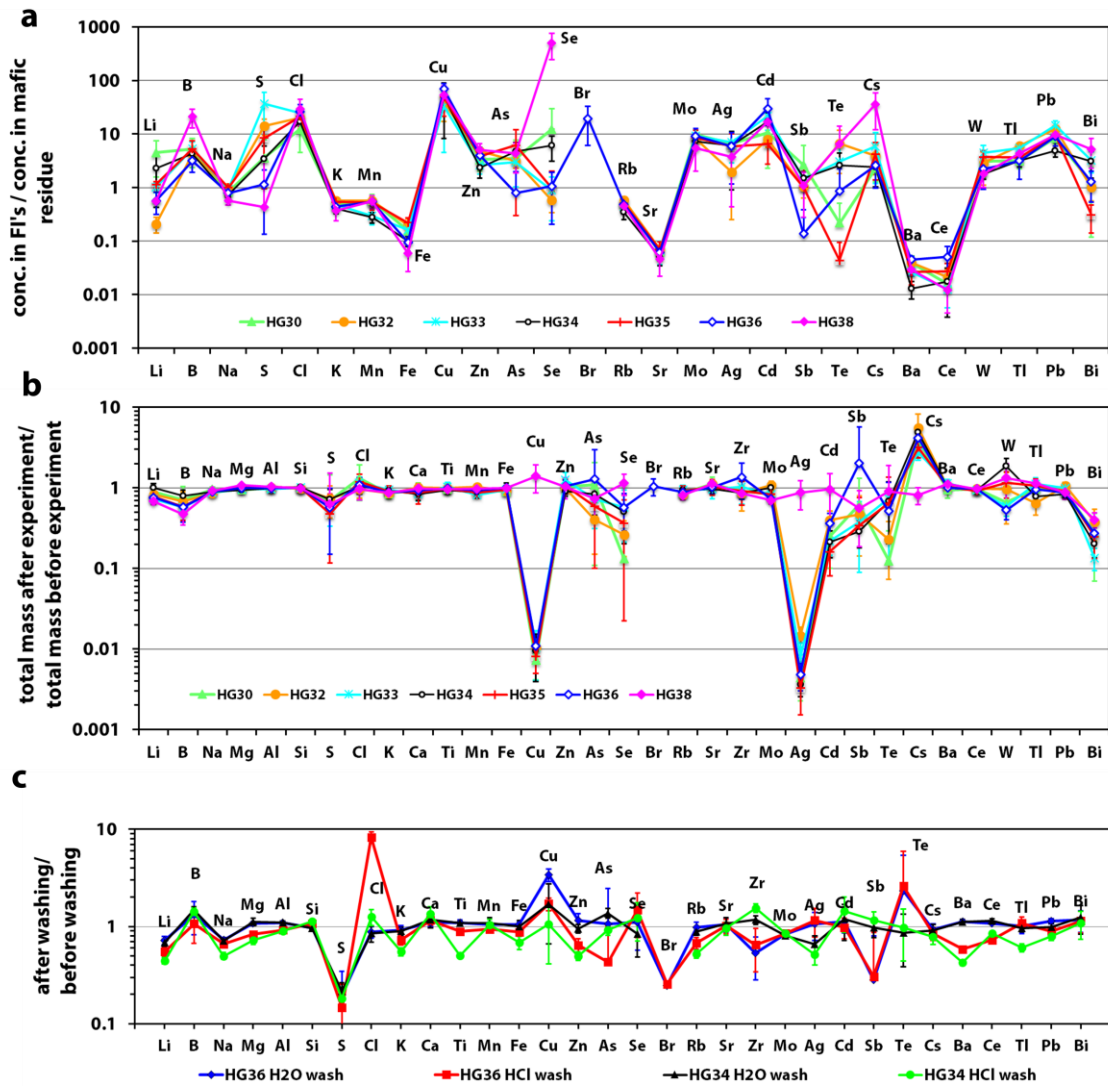


**Fig. 6.8.** (a) Fluid/rock partition coefficients calculated by dividing element concentrations in the fluid inclusions (FI's) by their concentration in the mafic residue. The elements are arranged by ascending mass. (b) Mass balance diagram showing the calculated total mass of each element present within the sample capsule after the experiment, divided by its total mass before the experiment. In the experiments without quartz beaker significant amounts of Cu, Se, Ag, Cd, Sb, Te and Bi were apparently lost to the gold capsule. (c) Element concentrations in mafic residues after washing them in H<sub>2</sub>O or diluted HCl solution, relative to the element concentrations before washing.

capsules in the runs performed without quartz beaker (Fig. 6.8b). In the run performed with quartz beaker (HG38) the loss of the latter elements was essentially zero (Fig. 6.8b). However, in the

beginning of this run a significant fraction of the added fluid apparently moved into the pore space of the quartz powder at the bottom of the capsule, such that the fluid abundance had to be reduced to 0.5 wt% to satisfy the mass balance of non-alloying elements. A test was made to see how much of originally fluid-dissolved material was present in the mafic residue and included in the bulk analyses, leading to artificially low fluid/rock partition coefficients. For this purpose, aliquots of two mafic residues were ground to fine powder and then washed for 30 minutes in hot (80 °C) diluted hydrochloric acid (5 wt% HCl) or distilled water. After rinsing the acid-treated samples once more in hot, distilled water, they were allowed to dry, pressed to dense pellets and finally re-analyzed by LA-ICP-MS. The results are shown in Fig. 6.8c and summarized in supplementary Table 6-S3. Except for sulfur and potentially bromine, no systematic differences between washed and untreated samples are evident, meaning that amount of originally fluid–dissolved material in the mafic residue is small, and thus that fluid–rock partition coefficients calculated from untreated samples are robust. This does not hold for sulfur (and potentially bromine), which occurs at ~5 times lower concentrations in washed samples compared to untreated samples (Fig. 6.8c). Since oxidized sulfur is easily soluble and anhydrite has been observed in on run (HG33), our preferred interpretation of this discrepancy is that all runs were saturated anhydrite. The consequence is that true  $D_S^{\text{fluid/rock}}$  values may be up to 5 times higher than shown in Fig. 6.8a.

In the two experiments in which the fluid was allowed to react with an overlying pool of felsic melt (HG42, HG47) relative element mobilities were calculated based on concentration changes in the mafic material. This approach turned out more practical than focusing on concentration changes in the felsic melt, as the starting concentrations of many elements in the felsic melt was essentially zero and corresponding gain factors would be infinitively large. We thus calculated relative element extraction efficiencies from the mafic material as follows:

$$\varepsilon = \frac{|C_0 - C_t|}{C_t} \quad (6-1)$$

where  $C_0$  is the element concentration in mafic starting glass and  $C_t$  is the element concentration in the mafic run product. Notice that the denominator in this equation is the concentration in the end product rather than that in the starting product, as this corresponds more closely to the fluid/rock partition coefficients measured in the previous experiments. The results are listed in supplementary Table 6-S2 and are compared in Fig. 6.9 with the fluid–rock partition coefficients

derived from the fluid inclusion-bearing experiments. Due to the fundamentally different ways to assess relative volatilities it was necessary to use two different scales in this Figure, hence only a qualitative comparison of the two data sets is possible.

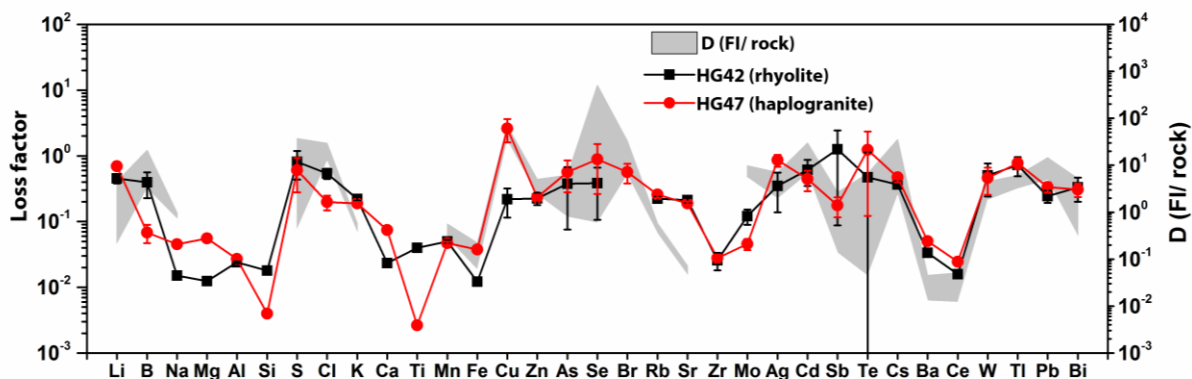


**Fig. 6.9.** Element extraction efficiencies calculated from experiments HG42 and HG47 (solid lines), compared to fluid–rock partition coefficients calculated from experiments involving synthetic fluid inclusions (shaded area). Notice the different scales.

## 6.5. Discussion

### 6.5.1. Attainment of equilibrium

Several lines of evidence suggest that equilibrium between fluid and mafic residue was reached in our experiments: (1) fluid inclusion compositions measured in forward versus reverse runs agree well with each other (Fig. 6.7); (2) the minerals in the mafic residue have a euhedral shape and are distinctly larger than the grain size of starting rock powder used in the reverse experiments; (3) the newly formed mineral assemblage is the same in both forward and reverse runs, but differs from that of the starting rock by the absence of olivine and a much higher abundance of phlogopite; and (4) profiles measured across the mafic residue reveal a homogenous trace element distribution. However, mass balance constraints and the comparison between runs without quartz beaker and the run with quartz beaker (Fig. 6.8b) suggest that in the former runs major amounts of Cu, Ag, Se, Cd, Sb, Te and Bi were lost to the gold capsule. For these elements the fluid–rock partitioning coefficients determined in runs HG30 and HG32-36 are thus considered unreliable. They tend to be too low because the fluid inclusions formed in the vicinity of the Au capsule and thus trapped

fluid that was more strongly depleted in the alloying elements than the analyzed mafic rock reservoirs above and below the central quartz piece (Fig. 6.4a). Corresponding partitioning values of Cu, Ag, Se, Cd, Sb, Te and Bi should thus be regarded as minimum values. As was mentioned earlier, the experiment conducted with quartz beaker (HG38) has the advantage that alloying problems are minimized, but the disadvantage that the timing of fluid inclusion formation could not be controlled by in-situ cracking because that would also have led to cracks in the quartz beaker. However, the fluid–rock partition coefficients obtained for non-alloying elements in this run are virtually the same as those obtained in the previous runs, suggesting that the fluid reached equilibrium before it was trapped within fluid inclusions also in this experiment.

In the two runs conducted with an overlying trap of felsic melt the mafic starting material was a hydrous glass, hence the metal-bearing fluids exsolved as a result of crystallization and thus should have been equilibrium with the crystallizing mineral assemblage. Furthermore, the fluid-mobile elements are rather homogeneously distributed within the recovered felsic trap, meaning that their abundances were not controlled by diffusivities within the silicate melt. The trends obtained from the runs with felsic melt traps are similar to those obtained from the runs with synthetic fluid inclusions, although small differences exist (Fig. 6.9). The reason for these small differences is not known.

Taking the results of all experiments together, one can group the investigated elements into four classes according to their mobility in the fluid phase: S, Cl, Cu, Se, Br, Cd and Te are most fluid-mobile ( $D_{\text{fluid/rock}} > 10$ ), followed by Li, B, Zn, As, Ag, Sb, Cs, W, Tl, Pb and Bi ( $D_{\text{fluid/rock}} = 1-10$ ). Less fluid-mobile are Na, Mg, K, Ca, Mn, Fe, Rb, Sr, Mo and Rb ( $D_{\text{fluid/rock}} 0.1-1$ ), and the least fluid-mobile elements are Al, Si, Ti, Zr, Ba and Ce ( $D_{\text{fluid/rock}} < 0.1$ ).

### **6.5.2. Comparison with data from natural samples**

Evidence for selective metal transport by magmatic fluids has been documented in many previous studies. By investigating the compositions of magmatic sulfides in the rhyodacite of Mount Pinatubo and comparing them with those in contemporaneous mafic magma, Hattori (1993, 1996) found that the former are enriched in Cu, Zn, Se and probably Ag, Cd and Te. Based on independent evidence for addition of sulfur to the rhyodacite it was concluded that these elements were added by means of sulfur-rich fluids that exsolved from underplating mafic magma. This

interpretation is strongly supported by the present study, as the above-mentioned elements are amongst the 10 most volatile elements identified in our experiments. Similarly, anomalously high concentrations of Li and/or Cu in melt inclusions and silicate minerals have been interpreted by Berlo et al. (2004), Kent et al. (2007), Rowe et al. (2008) and Collins et al. (2009) to reflect addition of a Cu- and Li-rich fluid phase. The most direct evidence for metal transport by magmatic fluids, however, stems from the analysis of fluid inclusions (e.g., Williams-Jones and Heinrich, 2005), volcanic plume particles (e.g., Moune et al., 2010), and fumarolic condensates (e.g., Zelenski et al., 2014). Especially the latter approach provided a wealth of data on otherwise little-studied trace elements such as Se, Tl, Te, Cd and Bi (e.g., Symonds et al., 1987; Taran et al., 1995; Aiuppa et al., 2003; Zelenski et al., 2013; 2014; Menard et al., 2014). In most of these studies, element concentrations measured in the fumarolic condensates were normalized to a fluid-immobile reference element and compared to corresponding element ratios in the likely source magma in terms of relative enrichment factors (EF) defined by (e.g., Lepel et al., 1978):

$$EF=(X_f/R_f)/(X_m/R_m) \quad (6-2)$$

where X refers to the concentration of the element of interest, R refers to the concentration of the reference element, and f and m refer to fluid and magma, respectively. Usually, Ti is chosen as immobile reference element because it occurs at relatively high and constant concentration in magmas and has a very low solubility in fluids and gases (e.g., Symonds et al., 1987).

To be able to compare our experimental data with those obtained from the study of volcanic fumaroles we converted the data listed in Tables 6.2 and 6.4 into enrichment factors relative to Ti. Since Ti was below the detection limit in all analyzed fluid inclusions we used the lowest obtained detection limit of ~0.005 wt% Ti as reference value. For sulfur we expanded the range to include the possibility that actual volatilities are up to five times higher than shown in Figs. 6.8 and 6.9. The results are shown in Fig. 6.10, where they are compared with enrichment factors calculated from volcanic condensates of Tolbachik volcano (Zelenski et al., 2014), Erta Ale (Zelenski et al., 2013), Kudryavy (Taran et al., 1995), Lascar (Menard et al., 2014) and Etna (Aiuppa et al., 2003). In general, the trends displayed by the two data sets are similar, with the highest enrichment factors observed for S, Cl, Se, Br, Cd and Te ( $\pm$ Li, B, Cu, As, Ag, Tl, Bi), intermediate enrichment factors observed for Na, K, Zn, Mo, Sb, Cs, W Pb, and the lowest enrichment factors observed for Al, Si,

Ca, Ti, Fe, Sr, Zr, Ba and Ce. However, the absolute range of enrichment factors determined in our experiments is significantly smaller than that determined on volcanic gas condensates. This is probably due to the lower density of fumarolic gases compared to fluids exsolved at depth, as the behavior of volatile versus non-volatile elements is more contrasting at low pressure than at high pressure. For example, a rock or magma that equilibrates with a gas phase at 1 atm loses virtually all of its contained S and Cl but hardly any Ti and Al, whereas fluids exsolving at high pressure transport comparatively more Ti and Al (e.g., Kessel et al., 2005; Hermann and Spandler, 2008). Other potential factors leading to discrepancies between our experimental data and enrichment factors determined on natural fumaroles are discussed in the supplementary material. Importantly, the trends displayed by the two data sets are very similar, which supports the idea that specific element abundances or element ratios can be used to monitor volatile fluxing events in geological samples. In the remaining sections we will discuss which elements and which type of samples may be best suited for this purpose. The ideal element should not only be highly volatile, but also occur at similar or higher concentrations in mafic magmas than in felsic magmas, as fluxing of a specific element into a felsic magma will not be recognized if this element occurs at much higher concentrations in the felsic magma anyway. Lithium, B and Tl occur at considerably higher concentrations in felsic magmas than in mafic magmas (e.g., Taylor, 1964; Parker, 1967), hence they are not suitable to monitor volatile fluxing and thus will not be considered further.

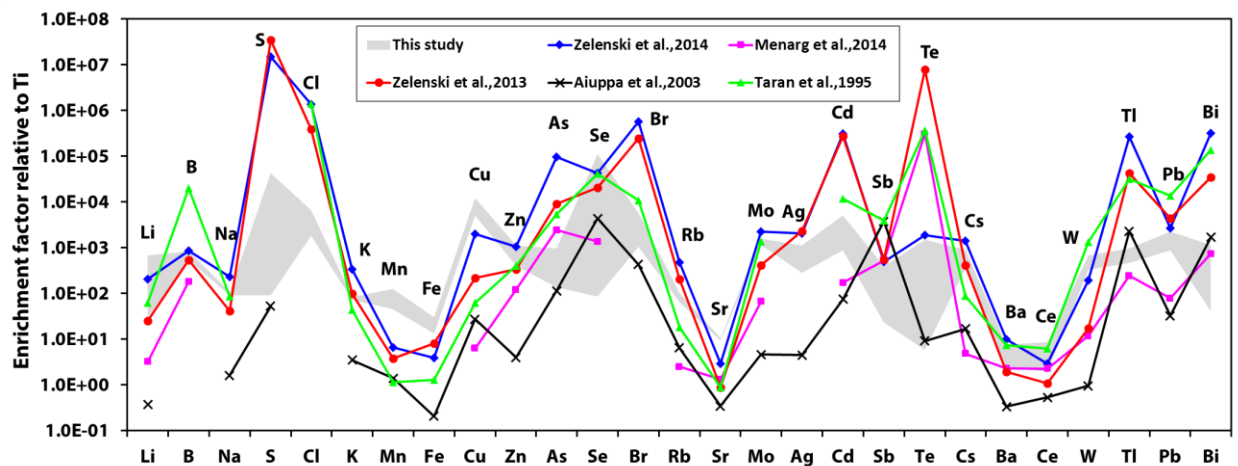


**Fig. 6.10.** Enrichment factors (EF) of elements in the fluid phase relative to the mafic source, normalized to corresponding Ti contents. Data obtained from our experiments involving synthetic fluid inclusions (gray array) are compared with data obtained from the analysis of fumarolic gases/aerosols and whole-rocks from

five arc volcanoes worldwide: Tolbachik (Zelenski et al., 2014), Erta Ale (Zelenski et al., 2013), Kudryavy (Taran et al., 1995), Lascar (Menard et al., 2014) and Etna (Aiuppa et al., 2003).

### 6.5.3. Effect of magmatic sulfides

Magmatic sulfide phases strongly sequester some of the elements that have been identified as highly volatile in this study. Depending on temperature, pressure and sulfide composition, magmatic sulfides can occur in either crystalline state (typically either monosulfide solid solution (MSS) or intermediate solid solution (ISS)) or sulfide liquid (SL) (Kullerud et al., 1969). The partitioning behavior of As, Cu, Zn, Mo, Ag, Sb, W, Pb and Bi between monosulfide solid solution, sulfide liquid and silicate melt has been studied by Li and Audétat. (2012, 2015), whereas sulfide liquid – silicate melt partition coefficients of Cu, Zn, Ag, Cd, Sb, Tl and Pb are reported by Kiseeva and Wood (2013, 2015). Sulfide liquid – silicate melt partition coefficients ( $D_{SL/SM}$ ) of Cu, Zn, Se, Ag, Cd, Te, Pb and Bi were determined on natural MORB samples by Patten et al. (2013), and partition coefficients of As, Se, Sb, Te and Bi between MSS, ISS and SL were determined by Liu and Brenan (2015). Due to the scarcity of data regarding  $D_{MSS/SM}$  partition coefficients we established an additional data set by analyzing MSS grains and coexisting rhyolite glass by LA-ICP-MS in two natural samples: (i) an obsidian sample from Clear Lake, California, that was previously studied by Stimac et al. (1994), and (ii) a vitrophyre sample from the Banco Bonito flow in the Valles Caldera, New Mexico. Details on the samples and the analytical procedure are given in the supplementary material. The results are listed in supplementary Table 6-S5, together with literature data on  $D_{MSS/SM}$ ,  $D_{SL/SM}$  and  $D_{ISS/SL}$  partition coefficients. The data suggest that Cu and Ag partition strongly into all three types of magmatic sulfides (MSS, ISS, SL). This means that the concentrations of Cu and Ag in sulfides, minerals and the silicate melt are mainly a function of the amount of sulfides present, and thus that these elements are not well suited to monitor potential additions (or losses) by means of a fluid phase. The same is true for Te if the magmatic sulfide phase is a sulfide liquid ( $D_{Te}^{SL/SM} = 1,000-17,000$ ) or ISS ( $D_{Te}^{ISS/SM} \sim 0.7 * D_{Te}^{SL/SM}$ ), and probably also for Bi if the magmatic sulfide phase is sulfide liquid ( $D_{Bi}^{SL/SM} \leq 1,000$  in mafic magmas, but up to 50,000 in cool, felsic magmas). However, it needs to be noted that reported compositions of Cu-rich sulfides in felsic magmas plot in the ISS field rather than in the sulfide liquid field at the reconstructed magma temperatures (Parat et al., 2011; Chapter in RiMG volume 73), hence sulfide liquid does not seem to be common in felsic magmas. The affinity of Bi

to sulfide phases in felsic magmas is thus probably not so high:  $D_{\text{Bi}}^{\text{MSS/SM}} = 4-6$ , and  $D_{\text{Bi}}^{\text{ISS/SM}}$  is  $<200$  based on  $D_{\text{Bi}}^{\text{MSS/ISS}}$  value of 0.04 reported in Liu and Brenan (2015). Similarly, our  $D_{\text{MSS/SM}}$  values obtained for As, Se and Cd and corresponding  $D_{\text{ISS/SM}}$  values inferred from MSS/ISS partition coefficients reported by Liu and Brenan (2015) are all below 100. The point is that sulfide – silicate melt partition coefficients smaller or equal to  $\sim 200$  are not expected to cause any depletion of these elements in the silicate melt because the sulfide content of the magma is unlikely to exceed 0.5 wt%. The concentrations of As, Se, Cd and Bi in the silicate melt (and in minerals crystallizing therefrom) thus should be largely independent on the presence/absence and the amount of magmatic sulfides. Consequently, from the group of chalcophile elements we regard these four highly volatile elements as the most promising candidates in the search of new monitors for volatile fluxing.

#### **6.5.4. Monitors of volatile fluxing**

Among the various volatile fluxing monitors used in previous studies the  $\text{CO}_2$  content of melt inclusions is probably the most robust one, as crystallizing mafic magmas always exsolve  $\text{CO}_2$ , and fluxing of  $\text{CO}_2$  into overlying felsic magma reservoirs has been confirmed by numerous studies (e.g., Saito et al., 1993; Roberge et al., 2009; Christopher et al., 2010). However, application of this monitor in fossil volcanic systems requires the availability of exceptionally well-preserved (preferentially glassy) melt inclusions, which is seldom met. Sulfur certainly gets added to overlying felsic magma reservoirs, too (e.g., Roberge et al., 2009; Christopher et al., 2010), but its concentration in the silicate melt and coexisting minerals is buffered by the precipitation of sulfides and sulfates. Hence, in the common case of sulfur-saturated magmas the total abundance of sulfur in the magma can only be monitored by the abundance of sulfides and sulfates, but not by the sulfur content of individual minerals (e.g., Streck and Dilles, 1998). For chlorine and bromine the chances to find suitable monitors are better, but the partitioning behavior of Cl into apatite (the most obvious choice regarding Cl) was shown to be a complex function of melt composition and Cl concentration of the system (Webster et al., 2009), and analysis of Br is challenging due to its very low abundance (e.g., Marks et al., 2012; Kendrick, 2012). Other elements that have previously been used to monitor addition of fluid to (or loss of fluid from) intermediate and mafic magmas are Cu and Li (Berlo et al., 2004; Kent et al., 2007; Rowe et al., 2008; Collins et al., 2009). However, as shown above, Cu abundances are strongly controlled by

the presence of magmatic sulfides, whereas Li, B and Tl are enriched in felsic magmas anyway (supplementary Table 6-S5). An additional problem with Li is that this element is rather mobile in many minerals (Zhang and Cherniak, 2010) and thus is prone for resetting. Therefore, of the 13 most volatile elements identified in this study (S, Cl, Se, Br, Cd, Te,  $\pm$ Li, B, Cu, As, Ag, Tl, Bi) the elements S, Cl, Br, Te, Li, B, Cu, Ag and Tl all do not seem to be suitable to monitor volatile fluxing because their concentration in the felsic silicate melt and coexisting minerals is either buffered, too high from begin with (compared to the mafic endmember), too low to be routinely measured (Br), or too strongly affected by the amount of sulfides present. What remains are the elements Se, Cd, As and Bi.

All these elements usually occur at very low concentrations in silicate melts (As at the ppm level; Se, Cd and Bi at sub-ppm levels; supplementary Table 6-S5), hence potential monitors should preferentially take up these elements. Obvious candidates are magmatic sulfides because  $D_{MSS/SM}$  and  $D_{ISS/SM}$  values of Se, Cd and Bi are relatively high (typically 4-10; in the case of Se even >100; supplementary Table 6-S5). Indeed, high contents of Se and Cd (plus Cu, Zn and Ag) in Cu-rich sulfides of the white pumice at Mount Pinatubo have previously been interpreted by Hattori (1993, 1996) to record volatile fluxing from underlying mafic magma. Arsenic was detected in these sulfides as well, but not at higher quantities than in the sulfides analyzed from basaltic enclaves (Hattori, 1996).

Another potentially useful mineral phase to monitor for As, Se, Cd and Bi abundances in magmas may be apatite. Arsenic is extremely compatible in apatite, as is demonstrated by a complete solid solution between  $Ca_{10}(PO_4)_6(F,OH)_2$  and  $Ca_{10}(AsO_4)_6(F,OH)_2$  (Pan and Fleet, 2002) and reports of As-rich apatite (up to 15 wt%  $AsO_4$ ) in altered lavas from the Mt. Etna region (Gianfagna et al., 2014). Under oxidizing conditions, also selenium can replace phosphorous in the apatite crystal structure (Pascher, 1963; Ma et al., 2013) and thus should be easily taken up by apatite. The same is probably true for Cd, which can completely replace Ca in the apatite structure (Pan and Fleet, 2002), and for Bi, which can be incorporated in large quantities as well (Mayer and Semadja, 1983). Therefore, all four elements that we regard as most promising to monitor volatile fluxing are compatible in apatite. To test this hypothesis we analyzed 14 apatite grains from latitic to rhyodacitic rocks associated with the porphyry Cu-Mo-Au deposits at Santa Rita, New Mexico, and Bingham Canyon, Utah, plus 2 apatite grains from a quartz-latite dike near the Questa Mine,

New Mexico. All of these rocks were saturated in anhydrite based on the presence of anhydrite inclusions within apatite-, amphibole- and quartz phenocrysts, plus remains of altered anhydrite phenocrysts in the matrix, and they show evidence for interaction with mafic magmas, hence it is possible that they became enriched in sulfur by means of volatile fluxing. The results (listed in supplementary Table 6-S6) demonstrate that the concentrations of As (1.3-3.0 ppm), Se (0.9-3.4 ppm), Cd (0.07-0.42 ppm) and Bi (0.04-0.11 ppm) in these apatites are well measurable (corresponding detection limits for a laser pit size of 50  $\mu\text{m}$ : As – 0.08 ppm; Se – 0.6 ppm; Cd – 0.05 ppm; Bi – 0.01 ppm), but due to a lack of reference data we cannot say whether these values are high compared to other magmatic apatites. In summary, of the suite of trace elements investigated in this study the best candidates for monitoring volatile fluxing in felsic magmas are As, Se, Cd and Bi because they are highly volatile but are not too strongly sequestered by magmatic sulfides. Anomalously high concentrations of these elements in a given magma may be recorded by magmatic sulfides themselves, or by their abundance in magmatic apatite.

## **6.6. Conclusions**

This study demonstrates that volatilities of various elements during fluid-mediated magma chamber processes can be experimentally determined at geologically realistic pressure and temperature conditions. In the most direct approach, fluids equilibrated with minerals and melts are trapped after a given time of equilibration in the form of synthetic fluid inclusions, and their composition can subsequently be measured by LA-ICP-MS. A more indirect but more sensitive approach is to let the fluids react with an overlying pool of felsic melt, and then determine relative volatilities by mass balance. In the present study volatilities of 33 elements ranging from Li to Bi were determined in this manner. The results agree with relative element abundances in volcanic gas condensates, but there are also certain differences, likely caused by the higher pressures prevailing in our experiments. The combined data sets suggest that S, Cl, Cu, As, Se, Br, Cd, Te, Tl and Bi are among the most volatile elements. Of those, Cu is very strongly sequestered by magmatic sulfides, and thus may be not suitable to monitor volatile fluxing. Arsenic, Se, Cd and Bi, on the other hand, are only moderately sequestered by sulfides, and thus are more promising to be utilized as indicators for volatile fluxing. They may be analyzed in magmatic sulfides (if available) and potentially also in apatite.

## 6.7. Acknowledgments

We like to thank Hans Keppler and Dan Frost for scientific advice, Raphael Njul for polishing work, and Detlef Krauß and Anke Potzel for help with the microprobe measurements. We also thank Sebastien Jégo, John Mavrogenes, and an anonymous reviewer for their thoughtful comments that greatly helped to improve the manuscript. The first author acknowledges financial support from the China Scholarship Council program.

## 6.8. References

- Aiuppa, A., Dongarrà, G., Valenza, M., Federico, C. and Pecoraino, G. (2003) Degassing of trace volatile metals during the 2001 eruption of Etna. In *Volcanism and the Earth's Atmosphere* (eds. A. Robock and C. Oppenheimer). Geophysical Monograph **139**, American Geophysical Union Washington, DC, pp. 41–54.
- Andres, R., Rose, W., Kyle, P., DeSilva, S., Francis, P., Gardeweg, M. and Roa, H.M. (1991) Excessive sulfur dioxide emissions from Chilean volcanoes. *J. Volcanol. Geotherm. Res.* **46**, 323-329.
- Audétat, A. and Pettke, T. (2006) Evolution of a porphyry-Cu mineralized magma system at Santa Rita, New Mexico (USA). *J. Petrol.* **47**, 2021-2046.
- Audétat, A. and Simon, A.C. (2013) Magmatic controls on porphyry Cu genesis. In *Geology and genesis of major copper deposits and districts of the world: a tribute to Richard Sillitoe* (eds. J. W. Hedenquist, M. Harris and F. Camus). Society of Economic Geologists Special Publication 16, 553-572.
- Berlo, K., Blundy, J., Turner, S., Cashman, K., Hawkesworth, C. and Black, S. (2004) Geochemical precursors to volcanic activity at Mount St. Helens, USA. *Science* **306**, 1167-1169.
- Bodnar, R. and Vityk, M.O. (1994) Interpretation of microthermometric data for H<sub>2</sub>O-NaCl fluid inclusions. In *Fluid Inclusions in Minerals, Methods and Applications* (eds. B. D. Vivo and M. L. Frezzotti). Virginia Tech, Blacksburg, pp. 117-130.
- Bose, K. and Ganguly, J. (1995) Quartz-coesite transition revisited; reversed experimental determination at 500-1200 °C and retrieved thermochemical properties. *Am. Mineral.* **80**, 231-238.

- Christopher T., Edmonds M., Humphreys M. C. S. and Herd R. A. (2010) Volcanic gas emissions from Soufrière Hills Volcano, Montserrat 1995-2009, with implications for mafic magma supply and degassing. *Geophys. Res. Lett.* **37**, L00E04, doi:10.1029/2009GL041325.
- Collins, S.J., Pyle, D.M. and MacLennan, J. (2009) Melt inclusions track pre-eruption storage and dehydration of magmas at Etna. *Geology* **37**, 571-574.
- Davis, L.L. and Smith, D. (1993) Ni-rich olivine in minettes from Two Buttes, Colorado: A connection between potassic melts from the mantle and low Ni partition coefficients. *Geochim. Cosmochim. Acta* **57**, 123-129.
- Davis, L.L., Smith, D., McDowell, F.W., Walker, N.W. and Borg, L.E. (1996) Eocene potassic magmatism at Two Buttes, Colorado, with implications for Cenozoic tectonics and magma generation in the western United States. *Geol. Soc. Am. Bull.* **108**, 1567-1579.
- De Hoog, J., Hattori, K. and Hoblitt, R. (2004) Oxidized sulfur-rich mafic magma at Mount Pinatubo, Philippines. *Contrib. Mineral. Petrol.* **146**, 750-761.
- Eichelberger, J.C. (1980) Vesiculation of mafic magma during replenishment of silicic magma reservoirs. *Nature* **288**, 446-450.
- Gianfagna, A., Mazziotti-Tagliani, S., Croce, A., Allegrina, M. and Rinaudo, C. (2014) As-rich apatite from Mt. Calvario: Characterization by Micro-Raman spectroscopy. *Can. Mineral.* **52**, 799-808.
- Günther, D., Audétat, A., Frischknecht, R. and Heinrich, C.A. (1998) Quantitative analysis of major, minor and trace elements in fluid inclusions using laser ablation inductively coupled plasma mass spectrometry. *J. Anal. At. Spectrom.* **13**, 263-270.
- Halama, R., Boudon, G., Villemant, B., Joron, J.L., Le Friant, A. and Komorowski, J.C. (2006) Pre-eruptive crystallization conditions of mafic and silicic magmas at the Plat Pays volcanic complex, Dominica (Lesser Antilles). *J. Volcanol. Geotherm. Res.* **153**, 200-220.
- Halter, W.E., Heinrich, C.A. and Pettke, T. (2005) Magma evolution and the formation of porphyry Cu–Au ore fluids: evidence from silicate and sulfide melt inclusions. *Mineral. Deposita* **39**, 845-863.
- Hattori, K. (1993) High-sulfur magma, a product of fluid discharge from underlying mafic magma: evidence from Mount Pinatubo, Philippines. *Geology* **21**, 1083-1086.

- Hattori, K. (1996) Occurrence and origin of sulfide and sulfate in the 1991 Mount Pinatubo eruption products. In *Fire and Mud: Eruptions and Lahars of Mount Pinatubo, Philippines* (eds. C.G. Newhall, R.S. Punongbayan). University of Washington Press, pp. 807–824.
- Hattori, K.H. and Keith, J.D. (2001) Contribution of mafic melt to porphyry copper mineralization: evidence from Mount Pinatubo, Philippines, and Bingham Canyon, Utah, USA. *Mineral. Deposita* **36**, 799-806.
- Heinrich, C.A., Pettke, T., Halter, W.E., Aigner-Torres, M., Audétat, A., Günther, D., Hattendorf, B., Bleiner, D., Guillong, M. and Horn, I. (2003) Quantitative multi-element analysis of minerals, fluid and melt inclusions by laser-ablation inductively-coupled-plasma mass-spectrometry. *Geochim. Cosmochim. Acta* **67**, 3473-3497.
- Hermann, J. and Spandler, C.J. (2008) Sediment melts at sub-arc depths: an experimental study. *J. Petrol.* **49**, 717-740.
- Jochum, K.P., Weis, U., Stoll, B., Kuzmin, D., Yang, Q., Raczek, I., Jacob, D.E., Stracke, A., Birbaum, K., Frick, D.A., Günther, D. and Enzweiler, J. (2011) Determination of Reference Values for NIST SRM 610-617 Glasses Following ISO Guidelines. *Geostand. Geoanal. Res.* **35**, 397-429.
- Kaneko, K., Kamata, H., Koyaguchi, T., Yoshikawa, M. and Furukawa, K. (2007) Repeated large-scale eruptions from a single compositionally stratified magma chamber: An example from Aso volcano, Southwest Japan. *J. Volcanol. Geotherm. Res.* **167**, 160-180.
- Keith, J., Whitney, J., Hattori, K., Ballantyne, G., Christiansen, E., Barr, D., Cannan, T. and Hook, C. (1997) The role of magmatic sulfides and mafic alkaline magmas in the Bingham and Tintic mining districts, Utah. *J. Petrol.* **38**, 1679-1690.
- Kendrick, M.A. (2012) High precision Cl, Br and I determinations in mineral standards using the noble gas method. *Chem. Geol.* **292-293**, 116-126.
- Kendrick, M.A., Arculus, R., Burnard, P. and Honda, M. (2013) Quantifying brine assimilation by submarine magmas: Examples from the Galápagos Spreading Centre and Lau Basin. *Geochim. Cosmochim. Acta* **123**, 150-165.
- Kent, A.J.R., Blundy, J., Cashman, K.V., Cooper, K.M., Donnelly, C., Pallister, J.S., Reagan, M., Rowe, M.C. and Thornber, C.R. (2007) Vapor transfer prior to the October 2004 eruption of Mount St. Helens, Washington. *Geology* **35**, 231.

- Kessel, R., Schmidt, M.W., Ulmer, P. and Pettke, T. (2005) Trace element signature of subduction-zone fluids, melts and supercritical liquids at 120–180 km depth. *Nature* **437**, 724-727.
- Kiseeva, E.S. and Wood, B.J. (2013) A simple model for chalcophile element partitioning between sulphide and silicate liquids with geochemical applications. *Earth Planet. Sci. Lett.* **383**, 68-81.
- Kiseeva, E.S. and Wood, B.J. (2015) The effects of composition and temperature on chalcophile and lithophile element partitioning into magmatic sulphides. *Earth Planet. Sci. Lett.* **424**, 280-294.
- Koyaguchi, T. (1986) Life-time of a stratified magma chamber recorded in ultramafic xenoliths from Ichinomegata volcano, northeastern Japan. *Bull. Volcanol.* **48**, 313-323.
- Kullerud, G., Yund, R. and Moh, G. (1969) Phase relations in the Cu-Fe-S, Cu-Ni-S and Fe-Ni-S systems. In *Magmatic Ore Deposits* (eds. H.D.B Wilson). Econ. Geol. Monogr. **4**, pp. 232–243.
- Lepel, E., Stefansson, K. and Zoller, W. (1978) The enrichment of volatile elements in the atmosphere by volcanic activity: Augustine volcano 1976. *J. Geophys. Res.* **83**, 6213-6220.
- Lerchbaumer, L. and Audétat, A. (2012) The quartz capsule - a new method to avoid alloying problems with noble-metal capsules in hydrothermal experiments. *Eur. J. Mineral.* **24**, 683-693.
- Li, Y. and Audétat, A. (2009) A method to synthesize large fluid inclusions in quartz at controlled times and under unfavorable growth conditions. *Am. Mineral.* **94**, 367-371.
- Li, Y. and Audétat, A. (2012) Partitioning of V, Mn, Co, Ni, Cu, Zn, As, Mo, Ag, Sn, Sb, W, Au, Pb, and Bi between sulfide phases and hydrous basanite melt at upper mantle conditions. *Earth Planet. Sci. Lett.* **355**, 327-340.
- Li, Y. and Audétat, A. (2015) Effects of temperature, silicate melt composition, and oxygen fugacity on the partitioning of V, Mn, Co, Ni, Cu, Zn, As, Mo, Ag, Sn, Sb, W, Au, Pb, and Bi between sulfide phases and silicate melt. *Geochim. Cosmochim. Acta* **162**, 25-45.
- Liu, Y. and Brenan, J. (2015) Partitioning of platinum-group elements (PGE) and chalcogens (Se, Te, As, Sb, Bi) between monosulfide-solid solution (MSS), intermediate solid solution (ISS) and sulfide liquid at controlled  $f_{O_2}$ – $f_{S_2}$  conditions. *Geochim. Cosmochim. Acta* **159**, 139-161.
- Luhr, J.F. (2008) Primary igneous anhydrite: Progress since its recognition in the 1982 El Chichón trachyandesite. *J. Volcanol. Geotherm. Res.* **175**, 394-407.

- Ma, J., Wang, Y., Zhou, L. and Zhang, S. (2013) Preparation and characterization of selenite substituted hydroxyapatite. *Mater Sci Eng C Mater Biol Appl* **33**, 440-445.
- Marks, M.A.W., Wenzel, T., Whitehouse, M.J., Loose, M., Zack, T., Barth, M., Worgard, L., Krasz, V., Eby, G.N., Stosnach, H. and Markl, G. (2012) The volatile inventory (F, Cl, Br, S, C) of magmatic apatite: An integrated analytical approach. *Chem. Geol.* **291**, 241-255.
- Matthews, W., Linnen, R.L. and Guo, Q. (2003) A filler-rod technique for controlling redox conditions in cold-seal pressure vessels. *Am. Mineral.* **88**, 701-707.
- Matthews, S., Sparks, R. and Gardeweg, M. (1999) The Piedras Grandes–Soncor eruptions, Lascar volcano, Chile; evolution of a zoned magma chamber in the central Andean upper crust. *J. Petrol.* **40**, 1891-1919.
- Mayer, I. and Semadja, A. (1983) Bismuth-substituted calcium, strontium, and lead apatites. *J. Solid State Chem.* **46**, 363-366.
- Menard, G., Moune, S., Vlastelic, I., Aguilera, F., Valade, S., Bontemps, M. and Gonzalez, R. (2014) Gas and aerosol emissions from Lascar volcano (Northern Chile): Insights into the origin of gases and their links with the volcanic activity. *J. Volcanol. Geotherm. Res.* **287**, 51-67.
- Métrich, N. and Clochiatti, R. (1996) Sulfur abundance and its speciation in oxidized alkaline melts. *Geochim. Cosmochim. Acta* **60**, 4151-4160.
- Moune, S., Gauthier, P.-J. and Delmelle, P. (2010) Trace elements in the particulate phase of the plume of Masaya Volcano, Nicaragua. *J. Volcanol. Geotherm. Res.* **193**, 232-244.
- Pallister, J.S., Hoblitt, R.P., Meeker, G.P., Knight, R.J. and Siems, D.F. (1996) Magma mixing at Mount Pinatubo: petrographic and chemical evidence from the 1991 deposits, In *Fire and mud: eruptions and lahars of Mount Pinatubo, Philippines* (eds. C.G. Newhall and R.S. Punongbayan). Washington Press, Seattle, WA, pp. 687-731.
- Pallister, J.S., Hoblitt, R.P. and Reyes, A.G. (1992) A basalt trigger for the 1991 eruptions of Pinatubo Volcano? *Nature* **356**, 426-428.
- Pan, Y. and Fleet, M.E. (2002) Compositions of the apatite-group minerals: substitution mechanisms and controlling factors. *Rev. Mineral. Geochem.* **48**, 13-49.
- Parat, F., Holtz, F. and Streck, M.J. (2011) Sulfur-bearing Magmatic Accessory Minerals. *Rev. Mineral. Geochem.* **73**, 285-314.

- Parker, R.L. (1967) Composition of the Earth's crust. In *Data of Geochemistry, Sixth Edition* (ed. Fleischer, M.). U.S. Geological Survey Professional Paper **440-D**, 1-19.
- Pascher, F. (1963) Untersuchungen über die Austauschbarkeit des Phosphors durch Chrom, Selen, Molybdän, Wolfram und Titan im Apatitgitter. Springer.
- Patten, C., Barnes, S.-J., Mathez, E.A. and Jenner, F.E. (2013) Partition coefficients of chalcophile elements between sulfide and silicate melts and the early crystallization history of sulfide liquid: LA-ICP-MS analysis of MORB sulfide droplets. *Chem. Geol.* **358**, 170-188.
- Richer, M., Mann, C.P. and Stix, J. (2004) Mafic magma injection triggers eruption at Ilopango Caldera, El Salvador, Central America, In *Natural hazards in El Salvador: Boulder, Colorado* (eds. W.I. Rose, J.J. Bommer, D.L. López, M.J. Carr and J.J. Major). Geological Society of America Special Papers 375, pp. 175-190.
- Riehle, J.R., Champion, D.E., Brew, D.A. and Lanphere, M.A. (1992) Pyroclastic deposits of the Mount Edgecumbe volcanic field, southeast Alaska: eruptions of a stratified magma chamber. *J. Volcanol. Geotherm. Res.* **53**, 117-143.
- Roberge J., Delgado-Granados H. and Wallace P. J. (2009) Mafic magma recharge supplies high CO<sub>2</sub> and SO<sub>2</sub> gas fluxes from Popocatepétl volcano, Mexico. *Geology* **37**, 107-110.
- Rowe, M.C., Kent, A.J.R. and Thornber, C.R. (2008) Using amphibole phenocrysts to track vapor transfer during magma crystallization and transport: An example from Mount St. Helens, Washington. *J. Volcanol. Geotherm. Res.* **178**, 593-607.
- Roberge, J., Delgado-Granados, H. and Wallace, P.J. (2009) Mafic magma recharge supplies high CO<sub>2</sub> and SO<sub>2</sub> gas fluxes from Popocatepetl volcano, Mexico. *Geology* **37**, 107-110.
- Saito G., Kazahaya K. and Shinohara H. (2003) Volatile evolution of Satsuma-Iwojima volcano: degassing process and mafic-felsic interaction In *Melt inclusions in volcanic systems - Methods, applications and problems* (eds. B. De Vivo and R. J. Bodnar). Elsevier.
- Seo, J.H., Guillong, M., Aerts, M., Zajacz, Z. and Heinrich, C.A. (2011) Microanalysis of S, Cl, and Br in fluid inclusions by LA-ICP-MS. *Chem. Geol.* **284**, 35-44.
- Spilliaert, N., Allard, P., Métrich, N. and Sobolev, A. (2006) Melt inclusion record of the conditions of ascent, degassing, and extrusion of volatile-rich alkali basalt during the powerful 2002 flank eruption of Mount Etna (Italy). *J. Geophys. Res.* **111**, B04203, doi:10.1029/2005JB003934.

- Stern, C.R., Funk, J.A., Skewes, M.A. and Arévalo, A. (2007) Magmatic anhydrite in plutonic rocks at the El Teniente Cu-Mo deposit, Chile, and the role of sulfur-and copper-rich magmas in its formation. *Econ. Geol.* **102**, 1335-1344.
- Stimac, J. and Hickmott, D. (1994) Trace-element partition coefficients for ilmenite, orthopyroxene and pyrrhotite in rhyolite determined by micro-PIXE analysis. *Chem. Geol.* **117**, 313-330.
- Streck, M.J. and Dilles, J.H. (1998) Sulfur evolution of oxidized arc magmas as recorded in apatite from a porphyry copper batholith. *Geology* **26**, 523-526.
- Symonds, R.B., Rose, W.I., Reed, M.H., Lichte, F.E. and Finnegan, D.L. (1987) Volatilization, transport and sublimation of metallic and non-metallic elements in high temperature gases at Merapi Volcano, Indonesia. *Geochim. Cosmochim. Acta* **51**, 2083-2101.
- Taran, Y.A., Hedenquist, J., Korzhinsky, M., Tkachenko, S. and Shmulovich, K. (1995) Geochemistry of magmatic gases from Kudryavy volcano, Iturup, Kuril Islands. *Geochim. Cosmochim. Acta* **59**, 1749-1761.
- Taylor, S. (1964) Trace element abundances and the chondritic earth model. *Geochim. Cosmochim. Acta* **28**, 1989-1998.
- Vigouroux, N., Wallace, P.J. and Kent, A.J. (2008) Volatiles in high-K magmas from the western Trans-Mexican Volcanic Belt: evidence for fluid fluxing and extreme enrichment of the mantle wedge by subduction processes. *J. Petrol.* **49**, 1589-1618.
- Wallace, P.J. and Edmonds, M. (2011) The sulfur budget in magmas: evidence from melt inclusions, submarine glasses, and volcanic gas emissions. *Rev. Mineral. Geochem.* **73**, 215-246.
- Webster, J.D., Tappen, C.M. and Mandeville, C.W. (2009) Partitioning behavior of chlorine and fluorine in the system apatite–melt–fluid. II: Felsic silicate systems at 200MPa. *Geochim. Cosmochim. Acta* **73**, 559-581.
- Wiebe, R.A. (2016) Mafic replenishments into floored silicic magma chambers. *Am. Mineral.* **101**, 297-310.
- Williams-Jones, A.E. and Heinrich, C.A. (2005) 100th Anniversary special paper: vapor transport of metals and the formation of magmatic-hydrothermal ore deposits. *Econ. Geol.* **100**, 1287-1312.

Zelenski, M., Malik, N. and Taran, Y. (2014) Emissions of trace elements during the 2012–2013 effusive eruption of Tolbachik volcano, Kamchatka: enrichment factors, partition coefficients and aerosol contribution. *J. Volcanol. Geotherm. Res.* **285**, 136-149.

Zelenski, M.E., Fischer, T.P., de Moor, J.M., Marty, B., Zimmermann, L., Ayalew, D., Nekrasov, A.N. and Karandashev, V.K. (2013) Trace elements in the gas emissions from the Erta Ale volcano, Afar, Ethiopia. *Chem. Geol.* **357**, 95-116.

Zhang, Y. and Cherniak, D.J. (2010) Diffusion in minerals and melts. *Rev. Mineral. Geochem.* **72**.

### 6.9. Supplementary material

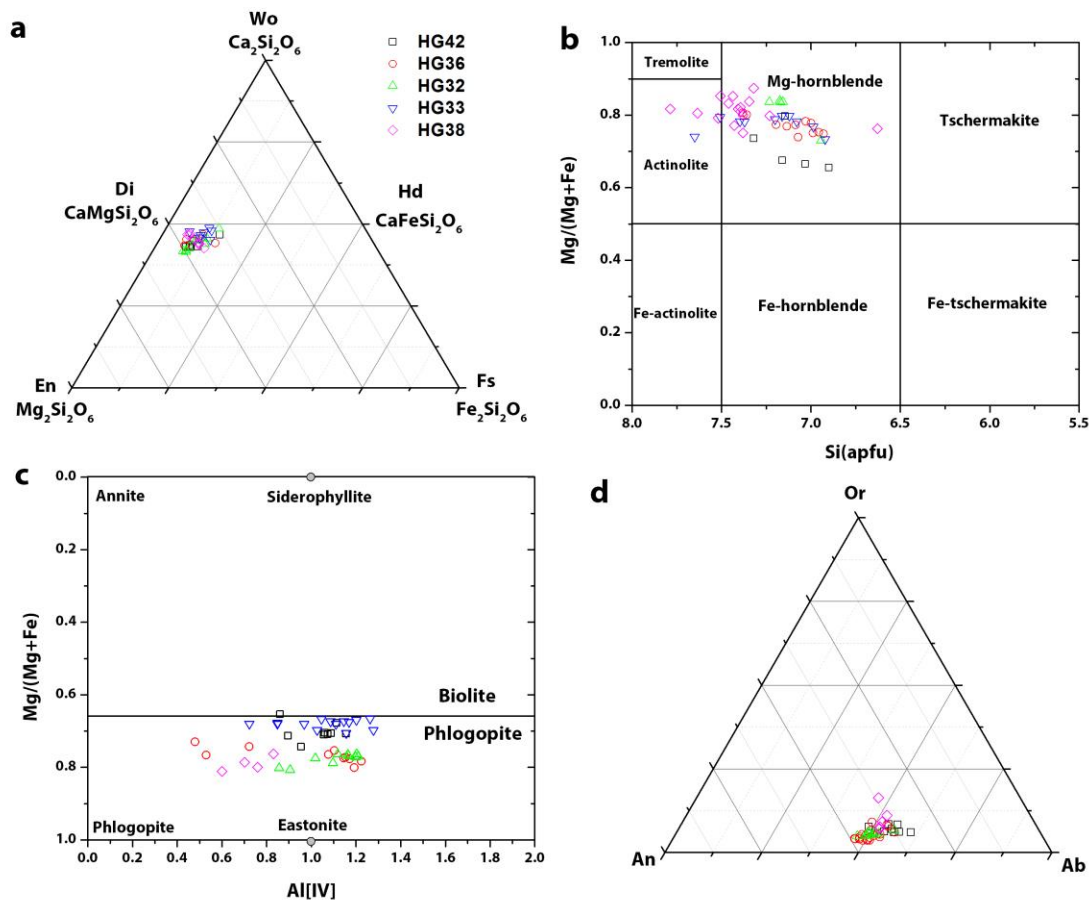


**Fig. 6-S1.** Compositions of minerals analyzed by electron microprobe. (a) Plot of pyroxene compositions in the En-Wo-Fs diagram (En—enstatite, Wo—wollastonite, Fs—ferrosilite, Di—diopside, Hd—hedenbergite); (b) Amphibole compositions in the classification diagram for amphiboles with atomic content of  $Ca_B > 1.5$  and  $(Na+K)_A < 0.5$  (Leake et al., 1997); (c) Phlogopite compositions; (d) Feldspar compositions plotted in the Ab-An-Or diagram (Ab—albite, An—anorthite, Or—orthoclase).

### 6.9.1. Potential other reasons for the discrepancies between our experimental data and enrichment factors determined on natural fumarole condensates

A potential way to obtain artificially low enrichment factors in our experiments is by incomplete removal of fluid components from the mafic residue after quenching. If parts of the fluid content are still present in the mafic residue and are ablated together with the mafic residue, calculated enrichment factors for fluid-mobile elements will be too low. In the extreme scenario that all solutes of the fluid are still present in the mafic residue (i.e., that only H<sub>2</sub>O evaporated), then the calculated enrichment factors cannot exceed 100 if the fluid content of the charge is 1 wt%, or they cannot exceed 20 if the fluid content is 5 wt%. To test whether our results were affected by this problem we washed the mafic residues of two samples and re-analyzed them. More precisely, the mafic residues were ground to fine powder and then split in two parts. One part was boiled for 30 minutes at 80 °C in distilled water, and the other part in a similar manner in diluted hydrochloric acid (5 wt% HCl), followed by washing it twice in hot distilled water. After this treatment the powders were dried, pressed to dense pellets, and then analyzed by LA-ICP-MS. The results are shown in supplementary Table 6-S3 and supplementary Fig. 6-S2. Most element concentrations in the washed powers are very similar to those in the untreated powders, suggesting that the amount of fluid components remaining in untreated powders was small. Consistently lower sulfur contents in the washed powders are probably due to dissolution of anhydrite, which was optically observed only in one run, but may in fact have been present in all of them. We thus conclude that the fluid–rock partition coefficients and enrichment factors calculated from untreated samples are robust.

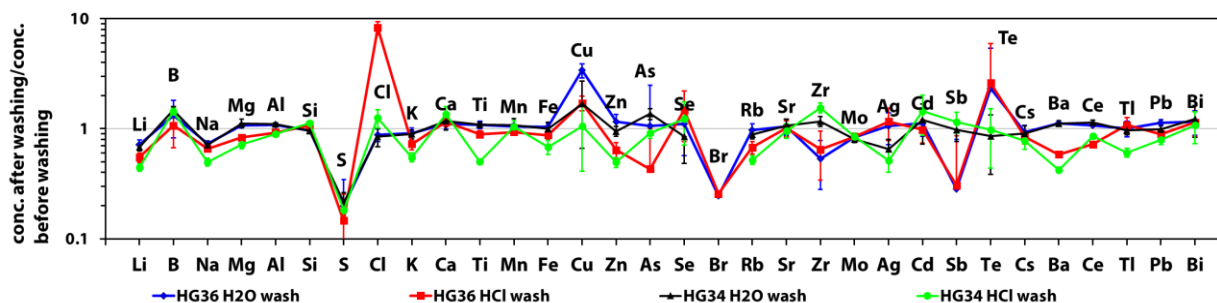


**Fig. 6-S2.** Concentration of mafic residues after washing them in H<sub>2</sub>O or diluted HCl solution, relative to the element concentrations measured before washing.

Another potential reason for discrepancies between our experimental results and data obtained from fumarole condensates is that element ratios were affected by vapor–brine fractionation. In our experiments the fluid was single-phase, whereas the fluids emanating from fumaroles are low-density vapors after extensive fractionation of brine. In order to see how element ratios change during vapor–brine separation we determined vapor–brine partition coefficients for the entire suite of trace elements investigated in this study. For this purpose, three experiments were conducted using the quartz capsule method described in Lerchbaumer and Audétat (2012). One run (HG48) was performed at 2.3 kbar in the single-phase fluid field to check how well the concentrations measured in the fluid inclusions agree with those of the starting solution. Two other runs (HG49 and HG50) were conducted at 800 °C and 1.3 kbar, at which conditions the fluid was in the two-phase field. In all cases the capsules were prepared as follows: first, minor amounts of Ag<sub>2</sub>O, MoS<sub>2</sub>, PbCl<sub>2</sub> and elemental Bi were loaded into the quartz beaker, then a 1×1.8×10 mm etched quartz was inserted, then equal amounts of solutions A, B and C were inserted, and in the end NaCl powder was added. The quartz beaker was then closed with a neatly fitting plug of SiO<sub>2</sub> glass and a lid of quartz which sealed onto the quartz beaker during the experiment. The entire setup was sealed into gold tubing with 5.0 mm O.D. and 4.6 mm I.D. Microthermometric data suggest that the fluid in the two lower-pressure experiments split into ~85 wt% vapor with a salinity of 1.4–2.2 wt% NaCl<sub>equiv</sub> and ~15 wt% brine with a salinity of 13.6–18.6 wt% NaCl<sub>equiv</sub>. Both types of fluid inclusions were analyzed by LA-ICP-MS. The results of the single-phase fluid experiment agree reasonably well with the concentrations in the starting fluid (except for boron; Fig. 6-S3a and Table 6-S4; Ag, Mo, Pb and Bi were added as excess solids and thus cannot be compared), suggesting that alloying problems with the outer gold capsule were effectively minimized. The fact that most values in Fig. 6-S3a plot slightly below unity may be caused by the addition of NaCl in solid form. If any solution left the quartz capsule before the lid was closed, the true Na content of the remaining fluid would have been slightly higher than the value that was used as internal standard, and the calculated concentrations of all other elements thus would have become slightly too low. The results of the two experiments conducted in the two-phase field (Fig. 6-S3b; Table 6-S4) suggest that B, As, Se and Sb (and potentially S, Br, Mo, Bi) had a greater affinity towards the vapor phase than the other elements but may not have reached vapor/brine partition coefficients greater than unity. Fractionation of these elements from the remaining elements is likely enhanced at lower pressures and/or during open-system vapor–brine separation. However, the largest discrepancies

between our experimentally determined enrichment factors and those determined on fumarole condensates are actually observed for S, Cl, Te, Tl and Bi, i.e., elements that did not significantly fractionate in our vapor–brine partitioning experiments. Therefore, vapor-brine fractionation does not seem to be the cause of the observed discrepancies.

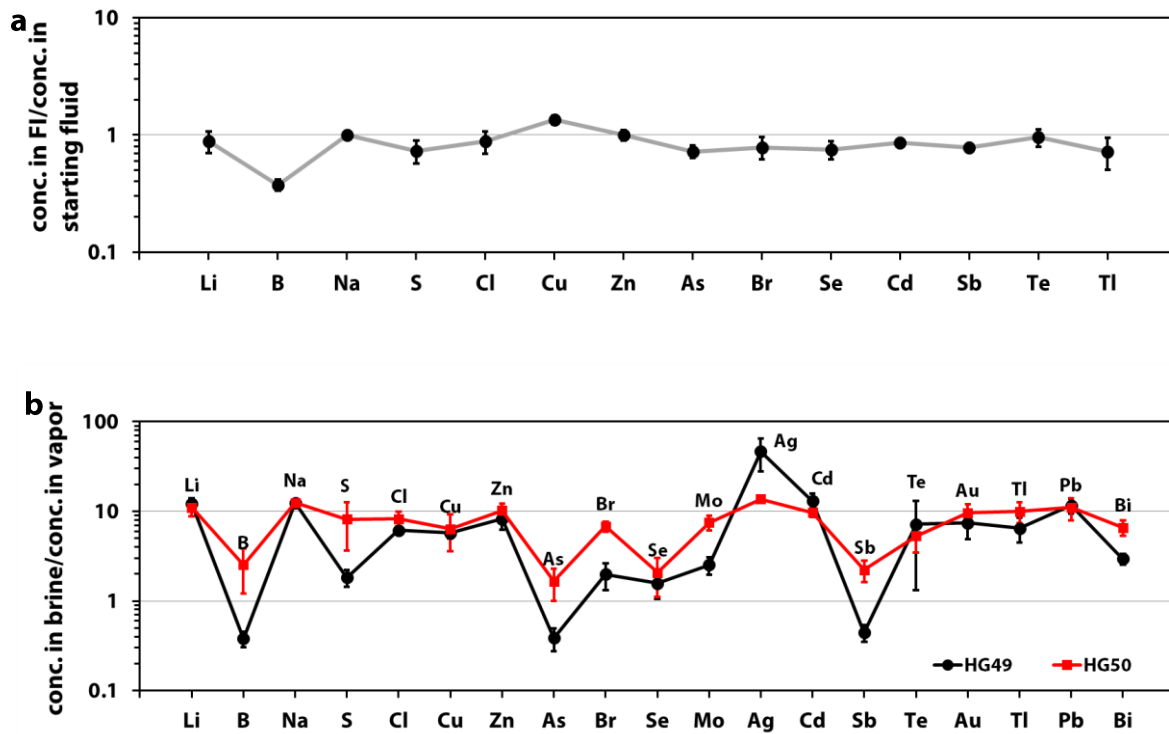


**Fig. 6-S3.** (a) Composition of fluid inclusions trapped in the single-phase field vs. that of the starting fluid (HG48). (b) Partition coefficients between brine and vapor in two experiments performed in the two-phase field (HG49 + HG50).

Apart from the contrast in fluid density, which we think is the main reason for the observed differences, the following additional factors may have played a role: (1) differences in the chemistry of the rocks that equilibrated with the fluid; (2) differences in the major element chemistry of the fluid (for example, our fluids did not contain CO<sub>2</sub>, but this should have only a minor effect on metal solubilities – see Kokh et al., 2015); and (3) the presence of magmatic sulfides.

### 6.9.2. Determination of MSS/SM partition coefficients in natural rhyolite samples

The obsidian from Clear Lake, California, has been described in detail by Stimac and Hickmott (1994). It contains (micro)-phenocrysts of plagioclase, orthopyroxene, ilmenite and pyrrhotite (MSS) in a glassy matrix. Estimated formation conditions are  $930\pm 60$  °C and  $\log f_{\text{O}_2} \sim \text{FMQ} + 0.5$  ( $\pm 0.5$ ). The Banco Bonito vitrophyre from the Valles Caldera, New Mexico, has been described in detail in Eichler (2012) and contains (micro)-phenocrysts of plagioclase, biotite, amphibole, sanidine, orthopyroxene, clinopyroxene, quartz, ilmenite, magnetite, zircon, apatite and pyrrhotite (MSS) in a glassy matrix. Its estimated formation conditions are  $780\pm 30$  °C and  $\log f_{\text{O}_2} \sim \text{FMQ} + 2.0$  ( $\pm 1.0$ ). In both samples, entire, unexposed MSS crystals were drilled out of the surrounding glass by LA-ICP-MS, and original compositions computed by subtracting co-ablated host until no Na was left in the signal and then normalizing the sum of S, Fe, Cu, Mn and Ni to 100 wt%. Similarly, the composition of the silicate glass was calculated by normalizing the sum of all major element oxides to 100 wt%. Calculated MSS-SM partition coefficients are tabulated in supplementary Table 6-S5.

### 6.9.3. References

Eichler, C.M. (2012) Petrogenesis of the East Fork Member Rhyolites, Valles Caldera, New Mexico. MSc. thesis, University of Las Vegas.

Kokh, M., Pokrovski, G., Akinfiyev, N., Guillaume, D., Salvi, S. (2015). The effect of CO<sub>2</sub> on metal transport and fractionation by geological fluids. Abstract of the 25th anniversary Goldschmidt Conference held in Prague, Czech Republic.

Leake, B.E., Woolley, A.R., Arps, C.E., Birch, W.D., Gilbert, M.C., Grice, J.D., Hawthorne, F.C., Kato, A., Kisch, H.J. and Krivovichev, V.G. (1997) Nomenclature of amphiboles; report of the subcommittee on amphiboles of the International Mineralogical Association, Commission on New Minerals and Mineral Names. *Can. Mineral.* **35**, 219-246.

**Table 6-S1**

Compositions of the three aqueous solutions that were used in the experiments.

Solution No.	Components	Concentrations
A	H <sub>2</sub> SO <sub>4</sub> , HCl, LiCl, CuCl <sub>2</sub> , ZnCl <sub>2</sub> , CdCl <sub>2</sub> , SbCl <sub>3</sub>	S ~10wt%, Cl ~6.6wt%, Li,Cu,Zn,Cd,Sb ~3000 ppm each
B	H <sub>2</sub> SO <sub>4</sub> , HCl, Na <sub>2</sub> SeO <sub>3</sub> ·5H <sub>2</sub> O, Na <sub>2</sub> TeO <sub>4</sub> , NaBr	S ~10wt%, Cl ~6.6wt%, Br ~0.5wt%, Se, Te ~3000 ppm each
C	H <sub>3</sub> BO <sub>3</sub> , As <sub>3</sub> O <sub>5</sub> , TlCl	B, As, Tl ~3000 ppm each

**Table 6-S2**

Logarithmic values (log) of calculated element extraction efficiencies

	HG42	$\delta$	HG47	$\delta$
Li	0.45	0.07	0.69	0.07
B	0.4	0.17	0.07	0.02
Na	0.02	0.001	0.05	0.002
Mg	0.01	0.0005	0.06	0.003
Al	0.02	0.001	0.03	0.001
Si	0.02	0.0002	0.004	0.0001
S	0.81	0.37	0.6	0.33
Cl	0.54	0.1	0.2	0.05
K	0.22	0.01	0.19	0.01
Ca	0.02	0	0.07	0.004
Ti	0.04	0.002	0.0026	0.0002
Mn	0.05	0.0032	0.05	0.002
Fe	0.01	0.0004	0.04	0.002
Cu	0.22	0.1	2.6	1
Zn	0.23	0.05	0.23	0.02
As	0.38	0.3	0.57	0.29
Se	0.39	0.28	0.89	0.62
Br	n.a.	n.a.	0.57	0.19
Rb	0.22	0.02	0.26	0.03
Sr	0.21	0.02	0.19	0.01
Zr	0.03	0.008	0.03	0.004
Mo	0.12	0.03	0.05	0.01
Ag	0.35	0.21	0.86	0.18
Cd	0.61	0.26	0.44	0.15
Sb	1.3	1.2	0.18	0.06
Te	0.47	0.66	1.2	1.1
Cs	0.37	0.05	0.47	0.07
Ba	0.033	0.002	0.05	0
Ce	0.016	0.001	0.02	0
W	0.5	0.26	0.46	0.2
Tl	0.72	0.23	0.77	0.15
Pb	0.24	0.05	0.33	0.06
Bi	0.33	0.13	0.31	0.07

Abbreviations:  $\delta$  – 1 sigma standard deviation of the measurements.**Table 6-S3**Composition of rock powders after washing in H<sub>2</sub>O or diluted HCl solution.

Sample No.	HG34 H <sub>2</sub> O	HG34 HCl	HG36 H <sub>2</sub> O	HG36 HCl
wt%				
Na <sub>2</sub> O	1.8	1.2	1.8	1.7
MgO	8.5	5.5	8.6	6.7
Al <sub>2</sub> O <sub>3</sub>	14	11.5	14	11.8
SiO <sub>2</sub>	54.2	63.6	53.6	59.7
K <sub>2</sub> O	4.8	3	4.7	3.7
CaO	8.6	10	9	9.4
FeO <sub>T</sub>	6.9	4.7	7.1	6
TiO <sub>2</sub>	1.2	0.5	1.2	1
S	0.054	0.046	0.043	0.032
Cl	0.18	0.27	0.18	1.7
ppm				
Li	37	24	40	31
B	48	46	48	39
Mn	930	900	950	850
Cu	2.1	1.3	3.9	2
Zn	130	69	150	85
As	53	36	69	28
Se	22	32	30	41
Br	16	13	43	45
Rb	150	88	150	107
Sr	1000	940	1100	1000
Zr	610	810	430	530
Mo	40	42	27	28
Ag	0.11	0.09	0.23	0.25
Cd	11	13	13	11
Sb	24	28	31	34
Te	36	41	58	64
Cs	17	14	15	13
Ba	1400	540	1400	740
Ce	120	90	120	78
W	21	42	62	330
Tl	41	26	46	50
Pb	55	44	58	46
Bi	13	12	16	15

**Table 6-S4**

Results of vapor–brine partitioning experiments

Exp No.	starting fluid	HG48		HG49						HG50					
		scrit.	$\delta$	brine	$\delta$	vapor	$\delta$	$D_{\text{brine/vapor}}$	$\delta$	brine	$\delta$	vapor	$\delta$	$D_{\text{brine/vapor}}$	$\delta$
Li	860	760	160	3600	500	280	16	13	2	2300	160	430	79	5.3	1.1
B	760	290	31	225	19	550	98	0.41	0.08	190	18	160	79	1.2	0.6
Na	3.5	3.5	0	18.6	2.1	1.4	0.9	13	8.7	13.6	0.3	2.2	0.3	6.1	0.7
S	5.7	4.2	0.9	9.2	0.4	4.7	1	2	0.4	12	1.5	3.1	1.7	3.9	2.2
Cl	3.8	3.3	0.7	13.6	1	2.1	0.1	6.6	0.7	8.9	1.1	2.2	0.4	4	0.8
Cu	860	1200	110	2400	170	390	45	6.2	0.8	3000	140	980	430	3.1	1.4
Zn	860	850	84	2900	60	330	79	8.9	2.1	2500	120	510	93	4.9	0.9
As	760	550	69	380	70	920	200	0.4	0.1	320	53	400	150	0.8	0.3
Br	4400	3500	740	9900	420	4600	1500	2.1	0.7	7200	870	2200	95	3.3	0.4
Se	860	650	110	170	58	100		1.7	0.6	490	58	480	220	1	0.5
Mo	sat.	520	86	2900	200	1100	220	2.7	0.6	1200	75	330	59	3.6	0.7
Ag	sat.	2100	790	2200	120	44	18	50	20	8900	420	1300	84	6.6	0.5
Cd	860	740	50	2400	45	170	37	14	3	2300	110	490	49	4.7	0.5
Sb	860	670	29	380	37	790	150	0.5	0.1	390	45	370	88	1.1	0.3
Te	860	820	140	1200	69	158	130	7.8	6.3	1400	77	550	190	2.6	0.9
Au	sat.	4100	2500	10300	2100	1300	360	8	2.7	8200	1800	1800	210	4.7	1.2
Tl	760	550	170	2700	220	390	120	7	2.2	2000	92	420	110	4.8	1.3
Pb	sat.	3700	490	4100	280	330	57	13	2.3	18000	2000	3400	870	5.3	1.5
Bi	sat.	6400	740	11800	660	3700	450	3.2	0.4	19800	1200	6200	1200	3.2	0.6

Na, S and Cl concentrations are reported in wt%; all other elements in ppm.

Abbreviations:  $\delta$  – 1 sigma standard deviation of the measurements.

**Table 6-S5**

Summary of sulfide–silicate melt partition coefficients and element abundances in felsic vs. mafic magmas

	Banco Bonito Obsidian			Clear Lake Obsidian			Li '15 <sup>b</sup>	Brenan '15 <sup>c</sup>	Patten '13 <sup>d</sup>	Brenan '15 <sup>c</sup>	Li '15 <sup>b</sup>	Kiseeva '13 <sup>e</sup>	Liu '15 <sup>f</sup>	Liu '15 <sup>f</sup>	Taylor '64 <sup>g</sup>	Taylor '64 <sup>g</sup>
	D <sub>MSS/SM</sub>		δ	D <sub>MSS/SM</sub>		δ	D <sub>MSS/SM</sub>	D <sub>MSS/SM</sub>	D <sub>SL/SM</sub>	D <sub>SL/SM</sub>	D <sub>SL/SM</sub>	D <sub>SL/SM</sub>	D <sub>ISS/SL</sub>	D <sub>MSS/ISS</sub>	avg. conc. in granite <sup>h</sup>	avg. conc. in basalt <sup>h</sup>
	n <sup>a</sup>	avg		n <sup>a</sup>	avg											
Li															30	10
B															15	5
V	2	1.1	0.6	5	≤1		1.3								20	250
Mn	10	2.8	0.8	2	2.5	3.0	4				0.6	3			400	1,500
Fe	10	100	3.9	9	59	5.0									2.7	8.6
Co	5	2,600	310	5	1,100	100	1,100		45		800				1	48
Ni	10	22,000	8,000	9	20,000	10,000	24,000		780		17,000	4,500			0.5	150
Cu	10	54,000	24,000	9	4,700	1,300	4,000	500-600	1,300	400-1,600	49,000	2,200	1.00	0.15	10	100
Zn	5	5.2	1.1	1	2.1	0.1	11.0		3.5		4.0	14			40	100
As	3	0.6	0.4	8	12	5	2				400		0.20	0.90	1.5	2
Se	5	43	24	3	>107			900-1,500	350	200-2,000			1.00	0.80	0.05	0.05
Mo	5	2.9	1.1	5	720	100	9				1				2	1
Ag	10	1,600	600	8	52	28	100		1100		2,400	2,900	0.50	0.04	0.04	0.1
Cd	5	4.7	2.2	3	6.8	2.0			110			490			0.2	0.2
Sn	5	<3.2		5	≤1				11		11				3	1
Sb	2	0.26	0.04	8	≤1			0.2-0.3		7-40	200	360			0.2	0.2
Te	3	32	32	3	120	80		600-1,200	4,500	1,000-17,000			0.70	0.07	n.a.	n.a.
W	6	0.6	0.02	5	≤1										2	1
Au	5	<35		2	150	100	200				170,000				0.004	0.004
Tl	2	0.25	0.26	3	<0.3							73			0.75	0.10
Pb	2	0.24	0.10	2	0.07	0.01	1		57		120	440			20	5
Bi	8	3.8	1.9	8	6.3	1.6	40		320		47,000		0.07	0.04	0.18	0.15

<sup>a</sup> number of measurements<sup>b</sup> Li and Audétat (2015) Effects of temperature, silicate melt composition, and oxygen fugacity on the partitioning of V, Mn, Co, Ni, Cu, Zn, As, Mo, Ag, Sn, Sb, W, Au, Pb, and Bi between sulfide phases and silicate melt; *Geochimica et Cosmochimica Acta* 162:25-45; values calculated for 850 °C, QFM+2, 1.0 wt% FeO<sup>c</sup> Brenan (2015) Se–Te fractionation by sulfide–silicate melt partitioning: Implications for the composition of mantle-derived magmas and their melting residues; *Earth and Planetary Science Letters* 422:45-57; experiments performed at 9-15 kbar and 1200-1300 °C<sup>d</sup> Patten et al. (2013) Partition coefficients of chalcophile elements between sulfide and silicate melts and the early crystallization history of sulfide liquid: LA-ICP-MS analysis of MORB sulfide droplets; *Chemical Geology* 358:170-188<sup>e</sup> Kiseeva and Wood (2013) A simple model for chalcophile element partitioning between sulphide and silicate liquids with geochemical application; *Earth and Planetary Science Letters* 383:68-81; values calculated for 1400 °C and 1 wt% FeO<sup>f</sup> Liu and Brenan (2015) Partitioning of platinum-group elements (PGE) and chalcogens (Se, Te, As, Sb, Bi) between monosulfide-solid solution (MSS), intermediate solid solution (ISS) and sulfide liquid at controlled  $f_{O_2}$ - $f_{S_2}$  conditions; *Geochimica et Cosmochimica Acta* 159:139-161; experiments performed at 1 atm and 860-930 °C<sup>g</sup> Taylor (1964) Abundance of chemical elements in the continental crust: a new table; *Geochimica et Cosmochimica Acta* 28:1273-1285<sup>h</sup> Fe is reported as wt% Fe, all other elements are in ppm.

Abbreviations: δ – 1 sigma standard deviation of the measurements.

**Table 6-S6**

Composition of apatites from natural rocks.

Sample name	Rock type	CaO wt%	P <sub>2</sub> O <sub>5</sub> wt%	Na <sub>2</sub> O wt%	MgO wt%	SiO <sub>2</sub> wt%	FeO wt%	S ppm	Cl ppm	Mn ppm	Cu ppm	As ppm	Se ppm	Sr ppm	Y ppm	Cd ppm	Ba ppm	La ppm	Ce ppm	Bi ppm
SR8 apa A core	Quartz-monzoiorite	55.4	38.8	0.1	0.05	0.5	0.14	620	8800	1400	(0.2)	2.2	1.8	1000	490	0.20	6.5	1700	3400	0.11
SR8 apa A rim	Quartz-monzoiorite	55.4	39.4	0.1	0.05	0.4	0.15	560	9000	1400	(0.2)	2.1	1.3	1000	400	0.10	6.9	1600	3100	0.10
SR8 apa B core	Quartz-monzoiorite	55.4	38.3	0.1	0.05	0.4	0.15	670	8900	1400	0.5	1.9	1.4	1000	400	0.19	8.9	1300	2700	0.08
SR8 apa B rim	Quartz-monzoiorite	55.4	38.9	0.1	0.05	0.4	0.15	600	9000	1400	0.3	2.2	2.0	1100	470	0.12	6.1	1500	3200	0.10
SR9 apa core	Rhyodacite	55.4	38.3	0.1	0.02	0.3	0.07	500	2400	1200	(0.2)	2.0	2.0	970	480	0.07	1.0	830	2000	0.11
SR9 apa rim	Rhyodacite	55.4	37.6	0.1	0.02	0.3	0.07	440	2400	1200	(0.2)	1.7	2.0	830	450	0.09	1.4	750	1900	0.08
Questa Q2 apa A	Quartz-latite	55.4	38.8	0.1	0.03	0.2	0.09	520	3500	730	(0.3)	1.3	0.9	740	140	0.30	3.9	1200	1700	0.10
Questa Q2 apa B	Quartz-latite	55.4	38.7	0.1	0.05	0.3	0.14	560	3700	830	(0.3)	1.8	1.0	830	240	0.40	4.7	1500	2600	0.12
Bing 14 apa A	Latite	55.4	37.2	0.2	0.2	0.2	0.26	640	5000	800	0.2	1.4	3.4	1300	600	0.25	15	790	1900	0.04
Bing 14 apa B	Latite	55.4	37.2	0.2	0.4	<u>1.5</u>	<u>0.46</u>	720	5300	<u>870</u>	<u>5.8</u>	2.6	1.1	<u>1900</u>	210	0.41	<u>110</u>	<u>1400</u>	<u>2900</u>	0.06
Bing 14 apa C	Latite	55.4	37.8	0.2	0.7	<u>2.2</u>	<u>0.73</u>	1700	5400	<u>910</u>	<u>40</u>	1.8	1.2	<u>1600</u>	200	0.42	<u>20</u>	<u>1400</u>	<u>2800</u>	0.10
Bing 14 apa D	Latite	55.4	40.3	0.2	0.2	0.3	0.35	1270	6100	960	0.3	3.0	1.7	2100	300	0.15	20	1700	4300	0.08
Bing 14 apa E	Latite	55.4	38.2	0.3	0.2	1.3	0.38	1660	5200	770	4.0	1.8	1.1	1900	200	0.37	41	1400	2800	0.07
Bing 12 apa A	Latite	55.4	38.2	0.3	0.2	<u>5.0</u>	<u>0.30</u>	1170	5800	<u>1000</u>	<u>2.2</u>	3.0	1.7	<u>1500</u>	270	0.26	<u>120</u>	<u>1900</u>	<u>4300</u>	0.08
Bing 12 apa B	Latite	55.4	37.5	0.1	0.2	0.4	0.27	630	5000	800	0.3	2.4	1.9	1500	300	0.31	14	730	1600	0.11
Bing 12 apa C	Latite	55.4	37.4	0.1	0.2	<u>0.4</u>	<u>0.29</u>	650	5300	<u>790</u>	<u>0.9</u>	2.7	1.5	<u>1900</u>	200	0.41	<u>21</u>	<u>1300</u>	<u>2900</u>	0.09

Underlined values are not representative due to contamination by silicate matrix during the measurement; red values in parentheses denote detection limits.

## 7. Solubility of gold in oxidized, sulfur-bearing fluids at 500-850 °C and 200-230 MPa: a synthetic fluid inclusion study

Haihao Guo, Andreas Audétat

*Bayerisches Geoinstitut, Universität Bayreuth, D-95440 Bayreuth, Germany*

### 7.1. Abstract

Although Au solubility in magmatic-hydrothermal fluids has been investigated by numerous previous studies, there is a dearth of data on oxidized ( $\log fO_2 > \text{FMQ} + 2.5$ ; FMQ: fayalite-magnetite-quartz buffer), sulfur-bearing fluids such as those that formed porphyry Cu-Au (-Mo) deposits. We performed experiments to constrain the effects of fluid salinity, HCl-content, sulfur content,  $fO_2$  and temperature on Au solubility in such oxidized, sulfur-bearing fluids. For this purpose, small aliquots of fluids equilibrated with Au metal were trapped at high pressure and temperature in the form of synthetic fluid inclusions in quartz and were subsequently analyzed by LA-ICP-MS. Additionally, Raman spectra were collected from quartz-hosted fluid inclusions at up to 600 °C to help to identify the nature of dissolved gold- and sulfur species. Gold solubility was found to be affected most strongly by the HCl content of the fluid, followed by  $fO_2$ , fluid salinity and temperature. Compared to these factors the sulfur content of the fluid has relatively little influence. At 600 °C and 200 MPa, fluids with geologically realistic HCl contents (~1.1 wt%) and salinities (7-50 wt% NaCl<sub>equiv</sub>) dissolve ~1000-3000 ppm at oxygen fugacities buffered by the magnetite-hematite buffer. At even more oxidized conditions (three log units above the hematite-magnetite  $fO_2$  buffer), HCl-, NaCl- and H<sub>2</sub>SO<sub>4</sub>-rich fluids can dissolve up to 5 wt% Au at 800 °C. The observed Au solubility trends suggest that most of the Au dissolved in the form of NaAuCl<sub>2</sub> in our experiments.

Natural high-temperature fluid inclusions from porphyry Cu-Au (-Mo) deposits contain at least 100 times less Au than the solubilities predicted based on our experimental data, implying that at temperatures >500 °C the natural fluids were strongly Au-undersaturated. Consequently, gold grades in Au-rich porphyries were not controlled by the precipitation of native Au, but rather by factors that caused the precipitation of Au-rich hydrothermal sulfides such as bornite.

### 7.2. Introduction

Gold is one of the most noble of all metals, existing dominantly as a native metal in the solid state and dissolving only scarcely into liquids or gases. However, the widespread occurrence of economic gold deposits that formed by means of hydrothermal fluids (e.g., Kesler, 1994; Robb, 2005) implies that gold transport and deposition by geological fluids is a common process in the Earth's crust. Therefore, knowledge of the factors that influence gold solubility in hydrothermal fluids is essential for understanding the formation of ore deposits.

Previous experimental studies on gold solubility in hydrothermal fluids focused either on relatively low temperatures representative of epithermal environments (e.g., Gibert et al., 1998; Kokh et al., 2016; 2017; Pokrovski et al., 2009b; Zotov et al., 1989; 1991; ), on sulfur-free fluid systems (e.g., Frank et al., 2002; Hanley et al., 2005; Simon et al., 2005), or on fluids containing reduced sulfur species (e.g., Loucks and Mavrogenes, 1999; Tagirov et al., 2005; Simon et al., 2007; Zajacz et al., 2010). Loucks and Mavrogenes (1999) used synthetic fluid inclusions to investigate Au solubility in H<sub>2</sub>S-bearing fluids at 550-700 °C and 110-400 MPa. They observed solubilities up to 1000 ppm (by weight) Au and proposed AuHS(H<sub>2</sub>S)<sub>3</sub> as the dominant Au species. Subsequent studies on compositionally similar fluids identified Au(HS)<sub>2</sub><sup>-</sup>, Au(HS), Au(OH) as major Au species (Tagirov et al., 2005; Pokrovski et al., 2009b; Liu et al., 2011). Frank et al. (2002) investigated sulfur-free brines at 800 °C and 100 MPa and found that Au solubility increases with increasing HCl content, reaching 840 ppm Au at ~4.0 wt% HCl. They proposed HAuCl<sub>2</sub> as the dominant gold species. Simon et al. (2005; 2007) conducted experiments with NaCl-KCl-HCl-FeAsS fluids at 800 °C, 110-145 MPa and concluded that gold chloride complexes dominate both in sulfur-free and in (reduced) sulfur-bearing fluids. In contrast, Hanley et al. (2005) proposed Au(OH) as the dominant species in their salt-rich fluids at 600-800 °C, 150 MPa based on a negative correlation of Au solubility with fluid salinity. Most recently, Pokrovski et al. (2014, 2015) suggested an important role of the trisulfur ion (S<sub>3</sub><sup>-</sup>) in complexing gold, leading to Au solubilities up to ~640 ppm in K<sub>2</sub>S<sub>2</sub>O<sub>3</sub>-HCl-bearing fluids at 350 °C, 35 MPa. It needs to be noticed that all these studies were carried at relatively reduced conditions, in which sulfur occurs either in reduced state (S<sup>2-</sup>) or had a near-neutral valence (S<sub>3</sub><sup>-</sup>). However, evidence from porphyry Cu-Au (±Mo) deposits, which are one of our most important sources of Au (Kesler, 1994; Sillitoe, 2010), suggest that the ore-forming fluids in these deposits were highly oxidized (3-5 log units above the fayalite-magnetite-quartz (FMQ) buffer; e.g., Burnham and Ohmoto, 1980; Hedenquist and Richards, 1998), where S<sup>4+</sup> or S<sup>6+</sup> (in SO<sub>2</sub> and sulfate, respectively) is the dominant sulfur valence

(e.g., Binder and Keppler, 2011; Ni and Keppler, 2012). The present study thus aims at investigating gold solubility in oxidized ( $\log f_{\text{O}_2} > \text{FMQ}+2.5$ ), sulfur-bearing aqueous fluids similar to those responsible for porphyry Cu-Au ( $\pm\text{Mo}$ )-formation.

### 7.3. Methods

#### 7.3.1. Experimental methods

We used synthetic fluid inclusions to trap fluids at high temperature and pressure and subsequently analyze their composition by LA-ICP-MS. Aqueous solutions containing various amounts of HCl, H<sub>2</sub>SO<sub>4</sub>, Na<sub>2</sub>SO<sub>4</sub>, LiCl, KCl, CsCl and MnCl<sub>2</sub> were prepared from analytical-grade chemicals and deionized water. Sodium chloride, and in two cases elemental sulfur, were added as solids. Quartz pieces of 1.0×1.6×10 mm size were cut from inclusion-free synthetic quartz in a way that their longest dimension was parallel to the c-axis of quartz crystal. The quartz pieces were then etched in concentrated hydrofluoric acid for about 1 hour to form numerous etched channels, which favor the formation of large fluid inclusions during overgrowth of new quartz (Li and Audétat, 2009).

Three capsule setups were used in our experiments. In the first setup (Fig. 7.1a), gold capsules of 3.5 mm O.D. (outer diameter), 3.1 mm I.D. (inner diameter) and 20 mm length were loaded with a piece of etched quartz, ~40 mg solution, 0-16 mg of NaCl, 0-1 mg S, and a small SiO<sub>2</sub> glass rod (~4 mg). Run durations using this setup were kept short (10 hrs at 800 °C, 20 hrs at 700 °C; 40 hrs at 600 °C; 80 hrs at 500 °C), such that  $f_{\text{O}_2}$  was controlled by the starting materials rather than by the intrinsic  $f_{\text{O}_2}$  of the pressure vessel. In the second setup (Fig. 7.1b), which was used for runs #15, 28, 30, 33, 34, 48 and 49, the starting materials were contained in an inner Au or Au<sub>80</sub>Pd<sub>20</sub> capsule of 3.0 mm O.D., 2.7 mm I.D. and 20 mm length, which was then loaded with ~40 mg H<sub>2</sub>O and solid oxygen buffers (Re-ReO<sub>2</sub> (RRO), MnO-Mn<sub>3</sub>O<sub>4</sub> (MMO) or hematite-magnetite (HM)) into an outer Au capsule (O.D. 4.6 mm; I.D. 4.3 mm; 35 mm length). Gold rather than Au<sub>80</sub>Pd<sub>20</sub> had to be used as inner capsules in the sulfur-bearing experiments because Au<sub>80</sub>Pd<sub>20</sub> was found to react with sulfur and to become very brittle during this process. In this setup, entrapment of fluid was initiated after 24-192 hours by in-situ cracking, after which the runs were continued for another 24-120 hours to allow for crack healing. However, in order to obtain larger fluid inclusions, the runs were started either with an etched quartz piece and a SiO<sub>2</sub> glass rod as in the previous capsule setup, or with a quartz piece that already contained large fluid inclusions that were pre-

synthesized from H<sub>2</sub>O-KCl fluid. In both cases, already existing fluid inclusions were re-opened during the in-situ cracking, leading to distinctly larger fluid inclusions than if fluid inclusion-free quartz pieces were used (Li and Audétat, 2009). Fluid inclusions that were re-opened during in-situ cracking could be recognized by small fluid inclusion trails leading to them, and in the case of pre-synthesized ones by the absence of K-signals during LA-ICP-MS analysis. It is those re-opened inclusions that were preferentially chosen for LA-ICP-MS analysis (Li and Audétat, 2009). The third setup (Fig. 7.1c), which was used for runs #29, 38, 41 and 45, is similar to setup b, except that an unetched quartz piece was used (to avoid fluid entrapment before Au solubility became low) and that the external nickel-nickel oxide (NNO) buffer was placed in an open Au capsule below the sample capsule instead of in a sealed outer capsule. The latter is possible because the material of the pressure vessel is very Ni-rich (~76 wt% Ni) and thus imposes a  $fO_2$  that is already close to the NNO-buffer. In all setups the sample-containing capsules were crimped, welded with a pulsed arc welder, then pre-shrunk at ~100 MPa H<sub>2</sub>O pressure, and finally weighed to check for potential leaks.

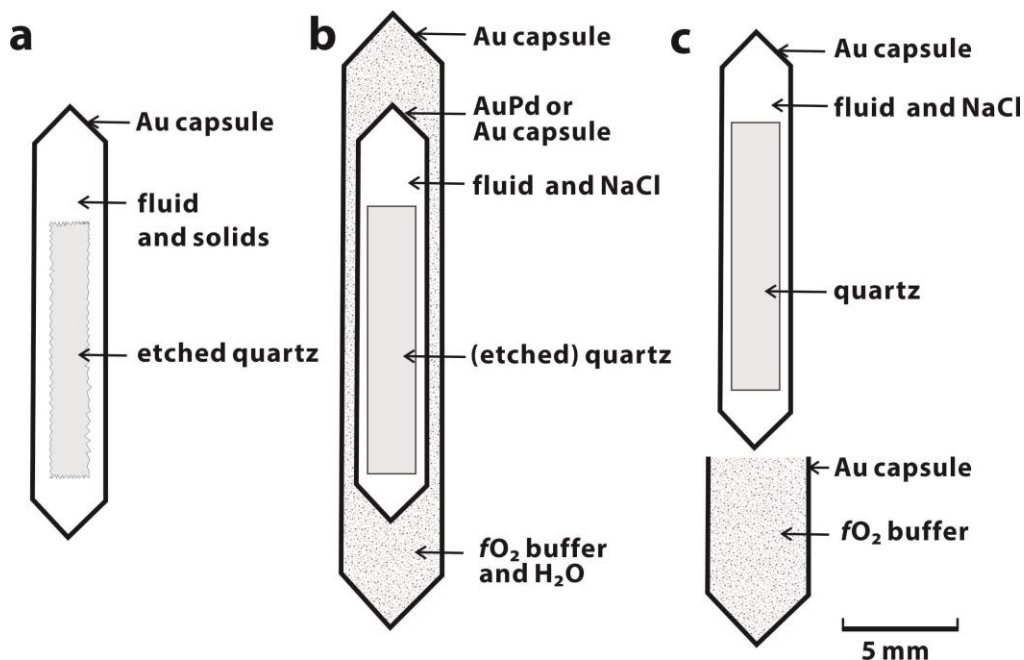


**Fig. 7.1.** Schematic illustration of the three capsule designs used in our experiments: (a) Gold capsule loaded with etched quartz, fluid and solids (NaCl, Na<sub>2</sub>SO<sub>4</sub>, S, LiCl, KCl or MnCl<sub>2</sub>). (b) Double-capsule design containing an oxygen fugacity buffer + H<sub>2</sub>O filled into an outer gold capsule, and the sample placed into an inner Au(±Pd) capsule. (c) Design used for the Ni-NiO-buffered runs, featuring an open capsule filled with Ni and NiO below the sample capsule.

All except for two runs were performed in rapid-quench cold-seal pressure vessels made of Inconel 713LC super alloy, using water as pressure medium. Temperature was measured with NiCr-Ni (type K) thermocouples placed in an external borehole of the vessels. The remaining two runs were performed in argon-pressurized autoclaves made of TZM alloy (Ti- and Zr-reinforced molybdenum). Uncertainties in the temperature and pressure readings are considered  $\pm 5$  °C and  $\pm 20$  bar, respectively, in both vessel types. The experiments were started by pressurizing the capsules to ~50% of the final value and then heating them along an isochoric path defined by the entire volume of the pressure medium to the final run conditions of 500-850 °C and 200-230 MPa, which took about 30 minutes. In-situ cracking of the quartz pieces was performed after 24-192 hours by dragging the capsule with the help of an external magnet within a few seconds from the hot end of the vessel to its cold end and then back up to the hot end. The experiments were stopped by removing the autoclaves from the furnace and allowing them to cool to room temperature within about 40 minutes. One run (#14) was terminated by in-situ quenching (cooling to  $< 50$  °C within a few seconds) in order to minimize back-reactions within the fluid inclusions during cooling. Recovered capsules were weighed to check for leaks occurring during the experiments and then opened with a razor blade. The pH of the quench solution was measured with pH-indicator papers. The quartz pieces were gently polished on Al<sub>2</sub>O<sub>3</sub> and SiC grit papers and subsequently using diamond spray on paper to remove excess quartz on the sample surface and render fluid inclusions ready for observation and analysis.

### **7.3.2. Analytical methods**

#### *7.3.2.1. LA-ICP-MS analyses*

The major- and trace-element content of synthetic fluid inclusions was measured by LA-ICP-MS. The utilized systems consist of a 193 nm ArF Excimer laser (GeolasPro, Coherent, USA) attached to an Elan DRC-e (Perkin Elmer, Canada) quadrupole mass spectrometer (Günther et al., 1998). The laser was operated at a frequency of 10 Hz with  $\sim 10$  J·cm<sup>-2</sup> energy density at the sample surface, using a laser pit size of 40  $\mu$ m for the standards and 30-50  $\mu$ m for the fluid inclusions. Measured isotopes include <sup>7</sup>Li, <sup>23</sup>Na, <sup>30</sup>Si, <sup>32</sup>S, <sup>35</sup>Cl, <sup>39</sup>K, <sup>43</sup>Ca, <sup>55</sup>Mn, <sup>133</sup>Cs and <sup>197</sup>Au, which were measured using dwell times of 10-50 ms per isotope. A representative LA-ICP-MS signal of a fluid inclusion analysis is shown in Fig. 7.2. Corrections for contributions of ablated host quartz

were made for S and Cl, assuming that the fluid inclusions themselves do not contain any SiO<sub>2</sub> (Seo et al., 2011). External standardization was based on NIST SRM 610 (Jochum et al., 2011), except for S and Cl, which were quantified based on a well-characterized, natural afghanite crystal (Seo et al., 2011). Internal standardization was based on the Na content of the loaded solution (Heinrich et al., 2003), or – in the case of Na-free experiments (runs #22, 23 and 24) – on its Cs or K content. In four of our experiments (#13, 16, 17 and 18) the fluid split into two phases at run conditions (see below). Since no phase diagrams are available for Na<sub>2</sub>SO<sub>4</sub>-rich fluids that could be used to interpret microthermometric data, we calculated maximum Au contents of the bulk fluids in these runs by choosing the fluid phase that had higher Au/Na ratios and taking the Na content of the bulk fluid as internal standard.

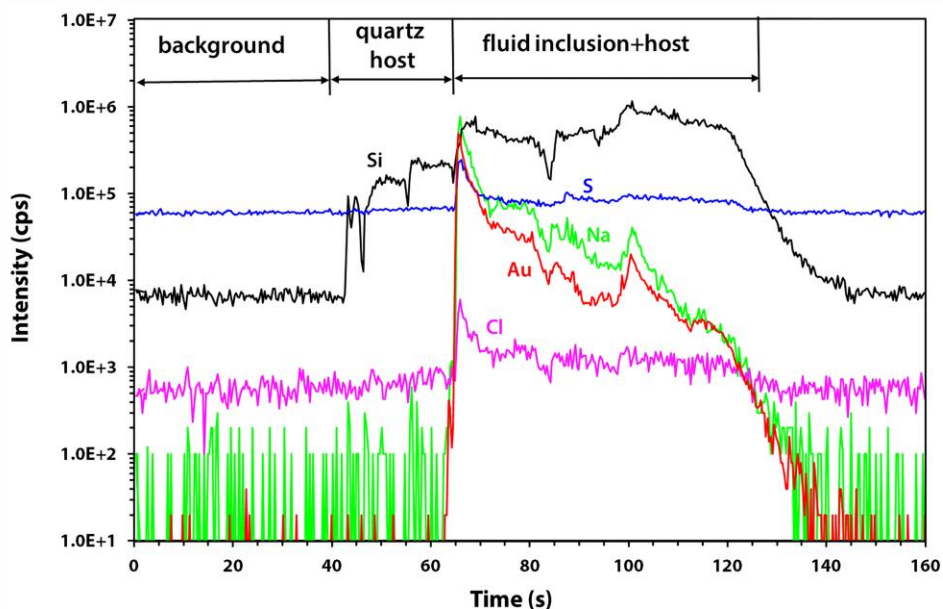


**Fig. 7.2.** LA-ICP-MS signal obtained from a 17 µm sized fluid inclusion (15Oc08k17) from run HG-AU-11. The fluid was trapped under very oxidized conditions at 800 °C, 2 kbar and contains 12 wt% Cl, 8.0 wt% Na, 4.3 wt% S, and 3.3 wt% Au.

Since the measurement of <sup>197</sup>Au (the only natural isotope of Au) is affected by an interference from <sup>181</sup>Ta<sup>16</sup>O and NIST SRM 610 contains significantly more Ta (482±4 ppm) than Au (23.6±1.7 ppm), one needs to determine how much error is introduced by this interference. Our ICP-MS was tuned to a ThO rate of 0.05-0.14 % and a rate of doubly charged Ca ions of 0.1-0.2% based on measurements on NIST SRM 610 at the beginning of each session. If one assumes that the rate of TaO formation is the same as that of ThO, then one obtains an error of 4-6%. However, a more

precise estimate is obtained by determining the *actual* rate of TaO formation, which was obtained by measuring  $^{197}\text{Au}$  in two Ta-rich samples that were presumably Au-free, i.e., a synthetic silicate glass containing 1300 ppm Ta (synthesized in a Pt capsule), and an ilmenite containing 570 ppm Ta. In both cases the observed  $^{197}\text{Au}$  signal corresponds to a TaO rate of 0.031%. Applying this oxide rate to NIST SRM 610 results in an error of 1.4%, i.e., Au concentrations in Ta-free unknowns will be underestimated by this percentage. Calculated Au concentrations in the fluid inclusions were thus consistently multiplied by a factor of 1.014. The overall uncertainty associated with LA-ICP-MS analyses of synthetic fluid inclusions with known internal standard element concentration is about 10% (Heinrich et al., 2003); for S and Cl it is about 20% (Seo et al., 2011).

#### 7.3.2.2. *Raman spectroscopy*

Raman spectra of fluid inclusions were taken in confocal mode using a Horiba LabRAM HR UV spectrometer equipped with a CCD detector,  $1800\text{ mm}^{-1}$  grating, and a  $50\times$  magnification objective. The spectral resolution of this instrument setup is  $3.5\text{ cm}^{-1}$ , and a confocal pinhole of 30-60  $\mu\text{m}$  was used for the measurements. Excitation was promoted using the 514.5 nm line of an  $\text{Ar}^+$  ion laser with an output laser power of 0.2 W. Most spectra were taken at room temperature, using six overlapping windows with acquisition times of  $2\times 30\text{ s}$  each to cover the entire range of 100 to  $4500\text{ cm}^{-1}$ . A number of spectra covering the spectral range of  $350\text{-}1250\text{ cm}^{-1}$  were collected at temperatures up to  $600\text{ }^\circ\text{C}$  with an output laser power of 0.2 W in order to investigate potential changes in the speciation of sulfur and/or gold during heating. For the latter purpose, fluid inclusion-bearing quartz chips ( $\sim 2\times 1.6\times 0.5\text{ mm}$ ) were heated at  $100\text{ }^\circ\text{C}$  intervals in a hydrothermal diamond anvil cell of the Bassett type (Bassett et al., 1993) in which the diamond anvils were replaced with cylinders made of  $\text{SiO}_2$  glass. The upper cylinder contained a central borehole, such that no solid parts occurred between the sample and the microscope lens. Temperature was calibrated to an accuracy of  $\pm 5\text{ }^\circ\text{C}$  using the melting points of  $\text{NaNO}_3$  ( $308\text{ }^\circ\text{C}$ ),  $\text{CsCl}$  ( $645\text{ }^\circ\text{C}$ ) and  $\text{NaCl}$  ( $801\text{ }^\circ\text{C}$ ), but due to manual heating the overall accuracy during the collection of the Raman spectra was  $\pm 20\text{ }^\circ\text{C}$ . No force was applied to the quartz chip, but the pressure inside the fluid inclusions increased continuously during heating due to their isochoric behavior, reaching ca. 100 MPa at  $600\text{ }^\circ\text{C}$ .

To be able to quantitatively interpret the Raman Spectra, standard solutions of H<sub>2</sub>SO<sub>4</sub> and SO<sub>2</sub> (the latter in the form of H<sub>2</sub>SO<sub>3</sub> dissolved in water) were prepared as described in Binder and Keppler (2011), and ratios of the intensity integral areas of sulfur species over the intensity integral area of the ~1640 cm<sup>-1</sup> H<sub>2</sub>O absorption band were determined. The resulting conversion factors for HSO<sub>4</sub><sup>-</sup> (I<sub>HSO<sub>4</sub><sup>-</sup></sub>/I<sub>H<sub>2</sub>O</sub>=1.5799 molal HSO<sub>4</sub><sup>-</sup>), SO<sub>4</sub><sup>2-</sup> (I<sub>SO<sub>4</sub><sup>2-</sup></sub>/I<sub>H<sub>2</sub>O</sub> =31.0286 molal SO<sub>4</sub><sup>2-</sup>) and SO<sub>2</sub> (I<sub>SO<sub>2</sub></sub>/I<sub>H<sub>2</sub>O</sub>=1.9880 molal SO<sub>2</sub>) differ by up to a factor of 4 from those determined by Binder and Keppler (I<sub>HSO<sub>4</sub><sup>-</sup></sub>/I<sub>H<sub>2</sub>O</sub>=1.0453 molal HSO<sub>4</sub><sup>-</sup>), SO<sub>4</sub><sup>2-</sup> (I<sub>HSO<sub>4</sub><sup>2-</sup></sub>/I<sub>H<sub>2</sub>O</sub> =11.324 molal SO<sub>4</sub><sup>2-</sup>) and SO<sub>2</sub> (I<sub>SO<sub>2</sub></sub>/I<sub>H<sub>2</sub>O</sub>=0.5411 molal SO<sub>2</sub>), which may be due to the use of different Raman spectrometer setups.

## 7.4. Results

### 7.4.1. Appearance of fluid inclusions

Depending on the utilized capsule setup and run procedure, three types of synthetic fluid inclusions were produced: (1) in runs performed without in-situ cracking, dissolution of the SiO<sub>2</sub> glass rod and re-precipitation of crystalline SiO<sub>2</sub> on the etched quartz substrate led to the formation of numerous, often large (>30 μm mean diameter) fluid inclusions close to the sample surface (in the following called "primary" fluid inclusions; Figs. 7.3a, b, c); (2) in samples that were cracked in-situ, small inclusions (typically <10 μm) occur on planes cutting through the entire height of the quartz sample, representing fluid that was trapped in cracks that formed during in-situ cracking (in the following called "secondary" fluid inclusions; Fig. 7.3d); and (3) in runs that contained an etched quartz piece and were cracked in-situ, some of the primary fluid inclusions were re-opened and refilled with new fluid during the in situ cracking (called "refilled" inclusions; Fig. 7.3d). Such refilled fluid inclusions were our main target for LA-ICP-MS analysis, but in some runs primary or secondary inclusions were analyzed as well for the purpose of comparison.

In most experiments all fluid inclusions turned out to have intermediate densities and to contain constant proportions of vapor + liquid ± a small gold daughter crystal (Figs. 7.3b, c), suggesting that the fluid was trapped in the single-phase field. However, in four experiments (#13, 16, 17 and 18) both crystal-rich inclusions and lower-density, crystal-free inclusions are present (Figs. 7.3e, f), suggesting that the fluid was trapped in the two-phase field.

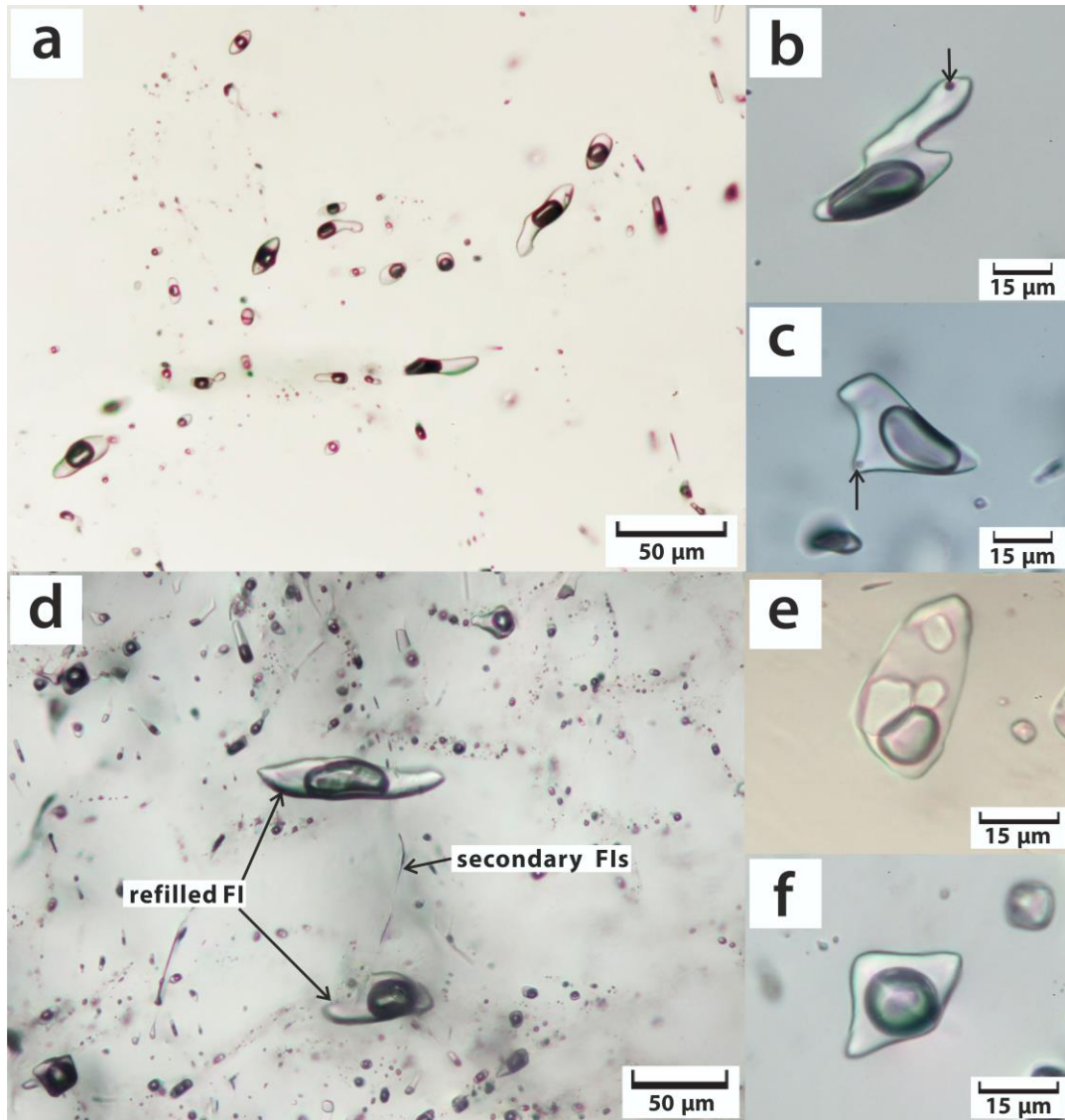


**Fig. 7.3.** Photomicrographs of fluid inclusions synthesized at 800 °C and 2 kbar: (a) Typical appearance of fluid inclusions that formed during overgrowth of new quartz over an etched quartz substrate (HG-AU-21). (b, c) Fluid inclusions synthesized at 800 °C, 2 kbar from aqueous starting fluids containing 3.5 wt% HCl, 16.4 wt% H<sub>2</sub>SO<sub>4</sub> and 20 wt% NaCl. (HG-AU-04 and HG-AU-14). The inclusions contain 4-5 wt% Au and an opaque daughter crystal consisting of metallic gold (indicated by arrows). (d) Two large "refilled" fluid inclusions (FIs), which represent primary fluid inclusions that were synthesized in a pre-run from a H<sub>2</sub>O-KCl fluid and later were cracked open and refilled with new fluid during a second experiment (HG-AU-38), plus small secondary fluid inclusions occurring on cracks that were produced via in-situ cracking during the second experiment. (e) A brine inclusion containing several Na<sub>2</sub>SO<sub>4</sub> daughter crystals, synthesized at 800 °C, 2 kbar from a starting mixture containing 23.8 wt% Na<sub>2</sub>SO<sub>4</sub> and 1.8 wt% HCl (HG-AU-17). (f) Vapor phase coexisting with the brine phase shown in (e).

### 7.4.2. Factors affecting Au solubility

An overview of the conducted experiments and obtained Au solubilities is provided in Table 7.1. The effects of individual parameters on Au solubility are summarized in Fig. 7.4. It should be noted that most experiments shown in Fig. 7.4 were not  $fO_2$ -buffered, except for the runs plotted in Fig. 7.4f. The  $fO_2$ -unbuffered experiments were run short enough that  $H_2$  could not significantly equilibrate through the noble capsules with the pressure medium of the autoclaves, hence the  $fO_2$  in these runs was controlled by the starting materials. This is proved by the fact that Au solubilities obtained in runs conducted in Ar-pressurized TZM vessels (which impose a very high intrinsic  $fO_2$  of around FMQ+3 to FMQ+4) are within uncertainty the same as those obtained in runs conducted in  $H_2O$ -pressurized Inconel 713LC alloy vessels (which impose an intrinsic  $fO_2$  of around NiNiO+0.5). Although the oxygen fugacities in these unbuffered experiments were much higher than in natural fluids (see below), the results are useful to constrain the influence of various parameters on Au solubility in fluids in which sulfur is present dominantly in  $S^{6+}$  state.

At constant  $H_2SO_4$  and HCl concentration in the fluid, gold solubility increases with increasing NaCl content (Fig. 7.4a), whereas at constant NaCl and HCl concentration in the fluid, gold solubility increases with increasing  $H_2SO_4$  (Fig. 7.4b). In NaCl-free fluids containing 23.8 wt%  $Na_2SO_4$  (i.e., same amount of sulfur as in the experiments with 16.4 wt%  $H_2SO_4$ ) gold solubility increases with increasing HCl content (Fig. 7.4c). Gold solubility also increases with increasing temperature (Fig. 7.4d). Notice that gold solubility is low (<1000 ppm) if either Na (Fig. 7.4a),  $H_2SO_4$  (Fig. 7.4b) or Cl (Fig. 7.4c) is missing in the system, but that it reaches weight percent levels at temperatures as low as 500 °C if the fluid contains  $\geq 7.7$  wt% Na,  $\geq 7.9$  wt% Cl, and  $\geq 4.6$  wt%  $SO_4^{2-}$  (Fig. 7.4d). Similarly high Au solubilities are obtained if Na is replaced by other alkalis (Li, K; Fig. 7.4e), whereas about five times lower values are obtained if Na is replaced by doubly-charged ions (Ca, Mn; runs #21, 24; Table 7.1). This is probably due to the fact that Ca-Cl and Mn-Cl ion pairs are much stronger than Na-Cl, leaving less  $Cl^-$  available for complexing with Au. The effect of  $fO_2$  on Au solubility in sulfur-free versus sulfur-bearing fluids at 800 °C, 200 MPa is depicted in Fig. 7.4f. Over the investigated range of  $fO_2$  Au solubility increases by a factor of about eight in both the S-free and the S-bearing fluids. Importantly, the highest Au solubility attained in the hematite-magnetite-buffered experiments ( $8,100 \pm 1,500$  ppm Au in sulfur-bearing run#34) is about five times lower than the Au solubilities attained in  $fO_2$ -unbuffered experiments

with the same fluid composition (4.1-5.1 wt% Au; runs #4, 11, 14; Table 7.1), which implies that the extremely high Au solubilities observed in the  $fO_2$ -unbuffered runs are a consequence of extremely high oxygen fugacities.

Geologically more realistic are our experiments #48 and 49, in which fluids containing 7 wt% NaCl, 3.06 wt% H<sub>2</sub>SO<sub>4</sub> (corresponding to 1.0 wt% S) and 1.1 wt% HCl were equilibrated at the MnO-Mn<sub>3</sub>O<sub>4</sub> buffer at 750-850 °C and 200-230 MPa. This fluid composition and the experimental conditions were chosen for the following reasons: the salinity of 7 wt% NaCl was chosen because it lies within the salinity range of 5-10 wt% NaCl<sub>equiv</sub> observed for intermediate-density bulk fluids in porphyry Cu-Au-(Mo) deposits (Ulrich et al., 2003; Heinrich et al., 2011; Redmond et al., 2004; Landtwing et al., 2005; Rusk et al., 2004, 2008; Stefanova et al., 2014); the concentration of 0.7 wt% S corresponds to the average S-content of fluid inclusions analyzed from Bingham Canyon (Seo et al., 2012), and the concentration of 1.1 wt% HCl corresponds to the value predicted for a fluid containing 8.9 wt% KCl (same molar quantity as 7 wt% NaCl) buffered by potassic feldspar and muscovite/andalusite at 600 °C, 100 MPa (Burnham, 1979; log mKCl/mHCl~-0.6). The MnO-Mn<sub>3</sub>O<sub>4</sub> buffer (FMQ+4.1 at 800 °C 2 kbar according to Chou, 1987; FMQ+4.5 according to O'Neill and Pownceby, 1993) was chosen because it lies within the range of oxygen fugacities estimated for the porphyry Cu mineralization environment based on the composition of hydrothermal biotite (Burnham and Ohmoto, 1980; log  $fO_2$  = FMQ+3 to FMQ+5). In these two geologically realistic experiments Au solubility reached 750±70 ppm at 750 °C, and 870±90 ppm at 850 °C (Table 7.1). Due to the low permeability of gold with respect to H<sub>2</sub> (Chou, 1986) it was not possible to conduct similar experiments at lower temperatures. However, Au solubility at lower temperature can be inferred via extrapolation (see below).

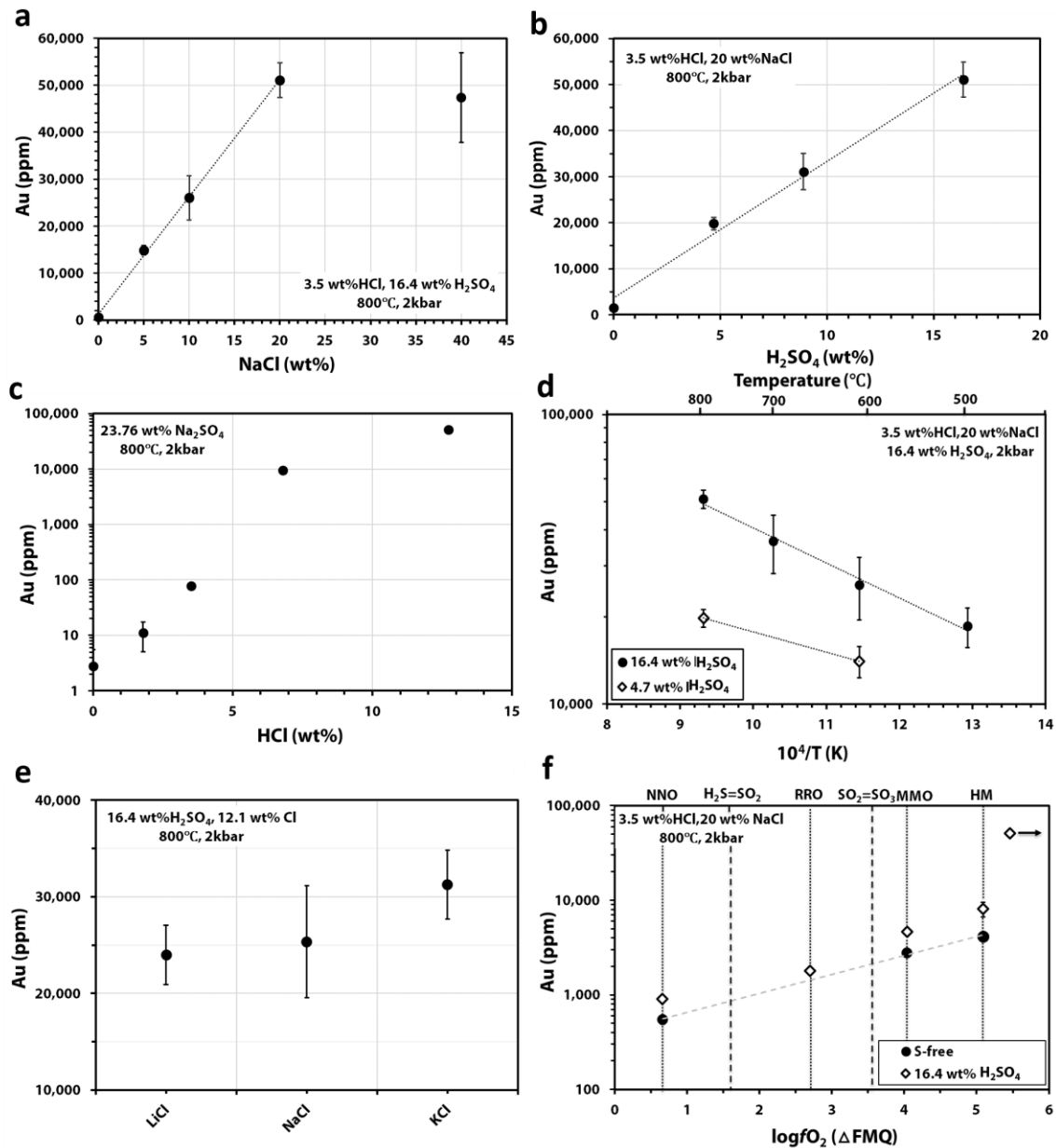


**Fig. 7.4.** Measured gold solubility (in ppm by weight) as a function of: (a) NaCl concentration in the starting fluid (runs #36, 25, 05, 06, 04), (b) H<sub>2</sub>SO<sub>4</sub> concentration in the starting fluid (#01-04), (c) HCl concentration in the starting fluid (runs #16-20), (d) temperature (runs #04, 08-10, 02, 31), (e) type of alkali ion (runs #22, 07, 23), and (f) oxygen fugacity (runs #38, 15, 30, 28, 29, 33, 34, 04). Sulfur speciation boundaries in (f) are from Binder and Keppler (2011). FMQ: fayalite-magnetite-quartz buffer. NNO – Ni-NiO buffer; RRO – Re-ReO<sub>2</sub> buffer; MMO – MnO-Mn<sub>3</sub>O<sub>4</sub> buffer; HM – hematite-magnetite buffer. Values for FMQ, NNO and HM were calculated based on Frost (1991); RRO is based on Pownceby and O'Neill (1994); and MMO is based on Chou (1987).

**Table 7.1**

Overview of performed experiments and obtained results.

Experiment number	T (°C)	P (kbar)	Duration (h) <sup>a</sup>	$f_{O_2}$ buffer <sup>b</sup>	Capsule materials <sup>c</sup>	Starting solution	Added solids	pH <sup>d</sup>	Pressure vessel <sup>e</sup>	fluid phases	Au (μg/g) avg.	stdev.	Species <sup>f</sup>
HG-AU-01	800	2.0	10	–	Au	3.5 wt% HCl	20 wt% NaCl	<0.3	CSPV	1	1,500	100	not measured
HG-AU-41	800	2.0	24+36	NNO	AuPd-Au	3.5 wt% HCl	5 wt% NaCl	<0.3	CSPV	1	150	10	not measured
HG-AU-45	800	2.0	24+36	NNO	AuPd-Au	3.5 wt% HCl	10 wt% NaCl	<0.3	CSPV	1	240	20	not measured
HG-AU-38	800	2.0	144+48	NNO	Au-Au	3.5 wt% HCl	20 wt% NaCl	<0.3	CSPV	1	550	60	not measured
HG-AU-15	800	2.0	24+24	MMO	AuPd-Au	3.5 wt% HCl	20 wt% NaCl	<0.3	CSPV	1	1,900	100	not measured
HG-AU-30	800	2.0	24+48	HM	AuPd-Au	3.5 wt% HCl	20 wt% NaCl	<0.3	CSPV	1	4,000	300	not measured
HG-AU-02	800	2.0	10	–	Au	3.5 wt% HCl+ 4.7 wt% H <sub>2</sub> SO <sub>4</sub>	20 wt% NaCl	<0.3	CSPV	1	20,000	1,000	not measured
HG-AU-35	800	2.0	10	–	Au	3.5 wt% HCl+ 6.8 wt% Na <sub>2</sub> SO <sub>4</sub>	20 wt% NaCl	<1	CSPV	1	7,200	1,100	not measured
HG-AU-31	600	2.0	40	–	Au	3.5 wt% HCl+ 4.7 wt% H <sub>2</sub> SO <sub>4</sub>	20 wt% NaCl	<0.3	CSPV	1	14,000	2,000	not measured
HG-AU-46	800	2.0	10	–	Au	1.75 wt% HCl+ 8.9 wt% H <sub>2</sub> SO <sub>4</sub>	20wt% NaCl	<0.3	CSPV	1	25,000	2,000	not measured
HG-AU-03	800	2.0	10	–	Au	3.5 wt% HCl+ 8.9 wt% H <sub>2</sub> SO <sub>4</sub>	20 wt% NaCl	<0.3	CSPV	1	31,000	4,000	not measured
HG-AU-47	800	2.0	10	–	Au	7 wt% HCl+ 8.9 wt% H <sub>2</sub> SO <sub>4</sub>	20wt% NaCl	<0.3	CSPV	1	41,000	4,000	not measured
HG-AU-04	800	2.0	10	–	Au	3.5 wt% HCl+16.4 wt% H <sub>2</sub> SO <sub>4</sub>	20 wt% NaCl	<0.3	CSPV	1	51,000	4,000	SO <sub>4</sub> <sup>2-</sup> , HSO <sub>4</sub> <sup>-</sup> , AuCl <sub>4</sub> <sup>-</sup>
HG-AU-11	800	2.0	10	–	Au	3.5 wt% HCl+16.4 wt% H <sub>2</sub> SO <sub>4</sub>	20 wt% NaCl	<0.3	TZM	1	44,000	18,000	SO <sub>4</sub> <sup>2-</sup> , HSO <sub>4</sub> <sup>-</sup> , AuCl <sub>4</sub> <sup>-</sup>
HG-AU-14	800	2.0	10	–	Au	3.5 wt% HCl+16.4 wt% H <sub>2</sub> SO <sub>4</sub>	20 wt% NaCl	<0.3	TZM	1	40,000	5,000	SO <sub>4</sub> <sup>2-</sup> , HSO <sub>4</sub> <sup>-</sup> , SO <sub>2</sub>
HG-AU-36	800	2.0	10	–	Au	3.5 wt% HCl+16.4 wt% H <sub>2</sub> SO <sub>4</sub> <sup>g</sup>	–	<0.3	CSPV	1	650	170	not measured
HG-AU-25	800	2.0	10	–	Au	3.5 wt% HCl+16.4 wt% H <sub>2</sub> SO <sub>4</sub>	5 wt% NaCl	<0.3	CSPV	1	15,000	1,000	not measured
HG-AU-05	800	2.0	10	–	Au	3.5 wt% HCl+16.4 wt% H <sub>2</sub> SO <sub>4</sub>	10 wt% NaCl	<0.3	CSPV	1	26,000	5,000	not measured
HG-AU-06	800	2.0	10	–	Au	3.5 wt% HCl+16.4 wt% H <sub>2</sub> SO <sub>4</sub>	40 wt% NaCl	<0.3	CSPV	1	47,000	10,000	not measured
HG-AU-08	700	2.0	20	–	Au	3.5 wt% HCl+16.4 wt% H <sub>2</sub> SO <sub>4</sub>	20 wt% NaCl	<0.3	CSPV	1	37,000	8,000	not measured
HG-AU-09	600	2.0	40	–	Au	3.5 wt% HCl+16.4 wt% H <sub>2</sub> SO <sub>4</sub>	20 wt% NaCl	<0.3	CSPV	1	26,000	6,000	not measured
HG-AU-10	500	2.0	80	–	Au	3.5 wt% HCl+16.4 wt% H <sub>2</sub> SO <sub>4</sub>	20 wt% NaCl	<0.3	CSPV	1	19,000	3,000	not measured
HG-AU-12	800	2.0	10	–	Au	16.4 wt% H <sub>2</sub> SO <sub>4</sub> +100 ppm Cs	–	<0.3	CSPV	1	<10	N/A	SO <sub>4</sub> <sup>2-</sup> , HSO <sub>4</sub> <sup>-</sup>
HG-AU-13	800	2.0	10	–	Au	5.0 wt% H <sub>2</sub> SO <sub>4</sub> +12.2 wt% Na <sub>2</sub> SO <sub>4</sub>	–	<0.3	CSPV	2	<5	N/A	SO <sub>4</sub> <sup>2-</sup> , HSO <sub>4</sub> <sup>-</sup>
HG-AU-16	800	2.0	10	–	Au	distilled H <sub>2</sub> O	23.8 wt% Na <sub>2</sub> SO <sub>4</sub>	~8	CSPV	2	<6	N/A	not measured
HG-AU-17	800	2.0	10	–	Au	1.79 wt% HCl (=0.5 m)	23.8 wt% Na <sub>2</sub> SO <sub>4</sub>	<0.3	CSPV	2	<80 <sup>h</sup>	80	not measured
HG-AU-18	800	2.0	10	–	Au	3.52 wt% HCl (=1.0 m)	23.8 wt% Na <sub>2</sub> SO <sub>4</sub>	<0.3	CSPV	2	<270 <sup>h</sup>	190	not measured

HG-AU-19	800	2.0	10	–	Au	6.80 wt% HCl (=2.0 m)	23.8 wt% Na <sub>2</sub> SO <sub>4</sub> <0.3	CSPV	1	9,400	1,000	not measured
HG-AU-20	800	2.0	10	–	Au	12.7 wt% HCl (=4.0 m)	23.8 wt% Na <sub>2</sub> SO <sub>4</sub> <0.3	CSPV	1	52,000	4,000	not measured
HG-AU-22	800	2.0	10	–	Au	16.4 wt% H <sub>2</sub> SO <sub>4</sub> + 100 ppm Cs	14.5 wt% LiCl <0.3	CSPV	1	24,000	3,000	not measured
HG-AU-07	800	2.0	10	–	Au	16.4 wt% H <sub>2</sub> SO <sub>4</sub>	20 wt% NaCl <0.3	CSPV	1	25,000	6,000	not measured
HG-AU-23	800	2.0	10	–	Au	16.4 wt% H <sub>2</sub> SO <sub>4</sub> + 100 ppm Cs	25.5 wt% KCl <0.3	CSPV	1	31,000	4,000	not measured
HG-AU-24	800	2.0	10	–	Au	16.4 wt% H <sub>2</sub> SO <sub>4</sub> + 100 ppm Cs	21.5 wt% MnCl <sub>2</sub> <0.3	CSPV	1	5,300	1,400	not measured
HG-AU-21	800	2.0	10	–	Au	3.5 wt% HCl	20 wt% NaCl <sup>i</sup> <0.3	CSPV	1	4,000	1,900	not measured
HG-AU-29	800	2.0	144+72	NNO	Au-Au	3.5 wt% HCl+16.4 wt% H <sub>2</sub> SO <sub>4</sub>	20 wt% NaCl <0.3	CSPV	1	910	70	H <sub>2</sub> S
HG-AU-28	800	2.0	120+72	RRO	Au-Au	3.5 wt% HCl+16.4 wt% H <sub>2</sub> SO <sub>4</sub>	20 wt% NaCl <0.3	CSPV	1	1,800	200	SO <sub>4</sub> <sup>2-</sup> , HSO <sub>4</sub> <sup>-</sup> , SO <sub>2</sub>
HG-AU-33	800	2.0	96+72	MMO	Au-Au	3.5 wt% HCl+16.4 wt% H <sub>2</sub> SO <sub>4</sub>	20 wt% NaCl <0.3	CSPV	1	4,600	300	SO <sub>4</sub> <sup>2-</sup> , HSO <sub>4</sub> <sup>-</sup> , SO <sub>2</sub>
HG-AU-34	800	2.0	96+72	HM	Au-Au	3.5 wt% HCl+16.4 wt% H <sub>2</sub> SO <sub>4</sub>	20 wt% NaCl <0.3	CSPV	1	8,100	1,500	SO <sub>4</sub> <sup>2-</sup> , HSO <sub>4</sub> <sup>-</sup> , SO <sub>2</sub>
HG-AU-32	700	2.0	72	–	Au	3 wt% S+0.2 wt% KOH	20 wt% NaCl ~1	CSPV	1	650	140	SO <sub>4</sub> <sup>2-</sup> , H <sub>2</sub> S
HG-AU-37	700	2.0	72	–	Au	3 wt% S+2 wt% KOH	20 wt% NaCl 1-2	CSPV	1	1,200	100	SO <sub>4</sub> <sup>2-</sup> , H <sub>2</sub> S
HG-AU-48	850	2.3	96+72	MMO	Au-Au	7 wt% NaCl+1 wt% S <sup>j</sup> +1.1 wt% HCl	– <0.3	CSPV	1	880	90	not measured
HG-AU-49	750	2.3	192+120	MMO	Au-Au	7 wt% NaCl+1 wt% S <sup>j</sup> +1.1 wt% HCl	– <0.3	CSPV	1	750	70	not measured

<sup>a</sup> for runs in which in-situ cracking was performed, the times before and after in-situ cracking are provided

<sup>b</sup> dash means that the oxygen fugacity was not buffered. NNO – Ni-NiO; MMO – MnO-Mn<sub>2</sub>O<sub>4</sub>; RRO – Re-ReO<sub>2</sub>; NM – hematite-magnetite

<sup>c</sup> two materials indicate double-capsule, with the first material referring to the inner capsule and the second material to the outer capsule.

<sup>d</sup> pH of the quench fluid.

<sup>e</sup> CSPV – cold-seal pressure vessel made of Inconel713LC (Ni-rich), pressurized with H<sub>2</sub>O; TZM – pressure vessel made of Ti-and Zr-reinforced Mo, pressurized with Ar

<sup>f</sup> species identified by Raman spectroscopy.

<sup>g</sup> plus 119 ppm Cs.

<sup>h</sup> maximum value based on the composition of the more Au-rich fluid phase

<sup>i</sup> plus excess CaSO<sub>4</sub> to cause CaSO<sub>4</sub> saturation

<sup>j</sup> added in the form of 80 mole% S<sup>6+</sup>(H<sub>2</sub>SO<sub>4</sub>) and 20 mole% S<sup>4+</sup>(SO<sub>2</sub>).

### 7.4.3. Raman spectra

Raman spectra of fluid inclusions from run #14 (800 °C, 200 MPa,  $f_{\text{O}_2}$  not buffered; containing 16.4 wt%  $\text{H}_2\text{SO}_4$ , 3.5 wt%  $\text{HCl}$ , 20 wt%  $\text{NaCl}$  and  $4.1 \pm 0.5$  wt%  $\text{Au}$ ) are shown in Fig. 7.5. This is the run that was quenched very rapidly in-situ in order to minimize back-reactions within the fluid during cooling. The spectra shown in Figs. 7.5a,b were taken at room temperature, whereas those of Fig. 7.5c were taken at 100 °C intervals during heating to 600 °C. The Raman spectra obtained from the liquid phase of the fluid inclusions at room temperature (Fig. 7.5a) show a broad absorption band centered on  $3450 \text{ cm}^{-1}$  that is related to  $\text{H}_2\text{O}$ , plus numerous narrower bands in the range of 100 to  $1200 \text{ cm}^{-1}$  that can be assigned to either quartz or various sulfur species (Fig. 7.5a). Of the sulfur species,  $\text{HSO}_4^-$  (with an absorption band located at  $\sim 1050 \text{ cm}^{-1}$ ; Burke, 2001) shows the largest intensity integral area, followed by  $\text{SO}_2$  ( $1151 \text{ cm}^{-1}$ ; Burke, 2001) and  $\text{SO}_4^{2-}$  ( $\sim 983 \text{ cm}^{-1}$ ; Burke, 2001). The ratios of these integral areas to the integral area of  $\text{H}_2\text{O}$  at  $\sim 1640 \text{ cm}^{-1}$  can be used in conjunction with the conversion factors given above to estimate the relative molar abundances of the sulfur species at  $\sim 79\%$  total sulfate and  $\sim 21\%$   $\text{SO}_2$ , which is in agreement with a dominance of  $\text{S}^{6+}$  at oxygen fugacities above  $\sim (\text{Re}-\text{ReO}_2) + 1$  (Binder and Keppler, 2011). The Raman spectra shown in Fig. 7.5b were taken from the liquid portion of a fluid inclusion that – in contrast to most other fluid inclusions in this sample (still run #14) – did not contain any  $\text{Au}$  daughter crystal. The presence of two absorption bands at 324 and  $347 \text{ cm}^{-1}$  indicate the presence of dissolved  $\text{AuCl}_4^-$  in the fluid (Pan and Wood, 1991). However, these absorption bands disappeared during heating to 200 °C and did not re-appear during cooling to room temperature (Fig. 7.5b), whereas a daughter crystal of native gold appeared instead. Similar observations were made by Pan and Wood (1991) and Pokrovski et al. (2009a) during heating of  $\text{AuCl}_4^-$ -bearing solutions in optical cells, from which they concluded that chloride complexes with  $\text{Au}^{3+}$  are unstable at temperatures above  $\sim 200$  °C. The behavior of sulfur in the same fluid inclusion during heating to 600 °C is shown in Fig. 7.5c. All Raman spectra in this Figure were collected in the liquid phase, as vapor–liquid homogenization was not reached yet at 600 °C (5–10 vol% vapor bubble remained). The size of the  $\text{HSO}_4^-$  signal relative to  $\text{SO}_2$  increases with increasing temperature, suggesting that  $\text{S}^{6+}$  becomes more prevalent at high temperature. However, Raman spectra collected from the vapor bubble (supplementary Fig. 7-S1) reveal distinct signals of  $\text{SO}_2$  at 400 °C and 500 °C, whereas no such signal is present at 20 °C, which means that  $\text{SO}_2$

preferentially entered the vapor phase at high temperature, and thus that the  $S^{6+}/S^{4+}$  ratio in the bulk fluid may actually have remained constant.

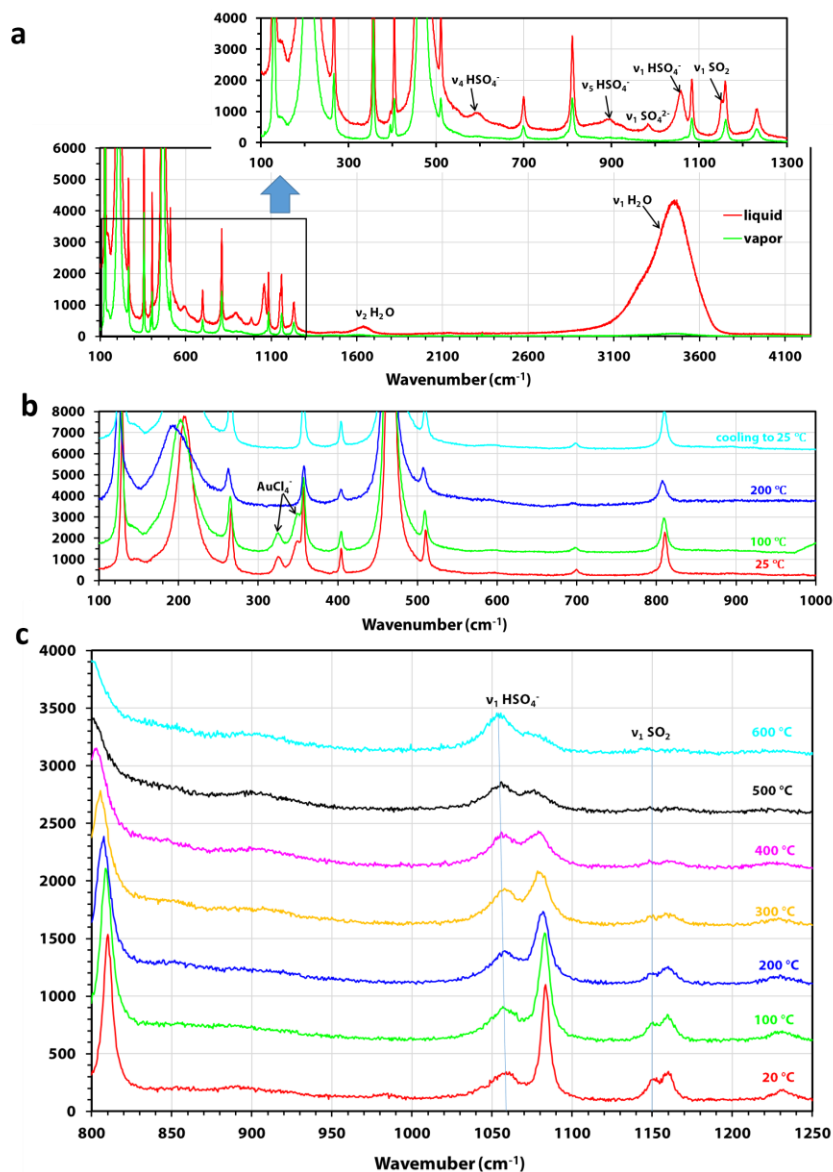


**Fig. 7.5.** Raman spectra taken from quartz-hosted fluid inclusions synthesized at 800 °C, 2 kbar from a starting fluid containing 3.5 wt% HCl, 16.4 wt% H<sub>2</sub>SO<sub>4</sub> and 20 wt% NaCl (HG-AU-14). (a) Spectra taken at ambient temperature from the liquid and the vapor phase of a fluid inclusion. Notice the prevalence of  $S^{6+}$  in the quench fluid. (b) Spectra taken from the liquid phase of a fluid inclusion that was heated from 25 °C to 200 °C and then cooled back to 25 °C. Notice the presence of AuCl<sub>4</sub><sup>-</sup> at until heating to 100 °C, and its absence at 200 °C and after cooling back to room temperature. (c) Spectra taken from the liquid phase of a fluid inclusion that was heated to 600 °C in a modified diamond anvil cell. All non-labeled Raman bands are from quartz.

Additional Raman spectra of fluid inclusions synthesized from aqueous starting fluids containing 3.5 wt% HCl, 16.4 wt% H<sub>2</sub>SO<sub>4</sub> and 20 wt% NaCl at *f*O<sub>2</sub> buffered by Ni-NiO (run #29), Re-ReO<sub>2</sub> (run #28), MnO-Mn<sub>3</sub>O<sub>4</sub> (run #33) or Fe<sub>2</sub>O<sub>3</sub>-Fe<sub>3</sub>O<sub>4</sub> (run #34) are shown in supplementary Figs. 7.2 and 7.3. Hydrogen sulfide (H<sub>2</sub>S; with a band at ~2590 cm<sup>-1</sup>; Burke, 2001) is the only sulfur species present in the run buffered at Ni-NiO, whereas SO<sub>2</sub> dominates at Re-ReO<sub>2</sub> (~60 mol% SO<sub>2</sub> and ~40 mol% HSO<sub>4</sub><sup>-</sup> according to the integrated intensity area ratios; supplementary Fig. 7-S2). With further increase in *f*O<sub>2</sub> the amount of sulfate relative to that of SO<sub>2</sub> increases (supplementary Fig. 7-S3; ~49% total sulfate vs. ~51% SO<sub>2</sub> at MnO-Mn<sub>3</sub>O<sub>4</sub>; ~58% total sulfate vs. ~42% SO<sub>2</sub> at Fe<sub>2</sub>O<sub>3</sub>-Fe<sub>3</sub>O<sub>4</sub>). However, the relative abundance of sulfate at the MnO-Mn<sub>3</sub>O<sub>4</sub> buffer is still considerably lower than that observed in the unbuffered runs (~79% total sulfate vs. ~21% SO<sub>2</sub>; see above), suggesting that the *f*O<sub>2</sub> in the unbuffered runs was higher.

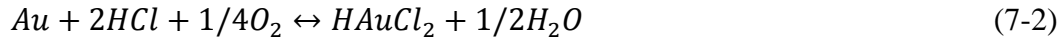
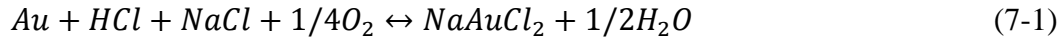
To test our ability to detect the potential presence of S<sub>3</sub><sup>-</sup> (Pokrovski and Dubrovinsky, 2011; Jacquemet et al., 2014) we also synthesized fluid inclusions from an aqueous solution containing 2 wt% KOH, to which 2 wt% elemental sulfur and 20 wt% NaCl were added in solid form (run #37). At room temperature the liquid phase of these fluid inclusions contained both SO<sub>4</sub><sup>2-</sup> (~983 cm<sup>-1</sup>) and H<sub>2</sub>S (~2590 cm<sup>-1</sup>), while the vapor phase contained H<sub>2</sub>S (~2613 cm<sup>-1</sup>) and H<sub>2</sub> (~589 cm<sup>-1</sup>; supplementary Fig. 7-S4a). During heating above 200 °C the absorption band of SO<sub>4</sub><sup>2-</sup> in the liquid phase disappeared, whereas a conspicuous new absorption band appeared at 530-540 cm<sup>-1</sup> (supplementary Fig. 7-S4b), which corresponds to the S-S stretching vibration of the trisulfur ion (S<sub>3</sub><sup>-</sup>) described by Pokrovski and Dubrovinsky (2011) and Jacquemet et al. (2014). The fact that no absorption bands appeared in the 530-540 cm<sup>-1</sup> region during the heating of our other samples (supplementary Fig. 7-S5) suggests that the amount of S<sub>3</sub><sup>-</sup> in these fluids was insignificant.

## 7.5. Discussion

### 7.5.1. Au speciation

At first sight, the trends in Fig. 7.4 appear to suggest the existence of a Au complex that involves sodium, chlorine and oxidized sulfur. However, because the abundances of NaCl, HCl, H<sub>2</sub>SO<sub>4</sub> and Na<sub>2</sub>SO<sub>4</sub> are interrelated (see below) this does not necessarily have to be true. We thus first check whether the observed trends can be explained by sulfur-free complexes such as Au-chlorides, as implied by Raman Spectroscopy.

Gold solubility in sulfur-free fluids containing 3.5 wt% HCl and 20 wt% NaCl increases with a slope of ~0.25 in log [Au] vs. log  $fO_2$  diagrams (Figs. 7.4f, 7.6a), suggesting that Au had a valence state of +1 in the Au-bearing complex(es). Potential dissolution reactions are as follows (e.g., Frank et al., 2002, Hanley et al., 2005, Zajacz et al., 2010):



The fact that Au solubility increases with a slope of ~1 in the log [Au] vs. log [NaCl] diagram (Fig. 7.6b) suggests that reaction (7-1) dominates and thus that that gold dissolved mainly in the form of NaAuCl<sub>2</sub> in sulfur-free fluids investigated in this study, consistent with the findings of Zajacz et al. (2010).

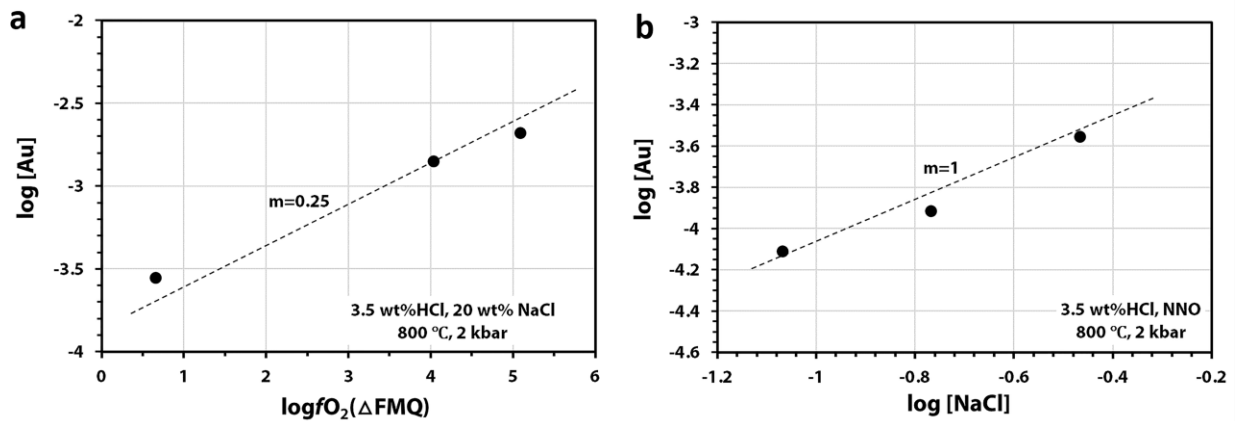


**Fig. 7.6.** Logarithmic plots showing the Au solubility in sulfur-free fluids at 800 °C, 2 kbar as a function of: (a)  $fO_2$  relative to the fayalite-magnetite-quartz (FMQ) buffer, and (b) starting NaCl concentration. All concentrations are given in moles per 100 g.

In the H<sub>2</sub>SO<sub>4</sub>-bearing experiments, Au solubility increases with increasing NaCl content, increasing HCl content, and increasing H<sub>2</sub>SO<sub>4</sub> content (Figs. 7.4a,b,c). However, in contrast to the sulfur-free experiments, these plots may not really reflect the effects of individual variables, but rather the combined effects of several variables because the concentrations of NaCl, H<sub>2</sub>SO<sub>4</sub>, HCl and Na<sub>2</sub>SO<sub>4</sub> are related to each other by the reaction:



Notice that this reaction is independent of  $f\text{O}_2$  and thus is in accord with the internally  $f\text{O}_2$ -buffered nature of the experiments shown in Figs. 7.4a-e. Actual abundances of the fluid species  $\text{H}_2\text{SO}_4$ ,  $\text{HSO}_4^-$ ,  $\text{SO}_4^{2-}$ ,  $\text{Na}_2\text{SO}_4$ ,  $\text{NaSO}_4^-$ ,  $\text{HCl}$ ,  $\text{Cl}^-$  and  $\text{NaCl}$  at 800 °C and 2 kbar were calculated using SUPCRT/SLOP98 and thermodynamic data of Shock et al. (1997) and Sverjensky et al. (1997), except for  $\text{H}_2\text{SO}_4$  which stability was estimated from electrical conductance data of Quist et al. (1965). The results suggest that the species  $\text{H}_2\text{SO}_4$ ,  $\text{Na}_2\text{SO}_4$  and  $\text{HCl}$  are almost fully associated at these P-T conditions, and that the reaction constant  $K$  for equation (7-4) is about 0.4 (i.e., the reaction goes ca. 30% to the right). If the Gibbs free energy for  $\text{NaSO}_4^-$  is taken from Pokrovski et al. (1995) (assuming a constant stepwise association from  $\text{SO}_4^{2-} + \text{Na}^+ = \text{NaSO}_4^-$  to  $\text{NaSO}_4^- + \text{Na}^+ = \text{Na}_2\text{SO}_4$ ), then  $K$  turns out at about 1.0 (i.e., the reaction goes 50% to the right). However, the uncertainties associated with these calculations are high (ca.  $\pm$  half a log unit; pers. comm. D. Dolejs). We thus calculated the abundances of  $\text{NaCl}$ ,  $\text{H}_2\text{SO}_4$ ,  $\text{HCl}$  and  $\text{Na}_2\text{SO}_4$  in the fluids at 800 °C and 2 kbar for hypothetical  $K$ -values of 0.1, 0.4, 1.0 and 4.0 and determined the effects of individual variables ( $\text{NaCl}$ ,  $\text{HCl}$ ,  $\text{H}_2\text{SO}_4$  content) on Au solubility via multiple linear regression (supplementary material). The results are summarized in Table 7.2. At an assumed  $K$ -value of 0.1 the solubility of gold would have to strongly decrease with increasing  $\text{NaCl}$  concentration in the fluid, which stands marked contrast to the qualitative trend Fig. 7.4a. Therefore, this  $K$ -value seems unreasonable. On the other hand, at a  $K$ -value of 0.4 the solubility of Au solubility is predicted to increase with a slope of  $0.9 \pm 0.6$  with increasing  $\text{NaCl}$  concentration, with a slope of  $1.2 \pm 0.5$  with increasing  $\text{HCl}$  concentration, and with a slope of  $0.7 \pm 0.4$  with increasing  $\text{H}_2\text{SO}_4$  concentration, which is in agreement with the qualitative trends in Figs. 7.4a, b and c. These slopes are in quantitative agreement (within error) with Au dissolution via the reaction:



The slopes obtained with a  $K$ -value of 1.0 are consistent with this reaction, too, whereas the slopes obtained with a  $K$ -value of 4.0 do not fit (the slope for  $\text{NaCl}$  is too low; the one for  $\text{HCl}$  is too high). Based on the fact that the  $K$ -values of 0.4 and 1.0 were our best estimates (as they represent actually calculated values) and that  $\text{NaAuCl}_2$  was already tentatively identified in our S-free

experiments and in similar experiment performed by Zajacz et al. (2010), we conclude that gold dissolved mainly in the form of  $\text{NaAuCl}_2$  also in our sulfate-bearing experiments.

**Table 7.2**

Summary of results from multiple linear regression analysis of the equation:  $\log [\text{Au}] = a \cdot \log[\text{NaCl}] + b \cdot \log[\text{HCl}] + c \cdot \log[\text{H}_2\text{SO}_4]$

	a			b			c		
K=0.1	-4.5	±	1.1	3.0	±	0.7	0.5	±	0.8
K=0.4	0.9	±	0.6	1.2	±	0.5	0.7	±	0.4
K=1.0	0.7	±	0.7	1.5	±	0.5	0.5	±	0.4
K=4.0	0.2	±	0.7	2.2	±	0.6	0.2	±	0.4

### 7.5.2. Comparison with Au solubility data of previous studies

Since at 800 °C and 2 kbar the reaction (4) proceeds only 30-50% to the right (see above) the solubility trends in Figs. 7.4a and 7.4c reflect indeed mostly the effect of NaCl and HCl, respectively, and thus can be compared with trends observed in previous studies. In our experiments Au solubility increased with increasing fluid salinity up to a salinity of 20-30 wt%, after which it decreases again (Fig. 7.4a). Over the salinity range of 5-20 wt% NaCl Au solubility increases by ca. a factor of three. These results are consistent with the positive correlation between Au solubility and salinity (2-19 wt%  $\text{NaCl}_{\text{equiv}}$ ) noticed by Simon et al. (2005), and they agree with the observation of Hanley et al. (2005) that Au solubility decreases with increasing NaCl from 20 wt% to 70 wt%. An increase in the HCl-content of our starting fluids from 0.2 to 2.0 wt% led to a ~10-fold increase in Au solubility (Fig. 7.4c). This finding agrees with the data of Zajacz et al. (2010), but it partly contrasts with the study of Frank et al. (2002), who noticed that Au solubility in sulfur-free NaCl-KCl brines 800 °C, 100 MPa at the Ni-NiO buffer is independent of the HCl content in the range of 0.3-1.1 wt% HCl, but increases with increasing HCl content at higher HCl concentrations. The effect of temperature on Au solubility is difficult to constrain in our experiments because it affects also the fluid speciation, hence the trends in Fig. 7.4d reflect the combined effects of both temperature and changing fluid speciation. Gold solubility in our fluids with 16.4 wt%  $\text{H}_2\text{SO}_4$  increases by a factor of about three over the temperature interval of 500 to 800 °C. A slightly larger temperature effect was noticed in the  $\text{H}_2\text{S}$ -bearing fluids studied by Loucks and Mavrogenes (1999), and in the sulfur-free fluids studied by Hanley et al. (2005), but

also in these studies Au solubility was probably indirectly affected by changes in fluid speciation. In our experiments Au solubility increases  $\pm$ linearly by a factor of eight as  $fO_2$  is increased from the NiNiO-buffer to the hematite-magnetite buffer (Fig. 7.4f). Compared to fluid salinity, HCl-content and  $fO_2$  the amount of sulfur in the fluid has relatively little influence on the Au solubility in our experiments (Fig. 7.4f): at  $fO_2$  conditions buffered by hematite-magnetite, Au solubility increases by only about a factor of two as the sulfur content is increased from 0 and 16.4 wt%  $H_2SO_4$ . Interestingly, a similarly small increase is observed at the Ni-NiO-buffer. This result stands in marked contrast to the work of Zajacz et al. (2010), who found that addition of 10 wt%  $H_2S$  to fluids containing 3 wt% NaCl and 0.3 wt% HCl leads to an increase in Au solubility by a factor of 50 at 1000 °C and 1.5 kbar. An even larger solubility increase (up to a factor of 30 relative to  $H_2S$ ) was noticed by Pokrovski et al. (2015) at 350 °C and 400-600 bar in fluids rich in  $S_3^{2-}$ . On the other hand, recent experiments of Zajacz et al. (2017) performed at 650 °C / 0.9 kbar and 900 °C / 1.3 kbar revealed that addition of 4 wt%  $H_2S$  to fluids containing 5 wt%  $NaCl_{equiv}$  and 0.7 wt% HCl leads to an increase in Au solubility by only a factor of 2-3 and 3-7, respectively. Hence, the effect of sulfur on the solubility of Au in fluids at oxygen fugacities  $<FMQ+1.5$  depends strongly on experimental conditions. For oxidized fluids such as the ones that formed porphyry Cu deposits the effect of adding sulfur appears to be small.

In summary, Au solubility in oxidized fluids depends most strongly on the HCl-content, followed by  $fO_2$ , fluid salinity and then temperature (the latter referring to a temperature interval of 300 °C). The amount of oxidized sulfur present in the fluid has comparatively little influence.

### **7.5.3. Implications for porphyry Cu-Au ore formation**

Linear extrapolation of our two geologically realistic experiments performed at 750 °C and 850 °C at the MnO-Mn<sub>3</sub>O<sub>4</sub>  $fO_2$  buffer (runs #48 and 49; containing 7 wt% NaCl, 1 wt% S, and 1.1 wt% HCl) to lower temperatures suggests that the Au solubility at  $\log fO_2 = FMQ+4$  at 600 °C is on the order of 600 ppm. It needs to be noted that this approach is rather rough because Au solubility depends also on fluid speciation, which is unlikely to change linearly. Similarly, based on the trend in Fig. 7.4f the Au solubility can be estimated at  $\sim$ 1000 ppm at  $fO_2$  conditions near the hematite-magnetite buffer (i.e., 5 log units above FMQ) at 600 °C. Higher fluid salinities may result in up

to three times higher Au solubilities (Fig. 7.4a). Hence, real porphyry Cu-Au-forming fluids at 600 °C should be able to dissolve on the order of 600-3000 ppm Au, depending on fluid salinity.

These values stand in marked contrast to Au concentrations of only 0.2-1.3 ppm measured in natural brines trapped at 500-680 °C and oxidized conditions ( $S^{6+}$  dominant) in porphyry Cu-Au ( $\pm$ Mo) environment (Ulrich et al., 1999; Ulrich et al., 2002; Williams-Jones and Heinrich, 2005; Seo et al., 2009; 2012), implying that these natural brines were strongly Au-undersaturated. The same conclusion was reached by Pokrovski et al. (2014) for temperatures  $>500$  °C, whereas at 400 °C the predicted Au solubilities overlap with Au contents measured in natural fluid inclusions. However, in Au-rich porphyry Cu deposits most of the Cu and Au appears to have precipitated at temperatures  $>500$  °C during potassic alteration (Sillitoe, 1995, 2010), which supports the hypothesis that the very small (typically  $<20$   $\mu$ m) Au particles in these deposits did not precipitate from fluids, but exsolved from Au-bearing bornite during cooling (Simon et al., 2000; Kesler et al., 2002). These observations suggest that Au precipitation in Au-rich porphyry Cu deposits is not directly controlled by the parameters discussed above, but indirectly by the factors that control the precipitation and spatial distribution of Au-rich hydrothermal sulfides such as bornite.

## 7.6. Conclusions

This work represents the first systematic study on Au solubility in sulfur-bearing magmatic-hydrothermal fluids at highly oxidized conditions. The results suggest that Au solubility is most strongly affected by the HCl content of the fluid, followed by  $fO_2$  and then fluid salinity and temperature. Compared to these factors the amount of oxidized sulfur present in the fluid has relatively little influence. Based on the observed Au solubility trends and multiple linear regression analysis of computed fluid species at experimental conditions we conclude that gold dissolved dominantly in the form of  $NaAuCl_2$ . Gold solubilities extrapolated to T-X- $fO_2$  conditions representative of porphyry Cu-Au-forming fluids are at least two orders of magnitude higher than actual Au concentrations measured in natural fluids inclusions, which means that at early mineralization stages around 600 °C the natural fluids were strongly Au-undersaturated. Therefore, the Au content of high-temperature mineralization associated with potassic alteration is unlikely to be controlled by factors that control the solubility of native Au, but rather by factors that control

the precipitation of Au-rich hydrothermal sulfides such as bornite, from which native Au may exsolve during cooling.

### 7.7. Acknowledgments

We would like to thank David Dolejs for calculating the speciation of the major fluid components at experimental conditions and for showing us how to interpret these data with regard to Au speciation. Hans Keppler and Dan Frost are thanked for scientific advice and for help with Raman analysis, Huaiwei Ni for discussion on sulfur speciation, Hubert Schulze for preparing quartz pieces, and Ulrike Trenz for help with chemicals. We are also indebted to Gleb Pokrovski, Zoltan Zajacz and Adam Simon for their thoughtful reviews, which greatly helped to improve the manuscript. Haihao Guo greatly acknowledges financial support from the China Scholarship Council (CSC) program.

### 7.8. References

- Bassett W.A., Shen A., Bucknum M. and Chou I.M. (1993) A new diamond anvil cell for hydrothermal studies to 2.5 GPa and from -190 to 1200 °C. *Rev. Sci. Instrum.* **64**, 2340-2345.
- Binder B. and Keppler H. (2011) The oxidation state of sulfur in magmatic fluids. *Earth Planet. Sci. Lett.* **301**, 190-198.
- Burnham C.W. (1979) Magmas and hydrothermal fluids, In *Geochemistry of Hydrothermal Ore Deposits* (ed. H.L. Barnes), John Wiley, New York, pp. 71-136.
- Burnham C.W. and Ohmoto H. (1980) Late-stage processes of felsic magmatism, In *Soc. Mining Geol. Jpn.* (eds. S. Ishihara and S. Takenouchi). Mining Geology, Special Issue 8, pp. 1-11.
- Burke E.A. (2001) Raman microspectrometry of fluid inclusions. *Lithos* **55**, 139-158.
- Chou I.-M. (1986) Permeability of precious metals to hydrogen at 2 kb total pressure and elevated temperatures. *Am. J. Sci.* **286**, 638-658.
- Chou I.-M. (1987) Oxygen buffer hydrogen sensor techniques at elevated pressures and temperatures (eds. G.C. Ulmer and H.L. Barnes). *Hydrothermal Experimental Techniques*, pp. 61-99.

- Frank M.R., Candela P.A., Piccoli P.M. and Glascock M.D. (2002) Gold solubility, speciation, and partitioning as a function of HCl in the brine-silicate melt-metallic gold system at 800 °C and 100 MPa. *Geochim. Cosmochim. Acta* **66**, 3719-3732.
- Frost B.R. (1991) Introduction to oxygen fugacity and its petrologic importance. *Rev. Mineral. Geochem.* **25**, 1-9.
- Gibert F., Pascal M.L. and Pichavant M. (1998) Gold solubility and speciation in hydrothermal solutions: Experimental study of the stability of hydrosulphide complex of gold (AuHS °) at 350 to 450 °C and 500 bars. *Geochim. Cosmochim. Acta* **62**, 2931-2947.
- Günther D., Audétat A., Frischknecht R. and Heinrich C.A. (1998) Quantitative analysis of major, minor and trace elements in fluid inclusions using laser ablation inductively coupled plasma mass spectrometry. *J. Anal. At. Spectrom.* **13**, 263-270.
- Hanley J.J., Pettke T., Mungall J.E. and Spooner E.T.C. (2005) The solubility of platinum and gold in NaCl brines at 1.5 kbar, 600 to 800°C: A laser ablation ICP-MS pilot study of synthetic fluid inclusions. *Geochim. Cosmochim. Acta* **69**, 2593-2611.
- Hedenquist J. and Richards J. (1998) The influence of geochemical techniques on the development of genetic models for porphyry copper deposits, In *Techniques in hydrothermal ore deposits geology* (eds. J.P. Richards and P.B. Larson). *Rev. Econ. Geol.* **10**, pp. 235-256.
- Heinrich C.A., Meier D., Erni M., von Quadt A. and Márquez-Zavalía M. (2011) Life-times and scales of Cu-Au-mineralizing magmatic-hydrothermal processes: Farallón Negro (Argentina), 11th Bienn SGA Meeting, Antofagasta, pp. 3-6.
- Heinrich C., Pettke T., Halter W., Aigner-Torres M., Audétat A., Günther D., Hattendorf B., Bleiner D., Guillong M. and Horn I. (2003) Quantitative multi-element analysis of minerals, fluid and melt inclusions by laser-ablation inductively-coupled-plasma mass-spectrometry. *Geochim. Cosmochim. Acta* **67**, 3473-3497.
- Jacquemet N., Guillaume D., Zwick A. and Pokrovski G.S. (2014) In situ Raman spectroscopy identification of the S<sub>3</sub><sup>-</sup> ion in S-rich hydrothermal fluids from synthetic fluid inclusions. *Am. Mineral.* **99**, 1109-1118.
- Jochum K.P., Weis U., Stoll B., Kuzmin D., Yang Q., Raczek I., Jacob D.E., Stracke A., Birbaum K., Frick D.A., Günther D. and Enzweiler J. (2011) Determination of Reference Values for NIST SRM 610-617 Glasses Following ISO Guidelines. *Geostand. Geoanal. Res.* **35**, 397-429.

- Keith J. D., Whitney J. A., Hattori K., Ballantyne G. H., Christiansen E. H., Barr D. L., Cannan T. M. and Hook C. J. (1997) The role of magmatic sulfides and mafic alkaline magmas in the Bingham and Tintic mining districts, Utah. *J. Petrol.* **38**, 1679-1690.
- Kesler S.E. (1994) Mineral resources, economics, and the environment. McMillan.
- Kesler S. E., Chryssoulis S. L. and Simon G. (2002) Gold in porphyry copper deposits: its abundance and fate. *Ore Geol. Rev.* **21**, 103-124.
- Kokh M.A., Lopez M., Gisquet P., Lanzasova A., Candaudap F., Besson P. and Pokrovski G.S. (2016) Combined effect of carbon dioxide and sulfur on vapor–liquid partitioning of metals in hydrothermal systems. *Geochim. Cosmochim. Acta* **187**, 311-333.
- Kokh M.A., Akinfiyev N.N., Pokrovski G.S., Salvi S. and Guillaume D. (2017) The role of carbon dioxide in the transport and fractionation of metals by geological fluids. *Geochim. Cosmochim. Acta* **197**, 433-466.
- Landtwing M.R., Pettke T., Halter W.E., Heinrich C.A., Redmond P.B., Einaudi M.T. and Kunze K. (2005) Copper deposition during quartz dissolution by cooling magmatic–hydrothermal fluids: the Bingham porphyry. *Earth Planet. Sci. Lett.* **235**, 229-243.
- Li Y. and Audétat A. (2009) A method to synthesize large fluid inclusions in quartz at controlled times and under unfavorable growth conditions. *Am. Mineral.* **94**, 367-371.
- Liu X., Lu X., Wang R., Zhou H. and Xu S. (2011) Speciation of gold in hydrosulphide-rich ore-forming fluids: Insights from first-principles molecular dynamics simulations. *Geochim. Cosmochim. Acta* **75**, 185-194.
- Loucks R.R. and Mavrogenes J.A. (1999) Gold solubility in supercritical hydrothermal brines measured in synthetic fluid inclusions. *Science* **284**, 2159-2163.
- Ni H. and Keppler H. (2012) In-situ Raman spectroscopic study of sulfur speciation in oxidized magmatic-hydrothermal fluids. *Am. Mineral.* **97**, 1348-1353.
- O'Neill H. C. and Pownceby M. I. (1993) Thermodynamic data from redox reactions at high temperatures. II. The MnO-Mn<sub>3</sub>O<sub>4</sub> oxygen buffer, and implications for the thermodynamic properties of MnO and Mn<sub>3</sub>O<sub>4</sub>. *Contrib. Min. Petrol.* **114**, 315-320.
- Pan P. and Wood S.A. (1991) Gold-chloride complexes in very acidic aqueous solutions and at temperatures 25–300 °C: a laser Raman spectroscopic study. *Geochim. Cosmochim. Acta* **55**, 2365-2371.

- Pokrovski G.S., Akinfiyev N.N., Borisova A.Y., Zotov A.V. and Kouzmanov K. (2014) Gold speciation and transport in geological fluids: insights from experiments and physical-chemical modelling, In *Gold-Transporting Fluids in the Earth's Crust* (eds. P. Garofalo and E. Ripley), Geological Society, London, Special Publications 402, pp. 9-70.
- Pokrovski G.S. and Dubrovinsky L.S. (2011) The  $S_3^-$  ion is stable in geological fluids at elevated temperatures and pressures. *Science* **331**, 1052-1054.
- Pokrovski G.S., Kokh M.A., Guillaume D., Borisova A.Y., Gisquet P., Hazemann J.-L., Lahera E., Del Net W., Proux O. and Testemale D. (2015) Sulfur radical species form gold deposits on Earth. *Proceedings of the National Academy of Sciences* **112**, 13484-13489.
- Pokrovski G.S., Tagirov B.R., Schott J., Bazarkina E.F., Hazemann J.-L. and Proux O. (2009a) An in situ X-ray absorption spectroscopy study of gold-chloride complexing in hydrothermal fluids. *Chem. Geol.* **259**, 17-29.
- Pokrovski G.S., Tagirov B.R., Schott J., Hazemann J.-L. and Proux O. (2009b) A new view on gold speciation in sulfur-bearing hydrothermal fluids from in situ X-ray absorption spectroscopy and quantum-chemical modeling. *Geochim. Cosmochim. Acta* **73**, 5406-5427.
- Pownceby M.I. and O'Neill H.S.C. (1994) Thermodynamic data from redox reactions at high temperatures. IV. Calibration of the Re-ReO<sub>2</sub> oxygen buffer from EMF and NiO + Ni-Pd redox sensor measurements. *Contrib. Mineral. Petrol.* **118**, 130-137.
- Quist A. S., Marshall W. L. and Jolley H. R. (1965) Electrical conductances of aqueous solutions at high temperature and pressure. II. The conductances and ionization constants of sulfuric acid-water solutions from 0 to 800°C and at pressures up to 4000 bars. *J. Phys. Chem.* **69**, 2726-2735.
- Redmond P., Einaudi M., Inan E., Landtwing M. and Heinrich C. (2004) Copper deposition by fluid cooling in intrusion-centered systems: New insights from the Bingham porphyry ore deposit, Utah. *Geology* **32**, 217-220.
- Robb L.J. (2005) Introduction to ore-forming processes. Oxford, Blackwell, p. 373.
- Rusk B.G., Reed M.H., Dilles J.H., Klemm L.M. and Heinrich C.A. (2004) Compositions of magmatic hydrothermal fluids determined by LA-ICP-MS of fluid inclusions from the porphyry copper-molybdenum deposit at Butte, MT. *Chem. Geol.* **210**, 173-199.
- Rusk B.G., Miller B.J. and Reed M.H. (2008) Fluid inclusion evidence for the formation of main stage polymetallic base-metal veins, Butte, Montana, USA.

- Seo J.H., Guillong M., Aerts M., Zajacz Z. and Heinrich, C.A. (2011) Microanalysis of S, Cl, and Br in fluid inclusions by LA-ICP-MS. *Chem. Geol.* **284**, 35-44.
- Seo J.H., Guillong M. and Heinrich C.A. (2009) The role of sulfur in the formation of magmatic–hydrothermal copper–gold deposits. *Earth Planet. Sci. Lett.* **282**, 323-328.
- Seo J.H., Guillong M. and Heinrich C.A. (2012) Separation of molybdenum and copper in porphyry deposits: The roles of sulfur, redox, and pH in ore mineral deposition at Bingham Canyon. *Econ. Geol.* **107**, 333-356.
- Shock E. L., Sassani D. C., Willis M. and Sverjensky D. A. (1997) Inorganic species in geologic fluids: Correlations among standard molal thermodynamic properties of aqueous ions and hydroxide complexes. *Geochim. Cosmochim. Acta* **61**, 907-950.
- Simon G., Kesler S. E. and Essene E. J. (2000) Gold in porphyry copper deposits: Experimental determination of the distribution of gold in the Cu-Fe-S system at 400° to 700°C. *Econ. Geol.* **95**, 259-270.
- Simon A.C., Frank M.R., Pettke T., Candela P.A., Piccoli P.M. and Heinrich C.A. (2005) Gold partitioning in melt-vapor-brine systems. *Geochim. Cosmochim. Acta* **69**, 3321-3335.
- Simon A.C., Pettke T., Candela P.A., Piccoli P.M. and Heinrich C.A. (2007) The partitioning behavior of As and Au in S-free and S-bearing magmatic assemblages. *Geochim. Cosmochim. Acta* **71**, 1764-1782.
- Stavast W. J. A., Keith J. D., Christiansen E. H., Dorais M. J., Larocque A. and Evans N. (2006) The fate of magmatic sulfides during intrusion or eruption, Bingham and Tintic Districts, Utah. *Econ. Geol.* **101**, 329-345.
- Stefanova E., Driesner T., Zajacz Z., Heinrich C.A., Petrov P. and Vasilev Z. (2014) Melt and Fluid Inclusions in Hydrothermal Veins: The Magmatic to Hydrothermal Evolution of the Elatsite Porphyry Cu-Au Deposit, Bulgaria. *Econ. Geol.* **109**, 1359-1381.
- Sverjensky D. A., Shock E. L. and Helgeson H. C. (1997) Prediction of the thermodynamic properties of aqueous metal complexes to 1000°C and 5 kb. *Geochim. Cosmochim. Acta* **61**, 1359-1412.
- Tagirov B.R., Salvi S., Schott J. and Baranova N.N. (2005) Experimental study of gold-hydrosulphide complexing in aqueous solutions at 350–500°C, 500 and 1000 bars using mineral buffers. *Geochim. Cosmochim. Acta* **69**, 2119-2132.

- Ulrich T., Günther D. and Heinrich C. (1999) Gold concentrations of magmatic brines and the metal budget of porphyry copper deposits. *Nature* **399**, 676-679.
- Ulrich T., Günther D. and Heinrich C. A. (2002) The evolution of a porphyry Cu-Au deposit, based on LA-ICP-MS analysis of fluid inclusions: Bajo de la Alumbrera, Argentina. *Econ. Geol.* **97**, 1889-1920.
- Ulrich T., Golding S.D., Kamber B.S., Khin Z. and Taube A. (2003) Different mineralization styles in a volcanic-hosted ore deposit: the fluid and isotopic signatures of the Mt Morgan Au-Cu deposit, Australia. *Ore Geol. Rev.* **22**, 61-90.
- Williams-Jones A.E. and Heinrich C.A. (2005) 100th Anniversary special paper: vapor transport of metals and the formation of magmatic-hydrothermal ore deposits. *Econ. Geol.* **100**, 1287-1312.
- Zajacz Z., Seo J.H., Candela P.A., Piccoli P.M., Heinrich C.A. and Guillong M. (2010) Alkali metals control the release of gold from volatile-rich magmas. *Earth Planet. Sci. Lett.* **297**, 50-56.
- Zajacz Z., Candela P.A. and Piccoli P.M. (2017) The partitioning of Cu, Au and Mo between liquid and vapor at magmatic temperatures and its implications for the genesis of magmatic-hydrothermal ore deposits. *Geochim. Cosmochim. Acta* (submitted).
- Zotov A., Baranova N., Dar'yina T. and Bannykt L. (1989) Gold (I) complexing in the KCl-HCl-H<sub>2</sub>O system at 450°C and 500 atm. *Geochem. Int.* **26**, 66-75.
- Zotov A. Baranova, N., Dar'yina T. and Bannykh L. (1991) The solubility of gold in aqueous chloride fluids at 350–500 °C and 500–1500 atm: Thermodynamic parameters of AuCl<sub>2</sub>– up to 750 °C and 5000 atm. *Geochem. Int.* **28**, 63-71.

## 7.9. Supplementary material

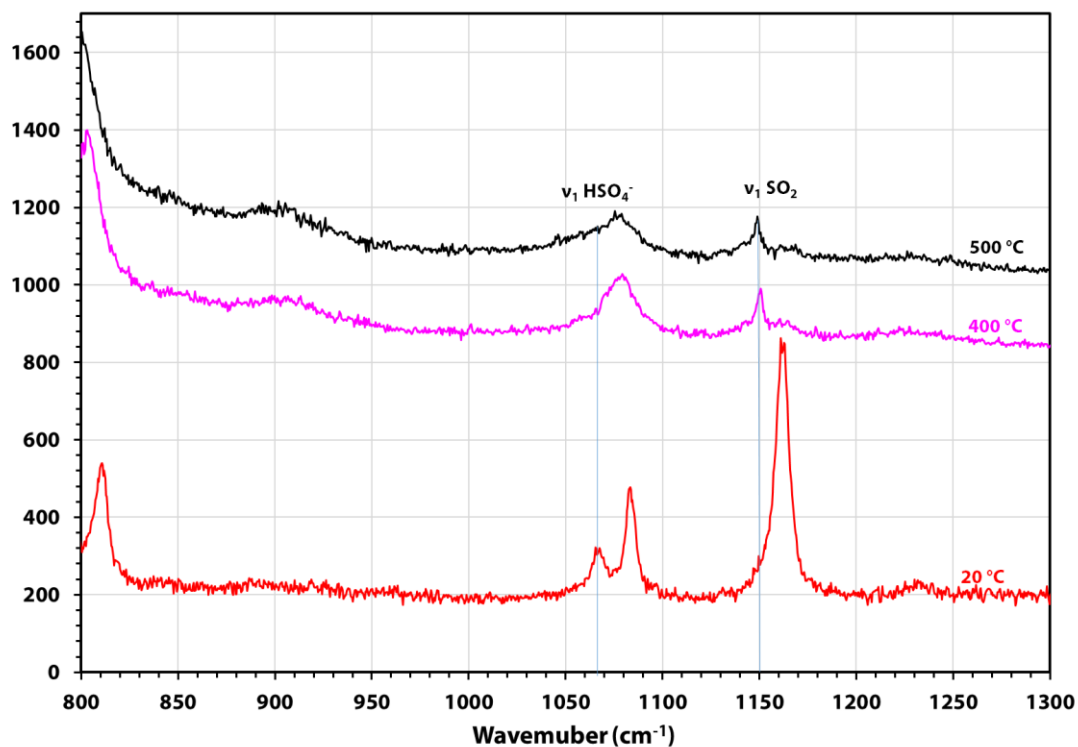


**Fig. 7-S1.** Raman spectra obtained at various temperatures (20, 400 and 500 °C) from the vapor bubble of a fluid inclusion synthesized at 800 °C, 2 kbar from a starting fluid containing 3.5 wt% HCl, 16.4 wt% H<sub>2</sub>SO<sub>4</sub> and 20 wt% NaCl (HG-AU-14). Unlabeled absorption bands are from quartz.

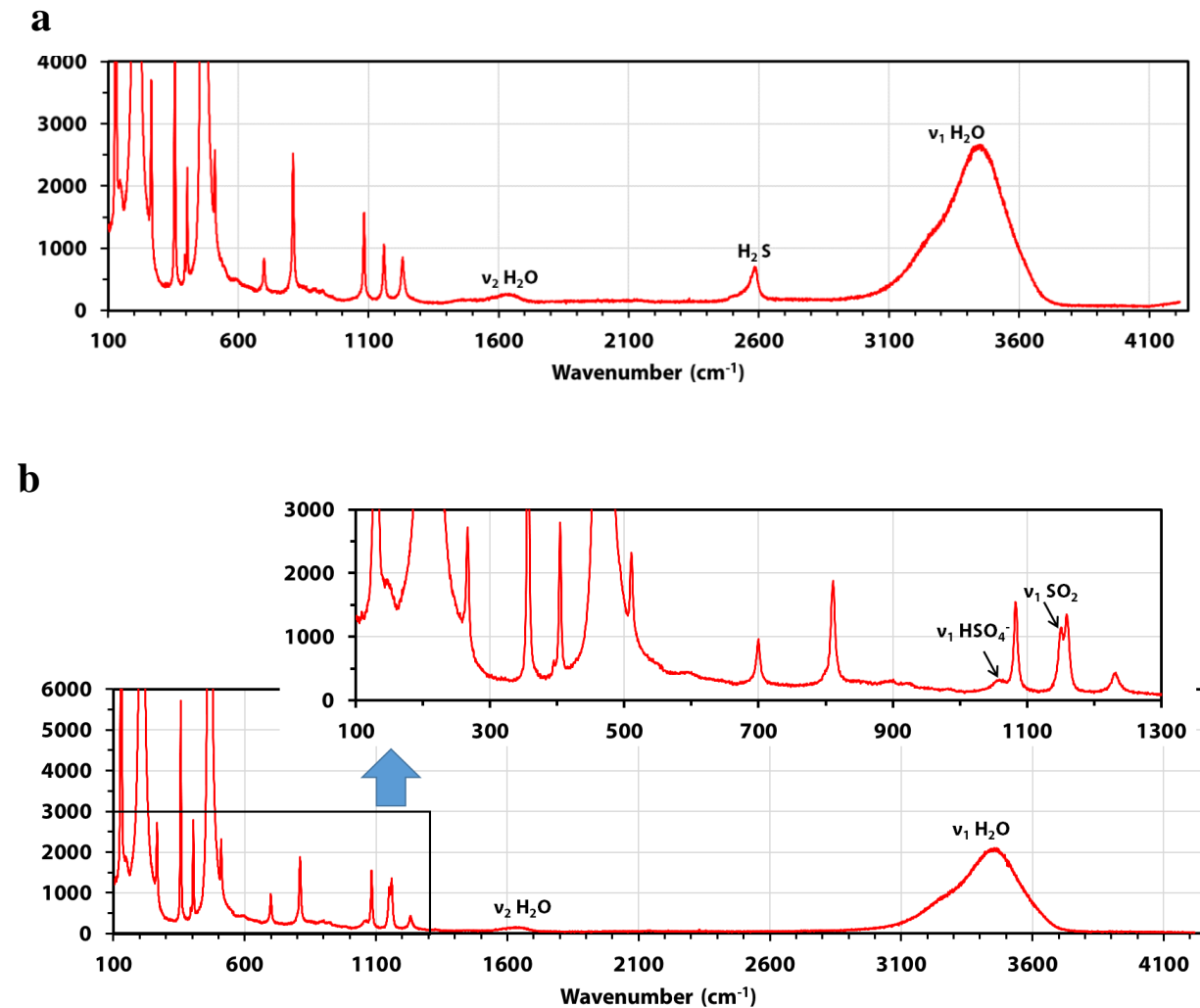


**Fig. 7-S2.** Raman spectra obtained at ambient temperature of the liquid phase of fluid inclusions synthesized at 800 °C, 2 kbar from starting fluids containing 3.5 wt% HCl, 16.4 wt% H<sub>2</sub>SO<sub>4</sub> and 20 wt% NaCl, with  $f\text{O}_2$  buffered at (a) Ni-NiO (HG-AU-29) and (b) Re-ReO<sub>2</sub> (HG-AU-28).

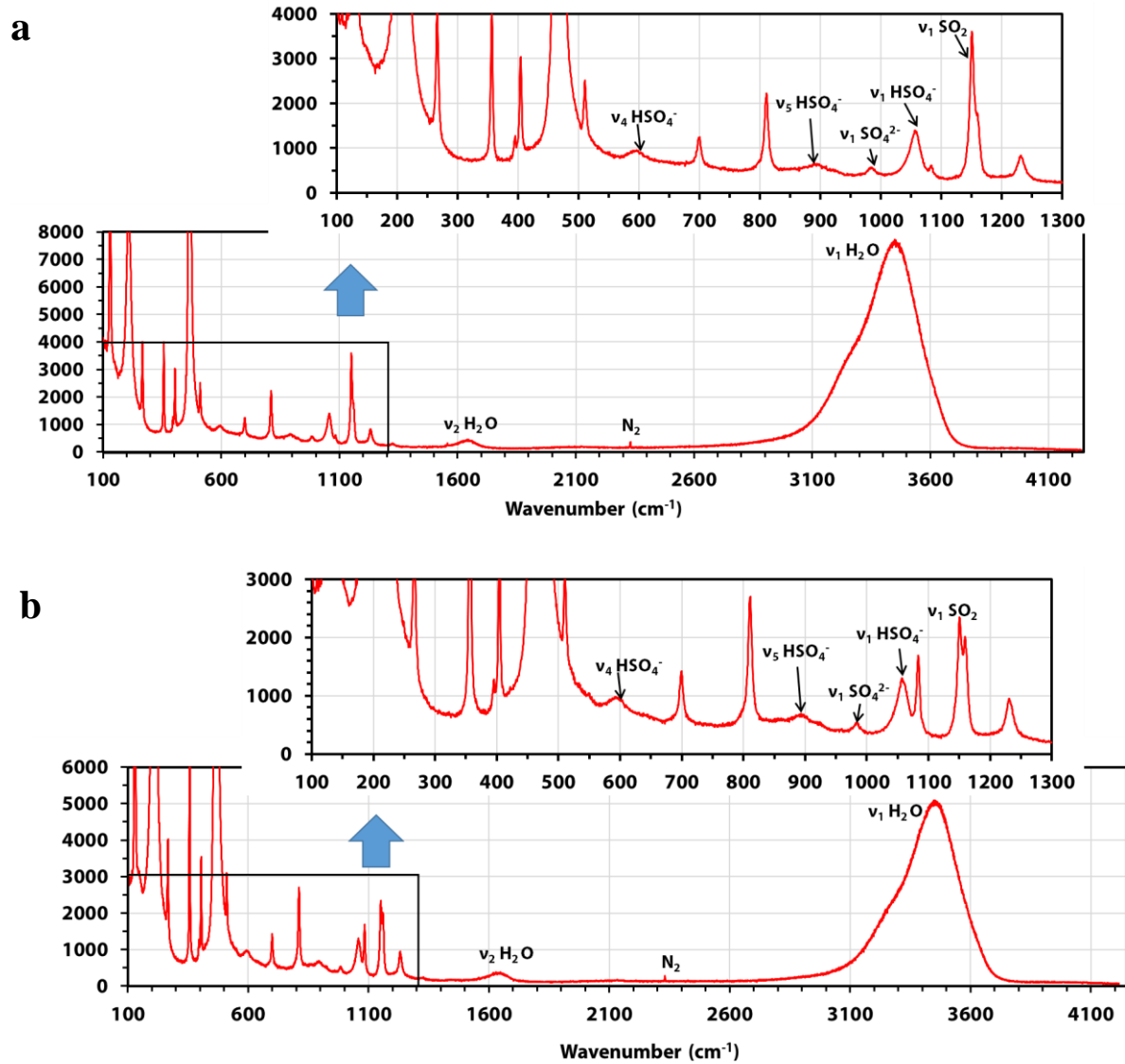


**Fig. 7-S3.** Raman spectra obtained at ambient temperature of the liquid phase of fluid inclusions synthesized at 800 °C, 2 kbar from starting fluids containing 3.5 wt% HCl, 16.4 wt% H<sub>2</sub>SO<sub>4</sub> and 20 wt% NaCl, with  $f_{\text{O}_2}$  buffered at (a) MnO-Mn<sub>3</sub>O<sub>4</sub> (HG-AU-33) and (b) hematite-magnetite (HG-AU-34).

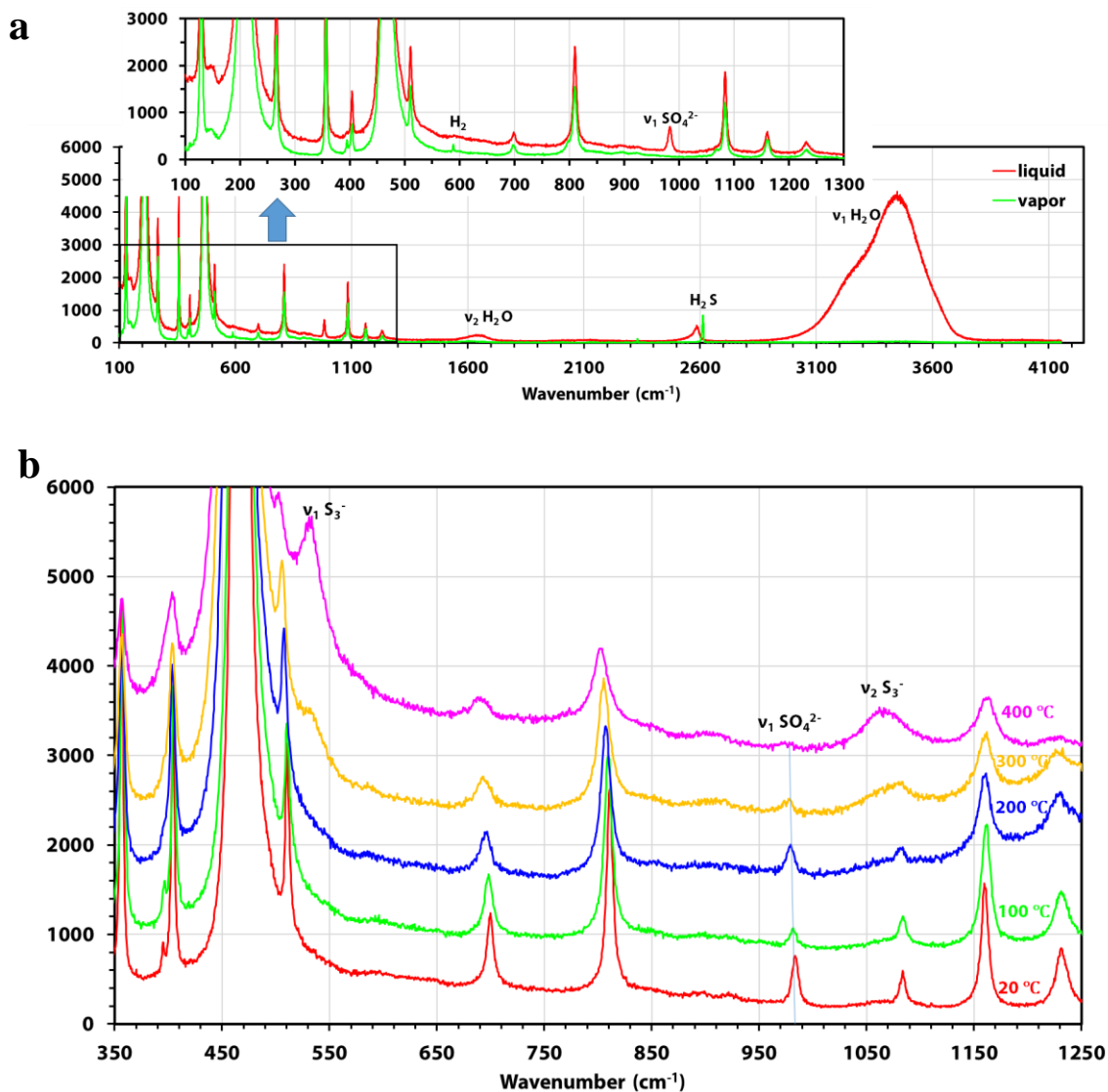


**Fig. 7-S4.** Raman spectra obtained from a fluid inclusion synthesized at 700 °C, 2 kbar from a starting fluid containing 3 wt% native sulfur, 2 wt% KOH and 20 wt% NaCl (a) spectra obtained at ambient temperature from the liquid phase and the vapor phase, Notice the difference between H<sub>2</sub>S that is dissolved in water (broad band at ~2590 cm<sup>-1</sup>; Burke, 2001) and H<sub>2</sub>S vapor (sharp band at 2611 cm<sup>-1</sup>; Burke, 2001). (b) spectra obtained at various temperatures from the liquid phase during heating to 400 °C. Notice the appearance of new absorption bands at ~ 530 cm<sup>-1</sup> and ~1060 cm<sup>-1</sup> during heating that can be ascribed to the formation of the trisulfur ion (S<sub>3</sub><sup>3-</sup>; Pokrovski and Dubrovinsky, 2011; Jacquemet et al., 2014).

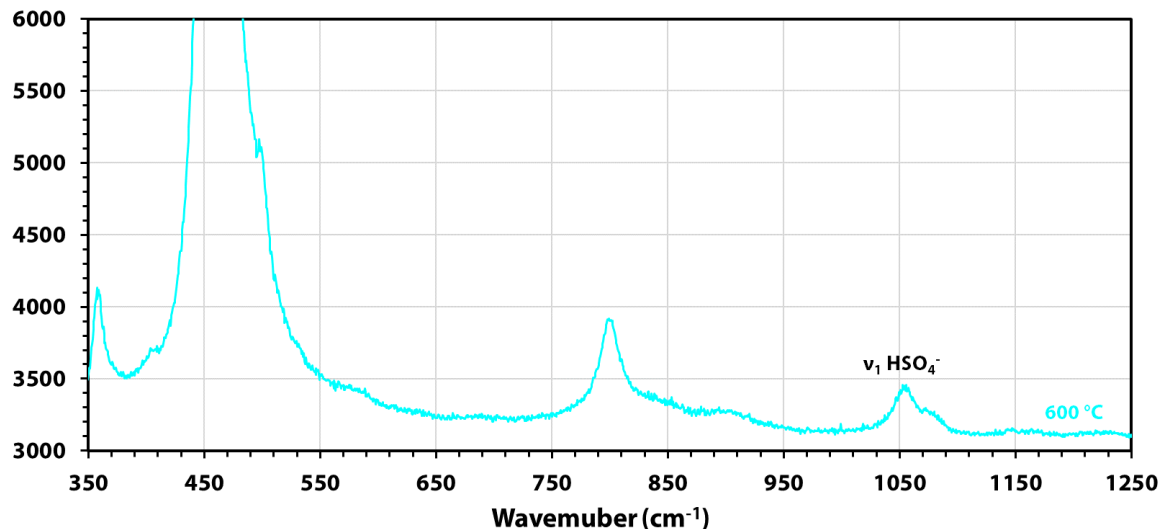


**Fig. 7-S5.** Raman spectrum obtained at 600 °C from the liquid phase of a fluid inclusion that was synthesized at 800 °C and 2 kbar from a starting fluid containing 3.5 wt% HCl, 16.4 wt% H<sub>2</sub>SO<sub>4</sub> and 20 wt% NaCl (HG-AU-14). Notice the absence of an absorption band in the 530-540 cm<sup>-1</sup> region, suggesting that no significant amounts of S<sub>3</sub><sup>-</sup> are present.

### 7.9.1. References

Burke E.A. (2001) Raman microspectrometry of fluid inclusions. *Lithos* **55**, 139-158.

Pokrovski G.S. and Dubrovinsky L.S. (2011) The S<sub>3</sub><sup>-</sup> ion is stable in geological fluids at elevated temperatures and pressures. *Science* **331**, 1052-1054.

Jacquemet N. Guillaume D. Zwick A. and Pokrovski G.S. (2014) In situ Raman spectroscopy identification of the S<sub>3</sub><sup>-</sup> ion in S-rich hydrothermal fluids from synthetic fluid inclusions. *Am. Mineral.* **99**, 1109-1118.

## 8. Gold diffusion into and out of quartz-hosted fluid inclusions during re-equilibration experiments at 600-800 °C and 2 kbar

Haihao Guo, Andreas Audétat

*Bayerisches Geoinstitut, Universität Bayreuth, D-95440 Bayreuth, Germany*

### 8.1. Abstract

Fluid inclusions were synthesized in quartz and subsequently re-equilibrated in fluids of different compositions to investigate whether the Au content of fluid inclusions can be modified via Au diffusion through the host quartz. In one experiment fluid inclusions containing 5 wt% KCl were synthesized in platinum capsules at 2 kbar, 800 °C and then re-equilibrated at the same conditions for 4 days in a fluid containing 20.1 wt% NaCl, 3.5 wt% HCl and ~100 ppm Cs enclosed in a gold capsule. LA-ICP-MS analyses of 5-10 fluid inclusions before and after the re-equilibration experiment demonstrate that the inclusions gained up to 570 ppm Au and up to 0.23 wt% Na during the re-equilibration process. Their unchanged high K-content and the absence of Cs within the inclusions proves that they remained physically closed during the re-equilibration, and thus that Na and Au were gained by diffusion through the quartz lattice. In a similar experiment conducted at 600 °C the fluid inclusions gained up to 140 ppm Au within 14 days. Reverse experiments were conducted by synthesizing Au-bearing fluid inclusions in gold capsules and then re-equilibrating them in platinum capsules, which caused the inclusions to lose up to several hundred ppm Au. In both type of experiments Au diffusion appears to have been driven by Au concentration gradients between the fluid inclusions and the external fluid. Additional experiments were performed to test whether Au is able to diffuse into fluid inclusions in response to loss of H<sup>+</sup>, or indirectly as a consequence of diffusional Cu-gain and corresponding formation of Cu-rich sulfide daughter crystals. However no evidence for Au uptake via such mechanisms was found.

If Au concentrations in natural, quartz-hosted fluid inclusions from magmatic-hydrothermal ore deposits are affected, then they likely lost Au rather than gained it. At temperatures below 400 °C diffusional loss or gain of Au is considered unlikely in magmatic-hydrothermal systems, but potentially was significant in samples from mesothermal Au gold deposits.

Keywords: Gold; Diffusion; Synthetic fluid inclusions; Quartz; Experimental; LA-ICP-MS.

## 8.2. Introduction

Fluid inclusions provide key information on the physical and chemical properties of geological fluids and thus are extensively studied in numerous research fields ranging from low-temperature, diagenetic processes to ultrahigh-pressure metamorphic rocks (e.g., Roedder, 1984; Goldstein and Reynolds, 1994). One of the most active fields of fluid inclusion research is that of hydrothermal ore deposits (e.g., Bodnar et al., 2014) in which the most common host mineral is quartz. Quartz is a particularly suitable host mineral because it is transparent, chemically simple, physically robust, and resistant against alteration and weathering. However, several studies have shown that both the volume and the chemical composition of quartz-hosted fluid inclusions can change after entrapment. For example, it was experimentally demonstrated that quartz-hosted fluid inclusions can gain or lose  $H_2$  (Mavrogenes and Bodnar, 1994), molecular  $H_2O$  (Bakker and Jansen, 1990, 1991; Sterner et al., 1995),  $D_2O$  (Doppler et al., 2013),  $Na^+$ ,  $Cu^+$ ,  $Ag^+$  and  $Li^+$  (Li et al., 2009; Zajacz et al., 2009; Lerchbaumer and Audétat (2012), and that both such compositional changes as well as changes in the inclusion volume can lead to changes in fluid density (e.g., Sterner and Bodnar, 1989; Bakker and Jansen, 1991; Sterner et al., 1995; Diamond et al., 2010; Tarantola et al., 2012; Baumgartner et al., 2014). There is ample evidence that many (if not most) natural fluid inclusions were affected by the same processes (e.g., Hollister, 1988; Hall et al., 1991; Mavrogenes and Bodnar, 1994; Audétat and Günther, 1999; Ridley and Hagemann, 1999; Lerchbaumer and Audétat, 2012; Seo and Heinrich, 2013; Lambrecht and Diamond, 2014; Diamond and Tarantola, 2015).

Small, single-charged ions such as  $H^+$ ,  $Li^+$ ,  $Na^+$ ,  $Cu^+$  and  $Ag^+$  are able to diffuse rapidly through quartz because they fit into the relatively large channels occurring parallel to the c-axis in the quartz structure (Verhoogen, 1952; Kats, 1962; White, 1968; Mortley, 1969; Girardet et al., 1988; Martin, 1988). This property is used in the synthetic quartz manufacturing industry to remove impurities from the grown quartz crystals by means of electrodiffusion (so-called "sweeping"). It was shown that also larger ions such as  $K^+$  (Verhoogen, 1952; Kats, 1962),  $Rb^+$  and  $Cs^+$  (White, 1970) can be mobilized to some extent, but these require much higher activation energies and they diffuse at much slower speed than the small ions mentioned above. In principle, one would expect that also  $Au^+$  (which has an ionic radius similar to that of  $K^+$ , Shannon, 1976) should be able to

diffuse at limited speed through quartz, but the only evidence we were able to find is a study by Suzuki et al. (1995), who reported that they managed to diffuse 10 ppb Au into synthetic quartz crystals via electrodiffusion, and that this uptake of Au was accompanied by a reduction of the number of etch channels.

The present study demonstrates that quartz-hosted fluid inclusions are able to gain or lose hundreds of ppm of Au within a few days at P-T conditions typical of high-temperature magmatic-hydrothermal fluids, provided that suitable Au concentration gradients between the trapped fluid and the external fluid exist.

### **8.3. Methods**

#### **8.3.1. Experimental procedure**

Each experiment consisted of two steps: a pre-run and a re-equilibration run. In the pre-runs, fluid inclusions were synthesized in pieces of etched synthetic quartz measuring  $\sim 1.0 \times 1.6 \times 10$  mm in size using the method described in Li and Audéat (2009). This method produces numerous and large fluid inclusions close to the sample surface by means of growing new quartz over an etched quartz surface. The quartz pieces were loaded with  $\sim 40$  mg aqueous solution (distilled H<sub>2</sub>O with analytical grade NaCl, HCl, KCl, RbCl, CsCl, and/or KOH)  $\pm$  solid NaCl, KCl (any concentrations  $>10$  wt%)  $\pm$  elemental sulfur and a small SiO<sub>2</sub> glass rod into either Pt capsules of 4.0 mm O.D. (outer diameter), 3.7 mm I.D. (inner diameter) and 20 mm length, or into Au capsules of 3.5 mm O.D., 3.1 mm I.D. and 20 mm length (Table 8.1). The capsules were crimped, the welded with a pulsed arc welder while being cooled with wet tissue, then shrunk at  $\sim 1$  kbar H<sub>2</sub>O pressure, and finally weighed again to check for the presence of leaks. Subsequently, the capsules were loaded into rapid-quench, cold-seal pressure vessels made of Inconel 713LC super alloy, in a setup similar to that shown in Matthews et al. (2003). All experiments were conducted at 2 kbar using water as pressure medium. Temperatures were measured with NiCr-Ni (K-type) thermocouples in an external borehole of the cold-seal autoclave. Uncertainties in the temperature and pressure readings are considered  $\pm 5$  °C and  $\pm 30$  bar, respectively. The pre-runs were terminated after 3-8 days by removing the autoclaves from the furnace and allowed to cool isochorically to room temperature within about 40 minutes. All capsules were weighed before and after experiments to ensure that no leaks occur during the experiments. The capsules were then opened with a razor blade and the

pH of solution was checked by pH-indicator paper. The recovered quartz pieces were gently polished to remove excess quartz on the sample surface to facilitate observation in the microscope and the analysis of selected fluid inclusions by LA-ICP-MS.

In the re-equilibration runs, the quartz pieces recovered from pre-runs were loaded together with a new piece of etched quartz and fluid into capsules made of gold, platinum, or Au<sub>95</sub>Cu<sub>05</sub> alloy in the following dimensions: 5.0 mm O.D., 4.6 mm I.D. and 20 mm length (Table 8.1). The new piece of etched quartz served to trap the new external fluid, whereas the fluid inclusions occurring in the pieces recovered from pre-runs diffusively re-equilibrated with the external fluid. All re-equilibration runs were performed at the same P-T conditions as the corresponding pre-runs to avoid any pressure gradients between the re-equilibrating fluid inclusions and the external fluid. At the conclusion of the experiments the capsules were again opened with a razor blade, the pH of the solution was checked by pH-indicator paper, and the recovered quartz pieces were prepared for optical observation and LA-ICP-MS analysis.

### **8.3.2. Analytical methods**

The composition of individual fluid inclusions was measured by Laser-ablation ICP-MS (LA-ICP-MS) using a 193 nm ArF Excimer laser (GeolasPro, Coherent, USA) attached to an Elan DRC-e (Perkin Elmer, Canada) quadruple mass spectrometer (Günther et al., 1998). The laser was operated at a frequency of 10 Hz and  $\sim 10 \text{ J}\cdot\text{cm}^{-2}$  energy density on the sample surface, using laser pit sizes of 30-50  $\mu\text{m}$  for fluid inclusions. The sample chamber was flushed with 0.4 l/min He, to which 5 ml/min H<sub>2</sub> was added on the way to the ICP-MS (Guillong and Heinrich, 2007). Measured isotopes include <sup>23</sup>Na, <sup>30</sup>Si, <sup>32</sup>S, <sup>35</sup>Cl, <sup>39</sup>K, <sup>63</sup>Cu, <sup>85</sup>Rb, <sup>133</sup>Cs and <sup>197</sup>Au, using dwell times of 10-50 ms per isotope. The instrument was tuned to an oxide rate of 0.05-0.10 % ThO and a doubly-charged Ca<sup>++</sup> rate of 0.2-0.3% based on measurements of NIST-610 glass. For S and Cl corrections were necessary to account for false signals generated by the ablation of quartz, which were done by removing host from the mixed (host + inclusion) signal until no SiO<sub>2</sub> was left. External standardization was based on NIST-610 (Jochum et al., 2011), except for S, and Cl, which were quantified on a natural afghanite standard (Seo et al., 2011). Since <sup>197</sup>Au (which is the only natural isotope of this metal) can be affected by an interference from <sup>181</sup>Ta<sup>16</sup>O, and NIST-610 contains  $\sim 20$  times more Ta than Au, the error introduced by using NIST-610 as external standard was

determined by analyzing Ta-rich, Au-free silicate glass and ilmenite, and recording the intensity of the false Au signal. It turned out that for our instrument our particular tuning (which was kept constant throughout the duration of the study) the  $^{181}\text{Ta}^{16}\text{O}$  interference on the Au signal from NIST-610 leads to an underestimation of the Au concentration in the unknowns by 1.4%. Measured Au concentrations in the fluid inclusions were thus corrected by multiplying them by a factor of 1.014. Absolute concentrations were obtained by using either Na or K as internal standard for newly-formed fluid inclusions, and either K (runs #2, 4) or Rb (runs #9, 10, 15, 17, 21, 23) for re-equilibrated fluid inclusions. Sodium could not be used as internal standard for re-equilibrated fluid inclusions because this element was significantly lost or gained during the re-equilibration experiments.

**Table 8.1**  
Overview of conducted experiments and obtained results

Run	T (°C)	P (kbar)	Time (days)	Type	Capsule	Fluid composition	Utilized pre-run	pH <sup>a</sup>	Au (ppm)		Na (wt%)	
									New FI's	Re-equil. FI's	New FI's	Re-equil. FI's
1	800	2	4	Pre-run	Pt	5.0 wt% KCl		~7	< 1	–	14 ± 3 ppm	–
2	800	2	4	Re-equilibr.	Au	20.1 wt% NaCl + 3.5 wt% HCl + Cs <sup>b</sup>	Run#1	<1	400 ± 70	30-570	7.8 <sup>e</sup>	0.03-0.23
3	600	2	8	Pre-run	Pt	5.0 wt% KCl		~7	< 1	–	14 ± 3 ppm	–
4	600	2	14	Re-equilibr.	Au	20.0 wt% NaCl + 3.5 wt% HCl + Cs <sup>b</sup>	Run#3	<1	110 ± 10	1-140	7.8 <sup>e</sup>	0.003-0.022
8	800	2	3	Pre-run	Au	20.6 wt% NaCl + 3.5 wt% HCl + Rb <sup>c</sup>		~0	1440 ± 250	–	8.1 <sup>e</sup>	–
9	800	2	4	Re-equilibr.	Au	20.2 wt% NaCl + 14.5 wt% KCl + 0.2 wt% KOH + Cs <sup>b</sup>	Run#8	~6	50 ± 1	430-1650	7.9 <sup>e</sup>	10.7 ± 1.0
10	800	2	4	Re-equilibr.	Pt	20.3 wt% NaCl + 14.9 wt% KCl + 0.2 wt% KOH	Run#8	~6	1-90	510-1720	8.0 <sup>e</sup>	11.8 ± 1.3
14	700	2	5	Pre-run	Au	20.6 wt% NaCl + 6.8 wt% HCl + Rb <sup>c</sup>		<0	2270 ± 340	–	8.1 <sup>e</sup>	–
15	700	2	7	Re-equilibr.	Au	19.4 wt% NaCl + 3.2 wt% S <sup>d</sup> + 1.9 wt% KOH + Cs <sup>b</sup>	Run#14	1-2	970 ± 120	2700 ± 340	7.6 <sup>e</sup>	14.1 ± 0.4
16	700	2	4	Pre-run	Au	19.3 wt% NaCl + 6.8 wt% HCl + Rb <sup>c</sup>		<0	2560 ± 390	–	7.6 <sup>e</sup>	–
17	700	2	7	Re-equilibr.	Au	24.2 wt% KCl + 3.2 wt% S <sup>c</sup> + 1.9 wt% KOH + Cs <sup>b</sup>	Run#16	1-2	1670 ± 180	2200 ± 300	0.016	2.0 ± 0.4
20	800	2	4	Pre-run	Au	20.0 wt% NaCl + 3.5 wt% HCl + Rb <sup>b</sup>		<1	1740 ± 130	–	7.9 <sup>e</sup>	–
21	800	2	7	Re-equilibr.	Pt	20.0 wt% NaCl + 4.0 wt% KCl + Cs <sup>b</sup>	Run#20	~4	< 1	700-2140	7.9 <sup>e</sup>	10.7 ± 0.8
22	800	2	4	Pre-run	Au	9.8 wt% NaCl + 2.3 wt % S <sup>c</sup> + Rb <sup>c</sup>		<1	370 ± 70	–	3.9 <sup>e</sup>	–
23	800	2	7	Re-equilibr.	AuCu	9.9 wt% NaCl + 1.5 wt% KOH + 1.5 wt% S <sup>c</sup> + Cs <sup>b</sup>	Run#22	~2	48 ± 13	340 ± 40	3.9 <sup>e</sup>	4.6 ± 0.5

**Table 8.1 (contd.)**

Run	K (wt%)		Rb (ppm)		Cs (ppm)		Cl (wt%)		S (wt%)		Cu (wt%)	
	New FI's	Re-equil. FI's	New FI's	Re-equil. FI's	New FI's	Re-equil. FI's	New FI's	Re-equil. FI's	New FI's	Re-equil. FI's	New FI's	Re-equil. FI's
1	2.6 <sup>e</sup>	–	–	–	<1	–	2.4	–	–	–	–	–
2	<0.1	2.6 <sup>e</sup>	–	–	115 ± 9	<1	13 ± 1	2.3 ± 0.2	–	–	–	–
3	2.6 <sup>e</sup>	–	–	–	<1	–	2.4	–	–	–	–	–
4	<0.1	2.6 <sup>e</sup>	–	–	110 ± 6	<1	13 ± 1	2.4 ± 0.3	–	–	–	–
8	<0.1	–	156 ± 11	–	<1	–	14 ± 1	–	–	–	–	–
9	8.2 ± 0.3	<0.1	<2	156 <sup>e</sup>	50 ± 4	<1	20 ± 2	16 ± 3	–	–	–	–
10	7.9 ± 0.2	<0.1	<2	156 <sup>e</sup>	<1	<1	17 ± 1	17 ± 3	–	–	–	–
14	<0.1	–	681 ± 39	–	<1	–	21 ± 3	–	–	–	–	–
15	1.2 ± 0.1	<0.1	<2	681 <sup>e</sup>	162 ± 13	<1	10 ± 2	24 ± 3	2.9 ± 1.0	–	–	–
16	<0.1	–	597 ± 97	–	<1	–	13 ± 2	–	–	–	–	–
17	14.1 <sup>e</sup>	<0.1	4 ± 2	597 <sup>e</sup>	481 ± 21	<1	12 ± 1	5.8 ± 1.4	5.7 ± 0.8	–	–	–
20	<0.1	–	154 ± 23	–	<1	–	13 ± 2	–	–	–	–	–
21	2.0 ± 0.2	<0.1	<2	154 <sup>e</sup>	3700 ± 290	<1	14 ± 2	14 ± 1	–	–	–	–
22	<0.1	–	393 ± 22	–	<1	–	4.7 ± 0.9	–	2.0 ± 0.3	–	<0.01	–
23	1.1 ± 0.1	<0.1	<2	393 <sup>e</sup>	72 ± 7	<1	5.9 ± 0.9	5.9 ± 0.8	0.5 ± 0.3	2.5 ± 0.3	0.6 ± 0.1	6.8 ± 2.1

Abbreviations: FI's – fluid inclusions; Re-equil. – Re-equilibrated

<sup>a</sup> pH of quenched fluid after the experiment

<sup>b</sup> 50-3700 ppm Cs added in the form of CsCl

<sup>c</sup> 154-681 ppm Rb added in the form of RbCl

<sup>d</sup> added in the form of grains of elementary sulfur

<sup>e</sup> used as internal standard to quantify the LA-ICP-MS analyses (element may differ between new FI's vs. re-equilibrated FI's)

## 8.4. Results

### 8.4.1. Appearance of fluid inclusions

The synthesized fluid inclusions were carefully photographed before and after re-equilibration to document changes in their shape and the presence of daughter crystals. Two examples are shown in Fig. 8.1. Fluid inclusions synthesized in pre-runs display a large variety shapes and measure up to ~50  $\mu\text{m}$  in length (Figs. 8.1a,c). After re-equilibration, some fluid inclusions show notable changes in morphology, i.e., originally irregular and elongated fluid inclusions attained more isometric and regular shapes (Figs. 8.1b,d). In fluid inclusions that gained Au during the re-equilibration experiments, no gold daughter crystals appeared in the fluid inclusions, despite the fact that Au did not occur in dissolved state in these inclusions (see below). In the sulfur-bearing re-equilibration experiment conducted in a  $\text{Au}_{95}\text{Cu}_{05}$  alloy capsule (runs #22+23) the fluid inclusions contained large Cu sulfide daughter crystals after the re-equilibration run (Fig. 8.1d), consistent with findings of Lerchbaumer and Audétat (2012).

### 8.4.2. Compositional modification of fluid inclusions during re-equilibration

Between 4 and 21 (average 8) fluid inclusions from each run were analyzed by LA-ICP-MS. Only fluid inclusions that were not intersected by any cracks were measured to assure their integrity during the re-equilibration. Despite this precaution some inclusions must have been opened during the re-equilibration run, as is evident from their high Cs content and the change in major element composition (e.g., K being replaced by Na). Analyses of such inclusions were rejected. Representative LA-ICP-MS signals are shown in Fig. 8.2, whereas the obtained results are summarized in Table 8.1. The full dataset is provided in supplementary Table 8-S1.

To test whether Au is able to diffuse into fluid inclusions in response to a Au concentration gradient, fluid inclusions synthesized from 5.0 wt% KCl solutions contained in Pt capsules were equilibrated in fluids containing 3.5 wt% HCl and 20.1 wt% NaCl enclosed in gold capsules, at either 800 °C, 2 kbar (runs #1+2) or 600 °C, 2 kbar (runs #3+4). HCl was added to the second solution to achieve relatively high Au solubilities, and to assure that the second solution was more acidic than the first solution. The latter was needed to assure that Au cannot be exchanged for

outward-diffusing  $H^+$ , which was the principal driving force for Cu uptake in the experiments of Lerchbaumer and Audétat (2012). LA-ICP-MS signals of fluid inclusions analyzed from the first two experiments (runs #1+2) are shown in Fig. 8.2, and the corresponding results are plotted in Fig. 8.3a (cf. also Fig. 8.4a). Notice that the Au signal in the re-equilibrated fluid inclusion (Fig. 2b) appears distinctly later than the signals of K and Na, which implies that the Au was not dissolved in the fluid but rather occurred in the form of a precipitate within the inclusion volume (during LA-ICP-MS analysis of quartz-hosted fluid inclusions the main inclusion volume typically gets ablated distinctly later than the first breaching of the inclusion, during which most of the fluid content escapes). However, no Au daughter crystals were optically visible within the inclusions. In some cases, distinct Au signals were obtained already before the fluid inclusion was breached, suggesting that the Au occurred within the quartz. The commonly staggered appearance of Au vs. Na+K signals in re-equilibrated fluid inclusions stands in stark contrast to the behavior of newly-formed inclusions, in which Au, Na and Cs always appear at the same time and thus Au clearly occurred in dissolved state in the fluid (Fig. 8.2c). The Au content of fluid inclusions measured after the pre-run was below 1 ppm (the lowest measured detection limit), hence we used this value as reference for plotting the data in Fig. 8.3a. Both Na and Au were clearly gained in the re-equilibrated fluid inclusions, with Na having increased from  $14 \pm 3$  ppm to 300-2300 ppm, and Au having increased from  $<1$  ppm to 33-570 ppm. According to analyses of fluid inclusions that formed during the re-equilibration experiment the external fluid contained  $115 \pm 9$  ppm Cs, 7.8 wt% Na,  $<0.1$  wt% K, and  $400 \pm 70$  ppm Au. The fact that the re-equilibrated fluid inclusions do not contain any detectable Cs unambiguously demonstrates that they remained physically closed during the experiments, and thus that Au and Na were gained in response to concentration gradients via diffusion through the quartz lattice. As in all experiments conducted in this study, there is no evidence for diffusional gain or loss of K.

Similar observations were made in an experiment conducted at 600 °C, 2 kbar (runs #3+4; Fig. 8.3b). In this experiment the Au content of the external fluids was lower ( $110 \pm 10$  ppm), for which reason also the amount of Au gained by the re-equilibrated fluid inclusions was lower (1-140 ppm, Table 8.1). It is interesting to note that in both of these experiments the maximum Au concentration attained in re-equilibrated inclusions is similar to that present in the external fluid (Figs. 8.3a, b), suggesting that some fluid inclusions attained equilibrium with respect to Au. On the other hand,

their Na content is still about 1-2 orders of magnitude lower than that of the external fluid. Despite the lower degree of equilibration of Na the number of gained Na atoms is about nine times higher than the number of gained Au atoms.

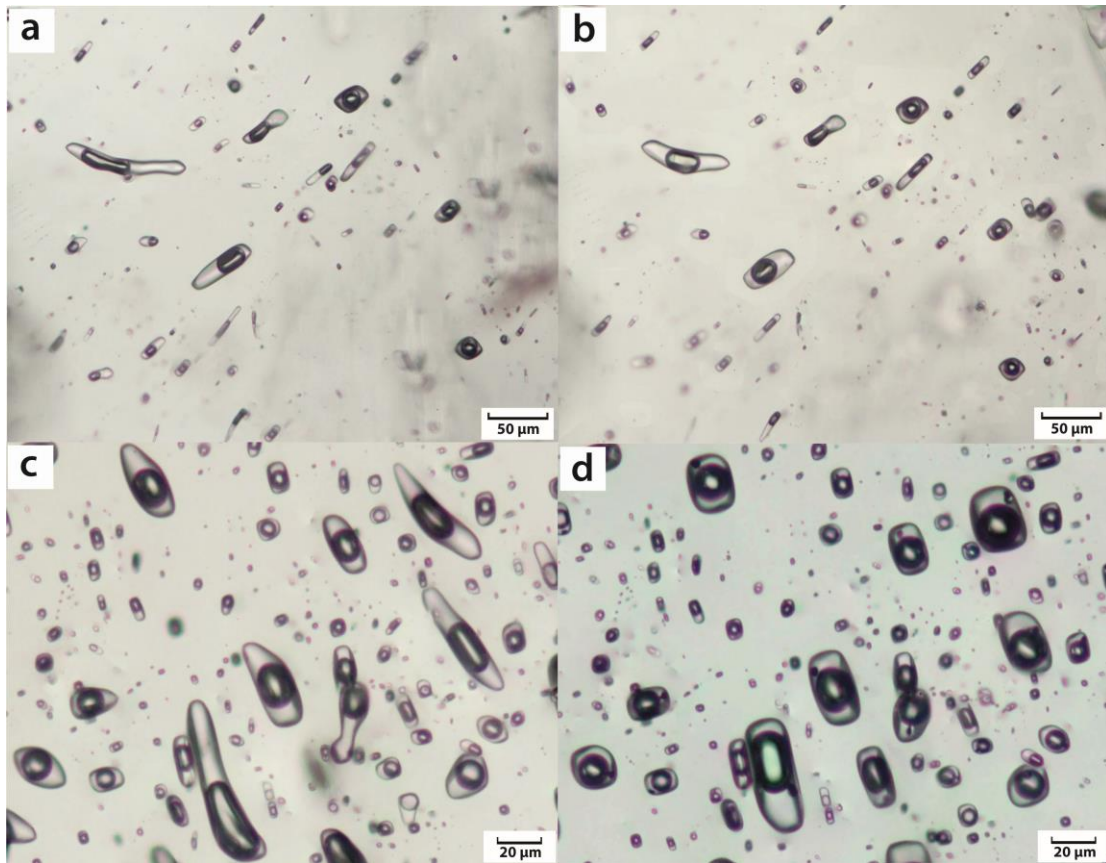


**Fig. 8.1.** Transmitted-light photomicrographs of fluid inclusions before and after re-equilibration: (a) fluid inclusions synthesized in pre-run #8 at 800 °C and 2 kbar (3 days), photographed before re-equilibration, (b) the same fluid inclusions after re-equilibration in run #10 at 800 °C and 2 kbar (4 days), (c) sulfur-bearing fluid inclusions synthesized in run #22 at 800 °C and 2 kbar (4 days) photographed before re-equilibration, (d) the same fluid inclusions after re-equilibration in run #23 at 800 °C and 2 kbar (7 days) in a  $\text{Au}_{95}\text{Cu}_{05}$  capsule. Notice the absence of daughter crystals in the fluid inclusions of run #22, but presence of daughter crystals in the fluid inclusions of run #23. Both transparent and opaque daughter crystals occur in the latter inclusions. The opaque ones are copper sulfides that precipitated due diffusional gain of  $6.8 \pm 2.1$  wt% Cu, and the transparent ones represent elemental sulfur.

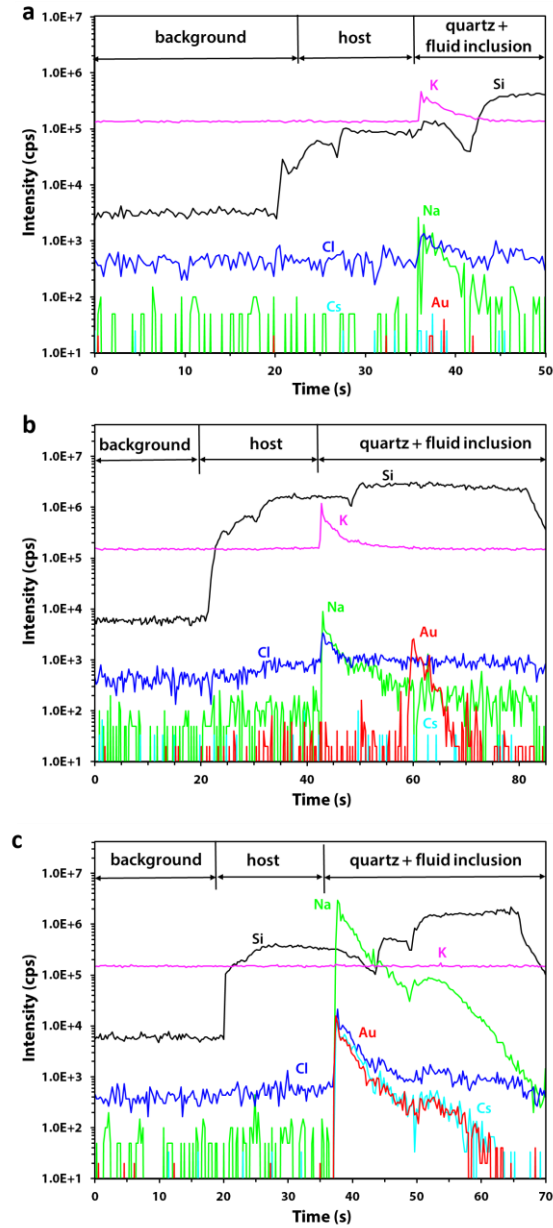


**Fig. 8.2.** LA-ICP-MS signals of fluid inclusions: (a) a fluid inclusion containing 5 wt% KCl, measured before re-equilibration (run #1). (b) a similar fluid inclusion from the same sample, measured after re-equilibration in an external fluid containing 7.8 wt% Na,  $115 \pm 9$  ppm Cs, and  $400 \pm 70$  ppm Au at 800 °C and 2 kbar for 4 days (run #2). The inclusion still contains 5 wt% KCl, but now also 82 ppm Au and 360 ppm Na. The signal of Au appears distinctly later than those of K, Na and Cl because the fluid was ejected before the main inclusion volume (which contained the Au) was ablated. The lack of any Cs signal proves that the inclusion remained physically closed during the equilibration process. (c) Newly-formed fluid inclusion that trapped the external fluid during the same experiment (run #2). Notice the large Cs signal and the absence of a K signal.

To test whether Au is able to diffuse into fluid inclusions in response to a Au concentration gradient, fluid inclusions synthesized from 5.0 wt% KCl solutions contained in Pt capsules were equilibrated in fluids containing 3.5 wt% HCl and 20.1 wt% NaCl enclosed in gold capsules, at either 800 °C, 2 kbar (runs #1+2) or 600 °C, 2 kbar (runs #3+4). HCl was added to the second solution to achieve relatively high Au solubilities, and to assure that the second solution was more acidic than the first solution. The latter was needed to assure that Au cannot be exchanged for outward-diffusing H<sup>+</sup>, which was the principal driving force for Cu uptake in the experiments of Lerchbaumer and Audétat (2012). LA-ICP-MS signals of fluid inclusions analyzed from the first two experiments (runs #1+2) are shown in Fig. 8.2, and the corresponding results are plotted in Fig. 8.3a (cf. also Fig. 8.4a). Notice that the Au signal in the re-equilibrated fluid inclusion (Fig. 8.2b) appears distinctly later than the signals of K and Na, which implies that the Au was not dissolved in the fluid but rather occurred in the form of a precipitate within the inclusion volume (during LA-ICP-MS analysis of quartz-hosted fluid inclusions the main inclusion volume typically gets ablated distinctly later than the first breaching of the inclusion, during which most of the fluid content escapes). However, no Au daughter crystals were optically visible within the inclusions. In some cases, distinct Au signals were obtained already before the fluid inclusion was breached, suggesting that the Au occurred within the quartz. The commonly staggered appearance of Au vs. Na+K signals in re-equilibrated fluid inclusions stands in stark contrast to the behavior of newly-formed inclusions, in which Au, Na and Cs always appear at the same time and thus Au clearly occurred in dissolved state in the fluid (Fig. 8.2c). The Au content of fluid inclusions measured after the pre-run was below 1 ppm (the lowest measured detection limit), hence we used this value as reference for plotting the data in Fig. 8.3a. Both Na and Au were clearly gained in the re-equilibrated fluid inclusions, with Na having increased from 14±3 ppm to 300-2300 ppm, and Au having increased from <1 ppm to 33-570 ppm. According to analyses of fluid inclusions that formed during the re-equilibration experiment the external fluid contained 115±9 ppm Cs, 7.8 wt% Na, <0.1 wt% K, and 400±70 ppm Au. The fact that the re-equilibrated fluid inclusions do not contain any detectable Cs unambiguously demonstrates that they remained physically closed during the experiments, and thus that Au and Na were gained in response to concentration gradients via diffusion through the quartz lattice. As in all experiments conducted in this study, there is no evidence for diffusional gain or loss of K.

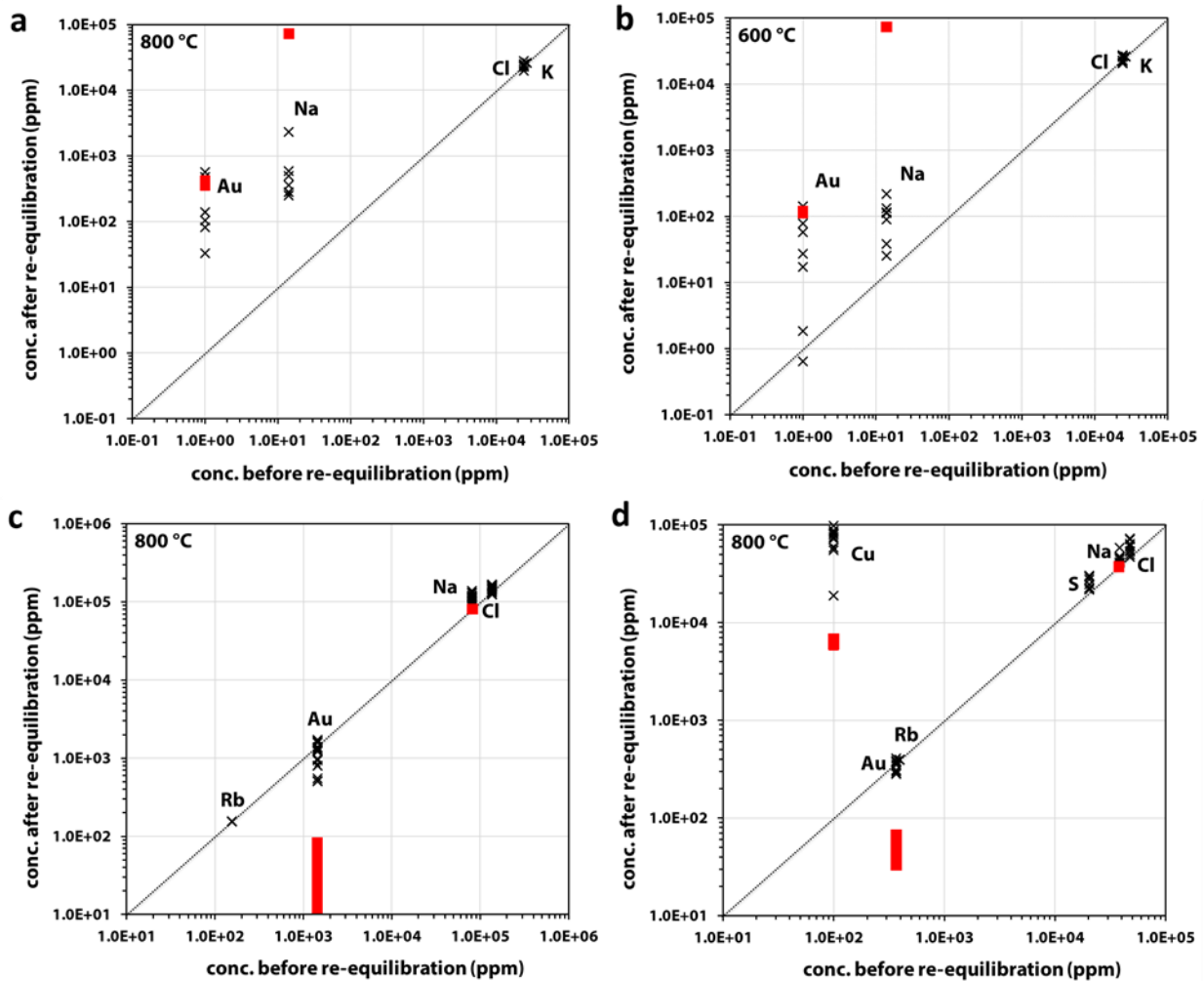


**Fig. 8.3.** Composition of fluid inclusions before vs. after re-equilibration (crosses), plus composition of the external fluid present during the re-equilibration experiment (red bars): (a) fluid inclusions containing 5.0 wt% KCl, re-equilibrated in an external fluid containing 3.5 wt% HCl + 20.1 wt% NaCl + 115±9 ppm Cs at 800 °C, 2 kbar for 4 days (runs #1+2). (b) similar fluid inclusions re-equilibrated at 600 °C, 2 kbar for 14 days (runs #3+4). (c) fluid inclusions which originally contained 20.6 wt% NaCl, 1440±250 ppm Au, and 156±11 ppm Rb, re-equilibrated in an external fluid containing 20.3 wt% NaCl + 14.9 wt% KCl + 0.2 wt% KOH within a Pt capsule at 800 °C, 2 kbar for 4 days (runs #8+10). (d) fluid inclusions which originally contained 9.8 wt% NaCl + 2.3 wt% elemental S + 393±22 ppm Rb + 370±70 ppm Au, re-equilibrated in an external fluid containing 9.9 wt% NaCl + 72±7 ppm Cs + 1.5 wt% KOH within a Au<sub>95</sub>Cu<sub>05</sub> capsule at 800 °C, 2 kbar for 7 days (runs #22+23). The Cu content of the fluid inclusions after the pre-run (run #22) was below the detection limit of 30-100 ppm.

Similar observations were made in an experiment conducted at 600 °C, 2 kbar (runs #3+4; Fig. 8.3b). In this experiment the Au content of the external fluids was lower ( $110\pm 10$  ppm), for which reason also the amount of Au gained by the re-equilibrated fluid inclusions was lower (1-140 ppm, Table 8.1). It is interesting to note that in both of these experiments the maximum Au concentration attained in re-equilibrated inclusions is similar to that present in the external fluid (Figs. 8.3a, b), suggesting that some fluid inclusions attained equilibrium with respect to Au. On the other hand, their Na content is still about 1-2 orders of magnitude lower than that of the external fluid. Despite the lower degree of equilibration of Na the number of gained Na atoms is about nine times higher than the number of gained Au atoms.

With the next three experiments we wanted to test whether Au is also able to diffuse *out* of fluid inclusions in response to a Au concentration gradient. In one experiment (runs #8+10; 800 °C, 2 kbar; 3+4 days), fluid inclusions synthesized from a fluid with 20.6 wt% NaCl, 3.5 wt% HCl,  $156\pm 11$  ppm Rb, and  $1440\pm 250$  ppm Au enclosed in a Au capsule were re-equilibrated in a fluid with the similar amount of NaCl (20.3 wt%) plus 14.5 wt% KCl, 0.2 wt% KOH,  $50\pm 4$  ppm Cs and 1-90 ppm Au contained in a Pt capsule. This time the external fluid was kept less acidic than the one trapped within the fluid inclusions, such that Au would not be lost as a result of inward-diffusing  $H^+$ . The results (Fig. 8.3c; cf. Fig. 4b) suggest that up to ~900 ppm Au were lost from small fluid inclusions ( $\leq 20$   $\mu m$ ), whereas the Au content of larger fluid inclusions remained unchanged (supplementary Fig. 8-S1). Again, significant amounts of Na were gained by the re-equilibrated fluid inclusions (from 7.9 wt% to  $11.8\pm 1.3$  wt%), but this time it cannot have been caused by a concentration gradient (both fluids contained similar amounts of NaCl), but rather happened as a compensation for outward-diffusing  $H^+$ . A similar re-equilibration experiment that was conducted in a Au capsule instead of a Pt capsule (runs #8+9) resulted in significant Au-loss in three out of 16 analyzed inclusions (supplementary Table 8-S1). Despite the use of Au as capsule material a major Au concentration gradient between fluid inclusions ( $1440\pm 250$  ppm) and the external fluid ( $50\pm 1$  ppm) existed also in this experiment. Sodium concentrations in the re-equilibrated fluid inclusions increased from 7.8 wt% to  $10.7\pm 1.0$  wt% Na. A third re-equilibration experiment was conducted in a Pt capsule (runs #20+21), using fluid inclusions that contained 20.0 wt% NaCl, 3.5 wt% HCl,  $154\pm 23$  ppm Rb,  $1740\pm 130$  ppm Au and a pH of  $< 1$ , and re-equilibrating them in a fluid containing 20.0 wt% NaCl, 5.0 wt% KCl,  $3700\pm 290$  ppm Cs,  $< 1$  ppm Au and a pH

of ~4. In this experiment, significant Au-loss (from ~1700 ppm to ~700 ppm) was observed only in one out of 16 analyzed fluid inclusions. Sodium concentrations in the re-equilibrated fluid inclusions increased from 7.9 wt% to  $10.7 \pm 0.8$  wt%. In summary, these experiments shows clear evidence for Au-loss in response to a Au concentration gradient. In all three cases the re-equilibrated fluid inclusions gained 2-3 wt% Na, most likely to compensate for outward-diffusing  $H^+$  (see below).

The next two experiments (runs #14+15 and #16+17) were performed to test whether Au could be gained by fluid inclusions only as a result of decreasing acidity in the external fluid (i.e., without Au concentration gradient), similar to the mechanism that causes Cu-diffusion into fluid inclusions in the experiments performed by Lerchbaumer and Audétat (2012). To be able to distinguish Au gain due to loss of  $H^+$  from Au gain due to a concentration gradient it was necessary to synthesize fluid inclusions that were already Au-bearing, and re-equilibrate these inclusions in a less acidic fluid that ideally contained the same amount of Au. However, producing fluids with contrasting pH but similar Au content is difficult, and only after a few failed attempts we managed to conduct two experiments in which the Au content of the external fluid agreed reasonably well (within a factor of 1.5 and 2.3, respectively) with that of the trapped fluid. In both of these experiments the pre-runs were conducted with a fluid containing 19.3-20.6 wt% NaCl, 6.8 wt% HCl, ~600 ppm Rb, ~2500 ppm Au and a pH <0, and the re-equilibration was performed in fluids which contained either 19.4 wt% NaCl or 24.2 wt% KCl, plus 1.9 wt% KOH, 3.2 wt% elemental sulfur (added to achieve a specific Au solubility), ~160-480 ppm Cs, ~1000-1700 ppm Au and a pH of 1-2. Therefore, large gradients existed with regard to  $H^+$  concentrations (remember that the pH value corresponds to the negative logarithm of the  $H^+$  concentration), but only little gradients with regard to Au concentrations, and the question now was whether the diffusion of  $H^+$  out of the fluid inclusions would cause simultaneous uptake of  $Au^+$ . However, in both experiments the Au content of re-equilibrated fluid inclusions remained unchanged within analytical uncertainty ( $2270 \pm 340$  ppm vs.  $2700 \pm 340$  ppm in runs 14+15;  $2560 \pm 390$  ppm vs.  $2200 \pm 300$  ppm in runs #16+17). The fluid inclusions of runs #14+15 gained considerable amounts of Na (from 8.1 wt% to  $14.1 \pm 0.6$  wt%), whereas those of runs 16+17 lost about three quarters of their original Na content (from 7.6 wt% to  $2.0 \pm 0.4$  wt%) because in that case the external fluid was devoid of Na (cf. Fig. 8.4c). In

summary, the results of these three experiments showed no evidence for Au gain in response to loss of H<sup>+</sup>.

In the last experiment (runs #22+23) we wanted to test whether the formation of Cu-rich sulfide daughter crystals within fluid inclusions can cause any Au uptake. Lerchbaumer and Audétat (2012) showed that acidic, sulfur-bearing fluid inclusions that are re-equilibrated in less acidic fluids can gain several weight percent of Cu, and that this process is responsible for unrealistically high Cu content measured in many natural, quartz-hosted fluid inclusions. Importantly, most of the Cu gained in this way precipitates in the form of Cu-rich sulfides (e.g., chalcopyrite, bornite) within the inclusions, and does not actually stay dissolved in the fluid. Because Au has a strong affinity to Cu-rich sulfides (e.g., Cygan and Candela, 1995; Simon et al., 2000; Fraley and Frank, 2014), it is thus conceivable that fluid inclusions could gain Au as a consequence of Cu gain. We thus performed an experiment similar to runs LL147+LL149 described in Lerchbaumer and Audétat (2012), in which up to 9 wt% Cu were gained in re-equilibrated vapor inclusions. In the present study, however, we wanted the fluid to be single-phase, for which reason the experiment were conducted at 800 °C, 2 kbar instead of 800 °C, 0.7-1.3 kbar. The fluid of the pre-run (which was performed in a Au capsule) contained 9.8 wt% NaCl, 2.3 wt% S, 393±22 ppm Rb, 370±70 ppm Au and had a pH of <1, whereas the fluid of the re-equilibration run (which was performed in a Au<sub>95</sub>Cu<sub>05</sub> alloy capsule) contained 9.9 wt% NaCl, 1.5 wt% KOH, 1.5 wt% sulfur, 72±7 ppm Cs, 48±13 ppm Au, and had a pH of 2. This treatment caused the fluid inclusions to gain 6.8 ± 2.1 wt% Cu and ~0.7 wt% Na, but no Au was gained within analytical uncertainty (370±70 ppm vs. 340±40 ppm). Therefore, the uptake of Cu and corresponding precipitation of Cu-rich sulfide daughter phases did not lead to any uptake of Au (Fig. 8.3d; cf. Fig. 8.4d).

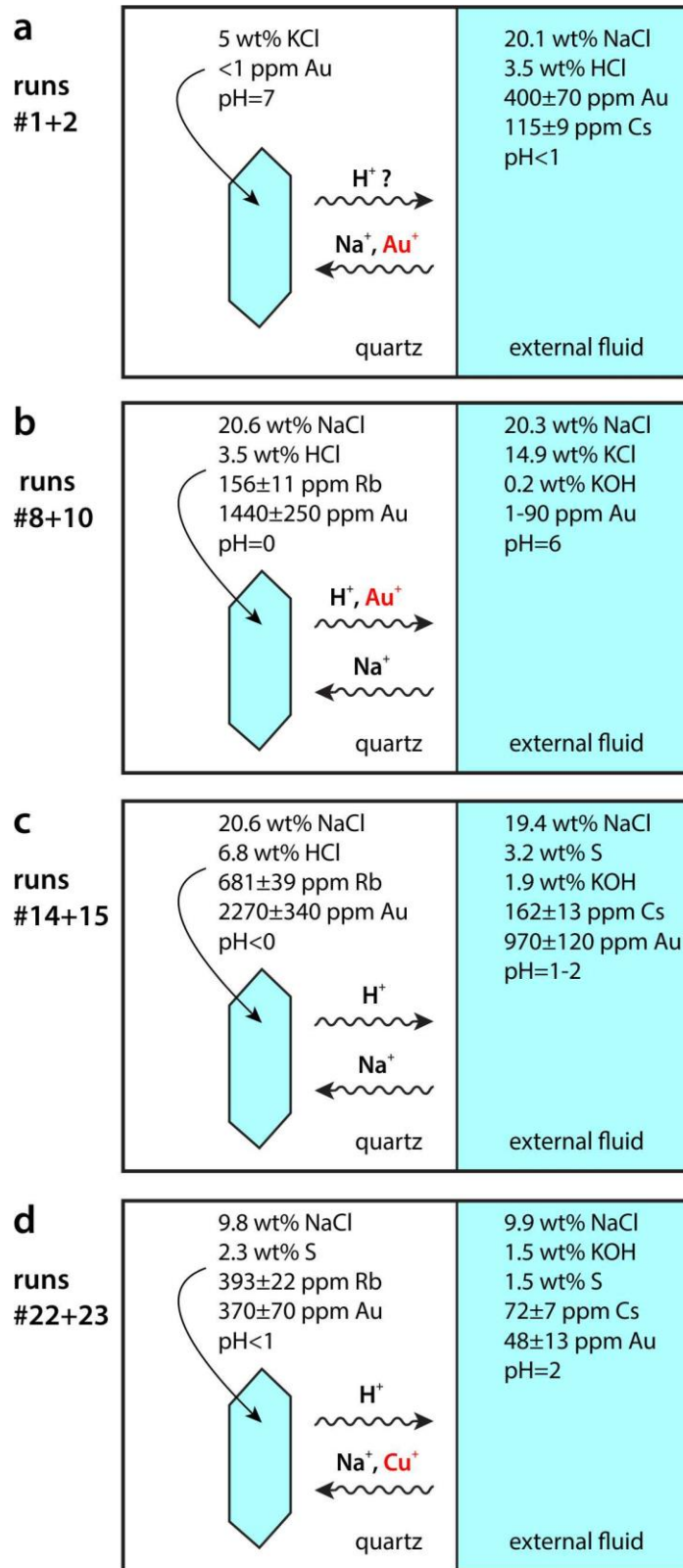


**Fig. 8.4.** Schematic setup of selected re-equilibration runs and interpreted diffusion paths of  $H^+$ ,  $Na^+$ ,  $Au^+$  and  $Cu^+$  through the host quartz.

## 8.5. Discussion

### 8.5.1. Interpretation of observed gains and losses

The setup of selected experiments and interpreted diffusion paths are summarized in Fig. 8.4. It should be remembered that the elements investigated in this study (Na, Au, Cu, H) diffuse principally in the form of ions through the quartz lattice (Verhoogen, 1952; Kats, 1962; White, 1968; Mortley, 1969; Girardet et al., 1988; Martin, 1988), hence if some elements diffuse into fluid inclusions, then some other elements must diffuse out them in order to keep the charge balance.

In the first experiment (runs #1+2) the re-equilibrated fluid inclusions clearly gained Na and Au (Fig. 8.3a), and due to the much lower pH of the external fluid they probably would also have liked to gain  $H^+$ . However, if also  $H^+$  diffused into the fluid inclusions it would have created a major charge imbalance, as no other ions would have been able to diffuse out. We thus envisage that  $H^+$  actually diffused *out* of the fluid inclusions in order to maintain the charge balance (Fig. 8.4a). The observation that the Au that was gained by the re-equilibrated fluid inclusions does not occur in dissolved state supports the interpretation because if significant amounts of  $H^+$  were gained, then at least part of the Au would now be dissolved in the fluid. If the gold precipitated in the form of optically invisibly small particles of metallic gold, then the gain of Au would not have affected charge balance. However, the reduction of  $Au^+$  to  $Au^0$  would have required some other component of the fluid inclusions to become oxidized, which may have been achieved by diffusion of small amounts of  $H_2$  out of them.

In the only experiment in which Au clearly was lost (runs #8+10) the fluid inclusions simultaneously gained several hundred times more  $Na^+$  on a molar basis, hence the loss of  $Au^+$  was probably accompanied by loss of  $H^+$ . In this case the  $H^+$  would have diffused downhill along the pH gradient (Fig. 8.4b).

In the experiment with runs #14+15, in which a Au-bearing fluid was equilibrated in an external fluid of similar composition with lower acidity, the fluid inclusions gained large amounts of Na (from 8.1 wt% to  $14.1 \pm 0.4$  wt%) despite the fact that the Na concentration in the external fluid was the same. We interpret this observation as  $Na^+$  uptake in response to outward diffusing  $H^+$  (Fig. 8.4c), with the  $Na^+$  combining with  $Cl^-$  that was left by broken-up HCl. The fact that much

Na was gained but no Au suggests that outward diffusing  $H^+$  is more easily compensated by  $Na^+$  than by  $Au^+$ , which makes sense because the  $Na^+$  ion is much smaller and thus diffuses more easily than  $Au^+$ . The results of the experiment with runs #16+17 are inconclusive because in this case the fluid inclusions lost major amounts of Na, which probably was compensated by gain of  $H^+$  against the acidity gradient. Hence, in contrast to the original plan,  $Au^+$  could not be gained in exchange to  $H^+$  that diffuses outwards.

In the experiment in which a potential link between Cu uptake and Au uptake was tested (runs #22+23) both  $Na^+$  and  $Cu^+$  were gained in major amounts, and this process likely was accompanied by diffusion of  $H^+$  out of the fluid inclusions along the pH gradient (Fig. 8.4d).

In summary, the experiments demonstrate that Au can be gained or lost in response to concentration gradients, but we found no evidence for Au gain in response to outward-diffusing  $H^+$  (in contrast to what was observed with Cu; Lerchbaumer and Audétat, 2012), neither directly nor indirectly as a consequence of Cu gain.

### **8.5.2. Geological implications**

In Au-bearing magmatic-hydrothermal systems the metal is extracted by means of fluids from magmas and precipitates from these fluids as they ascend, cool, react with the country rocks, and mix with external fluids (e.g., Barnes, 1997; Robb, 2005). Detailed studies on quartz veins from these systems revealed that most veins record an evolution of progressive cooling, although there are also exceptions (e.g., Rusk and Reed, 2002; Redmond et al., 2004; Landtwing et al., 2005; Mercer and Reed, 2013). For this reason, and because the solubility of Au in magmatic-hydrothermal fluids usually decreases with decreasing temperature (also here there are exceptions), one would expect that in most occasions Au would rather tend to diffuse out of fluid inclusions than into them. This view does not change if one considers the fact that the fluid trapped within the fluid inclusions cools in the presence of quartz only, whereas the external fluid cools in the presence of multiple minerals (i.e., rock-buffered), as modeled Au solubilities decrease more rapidly during fluid-buffered than during rock-buffered cooling (Heinrich et al., 2004; Heinrich, 2005). This means that the external fluid will be still Au-undersaturated when the trapped fluid already reached Au saturation. Hence, if fluid inclusions from porphyry deposits experienced any

postentrapmental changes in terms of Au concentrations, then they are more likely to have lost some than gained some. There is no reason why brine inclusions should lose Au more easily than vapor inclusions, hence the high vapor/brine partition coefficients calculated from Au contents of natural fluid inclusion assemblages may well be real. Of course the efficiency of Au diffusion depends also on temperature. Using the same approach that was used by Lerchbaumer and Audétat (2012) to estimate a minimum Cu diffusion coefficient one can estimate minimum Au diffusion coefficients based on the amounts of Au gained in the first two experiments conducted at 800 °C (runs #1+2) and 600 °C (runs #3+4), respectively. The results depend strongly on the amount of Au that can be dissolved in the quartz itself. For a gold solubility of 0.01 ppm (corresponding to the typical detection limit reached in our analyses) the diffusion coefficient turns out at  $\sim 2 \times 10^{-11}$  m<sup>2</sup>/s at 800 °C and  $\sim 1 \times 10^{-13}$  m<sup>2</sup>/s at 600 °C. These values are minimum values because the true Au solubility in the quartz may be lower (calculated diffusion coefficients increase by one order of magnitude for every order of magnitude decrease in the Au concentration), and because equilibrium within the fluid inclusions is reached asymptotically, hence a major portion of the Au was gained in a considerably shorter time than the duration of the experiment. Nevertheless, based on these two values and the assumption that they can be linearly extrapolated to lower temperatures it can be calculated that at a temperature of 400 °C it would take on the order of 100 years to diffuse 1 ppm Au into a 20 µm-sized fluid inclusion covered by 5 mm quartz. Hence, although this represents a maximum time estimate, it indicates that fluid inclusions trapped at <400 °C in magmatic-hydrothermal systems may record true Au concentrations.

The situation may be different for fluid inclusions from mesothermal (also called orogenic) gold deposits, which form over much longer time scales but typically at even lower temperatures (typically around 300±50 °C; Grove et al., 1998). These fluids carried on the order of 0.003-0.2 ppm Au (Pokrovski et al., 2014; Rauchenstein-Martinek et al., 2014, Kokh et al., 2017), and the maximum time required for a fluid inclusion to gain 0.05 ppm Au at 300 °C based on an extrapolated diffusion coefficient of  $1 \times 10^{-19}$  m<sup>2</sup>/s is 12,000 years.

## **8.6. Conclusions**

- Our experiments demonstrate that hundreds of ppm of Au are able to diffuse into or out of quartz-hosted fluid inclusions in a matter of a few days at 800 °C if suitable concentration gradients exist.
- In contrast to Cu, which can diffuse in large quantities into fluid inclusions in response to outward-diffusing H<sup>+</sup>, no evidence for Au gain by such a mechanism was found.
- There is also no evidence that Au could be gained indirectly as a consequence of Cu gain.
- If natural fluid inclusions from porphyry environments have been affected by postentrapmental diffusion of Au, then they probably lost Au than gained it.
- At temperatures <400 °C postentrapmental modification of Au concentrations in fluid inclusions was probably insignificant in the porphyry environment, but potentially was significant in samples from mesothermal Au deposits.

### **8.7. Acknowledgements**

We would like to thank Hubert Schulze and Raphael Njul for preparing quartz pieces, and Ulrike Trezz for helping with chemical work. Haihao Guo acknowledges financial support from the China Scholarship Council (CSC) program.

### **8.8. References**

- Audétat, A., Günther, D., 1999. Mobility and H<sub>2</sub>O-loss from fluid inclusions in natural quartz crystals. *Contrib. Mineral. Petrol.*, 137, 1-14.
- Bakker, R.J., Jansen, J.B.H., 1990. Preferential water leakage from fluid inclusions by means of mobile dislocations. *Nature*, 345, 58-60.
- Bakker, R.J., Jansen, J.B.H., 1991. Experimental post-entrapment water loss from synthetic CO<sub>2</sub>-H<sub>2</sub>O inclusions in natural quartz. *Geochim. Cosmochim. Acta*, 55, 2215-2230.
- Barnes, H.L., 1997. *Geochemistry of hydrothermal ore deposits*; 3rd edition. Wiley, New York, 972 pp.
- Bodnar, R.J., Lecumberri-Sanchez, P., Moncada, D., Steele-MacInnis, M., 2014. Fluid inclusions in hydrothermal ore deposits. In: Holland, H.D., Turekian, K.K. (Eds.), *Treatise on Geochemistry*, Second Edition. Elsevier, Oxford, pp. 119-142.

- Cygan, G.L., Candela, P.A., 1995. Preliminary study of gold partitioning among pyrrhotite, pyrite, magnetite, and chalcopyrite in gold-saturated chloride solutions at 600 to 700 °C, 140 MPa (1400 bars). In: Thompson, J.F.H. (Ed.), *Magma, fluids and ore deposits*. Mineralogical Association of Canada, Short Course Series. Mineralogical Association of Canada, Victoria, B.C., pp. 129-137.
- Diamond, L.W., Tarantola, A., 2015. Interpretation of fluid inclusions in quartz deformed by weak ductile shearing: Reconstruction of differential stress magnitudes and pre-deformation fluid properties. *Earth Planet. Sci. Lett.*, 417, 107-119.
- Diamond, L.W., Tarantola, A., Stünitz, H., 2010. Modification of fluid inclusions in quartz by deviatoric stress II: experimentally induced changes in inclusion volume and composition. *Contrib. Min. Petrol.*, 160, 845-864.
- Doppler, G., Bakker, R.J., Baumgartner, M., 2013. Fluid inclusion modification by H<sub>2</sub>O and D<sub>2</sub>O diffusion: the influence of inclusion depth, size, and shape in re-equilibration experiments. *Contrib. Min. Petrol.*, 165, 1259-1274.
- Fraley, K.J., Frank, M.R., 2014. Gold solubilities in bornite, intermediate solid solution, and pyrrhotite at 500 to 700 °C and 100 MPa. *Econ. Geol.*, 109, 407-418.
- Girardet, G., Plata, J., Breton, J., Hardisson, A., 1988. Electrodiffusion of alkali-metal ions and protons in quartz: a diffusion-compensation model. *Phys. Rev. B - Condensed Matter*, 38, 5648-5653.
- Goldstein, R.H., Reynolds, T.J., 1994. Systematics of fluid inclusions in diagenetic minerals. Society for Sedimentary Geology, Short Course Notes, 31. Society for Sedimentary Geology, Tulsa, Oklahoma, 199 pp.
- Groves, D.I., Goldfarb, R.J., Gebre-Mariam, M., Hagemann, S., Robert, F., 1998. Orogenic gold deposits: a proposed classification in the context of their crustal distribution and relationship to other gold deposit types. *Ore Geol. Rev.*, 13, 7-27.
- Guillong, M., Heinrich, C.A., 2007. Sensitivity enhancement in laser ablation ICP-MS using small amounts of hydrogen in the carrier gas. *J. Anal. Atom. Spectrom.*, 22, 1488-1494.
- Günther, D., Audétat, A., Frischknecht, R., Heinrich, C.A., 1998. Quantitative analysis of major, minor and trace elements in fluid inclusions using Laser Ablation-Inductively Coupled Plasma-Mass Spectrometry (LA-ICP-MS). *J. Anal. Atom. Spectrom.*, 13, 263-270.
- Hall, D.L., Bodnar, R.J., Craig, J.R., 1991. Evidence for postentrapment diffusion of hydrogen into peak metamorphic fluid inclusions from the massive sulfide deposits at Ducktown, Tennessee. *Am. Mineral.*, 76, 1344-1355.

- Heinrich, C.A., 2005. The physical and chemical evolution of low- to medium-salinity magmatic fluids at the porphyry to epithermal transition: A thermodynamic study. *Miner. Deposita*, 39, 864-889.
- Heinrich, C.A., Driesner, T., Stefánsson, A., Seward, T.M., 2004. Magmatic vapour contraction and the transport of gold from the porphyry environment to epithermal deposits. *Geology*, 32, 761-764.
- Hollister, L.S., 1990. Enrichment of CO<sub>2</sub> in fluid inclusions in quartz by removal of H<sub>2</sub>O during crystal-plastic deformation. *J. Struct. Geol.*, 12, 895-901.
- Jochum, K.P. et al., 2011. Determination of reference values for NIST SRM 610-617 glasses following ISO guidelines. *Geostand. Geoanal. Res.*, 35, 397-429.
- Kats, A., 1962. Hydrogen in alpha-quartz. *Philips Research Reports*, 17, 133-195.
- Lambrecht, G., Diamond, L.W., 2014. Morphological ripening of fluid inclusions and coupled zone-refining in quartz crystals revealed by cathodoluminescence imaging: Implications for CL-petrography, fluid inclusion analysis and trace-element geothermometry. *Geochim. Cosmochim. Acta*, 141, 381-406.
- Landtwing, M.R. et al., 2005. Copper deposition during quartz dissolution by cooling magmatic-hydrothermal fluids: The Bingham porphyry. *Earth Planet. Sci. Lett.*, 235, 229-243.
- Lerchbaumer, L., Audétat, A., 2012. High Cu concentrations in vapor-type fluid inclusions: an artifact? *Geochim. Cosmochim. Acta*, 88, 255-274.
- Li, Y., Audétat, A., 2009. A method to synthesize large fluid inclusions in quartz at controlled times and under unfavorable growth conditions. *Am. Mineral.*, 94, 367-371.
- Li, Y., Audétat, A., Lerchbaumer, L., Xiong, X.L., 2009. Rapid Na, Cu exchange between synthetic fluid inclusions and external aqueous solutions: evidence from LA-ICP-MS analysis. *Geofluids*, 9, 321-329.
- Martin, J.J., 1988. Electrodiffusion (sweeping) of ions in quartz - a review. *IEEE Transactions on ultrasonics, ferroelectrics, and frequency control*, 35, 288-296.
- Matthews, W., Linnen, R.L., Guo, Q., 2003. A filler-rod technique for controlling redox conditions in cold-seal pressure vessels. *Am. Mineral.*, 88, 701-707.
- Mavrogenes, J.A., Bodnar, R.J., 1994. Hydrogen movement into and out of fluid inclusions in quartz: experimental evidence and geologic implications. *Geochim. Cosmochim. Acta*, 58, 141-148.
- Mercer, C.N., Reed, M.H., 2013. Porphyry Cu-Mo stockwork formation by dynamic, transient hydrothermal pulses: mineralogical insights from the deposit at Butte, Montana. *Econ. Geol.*, 108, 1347-1377.

- Mortley, W.S., 1969. Diffusion paths in quartz. *Nature*, 221, 359-360.
- Pokrovski, G.S., Akinfiev, N.N., Borisova, A.Y., Zotov, A.V., Kouzmanov, K., 2014. Gold speciation and transport in geological fluids: insights from experiments and physical-chemical modeling. In: Garofalo, P.S., Ridley, J.R. (Eds.), *Gold-transporting hydrothermal fluids in the Earth's crust*. Geological Society, London, Special Publications, vol. 402. The Geological Society of London, London, UK, pp. 9-70.
- Rauchenstein-Martinek, K., Wagner, T., Wälle, M., Heinrich, C.A., 2014. Gold concentrations in metamorphic fluids: A LA-ICPMS study of fluid inclusions from the Alpine orogenic belt. *Chem. Geol.*, 385, 70-83.
- Redmond, P.B., Einaudi, M.T., Inan, E.E., Landtwing, M.R., Heinrich, C.A., 2004. Copper deposition by fluid cooling in intrusion-centered systems: New insights from the Bingham porphyry ore deposits, Utah. *Geology*, 32, 217-220.
- Ridley, J., Hagemann, S.G., 1999. Interpretation of post-entrapment fluid inclusion re-equilibration at the Three Mile Hill, Marvel Loch and Griffins Find high-temperature lode-gold deposits, Yilgarn Craton, Western Australia. *Chem. Geol.*, 154, 257-278.
- Robb, L., 2005. *Introduction to ore-forming processes*. Blackwell Publishing, Oxford, 373 pp.
- Roedder, E., 1984. Fluid inclusions. *Reviews in Mineralogy*, 12. Mineralogical Society of America, Washington DC, 644 pp.
- Rusk, B.G., Reed, M.H., 2002. Scanning electron microscope-cathodoluminescence analysis of quartz reveals complex growth histories in veins from the Butte porphyry copper deposit, Montana. *Geology*, 30, 727-730.
- Seo, J.H., Guillong, M., Aerts, M., Zajacz, Z., Heinrich, C.A., 2011. Microanalysis of S, Cl, and Br in fluid inclusions by LA-ICP-MS. *Chem. Geol.*, 284, 35-44.
- Seo, J.H., Heinrich, C.A., 2013. Selective copper diffusion into quartz-hosted vapor inclusions: evidence from other host minerals, driving forces, and consequences for Cu-Au ore formation. *Geochim. Cosmochim. Acta*, 113, 60-69.
- Shannon, R.D., 1976. Revised effective ionic radii and systematic studies of interatomic distances in halides and chalcogenides. *Acta Cryst. A*, 32, 751-767.
- Simon, G., Kesler, S.E., Essene, E.J., 2000. Gold in porphyry copper deposits: Experimental determination of the distribution of gold in the Cu-Fe-S system at 400° to 700°C. *Econ. Geol.*, 95, 259-270.
- Stern, S.M., Bodnar, R.J., 1989. Synthetic fluid inclusions VII. Re-equilibration of fluid inclusions in quartz during laboratory-simulated metamorphic burial and uplift. *J. Metamorph. Geol.*, 7, 243-260.

Sterner, S.M., Hall, D.L., Keppler, H., 1995. Compositional re-equilibration of fluid inclusions in quartz. *Contrib. Mineral. Petrol.*, 119, 1-15.

Suzuki, C.K. et al., 1995. Synchrotron radiation topography of thick swept quartz. *Proceedings of the 1995 IEEE International Frequency Control Symposium*, May31-June 2, San Francisco, California, USA, 679-684.

Tarantola, A., Diamond, L.W., Stünitz, H., Thust, A., Pec, M., 2012. Modification of fluid inclusions in quartz by deviatoric stress III: influence of principal stresses on inclusion density and orientation. *Contrib. Min. Petrol.*, 160, 537-550.

Verhoogen, J., 1952. Ionic diffusion and electrical conductivity in quartz. *Am. Mineral.*, 37, 637-655.

White, S., 1968. Decorated diffusion paths in quartz. *Nature*, 219, 1248-1249.

White, S., 1970. Ionic diffusion in quartz. *Nature*, 225, 375-376.

Zajacz, Z., Hanley, J.J., Heinrich, C.A., Halter, W.E., Guillong, M., 2009. Diffusive reequilibration of quartz-hosted silicate melt and fluid inclusions: are all metal concentrations unmodified? *Geochim. Cosmochim. Acta*, 73, 3013-3027.

## 8.9. Supplementary material

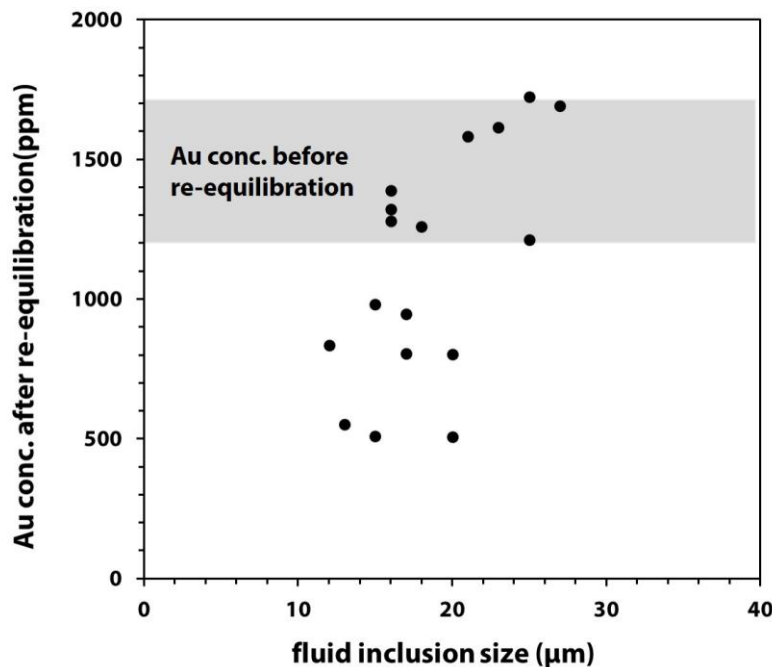


**Fig. 8-S1.** Au contents of fluid inclusions vs. fluid inclusion size after re-equilibration experiment (run #9).

**Supplementary Table 8-S1** LA-ICP-MS analyses of individual fluid inclusions

file name	sample name	Na wt%	K wt%	S wt%	Cl wt%	Cu wt%	Cs ppm	Rb ppm	Au ppm
17My29b04	HG-DIFF01 FI1~40um	0.0013	2.6	(0.0)	2.3	n.a.	(0.1)	(0.4)	(0.2)
17My29b05	HG-DIFF01 FI2~35um	0.0019	2.6	(0.1)	2.6	n.a.	(0.4)	(1.3)	(1.6)
17My29b06	HG-DIFF01 FI3~50um	0.0013	2.6	(0.0)	2.7	n.a.	(0.2)	(0.4)	(1.0)
17My29b07	HG-DIFF01 FI4~50um	0.0016	2.6	(0.1)	2.3	n.a.	(0.3)	(0.9)	(1.2)
17My29b08	HG-DIFF01 FI5~50um	0.0010	2.6	(0.1)	2.4	n.a.	(0.4)	(1.0)	(0.3)
17My29b09	HG-DIFF01 FI6~50um	0.0014	2.6	(0.1)	2.4	n.a.	(0.2)	(0.6)	(0.8)
HG-DIFF-01 pre-run	AVE SD	0.0014 0.0003	2.6 0.0		2.4 0.2				
16Fe26e11	HG-DIFF02 reequil FI1~35um **	0.233	2.6	(0.4)	2.8	n.a.	(1.5)	n.a.	567
16Fe26e12	HG-DIFF02 reequil FI2~40um ***	0.059	2.6	(0.3)	2.0	n.a.	(1.4)	n.a.	479
16Fe26e13	HG-DIFF02 reequil FI3~40um **	0.027	2.6	(0.1)	2.1	n.a.	(0.3)	n.a.	140
16Fe26e14	HG-DIFF02 reequil FI4~35um *	0.028	2.6	(0.4)	2.5	n.a.	(1.3)	n.a.	139
16Fe26e15	HG-DIFF02 reequil FI5~35um **	0.050	2.6	(0.3)	2.3	n.a.	(1.0)	n.a.	33
16Fe26e16	HG-DIFF02 reequil FI6~30um **	0.025	2.6	(0.3)	2.4	n.a.	(1.1)	n.a.	104
16Fe26e17	HG-DIFF02 reequil FI7~25um ***	0.036	2.6	(0.6)	2.3	n.a.	(1.9)	n.a.	82
HG-DIFF-02 re-equil.	AVE SD		2.6 0.0		2.3 0.2				
16Fe26f04	HG-DIFF02 new FI1~30um **	7.8	(0.2)	(0.3)	15.7	n.a.	129	n.a.	477
16Fe26f05	HG-DIFF02 new FI2~25um ***	7.8	(0.1)	(0.3)	12.1	n.a.	109	n.a.	448
16Fe26f06	HG-DIFF02 new FI3~20um ***	7.8	(0.2)	(0.4)	13.6	n.a.	115	n.a.	468
16Fe26f07	HG-DIFF02 new FI4~28um **	7.8	(0.1)	(0.3)	14.0	n.a.	125	n.a.	354
16Fe26f08	HG-DIFF02 new FI5~20um **(*)	7.8	(0.2)	(0.3)	11.8	n.a.	106	n.a.	305
16Fe26f09	HG-DIFF02 new FI6~30um ***	7.8	(0.1)	(0.2)	12.8	n.a.	107	n.a.	335
HG-DIFF-02 new	AVE SD	7.8			13.3 1.3		115 9		398 69
16Fe26f10	HG-DIFF04 reequil FI1~30um ***	0.004	2.6	(0.2)	2.3	n.a.	(0.9)	n.a.	2
16Fe26f11	HG-DIFF04 reequil FI2~25um ***	0.003	2.6	(0.1)	2.6	n.a.	(0.4)	n.a.	1
16Fe26f12	HG-DIFF04 reequil FI3~27um ***	0.009	2.6	(0.2)	2.8	n.a.	(0.6)	n.a.	143
16Fe26f13	HG-DIFF04 reequil FI4~20um ***	0.022	2.6	(0.2)	2.3	n.a.	(0.6)	n.a.	79
16Fe26f14	HG-DIFF04 reequil FI5~37um **	0.012	2.6	(0.2)	2.1	n.a.	(0.6)	n.a.	58
16Fe26f15	HG-DIFF04 reequil FI6~20um **	0.011	2.6	(0.4)	2.1	n.a.	(1.3)	n.a.	27
16Fe26f16	HG-DIFF04 reequil FI7~18um **	0.013	2.6	(0.6)	2.7	n.a.	(2.0)	n.a.	17
HG-DIFF-04 re-equil.	AVE SD		2.6 0.0		2.4 0.3				
16Fe26g04	HG-DIFF04 new FI1~20um ***	7.8	(0.2)	(0.4)	12.3	n.a.	113	n.a.	133
16Fe26g05	HG-DIFF04 new FI2~20um ***	7.8	(0.3)	(0.6)	13.1	n.a.	103	n.a.	108
16Fe26g06	HG-DIFF04 new FI3~25um **(*)	7.8	(0.1)	(0.3)	13.3	n.a.	105	n.a.	106
16Fe26g07	HG-DIFF04 new FI4~17um ***	7.8	(0.2)	(0.4)	13.8	n.a.	120	n.a.	114
16Fe26g08	HG-DIFF04 new FI5~30um **	7.8	(0.4)	(0.7)	10.5	n.a.	108	n.a.	102
HG-DIFF-04 new	AVE SD	7.8			12.6 1.2		110 6		113 11
16Ma15r04	HG-DIFF08 FI1~20um ***	8.1	(0.3)	(1.0)	13.1	n.a.	(3)	157	1752
16Ma15r05	HG-DIFF08 FI2~23um ***	8.1	(0.2)	(0.5)	13.1	n.a.	(2)	175	1422
16Ma15r06	HG-DIFF08 FI3~22um ***	8.1	(0.3)	(0.9)	14.8	n.a.	(3)	152	1784
16Ma15r07	HG-DIFF08 FI4~17um **	8.1	(0.5)	(1.2)	13.6	n.a.	(3)	159	1332
16Ma15r08	HG-DIFF08 FI5~25um ***	8.1	(0.3)	(0.7)	13.9	n.a.	(2)	155	1241

16Ma15r09	HG-DIFF08 FI6~32um ***	8.1	(0.2)	(0.5)	13.4	n.a.	(1)	138	1127
HG-DIFF-08 pre-run		AVE		8.1		13.6		156	1443
		SD		0.6				11	247
16Ma15r10	HG-DIFF09 re-equil FI1~40um ***	10.1	(0.1)	(0.3)	11.9	n.a.	(1)	156	1153
16Ma15r11	HG-DIFF09 re-equil FI2~30um ***	10.4	(0.1)	(0.3)	18.3	n.a.	(1)	156	1432
16Ma15r12	HG-DIFF09 re-equil FI3~20um ***	9.7	(0.2)	(0.4)	15.3	n.a.	(1)	156	770
16Ma15r13	HG-DIFF09 re-equil FI4~24um ***	9.6	(0.1)	(0.3)	15.4	n.a.	(1)	156	1176
16Ma15r14	HG-DIFF09 re-equil FI5~24um *(*)	10.0	(0.4)	(0.9)	19.3	n.a.	(4)	156	1275
17My29b10	HG-DIFF09 re-equil FI6~16um ***	11.0	(0.7)	(1.8)	16.6	n.a.	(3.8)	156	1231
17My29b11	HG-DIFF09 re-equil FI7~15um **	12.5	(0.5)	(1.2)	18.0	n.a.	(2.6)	156	1195
17My29b12	HG-DIFF09 re-equil FI8~12um ***	11.7	(1.3)	(3.3)	14.4	n.a.	(7.1)	156	1265
17My29b13	HG-DIFF09 re-equil FI9~15um ***	11.7	(0.6)	(1.5)	16.0	n.a.	(3.2)	156	1163
17My29b14	HG-DIFF09 re-equil FI10~17um ***	9.2	(0.4)	(1.2)	14.6	n.a.	(2.5)	156	1053
17My29b15	HG-DIFF09 re-equil FI11~14um ***	11.9	(0.8)	(2.2)	17.3	n.a.	(4.7)	156	1310
17My29b16	HG-DIFF09 re-equil FI12~10um ***	9.7	(1.7)	(4.5)	(18.9)	n.a.	(9.6)	156	1156
17My29b17	HG-DIFF09 re-equil FI13~10um ***	10.8	(0.4)	(1.2)	13.8	n.a.	(2.5)	156	426
17My29c04	HG-DIFF09 re-equil FI14~10um ***	11.2	(1.7)	(4.1)	14.7	n.a.	(12.4)	156	1016
17My29c05	HG-DIFF09 re-equil FI15~15um ***	12.2	(1.4)	(3.3)	14.0	n.a.	(10.2)	156	975
17My29c06	HG-DIFF09 re-equil FI16~10um ***	9.9	(1.7)	(4.0)	17.0	n.a.	(12.1)	156	1652
HG-DIFF-09 re-equil.		AVE		10.7		15.8			
		SD		1.0		1.9			
16Ma15r15	HG-DIFF09 new FI1~25um ***	7.9	8.2	(0.2)	20.6	n.a.	47	(4)	51
16Ma15r16	HG-DIFF09 new FI2~28um *(*)	7.9	8.6	(0.2)	19.2	n.a.	58	(3)	53
16Ma15r17	HG-DIFF09 new FI3~35um ***	7.9	8.1	(0.1)	18.5	n.a.	48	(2)	49
14Ma15s04	HG-DIFF09 new FI4~30um ***	7.9	7.6	(0.1)	17.3	n.a.	47	(2)	49
14Ma15s05	HG-DIFF09 new FI5~30um **(*)	7.9	8.4	(0.1)	22.3	n.a.	51	(2)	50
HG-DIFF-09 new		AVE		7.91		8.2		50	50
		SD		0.3		1.7		4	1
16My10g04	HG-DIFF10-re FI1~20um ***	11.8	(0.5)	(1.5)	15.8	n.a.	(3.9)	156	802
16My10g06	HG-DIFF10-re FI3~12um ***	12.0	(1.2)	(3.3)	15.1	n.a.	(8.3)	156	835
16My10g07	HG-DIFF10-re FI4~15um **	13.9	(1.2)	(3.3)	22.3	n.a.	(8.1)	156	981
16Oc06b04	HG-DIFF-10 FI6~25um ***	9.3	(0.5)	(1.0)	12.4	n.a.	(3.0)	156	1211
16Oc06b05	HG-DIFF-10 FI7~17um ***	10.1	(0.3)	(0.7)	16.7	n.a.	(2.0)	156	805
16Oc06b06	HG-DIFF-10 FI8~16um ***	11.1	(0.5)	(1.0)	15.3	n.a.	(3.1)	156	1388
16Oc06b07	HG-DIFF-10 FI9~18um ***	9.9	(0.2)	(0.5)	15.2	n.a.	(1.4)	156	1260
16Oc06b08	HG-DIFF-10 FI10~21um ***	9.2	(0.4)	(0.9)	14.4	n.a.	(2.5)	156	1581
16Oc06b09	HG-DIFF-10 FI11~23um ***	9.5	(0.1)	(0.3)	14.6	n.a.	(0.8)	156	1614
16De21105	HG-DIFF10-re FI13~16um **(*)	13.2	(1.0)	(1.8)	15.8	n.a.	(4.3)	156	1278
16De21106	HG-DIFF10-re FI14~16um ***	11.5	(0.7)	(1.2)	17.7	n.a.	(3.6)	156	1321
16De21109	HG-DIFF10-re FI17~27um **	10.4	(0.2)	(0.3)	13.6	n.a.	(0.7)	156	1691
16De21110	HG-DIFF10-re FI18~20um **	11.5	(0.4)	(0.7)	16.3	n.a.	(1.5)	156	506
16De21111	HG-DIFF10-re FI19~17um **	10.6	(0.3)	(0.5)	16.4	n.a.	(1.4)	156	946
16De21112	HG-DIFF10-re FI20~25um **(*)	12.9	(0.1)	(0.2)	14.6	n.a.	(0.6)	156	1723
16De21113	HG-DIFF10-re FI21~15um **(*)	11.2	(1.5)	(2.7)	20.5	n.a.	(7.1)	156	510
16De21114	HG-DIFF10-re FI22~13um **(*)	12.1	(1.2)	(2.6)	14.6	n.a.	(9.2)	156	553
HG-DIFF-10 re-equil.		AVE		11.8		16.6		156	
		SD		1.3		3.0			
16My10g10	HG-DIFF10-new FI1~20um ***	8.0	7.8	(0.5)	16.1	n.a.	47	(4)	(2)
16My10g11	HG-DIFF10-new FI2~25um ***	8.0	8.2	(0.4)	17.7	n.a.	48	(3)	(2)
16My10g12	HG-DIFF10-new FI3~27um **	8.0	7.7	(0.2)	18.2	n.a.	48	1	1
16My10g13	HG-DIFF10-new FI4~17um ***	8.0	7.6	(1.7)	15.8	n.a.	47	(13)	16
16My10g14	HG-DIFF10-new FI5~17um **	8.0	7.8	(0.9)	17.5	n.a.	46	(7)	27
16My10g15	HG-DIFF10-new FI6~17um ***	8.0	8.1	(1.1)	18.1	n.a.	55	(9)	90

HG-DIFF-10 new		AVE SD	7.96	7.9		17.2		49		
				0.2		0.9		3		
16Ju30b04	HG-DIFF-14 FI1~20um ***		8.1	(1)	(5.0)	25.7	n.a.	(8)	732	2635
16Ju30b05	HG-DIFF-14 FI2~10um **		8.1	(1)	(4.1)	21.3	n.a.	(6)	642	2272
16Ju30b06	HG-DIFF-14 FI3~20um **		8.1	(0)	(1.2)	23.4	n.a.	(2)	701	2622
16Ju30b07	HG-DIFF-14 FI4~15um **		8.1	(0)	(1.2)	18.2	n.a.	(2)	649	2395
16Ju30b08	HG-DIFF-14 FI5~10um **(*)		8.1	(1)	(3.8)	17.8	n.a.	(10)	723	1937
16Ju30b09	HG-DIFF-14 FI6~15um **		8.1	(1)	(2.7)	21.8	n.a.	(7)	638	1731
HG-DIFF-14 pre-run		AVE SD	8.11			21.3		681	2265	
						2.8		39	335	
16Ju30b10	HG-DIFF-15 re-equil FI1~25um ***		14.0	(0)	(1)	26.5	n.a.	(3)	681	2423
16Ju30b11	HG-DIFF-15 re-equil FI2~12um ***		13.7	(1)	(5)	22.1	n.a.	(12)	681	2294
16Ju30b12	HG-DIFF-15 re-equil FI3~14um ***		14.6	(1)	(4)	23.8	n.a.	(7)	681	2637
16Ju30b13	HG-DIFF-15 re-equil FI4~16um ***		14.6	(1)	(3)	25.2	n.a.	(5)	681	2968
16Ju30b14	HG-DIFF-15 re-equil FI5~17um **		15.2	(1)	(2)	25.5	n.a.	(4)	681	3213
16Ju30b15	HG-DIFF-15 re-equil FI6~13um ***		13.4	(1)	(4)	20.7	n.a.	(8)	681	2499
16Ju30b16	HG-DIFF-15 re-equil FI7~16um ***		14.1	(1)	(3)	28.9	n.a.	(4)	681	3180
16Ju30b17	HG-DIFF-15 re-equil FI8~15um ***		13.6	(1)	(3)	20.0	n.a.	(4)	681	2451
HG-DIFF-15 re-equil.		AVE SD	14.14			24.1		681	2708	
			0.6			2.8		0	338	
16Ju30c04	HG-DIFF15 new FI1~17um **		7.6	1.2	1.4	11.8	n.a.	157	(8.7)	1050
16Ju30c05	HG-DIFF15 new FI2~17um ***		7.6	1.1	(1.6)	9.4	n.a.	156	(10.8)	1163
16Ju30c07	HG-DIFF15 new FI4~17um ***		7.6	1.2	4.3	9.3	n.a.	144	(5.3)	850
16Ju30c08	HG-DIFF15 new FI5~29um **(*)		7.6	1.4	2.7	12.2	n.a.	184	(2.8)	1053
16Ju30c09	HG-DIFF15 new FI6~24um *		7.6	1.3	3.1	7.2	n.a.	167	(3.3)	873
HG-DIFF-15 new		AVE SD	7.61	1.2	2.9	10.1		162	972	
				0.1	1.0	1.7		13	122	
16Jy22f10	HG-DIFF-16 FI1~25um ***		7.6	(0.3)	(0.6)	11.2	n.a.	(1.3)	512	2273
16Jy22f11	HG-DIFF-16 FI2~20um **		7.6	(0.7)	(1.6)	16.2	n.a.	(3.3)	694	3184
16Jy22f12	HG-DIFF-16 FI3~12um **		7.6	(0.3)	(0.8)	13.0	n.a.	(2.3)	521	2148
16Jy22f13	HG-DIFF-16 FI4~25um **(*)		7.6	(0.2)	(0.7)	12.0	n.a.	(1.5)	597	2309
16Jy22f14	HG-DIFF-16 FI5~13um ***		7.6	(0.5)	(1.4)	13.0	n.a.	(3.5)	502	2441
16Jy22f15	HG-DIFF-16 FI6~14um **(*)		7.6	(0.6)	(1.6)	12.4	n.a.	(4.1)	756	2978
HG-DIFF-16 pre-run		AVE SD	7.59			13.0		597	2556	
						1.6		97	386	
16Jy22g04	HG-DIFF17 re-equil FI1~15um * s		1.4	(0.1)	(0.3)	3.0	n.a.	(0.8)	597	2379
16Jy22g05	HG-DIFF17 re-equil FI2~18um **		2.7	(0.1)	(0.3)	5.5	n.a.	(0.7)	597	1581
16Jy22g06	HG-DIFF17 re-equil FI3~15um *		2.4	(0.4)	(1.0)	6.2	n.a.	(2.8)	597	2091
16Jy22g07	HG-DIFF17 re-equil FI4~15um **(*)		2.0	(0.2)	(0.7)	4.6	n.a.	(1.8)	597	2202
16Jy22g08	HG-DIFF17 re-equil FI5~14um *		1.9	(0.3)	(0.9)	5.8	n.a.	(2.5)	597	2477
16Jy22g09	HG-DIFF17 re-equil FI6~12um *		1.8	(0.3)	(0.8)	5.4	n.a.	(2.3)	597	2075
16Jy22g10	HG-DIFF17 re-equil FI7~20um **		2.3	(0.3)	(0.7)	5.9	n.a.	(2.2)	597	2132
16Jy22g11	HG-DIFF17 re-equil FI8~13um ***		1.4	(0.4)	(1.0)	5.0	n.a.	(3.0)	597	2394
16Jy22g12	HG-DIFF17 re-equil FI9~12um *		1.7	(0.4)	(1.0)	7.4	n.a.	(2.5)	597	2572
16Jy22g13	HG-DIFF17 re-equil FI10~12um *		2.0	(0.4)	(0.5)	5.4	n.a.	(1.2)	597	2604
16Jy22g14	HG-DIFF17 re-equil FI11~18um **		1.6	(0.4)	(1.1)	6.2	n.a.	(2.8)	597	2200
16Jy22g15	HG-DIFF17 re-equil FI12~15um **		2.6	(0.2)	(0.5)	6.4	n.a.	(1.0)	597	1690
16Jy22g16	HG-DIFF17 re-equil FI13~13um **		1.7	(0.3)	(1.0)	9.0	n.a.	(1.8)	597	2309
HG-DIFF-17 re-equil.		AVE SD	2.0			5.8		597	2208	
			0.4			1.4		0.0	295	
16Jy22h04	HG-DIFF17 new FI1~25um **(*)		0.015	14.1	6.2	11.2	n.a.	459	2.5	1385

16Jy22h05	HG-DIFF17 new FI2~35um **	0.012	14.1	4.5	12.0	n.a.	509	2.9	1540
16Jy22h06	HG-DIFF17 new FI3~15um ***	0.020	14.1	(0.9)	11.1	n.a.	443	6.8	1813
16Jy22h07	HG-DIFF17 new FI4~15um ***	0.011	14.1	(0.6)	11.7	n.a.	462	4.4	1890
16Jy22h08	HG-DIFF17 new FI5~15um **	0.011	14.1	6.2	11.6	n.a.	494	2.5	1816
16Jy22h09	HG-DIFF17 new FI6~13um ***	0.028	14.1	(1.1)	11.7	n.a.	517	(7.2)	1577
<b>HG-DIFF-17 new</b>		<b>AVE</b>	<b>0.016</b>	<b>5.7</b>	<b>11.5</b>		<b>481</b>		<b>1670</b>
		<b>SD</b>	<b>0.006</b>	<b>0.8</b>	<b>0.3</b>		<b>28</b>		<b>181</b>
16Oc06b10	HG-DIFF-20 FI1~15um *	7.9	(0.4)	(0.9)	10.5	n.a.	(2.5)	151	1772
16Oc06b11	HG-DIFF-20 FI2~15um *	7.9	(0.8)	(2.0)	16.1	n.a.	(5.4)	165	1968
16Oc06b12	HG-DIFF-20 FI3~15um *	7.9	(0.1)	(0.2)	11.4	n.a.	(0.6)	126	1594
16Oc06b13	HG-DIFF-20 FI4~10um *	7.9	(0.6)	(1.6)	(6.7)	n.a.	(4.4)	147	1817
16Oc06b14	HG-DIFF-20 FI5~15um **	7.9	(0.2)	(0.6)	(2.6)	n.a.	(1.7)	148	1797
16Oc06b15	HG-DIFF-20 FI6~15um *	7.9	(0.3)	(0.9)	12.2	n.a.	(2.1)	140	1796
16Oc06b16	HG-DIFF-20 FI7~27um *	7.9	(0.6)	(1.6)	12.9	n.a.	(4.0)	151	1511
16Oc06b17	HG-DIFF-20 FI8~25um *	7.9	(0.1)	(0.3)	15.9	n.a.	(0.9)	207	1673
<b>HG-DIFF-20 pre-run</b>		<b>AVE</b>	<b>7.86</b>		<b>13.2</b>			<b>154</b>	<b>1741</b>
		<b>SD</b>	<b>0.00</b>		<b>2.1</b>			<b>23</b>	<b>134</b>
16Oc06c06	HG-DIFF-21re-equil FI1~20um ***	11.3	(0.4)	(1.0)	13.9	n.a.	(2.3)	153	1885
16Oc06c09	HG-DIFF-21re-equil FI2~30um ***	10.3	(0.2)	(0.3)	14.6	n.a.	(1.3)	153	1764
16Oc06c10	HG-DIFF-21re-equil FI3~40um **	9.0	(0.1)	(0.2)	12.9	n.a.	(0.6)	153	1972
16Oc06c11	HG-DIFF-21re-equil FI4~10um ***	10.3	(1.2)	(3.0)	(12.8)	n.a.	(8.9)	153	2133
16Oc06c12	HG-DIFF-21re-equil FI5~12um ***	10.5	(1.4)	(3.4)	12.7	n.a.	(10.1)	153	702
16De21m04	HG-DIFF21 re-equil FI6~15um ***	10.4	(1.6)	(2.8)	13.3	n.a.	(8.3)	153	1994
16De21m05	HG-DIFF21 re-equil FI7~13um ***	12.7	(4.8)	(9.3)	14.4	n.a.	(23.8)	153	1689
16De21m06	HG-DIFF21 re-equil FI8~16um **	11.8	(0.6)	(1.2)	15.6	n.a.	(3.1)	153	1567
17My29c07	HG-DIFF21 FI11~12um ***	9.8	(1.0)	(2.5)	12.7	n.a.	(7.6)	153	1649
17My29c08	HG-DIFF21 FI12~20um **	11.0	(0.5)	(1.3)	17.2	n.a.	(3.9)	153	1766
17My29c09	HG-DIFF21 FI13~13um ***	11.5	(2.1)	(5.4)	18.7	n.a.	(16.2)	153	1976
17My29c10	HG-DIFF21 FI14~16um ***	10.6	(0.6)	(1.3)	15.5	n.a.	(3.4)	153	1938
17My29c11	HG-DIFF21 FI15~8um ***	10.8	(1.5)	(3.4)	15.7	n.a.	(9.0)	153	2141
17My29c12	HG-DIFF21 FI16~8um ***	9.9	(2.0)	(4.5)	(21.2)	n.a.	(12.2)	153	1976
17My29c13	HG-DIFF21 FI17~5um ***	10.6	(3.0)	(6.5)	(29.9)	n.a.	(16.0)	153	1927
17My29c14	HG-DIFF21 FI18~7um ***	10.5	(1.6)	(3.5)	18.8	n.a.	(8.7)	153	1792
<b>HG-DIFF-21 re-equil.</b>		<b>AVE</b>	<b>10.7</b>		<b>15.1</b>			<b>153</b>	
		<b>SD</b>	<b>0.8</b>		<b>2.0</b>			<b>0</b>	
16Oc06c04	HG-DIFF-21 new FI1~27um ***	7.9	2.2	(0.3)	14.1	n.a.	4087	(2.6)	(1)
16Oc06c05	HG-DIFF-21 new FI2~15um *	7.9	2.0	(1.5)	12.2	n.a.	3840	(14.2)	(4)
16Oc06c07	HG-DIFF-21 new FI3~15um *	7.9	2.0	(0.6)	12.2	n.a.	3613	(4.2)	(3)
16Oc06c08	HG-DIFF-21 new FI4~27um ***	7.9	1.7	(1.2)	16.3	n.a.	3296	(8.4)	(6)
<b>HG-DIFF-21 new</b>		<b>AVE</b>	<b>7.9</b>	<b>2.0</b>	<b>14.2</b>		<b>3709</b>		
		<b>SD</b>	<b>0.2</b>	<b>1.7</b>	<b>1.7</b>		<b>292</b>		
16Oc06c13	HG-DIFF-22 FI1~20um ***	3.9	(0.3)	1.5	3.8	n.a.	(2.4)	400	498
16Oc06c14	HG-DIFF-22 FI2~22um ***	3.9	(0.2)	1.7	4.0	n.a.	(1.8)	382	328
16Oc06c15	HG-DIFF-22 FI3~30um ***	3.9	(0.1)	2.2	4.9	n.a.	(1.0)	396	337
16Oc06c16	HG-DIFF-22 FI4~30um ***	3.9	(0.3)	2.5	3.9	n.a.	(2.0)	425	421
16Oc06d04	HG-DIFF-22 FI5~40um *	3.9	(0.1)	1.8	6.0	n.a.	(0.6)	386	273
16Oc06d05	HG-DIFF-22 FI6~20um ***	3.9	(0.3)	2.1	5.8	n.a.	(2.2)	424	412
16Oc06d06	HG-DIFF-22 FI7~20um *	3.9	(0.2)	2.6	4.7	n.a.	(1.4)	357	334
16Oc06d07	HG-DIFF-22 FI8~25um **	3.9	(0.2)	2.0	(2.6)	n.a.	(1.7)	374	325
<b>HG-DIFF-22 pre-run</b>		<b>AVE</b>	<b>3.85</b>	<b>2.0</b>	<b>4.7</b>			<b>393</b>	<b>366</b>
		<b>SD</b>		<b>0.3</b>	<b>0.9</b>			<b>22</b>	<b>67</b>
16Oc06d08	HG-DIFF-23 re-equil FI1~25um ***	4.7	(0.2)	2.5	6.0	1.9	(1.7)	394	409

## Manuscripts

16Oc06d09	HG-DIFF-23 re-equil FI2~20um ***	4.4	(0.4)	3.0	6.1	8.4	(3.1)	394	289
16Oc06d10	HG-DIFF-23 re-equil FI3~23um ***	4.3	(0.3)	2.4	5.7	5.9	(1.8)	394	365
16Oc06d11	HG-DIFF-23 re-equil FI4~18um ***	4.8	(0.4)	(1.1)	7.2	9.9	(3.2)	394	384
16Oc06d12	HG-DIFF-23 re-equil FI5~18um ***	4.6	(0.4)	2.9	5.4	8.8	(2.7)	394	372
16Oc06d13	HG-DIFF-23 re-equil FI6~30um ***	4.1	(0.1)	2.2	6.4	5.5	(1.0)	394	380
16Oc06d14	HG-DIFF-23 re-equil FI7~20um ***	5.8	(0.3)	(0.7)	7.1	7.5	(1.9)	394	353
16Oc06d15	HG-DIFF-23 re-equil FI8~25um ***	4.7	(0.2)	2.3	4.7	5.9	(1.4)	394	281
16Oc06d16	HG-DIFF-23 re-equil FI9~20um ***	4.0	(0.3)	2.8	5.0	7.9	(1.9)	394	301
16Oc06d17	HG-DIFF-23 re-equil FI10~25um ***	4.1	(0.1)	2.2	5.3	7.2	(0.9)	394	308
<b>HG-DIFF-23 re-equil.</b>		<b>AVE</b>	<b>4.6</b>	<b>2.5</b>	<b>5.9</b>	<b>6.9</b>		<b>394</b>	<b>344</b>
		<b>SD</b>	<b>0.5</b>	<b>0.3</b>	<b>0.8</b>	<b>2.1</b>			<b>43</b>
						<b>0.0</b>			
16Oc06e04	HG-DIFF-23 new FI1~25um **	3.9	1.0	0.6	7.6	0.6	85	(5.6)	50
16Oc06e05	HG-DIFF-23 new FI2~20um **	3.9	1.0	0.4	5.5	0.5	66	(6.1)	71
16Oc06e06	HG-DIFF-23 new FI3~20um **	3.9	1.1	0.3	6.2	0.7	79	(9.2)	50
16Oc06e07	HG-DIFF-23 new FI4~30um ***	3.9	1.3	0.9	6.3	0.6	68	(9.2)	42
16Oc06e08	HG-DIFF-23 new FI5~20um ***	3.9	1.0	(0.4)	5.2	0.6	68	(2.3)	31
16Oc06e09	HG-DIFF-23 new FI6~30um ***	3.9	1.0	0.2	4.9	0.5	68	(5.6)	41
<b>HG-DIFF-23 new</b>		<b>AVE</b>	<b>3.85</b>	<b>1.1</b>	<b>0.5</b>	<b>5.9</b>	<b>0.6</b>	<b>72</b>	<b>48</b>
		<b>SD</b>	<b>0.1</b>	<b>0.3</b>	<b>0.9</b>	<b>0.1</b>	<b>7</b>		<b>13</b>

red numbers in parentheses denote detection limits  
n.a. – not analyzed

## 9. In-situ infrared spectra of OH in rutile up to 1000 °C

Haihao Guo

*Bayerisches Geoinstitut, Universität Bayreuth, D-95440 Bayreuth, Germany*

### 9.1. Abstract

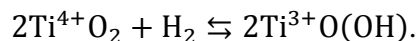
The infrared spectra of hydrous, oriented single crystals of synthetic Al-doped and pure rutile were measured from room temperature to 1000 °C at 1 bar using a heating stage. At room temperature, the spectra show only one band at  $\sim 3278 \text{ cm}^{-1}$  in pure rutile, and two additional bands at  $\sim 3303$  and  $\sim 3323 \text{ cm}^{-1}$  in Al-doped rutile. The main band associated with Al at  $\sim 3323 \text{ cm}^{-1}$  loses intensity as temperature increases and nearly disappears already at 300 °C. This suggests that the corresponding defect only forms during cooling and therefore, water speciation in rutile at room temperature is not representative of subduction zone or upper mantle conditions. All OH bands shift to lower wavenumbers at elevated temperatures with  $dv/dT = -0.0831 \text{ cm}^{-1}/\text{K}$  for the main band at  $3278 \text{ cm}^{-1}$ . This strong low-frequency shift is unexpected for an OH bond involved in hydrogen bonding, indicating decreasing O-O distance for the OH band. Together with the extreme broadening of the band at high temperature, it suggests some weakening of the OH bond strength and a rapid exchange of protons, consistent with rapid hydrogen diffusion in rutile.

**Keywords:** Hydroxyl; rutile; infrared spectra; high-temperature

### 9.2. Introduction

Among all nominally anhydrous minerals occurring in mantle xenoliths, Rutile ( $\text{TiO}_2$ ) often has the highest water contents, with maximum values reaching nearly 1 wt. % (e.g., Beran and Libowitzky, 2006; Hammer and Beran, 1991; Rossman and Smyth, 1990; Vlassopoulos et al., 1993; Zheng, 2009). Despite its low modal abundance, rutile may therefore be a significant carrier of water in eclogite during subduction into the mantle.

Rutile has a simple tetragonal crystal structure, with [TiO<sub>6</sub>] octahedra parallel to the c-axis, and oxygen atoms surrounded by three Ti<sup>4+</sup> ions (Deer et al., 1992). Infrared spectroscopic data suggest that hydrogen is incorporated in rutile as OH groups orientated perpendicular to the c-axis (Lucassen et al., 2012; Rossman and Smyth, 1990; Vlassopoulos et al., 1993). Very likely, the dissolution of hydrogen is related to the coupled substitution of H<sup>+</sup> + R<sup>3+</sup> for Ti<sup>4+</sup> in the structure, where R<sup>3+</sup> is a trivalent cation, such as Fe<sup>3+</sup>, Cr<sup>3+</sup>, V<sup>3+</sup> and Al<sup>3+</sup>, with different cations leading to separate bands in infrared spectra (e.g., Bromiley and Hilairt, 2005; Lucassen et al., 2012; Vlassopoulos et al., 1993). In pure, vacancy-free rutile H-incorporation is likely coupled to Ti-reduction according to the reaction:



Because of this relationship, the OH content in rutile could potentially also be used as a redox sensor in high-pressure experiments, i.e. as an oxybarometer (Colasanti et al., 2011).

Models on water dissolution in rutile so far were mostly derived from spectroscopic studies at ambient conditions. Yang et al. (2011) measured unpolarized FTIR spectra of a natural Fe-bearing rutile up to 500 °C. In order to investigate the association of protons with trivalent cations at high temperature, we have measured both unpolarized and polarized infrared spectra of hydrated, crystallographically oriented, synthetic Al-doped and pure rutile at 1 bar up to 1000 °C to constrain H speciation in rutile at elevated temperatures.

### **9.3. Methods**

#### **9.3.1. Synthesis of hydrous rutile**

Starting materials were a synthetic rutile crystal (Morion Company, Brighton, USA) containing about 200 ppm Al (as measured by laser-ablation ICP-MS) and a pure synthetic rutile crystal (Crystal GmbH, Berlin, Germany). Both crystals were cut into pieces of about 5×2×0.5 mm size with the long direction oriented parallel to the c-axis. Each crystal was loaded into a 20 mm long Au capsule with 3.5 mm outer diameter and 3.1 mm inner diameter, together with quartz powder, ultrapure water and an *f*O<sub>2</sub> buffer (MnO-Mn<sub>3</sub>O<sub>4</sub>). After loading, the Au capsule was arc-welded, pre-compressed at ~1 kbar using water as pressure medium, and then dried in a drying oven and

weighted to check for the presence of leaks. The sealed capsules were then annealed in rapid-quench cold-seal pressure vessels (made of the Inconel 713LC super alloy) with water as the pressure medium, in a setup similar to that described in Matthews et al. (2003). Temperatures were measured with NiCr-Ni thermocouples in an external borehole of the autoclave. Uncertainties in temperature and pressure are  $\pm 5$  °C and  $\pm 20$  bar, respectively. The experiments were run at 800 °C for the Al-doped rutile and at 900 °C for the pure rutile, both at 2 kbar and for  $\sim 1$  day. Runs were terminated by in-situ rapid quenching to room temperature within a few seconds. The run products were not contaminated by the  $fO_2$  buffer, as confirmed by measuring the Mn content by LA-ICP-MS. The initially yellowish rutile turned blue after the hydration experiments, which is due to the reduction from  $Ti^{4+}$  to  $Ti^{3+}$ , producing a broad absorbance peak with the center in the near infrared region ( $\sim 6500$   $cm^{-1}$ ) (e.g., Colasanti et al., 2011; Lucassen et al., 2012).

### **9.3.2. In situ infrared spectroscopy**

The hydrated rutile crystals were doubly polished into  $\sim 2 \times 2$  mm sections oriented parallel to the ac plane with a thickness of 100-420  $\mu m$ . Polarized and unpolarized infrared spectra were measured using a Bruker IFS 120 Fourier-transform infrared spectrometer coupled with an IR scope I all-reflecting microscope (tungsten source,  $CaF_2$  beam splitter, narrow-band mercury cadmium telluride detector, Al strip polarizer on KRS 5 substrate). A heating stage with  $CaF_2$  windows similar to the one described by Zapunyy et al. (1989) was used for reaching high temperatures. The stage was flushed with  $N_2$  to prevent changes in the redox state of the sample. At each temperature, 200 scans were acquired with 4  $cm^{-1}$  resolution on clear spots of about 400  $\mu m$  diameter. The polarizer was mounted above the heating stage (i.e., between the sample and the detector) so that it also absorbed some of the infrared radiation emitted from the hot sample and thereby increased the signal/noise ratio in the spectra at high temperature (Yang and Keppeler, 2011). The polarized spectra were measured with the electric field vector (E) parallel to the a-axis of different rutile sections, since none of the bands has a significant component in c direction. The background spectra were obtained through the  $CaF_2$  windows of the heating stage at room temperature. To check for water loss during heating, spectra were also measured at room temperature after the heating experiments. The initial water contents of the samples were  $\sim 197$  and 156 ppm as derived from the Beer-Lambert law and the extinction coefficient ( $38000 \pm 4000$   $L \cdot mol^{-1} \cdot cm^{-2}$ ) from Maldener et al. (2001).

#### 9.4. Results and discussions

Unpolarized and polarized (perpendicular *c*) FTIR spectra of the Al-doped and pure rutile up to 500 °C, as well as spectra of the same samples at room temperature after heating, are shown in Fig. 9.1. At room temperature, there are absorption bands at 3278, 3303, 3323  $\text{cm}^{-1}$  in the spectra of Al-doped rutile, while only the 3278  $\text{cm}^{-1}$  band is seen in the spectra of pure rutile. The band at 3278  $\text{cm}^{-1}$  is ascribed to  $\text{Ti}^{3+}$  associated OH groups, while the band at 3323  $\text{cm}^{-1}$  is believed to be related to Al (Lucassen et al., 2012; Vlassopoulos et al., 1993). Compared to the spectra before heating, the spectra after heating show some water loss as indicated by the reduced absorbance, consistent with the rather high diffusion coefficient of OH in rutile (Johnson et al., 1975). However, all major bands seen in the spectra before heating are still visible afterwards (Fig. 9.1; Table 9.1).

The most interesting observation in Fig.9.1 is that the Al-related band at 3323  $\text{cm}^{-1}$  disappears already at 300 °C. A small band (at 3303  $\text{cm}^{-1}$ ) which has never been described before, also disappears upon heating. The disappearance of the 3323  $\text{cm}^{-1}$  band cannot be due to water loss, as the diffusion coefficient of OH in rutile at these low temperatures is very small (Johnson et al., 1975). In addition, the band at 3323  $\text{cm}^{-1}$  appeared again after cooling (Fig. 9.1a and 9.1b). The effect cannot be caused by band overlap due to increased bandwidth either, as can be clearly seen in the Gaussian deconvolution of the bands in Fig.9.2. Also, the peak shifts of the Al-associated band (at 3323  $\text{cm}^{-1}$ ) and the  $\text{Ti}^{3+}$  associated band (at 3278  $\text{cm}^{-1}$ ) with temperature are similar and rule out the possibility of band overlap at 300 °C.

The decreased intensity of the 3323  $\text{cm}^{-1}$  band at low temperatures is unlikely to be due to a change in the extinction coefficient, as the occupancy of the vibrational ground state and of the excited state change only slightly within this limited temperature range. Therefore, the 3323  $\text{cm}^{-1}$  band corresponding to an OH species associated with Al formed only during cooling of the sample to room temperature, but did not exist at the high temperatures expected in subduction zones and the upper mantle. Apparently, protons can rapidly decouple from the  $\text{Al}^{3+}$ -related defect with increasing temperature, and then hop to another site. This process appears to be fully reversible upon cooling. Yang and Keppler (2011) observed a similar effect on the infrared spectra of hydrous olivine.

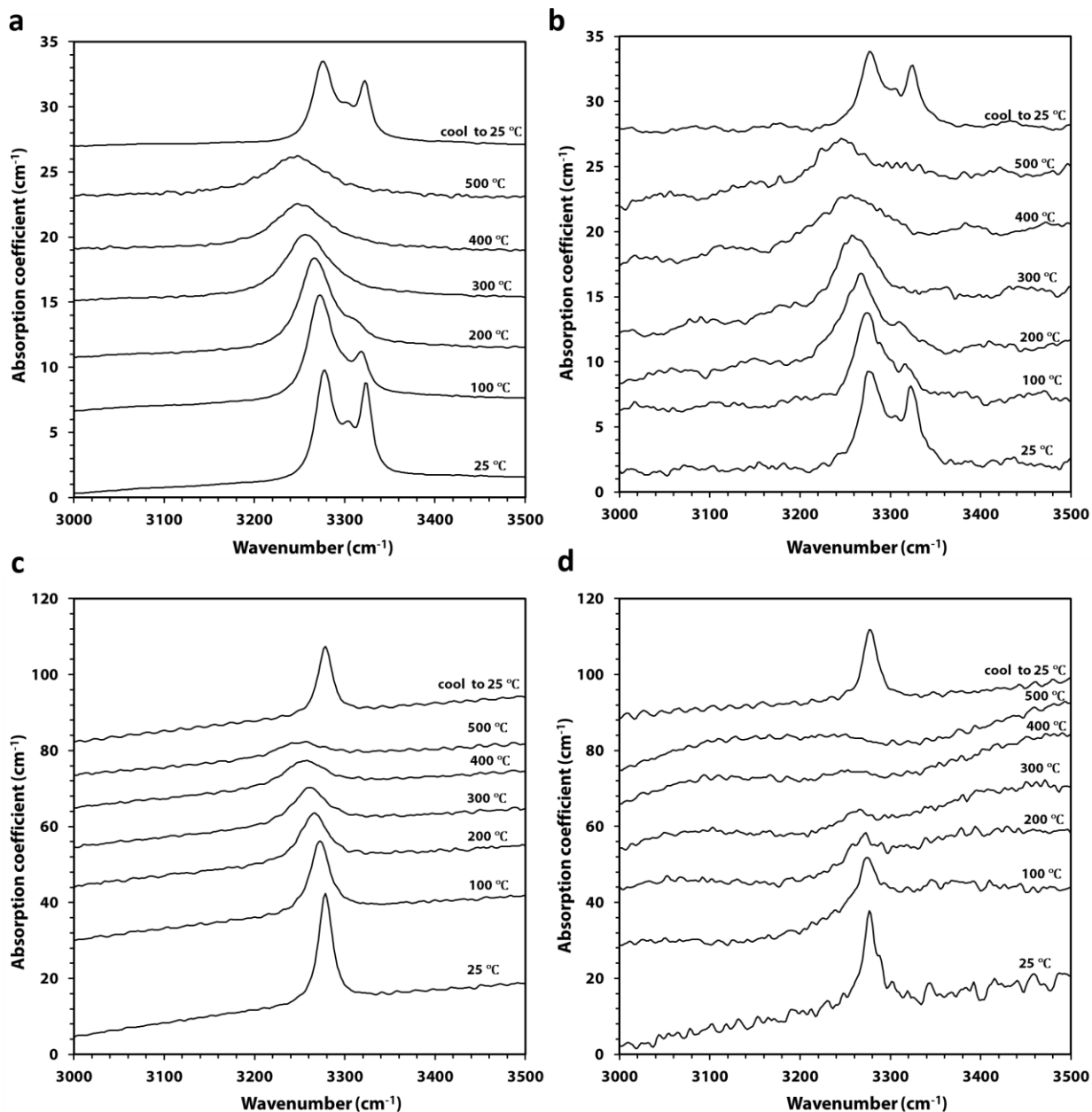


**Fig. 9.1** FTIR spectra of hydrous rutile at various temperatures: (a) unpolarized spectra of Al-doped rutile; (b) polarized spectra (E perpendicular c) of Al-doped rutile; (c) unpolarized spectra of pure rutile; (d) polarized spectra (E perpendicular c) of pure rutile. The initial water contents in the Al-doped rutile and pure rutile are ~197 and 156 ppm, respectively.

**Table 9.1**

OH band positions and band areas in hydrous rutile at various temperatures

T (°C)	Al-doped rutile (unpolarized)				pure rutile (unpolarized)		Al-doped rutile (polarized)				pure rutile (polarized)	
	frequency (cm <sup>-1</sup> )		area (cm <sup>-1</sup> )		frequency (cm <sup>-1</sup> )	area (cm <sup>-1</sup> )	frequency (cm <sup>-1</sup> )		area (cm <sup>-1</sup> )		frequency (cm <sup>-1</sup> )	area (cm <sup>-1</sup> )
25	3278.4	3303.5	3322.7	18.87	3278.3	7.21	3276.5	3305.3	3322.7	17.78	3276.5	5.03
100	3272.6		3317.0	17.10	3272.6	6.76	3274.5		3315.0	16.64	3272.6	4.03
200	3266.8		3311.2	15.28	3266.8	5.50	3266.8		3309.2	15.74	3272.6	2.25
300	3255.3			14.27	3259.1	5.16	3257.2			14.24	3266.8	1.08
400	3247.5			12.87	3255.3	4.25	3255.3			13.34	3253.3	0.73
500	3237.9			10.43	3241.8	2.58	3245.2			11.22		
25*	3276.5	3301.5	3322.7	14.00	3278.4	4.58	3276.5	3305.2	3324.7	14.53	3276.6	3.58

\* after cooling

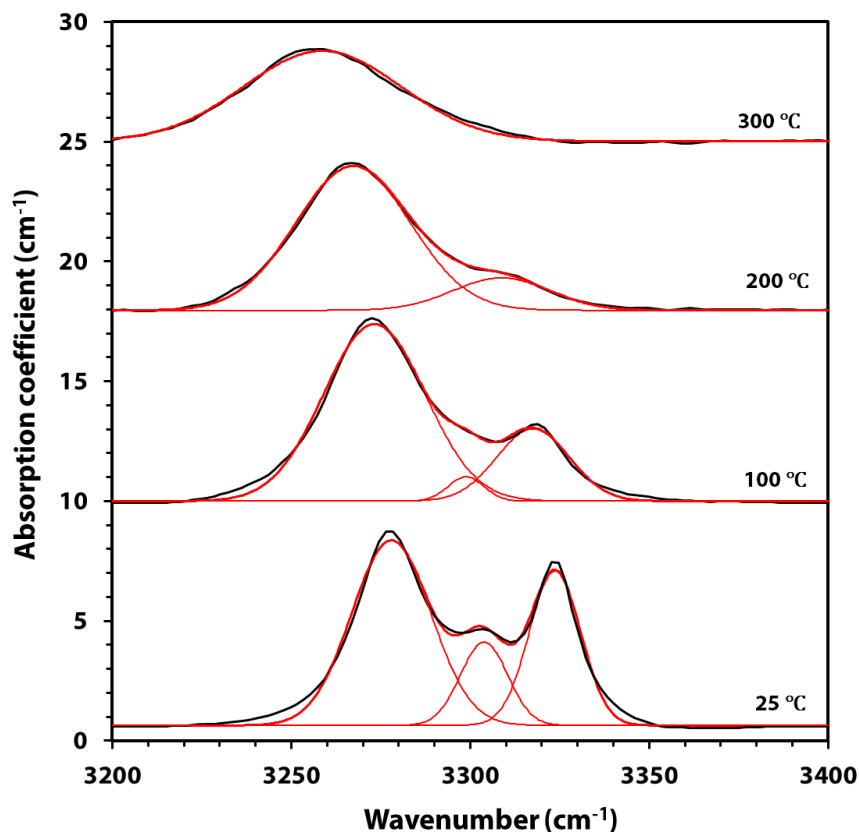


**Fig. 9.2** Deconvolution of the FTIR spectra shown in Figure 9.1a into Gaussian components ( $R^2 > 0.99$  for the fitting). Black lines represent measured spectra, red lines represent deconvolution of the spectra.

Fig. 9.3 and Table 9.1 show that the positions of the OH stretching bands in rutile are very sensitive to temperature. All bands shift to lower frequency with increasing temperature (Fig. 9.1 and Fig. 9.3), consistent with previous studies (Yang et al., 2011). No systematic correlation of  $dv/dT$  with frequency for the corresponding bands, suggesting different substitution mechanisms. This strong downshift is unexpected for a hydrogen-bonded OH group, as with temperature the distances between the oxygen atoms in rutile increase; according to Nakamoto et al. (1955), an increase in oxygen-oxygen distance should increase the OH stretching frequency. Indeed, OH in quartz shows a prominent band at  $3379 \text{ cm}^{-1}$  at room temperature, which shifts by about  $33 \text{ cm}^{-1}$  to higher frequency upon heating from  $-200$  to  $+300 \text{ }^\circ\text{C}$  (Suzuki and Nakashima 1999). The initial frequency of this band is about  $100 \text{ cm}^{-1}$  higher than for the main OH band in rutile, indicating weaker hydrogen bonding in the quartz OH band. Even more surprising is the negative shift of the

band in rutile. The negative shift likely relates to a strong anharmonicity, leading to a weakening of the OH bond (increasing anharmonicity of the OH bond) at high temperature. The OH bond can shift to lower or to higher wavenumbers with increasing temperature (decreasing pressure), depending on the response of the structure in respect to O-H...O, also demonstrated by the studies in other minerals (e.g., Koch-Müller et al., 2003; Mrosko et al., 2010; Watenphul and Wunder, 2010; Yang et al., 2014).

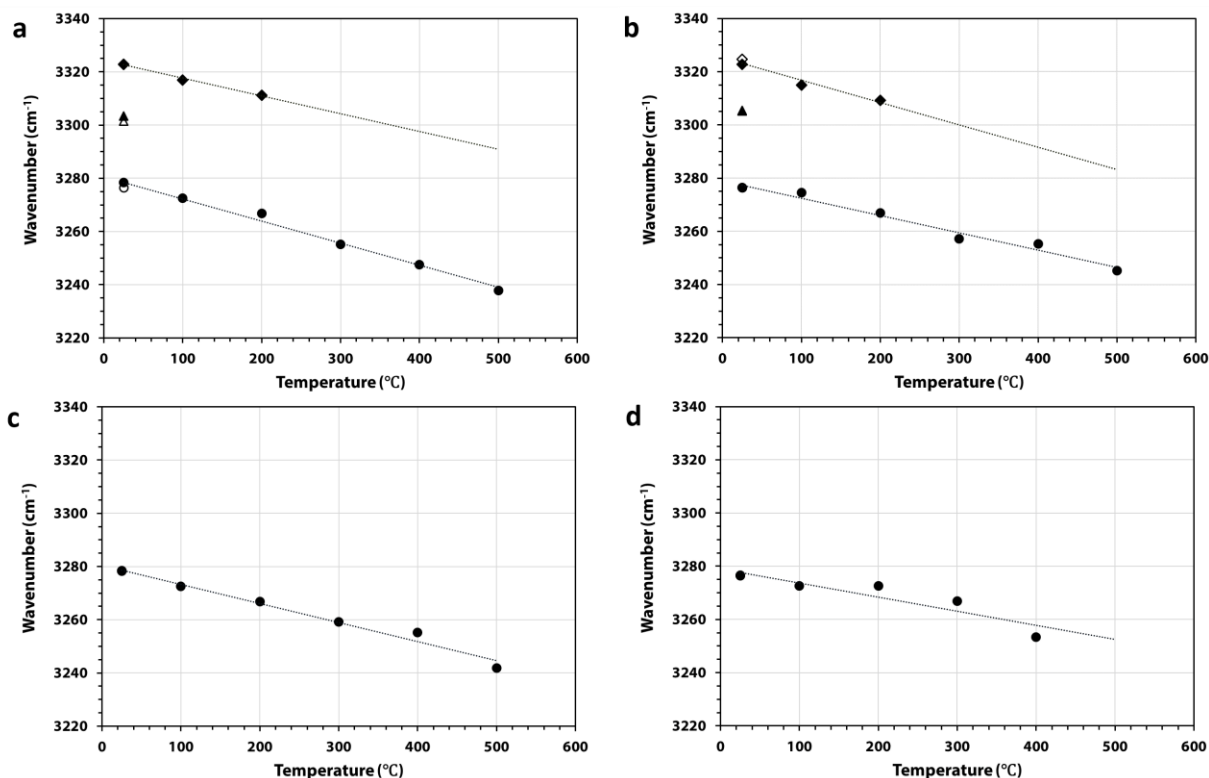


**Fig. 9.3** Temperature dependence of OH-band frequencies as obtained from (a) unpolarized spectra in Al-doped rutile ( $dv/dT$  (cm<sup>-1</sup>/°C) for the bands at 3323 and 3278 cm<sup>-1</sup> is -0.0666 and -0.0831); (b) polarized spectra in Al-doped rutile ( $dv/dT$  for the bands at 3323 and 3278 cm<sup>-1</sup> is -0.0842 and -0.0652); (c) unpolarized spectra in pure rutile ( $dv/dT$  for the bands at 3278 cm<sup>-1</sup> is -0.0716); (d) polarized spectra in pure rutile ( $dv/dT$  for the bands at 3278 cm<sup>-1</sup> is -0.0531). The dashed lines are from linear fits and the unfilled symbols represent the data that cooled to room temperature.

Another interesting observation in the spectra in Fig. 9.1 is the pronounced broadening of the OH band already at low temperatures, which becomes extreme upon heating to 1000 °C with shifting to lower wavenumber (Fig. 9.4). This broadening may be partially due to coupling with lattice

phonons; partially it may reflect the limited lifetime of the OH bond at high temperature. A significant lifetime broadening would be consistent with the observation of rapid proton exchange between different sites already at low temperature (i.e., the disappearance of the OH band related to an  $\text{Al}^{3+}$  defect). If lifetime effects were the only cause for the observed broadening, the average lifetime  $\tau$  of the OH bond could be estimated from the relationship  $\tau\Delta E = h/2\pi$ , where  $\Delta E$  is the width of the band in energy units and  $h$  is the Planck constant. This would yield a lifetime of the OH bond of  $3.5 \times 10^{-14}$  s at 1000 °C. However, since other effects likely also contribute to the observed broadening, this number should only be considered as a lower limit of the actual lifetime. Rapid proton exchange would, however, be consistent with experimental evidence for very high hydrogen mobility in hydrous rutile containing  $\text{Ti}^{3+}$  (Colasanti et al. 2011).

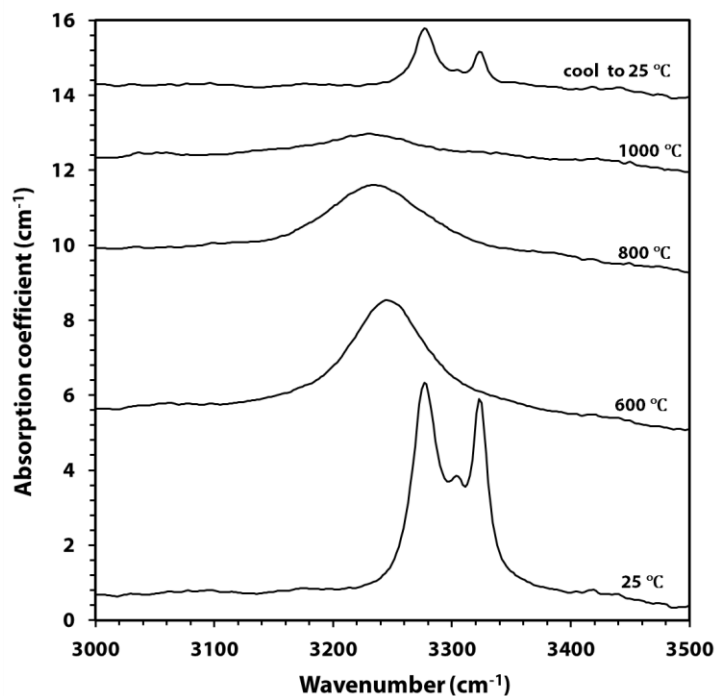


**Fig. 9.4** Unpolarized infrared spectra of OH groups in rutile. Notice the temperature dependence of line broadening.

## 9.5. Conclusion

We show here that H speciation in rutile at ambient conditions is not necessarily the same as in subduction zone and upper mantle conditions. The band at  $3323 \text{ cm}^{-1}$  assigned to OH groups

coupled to Al does not exist at high temperature. The strong downshift of the  $3278\text{ cm}^{-1}$  band and its extreme broadening with temperature indicate a weakening of OH bond strength and a high proton mobility. Since rutile is an important carrier of water and high field strength elements (HFSE), this observation may have major implications not only for understanding the dissolution mechanism for water in rutile, but also for understanding the coupled substitution of H and HFSE in rutile at subduction zone and upper mantle conditions (Lucassen et al., 2012; Vlassopoulos et al., 1993).

## 9.6. Acknowledgments

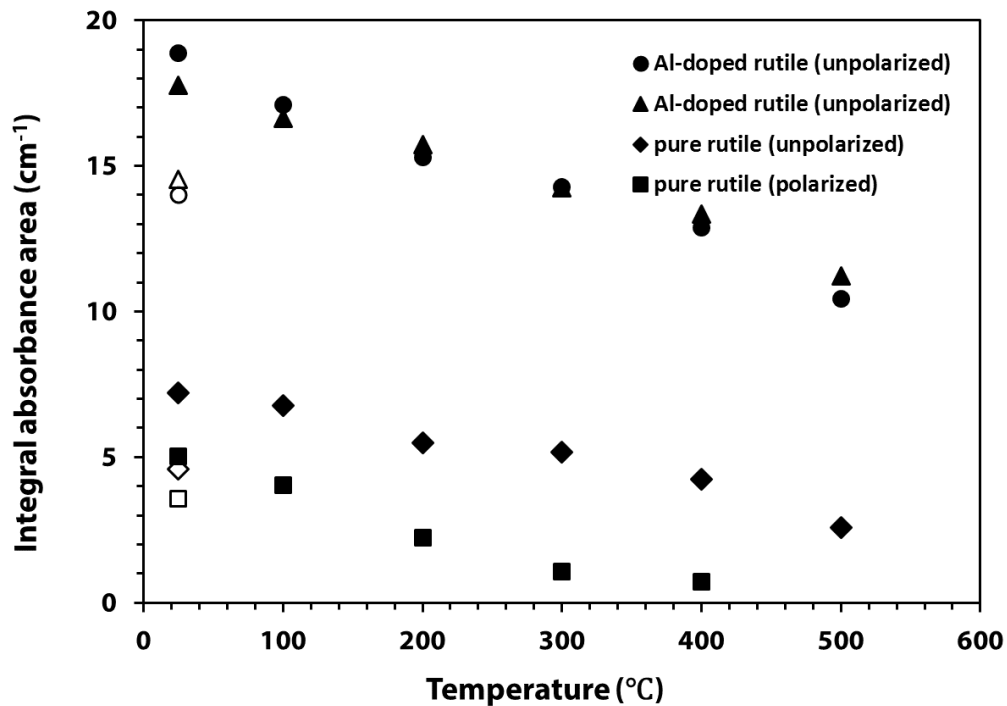
I thank Hans Keppler and Andreas Audéat for their scientific suggestions and helping with experiments, Xiaozhi Yang for discussions, Joanna Emilien for providing the hydrous pure rutile and Raphael Njul for polishing the samples. I also thank the reviewers Monika Koch-Müller and Anton Beran for the comments that help to improve the manuscript, and Milan Rieder for the effective editorial handling of the manuscript. Haihao Guo acknowledges financial support from the China Scholarship Council (CSC) program.

## 9.7. References

- Beran A, Libowitzky E (2006) Water in natural mantle minerals II: olivine, garnet and accessory minerals *Rev Mineral Geochem* 62:169-191
- Bromiley, G., and Hilairret, N. (2005) Hydrogen and minor element incorporation in synthetic rutile. *Mineral Mag* 69:345-358.
- Colasanti, C.V., Johnson, E.A., and Manning, C.E. (2011) An experimental study of OH solubility in rutile at 500-900 °C, 0.5-2 GPa, and a range of oxygen fugacities. *Am Mineral* 96: 1291-1299.
- Deer, W.A., Howie, R.A., and Zussman, J. (1992) An introduction to the rock-forming minerals. vol 696. Longman London.
- Hammer, V.M.F., and Beran, A. (1991) Variations in the OH concentration of rutiles from different geological environments. *Mineral Petrol* 45:1-9.

- Johnson, O.W., Paek, S.H., and DeFord, J.W. (1975) Diffusion of H and D in TiO<sub>2</sub>: Suppression of internal fields by isotope exchange. *Journal of Applied Physics* 46: 1026-1033.
- Koch-Müller M, Dera P, Fei Y, Reno B, Sobolev N, Hauri E, Wysoczanski R (2003) OH-in synthetic and natural coesite. *Am Mineral* 88:1436-1445.
- Lucassen, F., Koch-Müller, M., Taran, M., and Franz, G. (2012) Coupled H and Nb, Cr, and V trace element behavior in synthetic rutile at 600 °C, 400 MPa and possible geological application. *Am Mineral* 98: 7-18.
- Maldener, J., Rauch, F., Gavranic, M., and Beran, A. (2001) OH absorption coefficients of rutile and cassiterite deduced from nuclear reaction analysis and FTIR spectroscopy. *Mineral Petrol* 71: 21-29.
- Matthews, W., Linnen, R.L., and Guo, Q. (2003) A filler-rod technique for controlling redox conditions in cold-seal pressure vessels. *Am Mineral* 88: 701-707.
- Mrosko M, Koch-Müller M, Hartmann K, Wirth R, Dörsam G (2010) Location and quantification of hydrogen in Ca- and Sr-anorthite. *Eur J Mineral* 22:103-112.
- Nakamoto, K., Margoshes, M., and Rundle, R. (1955) Stretching frequencies as a function of distances in hydrogen bonds. *Journal of the American Chemical Society* 77: 6480-6486.
- Rossmann, G.R., and Smyth, J.R. (1990) Hydroxyl contents of accessory minerals in mantle eclogites and related rocks. *Am Mineral* 75: 775-780.
- Suzuki, S., and Nakashima, S. (1999) In-situ IR measurements of OH species in quartz at high temperatures. *Phys Chem Minerals* 26: 217-225.
- Vlassopoulos, D., Rossmann, G.R., and Haggerty, S.E. (1993) Coupled substitution of H and minor elements in rutile and the implications of high OH contents in Nb- and Cr-rich rutile from the upper mantle. *Am Mineral* 78: 1181-1191.
- Watenphul A, Wunder B (2010) Temperature dependence of the OH-stretching frequencies in topaz-OH. *Phys Chem Minerals* 37:65-72.

- Yang, X., and Keppler, H. (2011) In-situ infrared spectra of OH in olivine to 1100 °C. *Am Mineral* 96: 451-454.
- Yang X, Keppler H, Dubrovinsky L, Kurnosov A (2014) In-situ infrared spectra of hydroxyl in wadsleyite and ringwoodite at high pressure and high temperature. *Am Mineral* 99:724-729.
- Yang, Y., Xia, Q., Feng, M., and Gu, X. (2011) In situ FTIR investigations at varying temperatures on hydrous components in rutile. *Am Mineral* 96: 1851-1855.
- Zapunnyy, S., Sobolev, A., Bogdanov, A., Slutsky, A., Dmitriev, L., and Kunin, L. (1989) An apparatus for high-temperature optical research with controlled oxygen fugacity. *Geochem Int* 26:120-128.
- Zheng, Y.-F. (2009) Fluid regime in continental subduction zones: petrological insights from ultrahigh-pressure metamorphic rocks. *J Geol Soc* 166: 763-782.



**Supplementary Figure.** Integral absorbances of infrared bands of hydrous rutile as a function of temperature. The open symbols represent data measured after cooling to room temperature.

## **Acknowledgments**

I would like to sincerely express my thanks to my supervisors Prof. Hans Keppler and Dr. Andreas Audétat. Thank them for giving me the chance to study in Bayerisches Geoinstitut (BGI) in the form of combined master and Ph.D. project and helping me apply the China Scholarship Council (CSC) program. Thank them for their brilliant ideas and excellent helps in the research. They brought me into the high temperature and pressure study of geofluid in the Earth. Without their immense knowledge and great patience in all the time of research, the present thesis has not been possible.

I am very grateful to Andreas Audétat for his kind help in research and life. His patience, helpness and persistency will significantly affect me in the future. I thank Robert Arato and Johannes Buchen for translating the German parts of this thesis. I appreciate all BGI staff excellent helps, Raphael Njul and Hubert Schulze for preparing samples, Sven Linhardt for electric assists, Detlef Krauß and Anke Potzel for help with the microprobe measurements, Gerti Golner and Ulrike Trenz for help with chemicals, Stefan Keyssner, Petra Buchert and Lydia Kison-Herzing for administrative and general helps.

During the years in Bayreuth, I developed friendship with BGI members and other friends, thank all of them for long time helps and supports. Without them, my life would be boring and a lack of happiness.

I would also like to thank my family. My parents always did their best to provide better supports to us. Thank them for their supports for many years.

## **Erklärung**

Hiermit erkläre ich an Eides statt, dass ich die vorliegende Arbeit selbstständig verfasst und keine anderen als die angegebenen Quellen und Hilfsmittel verwendet habe. Weder wurde die Dissertation anderweitig zur Erlangung eines akademischen Grades eingereicht noch habe ich bisher diese oder eine gleichartige Doktorprüfung endgültig nicht bestanden. Weiterhin erkläre ich, dass ich keine Hilfe von gewerblichen Promotionsberatern bzw. -vermittlern oder ähnlichen Dienstleistern in Anspruch genommen habe und auch nicht beabsichtige, diese zukünftig in Anspruch zu nehmen. Mit einer gesonderten Überprüfung der elektronischen Fassung meiner Dissertation hinsichtlich ihrer eigenständigen Anfertigung bin ich einverstanden, sofern die Überprüfung unter Wahrung meiner Urheberrechte und des Datenschutzes erfolgt.

Bayreuth, den 17. Juli 2017

Haihao Guo